Band quantum geometry and electronic correlations

Florian Simon

université PARIS-SACLAY

Géométrie quantique de bandes et interactions électroniques

Band quantum geometry and electronic correlations

Thèse de doctorat de l'université Paris-Saclay

École doctorale n° 564, Physique en Île-de-France (PIF)
Spécialité de doctorat: Physique
Graduate School : Physique
Référent : Faculté des Sciences d'Orsay

Thèse préparée dans l'unité de recherche **Laboratoire de Physique des Solides (Université Paris-Saclay, CNRS)**, sous la direction de **Mark-Oliver GOERBIG**, directeur de recherche CNRS, la co-direction de **Marc GABAY**, professeur des universités à l'Université Paris-Saclay, et le co-encadrement de **Corentin MORICE**, maître de conférences à l'Université Paris-Saclay.

Thèse soutenue à Paris-Saclay, le 28 novembre 2024, par

Florian Roger Yvon SIMON

Composition du jury

Membres du jury avec voix délibérative

Pascal SIMON Professeur des universités, Université Paris-Saclay Laboratoire de Physique des Solides	Président
Jérôme CAYSSOL Professeur des universités, Université de Bordeaux Laboratoire Ondes et Matière d'Aquitaine	Rapporteur et Examinateur
Adolfo GRUSHIN Chargé de Recherche de classe nationale, CNRS Institut Néel	Rapporteur et Examinateur
Nicolas BERGEAL Professeur des universités, ESPCI Laboratoire de Physique et d'Étude des Matériaux	Examinateur
Emil Johansson BERGHOLTZ Professeur, Stockholms Unversitet Département de Physique	Examinateur
Cécile REPELLIN Chargée de Recherche de classe nationale, CNRS Laboratoire de Physique et Modélisation des Milieux Condensés	Examinatrice

THESE DE DOCTORAT
NNT : 2024UPASP151

université PARIS-SACLAY

ÉCOLE DOCTORALE
Physique en Île-de-France (PIF)

Titre: Géométrie quantique de bandes et intéractions électroniques.
Mots clés: Théorie des bandes, Géométrie quantique, Matière topologique, Corrélations électroniques, Supraconductivité, Fonctions de Green

Résumé: Deux des piliers actuels de la matière condensée sont d'une part la matière corrélée et d'autre part la matière topologique, avec la géométrie quantique comme sous-jaçent. La physique des matériaux corrélés, en tant que domaine de recherche, a pris forme vers le milieu du 20ème siècle avec la découverte des isolants de Mott et de l'effet Kondo. Le domaine des matiériaux topologiques a quant à lui ses origines dans les années 1980 avec l'effet Hall quantique entier, et a globalement pris forme dans les années 2000. La géométrie quantique, qui sous-tend la topologie, repose sur la théorie des bandes, qui décrit les matériaux en termes d'excitations élémentaires. Les domaines de la matière topologique et de la matière corrélée sont donc très différents, et se sont développés séparément. Un effort de recherche est en cours pour rapprocher ces deux domaines, et cette thèse en fait partie. En effet, dans cette thèse nous explorons des exemples de relations entre la géométrie quantique venant de la théorie des bandes et les interactions électroniques. Dans la première partie de cette thèse, nous passons en revue les fondements de la théorie des bandes ainsi que de ses extensions géométrique et topologique. Nous faisons ceci afin de soutenir que les excitations élémentaires décrites par la théorie des bandes sont des quasiparticules, appelées fermions de Bloch, dont le charactère émergent leur confère des propriétés que n'ont pas les électrons élémentaires. Un exemple notable est la géométrie quantique. Nous soutenons que cette dernière quantifie la non-localité du fermion de Bloch, qui elle-même provient des transitions interbandes virtuelle. Nous présentons de plus les fondements de la théorie BCS ainsi que des fonctions de Green. Motivés par l'éventuelle différence entre des paires de Cooper formées par des fermions de Bloch et par des électrons, la seconde partie de la thèse est dévouée à la relation entre la géométrie quantique de l'état normal et l'état supraconducteur. Nous trouvons que cette relation est ambivalente, et qu'elle peut largement être comprise en invoquant la non-localité des fermions de Bloch. D'une part, cette non-localité engendre un supercourant piloté par les mouvements de point-zéro. D'autre part, cette même non-localité affaiblit l'interaction d'appariement du fait d'un terme de Darwin émergent. Dernièrement, dans la troisième partie du manuscript nous explorons la relation entre la géométrie quantique, la topologie et les fonctions de Green. Nous montrons que dans les systèmes sans interactions les propriétés analytiques de la fonction de Green peuvent être mises à profit pour extraire les invariants topologiques $\mathbb{Z}_2$. Nous terminons en proposant une généralisation de la géométrie quantique au-delà de la limite des fermions libres en utilisant la fonction de Green.

Title: Band quantum geometry and electronic correlations.

Keywords: Band theory, quantum geometry, topological matter, electronic correlations, superconductivity, Green's function

Abstract: Two pillars of contemporary condensed matter physics research are correlated matter and topological matter, with its underlier quantum geometry. The physics of materials whose properties are governed electronic correlations as a research domain has taken shape around the midth of the 20th century with the discovery of Mott insulators and the Kondo effect. In contrast, the field of topological matter is more recent as it originated from the integer quantum Hall effect in the 1980s, and has largely taken shape in the 2000s. Quantum geometry relies on band theory, which describes materials in terms of single-particle excitations. The fields of topological matter and correlated matter are thus significantly different fields that have mostly evolved separately. A contemporary research effort is underway to bring these two pillars of condensed matter physics closer. As part of that effort, this PhD thesis explores interplays between quantum geometry and electronic interactions. In the first part of the manuscript, we extensively review the foundations of band theory and its geometrical and topological extensions. We do so to argue that the single-particle excitations described by band theory are quasiparticles, dubbed Bloch fermions, whose emergence endows them with properties not shared with elementary electrons, one notable example being quantum geometry. We argue that the latter quantifies the non-locality of the Bloch fermion that arises from virtual interband transitions. We additionally discuss the fundamentals of BCS theory and of Green's functions. Motivated by the apparent difference between Cooper pairs formed by Bloch fermions and by elementary electrons, the second part of the manuscript is devoted to the study of the relation between the normal state quantum geometry and the superconducting state. Our findings show that this relation is ambivalent, and can largely be understood using the non-locality argument. On one hand, the non-locality of the Bloch fermions allows for zero-point motion-driven supertransport. On the other hand, their non-locality weakens the pairing interaction through an emergent Darwin term. Lastly, in the third part of the manuscript we investigate interplays between quantum geometry, topology and Green functions. We show that in non-interacting systems the analytic properties of the Green's function can be used to extract the value of $\mathbb{Z}_2$ topological invariants. Finally, we propose a generalization of quantum geometry beyond the free-fermion limit using Green functions.

Remerciements/Acknowledgements

Mes premiers remerciements reviennent à ma direction de thèse. Tout d'abord à mon directeur de thèse Mark, pour m'avoir pris en thèse et laissé une très grande liberté scientifique. J'avais toujours la garantie d'avoir la décision finale sur les projets de recherche, avec qui je travallais, sur ce que j'écrivais dans les papiers et dans le manuscript, même quand tu n'étais pas forcément d'accord. Cette liberté n'est qu'un des nombreux enseignements que je tire à tes côtés. Une conséquence de cette liberté est notre collaboration avec Marc, qui est ainsi devenu mon codireceur. Merci Marc de m'avoir introduit à un pan de la physique de la matière condensée qui m'était largement inconnu. J'ai énormément appris de notre travail sur LAO/STO, même s'il a souvent été éprouvant de mon côté. Ce côté matériau et proche des expériences de la matière condensée reste néanmoins ma plus grosse lacune, et je m'efforcerais d'y remédier dans la suite de ma carrière. Au-delà de tout ça, nos discussions des Mardi et Jeudi me manqueront après mon départ du LPS, c'était un plaisir de te côtoyer. Enfin, merci aussi à Corentin, maintenant mon co-encadrant de thèse. C'était aussi un plaisir de bosser avec toi et de te côtoyer ! Je suis vraiment reconnaissant à bien des égards à vous trois pour cette thèse, et l'encadrement humain dont j'ai bénéficié.

Je tiens ensuite à remercier mon comité de suivi, c'est-à-dire Charis Quay et Benoît Douçot. J'aimerais aussi évidemment remercier le jury de thèse, notamment Adolfo Grushin et Jérôme Cayssol qui ont accepté d'être rapporteur de ce ~~pavé~~ manuscript. Je voudrais aussi remercier Cécile Repellin, Nicolas Bergéal ainsi que Emil J. Bergholtz d'avoir accepté le rôle d'examinateur.rice. Pour finir, merci bien sûr à Pascal d'avoir été le président de mon jury. Qui d'autre que Dr. Simon pour m'accorder ce même titre.

Ce fut aussi un plaisir d'effectuer ces trois (un peu plus) années dans le groupe Théo. De la part des permanents, notamment Mark, Marc, Corentin, Frédéric[1], Gilles, Andrej et Pascal. J'ai énormément bénéficié de votre part scientifiquement, ainsi que sur la Recherche en général. En ce qui concerne les non-permanents, je remercie d'abord ceux qui étaient là quand je suis arrivé en thèse. Étienne, Marina, Ansgar, Mateo, JB (mon premier coloc de bureau) et Baptiste, ainsi que Lise qui est arrivée en même temps que moi. Il y a ensuite ceux qui sont arrivés après moi. Merci à Antoine C., Adrien, Robin, Raphaël, Andrea, Andrii, Lena et Yinhong. Merci aussi aux trois mousquetaires de l'X: Olivier, Thibault (la relève) et Reda (mon deuxième coloc de bureau), notamment pour supporter mon humour.

Plus largement, ce fut un plaisir de faire ma thèse au LPS et profiter de la super ambiance du labo parmi les non-permanents. Là la liste devient un peu longue, mais merci entre autres à Xavier, Elina, Camille, Alice R., Marion, Malo, Yassine, Alice E-S, Matthieu, Malar, Greis, Sara, Jules, Kika, Lucas[2] ainsi qu'à Antoine, Antoine, Antoine et Antoine (puissance 4). Plus sérieusement, merci à Antoine Roll pour les moments de déconne et les quelques concerts[3] et à Antoine G-F pour les pastis en weekend non-permanents. Entre les weekends non-permanents, bars, Cookies club et les moments quotidiens, le labo va me manquer ! C'était un plaisir de spammer des memes dans la conv'.

[1] Merci d'être la sentinelle du groupe !

[2] J'avais dit c'était long

[3] Merci aussi à mini Poutine !

Maintenant, quelques mentions spéciales de la thèse. Merci à la rue de la Colline pour m'assurer un minimum de compétences en alpinisme. Merci à Notilus pour montrer parfaitement en quoi la sous-traitance et le management vertical[4] Macronien est le système de gouvernance parfait pour la recherche française. Merci aussi à l'ISMO qui fournit probablement la plus belle vue que j'aurais jamais depuis un bureau.

La thèse étant aussi l'aboutissement de mes études, j'aimerais aussi faire quelques remerciements à des personnes que j'ai rencontré avant ma thèse.

I'd like to thank the Nupace Sweatposting gang (aka the Free Hong Kong council of shitposting), with Corentin, Daisy, Clément, Ying, Duc, Esteban, Fraser, Gabriel, Seffy, Yoga and Saxon. Amongst you, men and women of culture, I learned the ways of shitposting and weebs. Some highlights include the endless nights on Strong Zeros and the ice cream incident. This year in Nagoya would clearly not have been as fun without you.

Merci évidemment au groupe des Jeudis chez Tristan: Tristan bien sûr, mais aussi PE, Chloé, Juliette, Thibault, Florine et Sophie. Le magistère (et le Get27) reste un super souvenir grâce à vous, et plus récemment avec les longs appels Discord et nos soutenances.

J'aimerais aussi remercier mes profs de prépa au Lycée Montesquieu, et notamment mes profs de Maths Yannick Le Bras et Frédéric Kuczma, mais aussi Antoine Bricard et David Devaux en physique. Même si j'ai changé pour la physique après la prépa, les maths ont quand même formé ma colonne vertébrale scientifique.

Merci aussi à l'état social français qui, bien qu'actuellement imparfait, est le seul vrai rempart à la reproduction sociale.

Je tiens aussi à remercier ma famille pour leur soutien dans ces longues études, même quand je suis parti à l'autre bout du monde.

Mes derniers remerciements vont à Alice, ma meilleure rencontre et un vrai bonheur et soutien depuis ce road trip entre Hakone et Tokyo, malgré la distance. Merci pour tout et plus encore dans le futur.

Allez, Tôpette !

[4] De quoi faire pâlir la rue de la Colline

Introduction générale de la thèse

De la même façon que l'eau est essentielle à la vie, l'électricité est essentielle à la vie moderne. Ce faisant, la physique de la matière condensée a eu un impact incommensurable sur la société moderne. En effet, la maîtrise de l'électronique et de l'âge de l'information lui ayant succédé ont largement été dues à l'usage des semiconducteurs, un produit de la recherche en matière condensée. Dans la recherche contemporaine, les supraconducteurs se sont aussi révélés indispensables. Les réacteurs de fusion nucléaire expérimentaux, tels que les stellarators ou les tokamaks, utilisent les supraconducteurs pour produire les champs magnétiques nécéssaires pour contenier le plasma. Les supraconducteurs se sont aussi révélés nécéssaires pour repousser les limites des accélérateurs de particules afin d'atteindre des énergies toujours plus élevées. Ces derniers sont eux-mêmes des outils primordiaux pour de nombreux domaines scientifiques comme la physique des hautes énergies. L'identification des molécules en chimie se fait grandement à l'aide de la résonance magnétique nucléaire, et ce même principe est grandement utilisé en médecine avec l'imagerie par résonance magnétique (IRM). Ces deux outils utilisent aussi des supraconducteurs pour produire les champs magnétiques nécéssaires. De nos jours, la physique de la matière condensée est devenue l'un des, si ce n'est le, domaine le plus vaste de la physique. Parmi les nombreux pilliers de la matière condensée, nous pouvons en identifier deux; les corrélations éléctroniques et les phases topologiques, cette dernière étant engendrée par la géométrie quantique. La recherche sur les corrélations électroniques se concentre naturellement sur les matériaux dont certaines propriétés sont gouvernées par les interactions électroniques. Ce domaine de recherche a pris forme dans la moitié du vingtième siècle avec la découverte des isolants de Mott ainsi que de l'effet Kondo, et n'a que grandi depuis. Quelques exemples notables de phases électroniquement corrélées sont les phases Mott et Kondo, mais aussi les matériaux à fermions lourds, les supraconducteurs, et l'effet Hall quantique fractionnaire. Contrairement à ces dernières, les phases topologiques dont le caractère topologique vient de leur structure de bandes, reposent sur la théorie des bandes dont la validité vient du fait que les électrons n'interagissent pas entre eux. De plus, les phases topologiques sont caractérisées par des invariants topologiques tandis que les phases électroniquement corrélées peuvent souvent être décrite dans un paradigme de Landau basé sur la brisure de symmétries. La matière topologique, en tant que domaine de recherche, trouve ses origines dans la découverte, et l'étude, de l'effet Hall quantique entier dans les années 1980. Il a ensuite largement pris forme dans les années 2000. Nous pouvons ainsi déclarer que les champs de recherche de la matière électroniquement corrélée et de la matière topologique sont radicalement différent, et ont grandement évolués indépendemment.

Un effort de recherche contemporain vise à rapprocher ces deux pilliers de la matière condensée, et cette thèse de doctorat en fait partie.

Dans cette thèse, nous étudions des exemples d'inter-influences entre la géométrie quantique, la topologie et les interactions électroniques. La structure du manuscript est basée sur l'observation que la relation entre la géométrie quantique et les interactions électroniques est à deux sens. En effet, dans la seconde partie du manuscript nous étudions quelques exemples d'influences de la géomtrie quantique de l'état normal sous-jaçent un état supraconducteur. Ce travail a été initialement motivé par la découverte, notamment dans notre groupe de recherche, de l'influence de la courbure de

Berry des composants d'un exciton sur des propriétés spectrales de ce dernier. Le questionnement a alors été d'explorer si de tels effets étaient aussi présents dans le cas des paires de Cooper. La seconde partie de ce manuscript confirme cette hypothèse. Une conclusion majeure de cette partie du manuscript est que la différence entre les électrons élémentaires et les fermions de Bloch émergents décrit par la théorie des bandes est cruciale afin de comprendre comment la géométrie quantique de bandes sans intéractions éléctroniques peut affecter une phase électroniquement corrélée. La troisième partie de ce manuscript se place en opposée de la seconde, se concentrant en effet sur la relation entre les fonctions de Green et la topologie et géométrie quantique de bandes, dans les systèmes avec et sans interactions électroniques.

Afin d'établir une base conceptuelle et formelle saine, de manière auto-cohérente, la première partie de ce manuscript vise à aller en profondeur sur les fondations de la théorie des bandes ainsi que de ces extensions topologique et géométrique. Cette motivation explique en partie sa longueur. Nous commençons donc par revisiter les fondations de la théorie des bandes et la méthode de liaisons fortes. L'objectif principal, d'ordre conceptuel, est d'établir que le théorème de Bloch (et donc la théorie des bandes) décrit des excitations à une particule *émergeant* de l'intéraction de Coulomb entre les électrons et les noyaux atomiques composant le crystal. En tant que tel, ces excitations peuvent être considérées comme des *quasiparticules* (dépendant directement du matériau), que nous appelons des fermions de Bloch. Nous procédons ensuite par décrire la théorie géométrique des bandes, où la géométrie quantique apparaît comme une conséquence direct du caractère quasiparticulaire des fermions de Bloch. Nous arguons en effet que la géométrie quantique est une conséquence, et une mesure directe, de la non-localité du fermion de Bloch, c'est à dire des fluctuations quantiques de la position de ce dernier. Ces fluctuations quantiques proviennent de transitions interbandes virtuelles. Nous procédons ensuite par introduire la théorie topologique des bandes, la supraconductivité, et les rudiments des fonctions de Green.

En partant de la première partie du manuscript, nous inférons les questions ouvertes suivantes: Qu'arrive-t'il si les paires de Cooper sont formées par des fermions de Bloch, et non des électrons ? Comme nous l'avons, une différence majeure entre les électrons et les fermions de Bloch est que ces derniers portent de la géométrie quantique. Ceci pose alors naturellement la question de l'effet de la géométrie quantique de l'état normal sur l'état supraconducteur associé. Comme mentionné précédemment, la second partie du manuscript se concentre alors sur cette question. Motivés par la découverte de l'effet de la courbure de Berry sur les excitons, nous commençons par étudier l'effet de la courbure de Berry de l'état normal sur un supraconducteur dans le cas où les fermions de Bloch sont des fermions de Dirac massifs. Nous nous attachons ensuite à étudier un effet de la métrique quantique de l'état normal sur un supraconducteur dans le cas des interfaces d'oxides orientées dans la direction (111). Nous finissons ensuite par formuler des interprétations physiques des effets dont nous avons discuté, basé sur l'interprétation de la géométrie quantique en terme de non-localité. Les résultats des deux premiers chapitres sont publiés dans les Références [1, 2] respectivement.

Enfin, comme mentionné précédemment la troisième partie du manuscript se concentre sur la relation entre les fonctions de Green d'une part et la géométrie quantique et topologie de bande d'autre part. Nous nous concentrons dans un premier temps sur les sytèmes sans interactions électroniques décrits par les invariants topologiques $\mathbb{Z}_2$. Nous nous concentrons ensuite sur les sytèmes avec interactions électroniques, où nous formulons une extension du tenseur quantique géométrique en

terme de fonctions de Green. Cette troisième partie représente une travail inachevé à l'écriture de ce manuscript, et présente donc des résultats partiels.

General introduction to the present PhD thesis

Water is essential to life, as electricity is for modern life. In doing so condensed matter physics has had enormous impacts on society. Indeed, the mastery of electricity in the form of electronics, and the contemporary information age were largely due to the use of semiconductors. In contemporary research, superconductors have become invaluable in many domains. Experimental nuclear fusion reactors, such as stellarators and tokamaks, all use superconductors to contain the plasma. Superconductors have proven necessary to reach ever higher energies in particle accelerators, themselves being invaluable to high-energy physics and other domains of research. The identification of molecules in chemistry is largely done using nuclear magnetic resonance (NMR). Even in medicine, magnetic resonance imaging (MRI) devices have become invaluable to diagnose patients. Nowadays, the research in condensed matter physics has become one of, if not the, largest domain of physics. Among its many pillars, we may identify two: electronic correlations and topological matter, with its underlying quantum geometry. The research on electronic correlations focuses on materials whose electronic properties are governed by electronic interactions. It has taken shape in the middle of the twentieth century with the discovery of Mott insulators and the Kondo effect, and has since grown to be a significant part of condensed matter physics. Notable examples of correlated phases are the Mott and Kondo phases, heavy fermion materials, superconductors, and the fractional quantum Hall phases. In contrast topological phases, which are topological due to their peculiar band structures, rely on band theory which is valid only when the electrons are considered independent. Additionally, topological phases are characterized by topological invariants whereas correlated phases can often be described by a Landau paradigm based on symmetry breaking. The field finds its origins in the discovery of the integer quantum Hall effect in the 1980s, and has largely taken shape in the 2000s. The fields of correlated matter and topological matter are therefore significantly different, and have mostly evolved separately.

A contemporary research effort is ongoing to bring these two pillars of condensed matter physics closer. The present PhD thesis is part of this effort.

In this PhD thesis, we study examples of interplay between quantum geometry, topology and electronic correlations. The structure of the manuscript is based on the observation of the two-way relationship between quantum geometry and electronic correlations. Indeed, the second part of the manuscript studies some examples of effects of the quantum geometry of the normal state on the superconducting phase. This work was at first motivated by preceding work in our group, where it was discovered that the quantum geometry of electrons affects the properties of excitons. The question then was whether similar effects could be unveiled in Cooper pairs. In the second part of the manuscript we answer positively to this question. One main conclusion of this part of the manuscript is that the difference between the elementary electrons and the emergent Bloch fermions described by band theory becomes necessary in order to understand how non-interacting quantum geometry affects phases ruled by electronic correlations. In contrast the third part focuses on how the Green's function relates to topology and quantum geometry, in the non-interacting and interacting regimes.

In order to have the needed theoretical and conceptual framework, in a self-contained manner, the first part of the manuscript aims to go in depth into the foundations of band theory as well as

its geometrical and topological extensions. This motivation explains the length of the first part of the manuscript. We begin by revisiting the foundations of band theory and of the tight-binding method. The main conceptual aim is to argue that the Bloch theorem describes single-particle excitations that *emerge* from the electron-nuclei Coulomb interaction, and can as such be considered as quasiparticles, that we call the Bloch fermions. We then consider the geometrical extension of band theory, where quantum geometry appears as a direct consequence of the quasiparticle character of the Bloch fermion. We argue that quantum geometry is a direct consequence, and quantifier, of the non-locality of the Bloch fermion, that is the quantum fluctuations of its position. These quantum fluctuations stem from virtual interband transitions. We also discuss the fundamentals of superconductivity and introduction some notions of Green functions.

From the first part of the manuscript we then infer the following open question: What if Cooper pairs are formed by Bloch fermions instead of elementary electrons ? As one difference between electrons and Bloch fermions is quantum geometry, this poses the question of the influence of the normal state quantum geometry on the superconducting state. The second part of the manuscript, the core of the PhD thesis, is then devoted to studying the relation between the normal state quantum geometry and superconductivity. Motivated by previous work where Berry curvature effects were found in excitons, we begin by studying the effect of the normal state Berry curvature on superconductivity in the example of massive Dirac fermions. We then study an effect of the normal state quantum metric in (111) oriented oxide interfaces. Finally, we formulate physical interpretations of the effects we have discussed thus far based on the link we have established between quantum geometry and the non-locality of the Bloch fermions forming the Cooper pairs. Part of the scientific results presented in this part of the manuscript were published in Refs. [1, 2].

The third part of the manuscript considers some interplays between Green functions and quantum geometry, as well as with topology. We first consider non-interacting systems and $\mathbb{Z}_2$ topological invariants, and then formulate an extension of the quantum geometric tensor beyond the free-fermion limit using Green's function. The third part is a less accomplished work and therefore presents incomplete results.

Résumé du manuscript

- Dans le Chapitre 1, nous revisitons les fondations de la théorie des bandes, en partant de l'Hamiltonien de la matière condensée ainsi que les approximations constituant le domaine de validité du théorème de Bloch. Nous prouvons ensuite ce dernier, en introduisant sur le chemin des notions fondamentales comme la zone de Brillouin ou le moment crystallin. La contribution personnelle principale de ce chapitre est la forte emphase sur l'idée que les excitations à une particule décrites par le théorème de Bloch sotn des quasiparticules, appelées fermions de Bloch, qui émergent de l'interaction de Coulomb entre les électrons et les nucléons formant le réseau crystallin. Nous finissons ensuite le chapitre en introduisant la méthode des liaisons fortes, suivi de l'exemple du réseau à nid d'abeilles. À partir de ce dernier, nous formulons le modèle de basse énergie du "graphène gappé", où les fermions de Bloch sont des fermions de Dirac massifs.

- Dans le Chapitre 2 nous introduisons en profondeur les différents aspects de la géométrie quantique, dans la théorie des bandes et au-delà. Nous commencons par formellement introduire les différents objets de la géométrie quantique, soit le tenseur quantique géométrique ainsi que la courbure de Berry et la métrique quantique. Ces derniers émergent alors directement de la partie de l'état de Bloch associée à l'interaction électron-nucléon. Nous discutons ensuite plusieurs propriétés de la géométrie quantique. L'essentiel du chapitre est dévoué à une série de six points de vue, chacun révélant la géométrie quantique sous différents angles. Le premier de ces points de vue explique comment la géométrie quantique s'inscrit dans le contexte plus large de la métrologie quantique. Le deuxième quant à lui se base sur le premier pour construire un pont formel entre la métrologie quantique et la théorie des bandes. Il en résulte que, dans les modèles de basse énergie, la géométrie quantique quantifie la non-localité du fermion de Bloch, c'est-à-dire les fluctuations quantique de sa position. Le trosième point de vue interprète alors ces fluctuations quantique comme une conséquence de transitions inter-bandes virtuelles. Le quatrième point de vue mentionne la dualité entre la courbure de Berry et le champ magnétique, et le cinquième introduit la vitesse de dérive de Karplus-Luttinger ainsi que l'effet Hall anomal. La courbure de Berry apparaît alors aussi comme l'axe d'hélicité du fermion de Bloch. Enfin, le sixième point de vue explore le côté mathématique de la géométrie quantique, où les fibrés vectoriels jouent un rôle significatif. Nous finissons ensuite le chapitre en listant quatre formulations différentes du tenseur géométrique quantique, et en considérant la géométrie quantique des fermions de Dirac massifs.

- Dans le Chapitre 3, nous introduisons l'extension topologique de la théorie des bandes. Nous commençons par nous baser sur le language des fibrés vectoriels afin d'expliquer comment la topologie apparaît dans la théorie des bandes. Nous mentionnons ensuite la relation d'équivalence topologique entre différents Hamiltoniens de Bloch, celle-ci étant liée à la persistence d'un gap de bande. Nous lions cette relation à la non-localité du fermion de Bloch. Nous procédons ensuite par discuter de la correspondence bord-volume. Le reste du chapitre est dédié aux deux invariants principaux de la théorie des bandes: le nombre de Chern et les invariants $\mathbb{Z}_2$.

Le premier intervient dans les sysèmes brisant la symétrie de renversement du temps, et signale une obstruction à une définition continue de la phase globale de l'état de Bloch à travers la zone de Brillouin. Nous présentons ensuite une preuve de la quantification du nombre de Chern, où ce dernier apparaît comme la somme de nombres d'enroulements. Nous discutons ensuite brièvement de l'histoire du nombre de Chern en théorie des bandes et mentionnons certains développements récents sur les bornes topologiques. Finalement, nous calculons le demi-nombre de Chern dans le cas des fermions de Dirac massifs. Pour ce qui est des invariants $\mathbb{Z}_2$, nous résumons les travaux de Fu, Kane et Mele qui ont progressibement menés à leur formulation des invariants $\mathbb{Z}_2$ dans les systèmes invariants par renversement du temps. Nous terminons cette discussion par la formule de Fu-Kane-Mele dans les systèmes centrosymétriques.

- Dans le Chapitre 4 nous introduisons les fondements de la supraconductivité, et particulièrement de la théorie BCS. Nous commencons par brièvement présenter l'histoire de la supraconductivité, en partant de la liquéfaction des gaz par Faraday en 1823 jusqu'à l'avènement de la théorie BCS dans les années 1950. Nous discutons ensuite des rudiments de la théorie BCS en passant par le problème de Cooper ainsi que la fonction d'onde BCS et l'Hamiltonien BCS. Nous finissons ensuite le chapitre en résumant la théorie de champ-moyen de la supraconductivité, de l'approche BCS variationnelle à la méthode de Bogoliubov-de Gennes. L'objectif de ce chapitre est de fournir le cadre théorique de la seconde partie du manuscript, particulièrement des chapitres 6 et 8.

- Dans le Chapitre 5, nous clôturons la première partie du manuscript en introduisant les fonctions de Green et les notions associées. Ceci a pour but d'établir le cadre théorique de la troisième partie du manuscript, soit les chapitres 9 et 10. Nous commencons par présenter le concept général de la fonction de Green, comme la solution fondamentale d'une équation différentielle. Le cas de la fonction de Green à une particule est alors présenté comme la solution fondamentale de l'équation de Schrödinger associée à un Hamiltonien à une particule. Ensuite, nous introduisons la self-energy comme la différence entre la fonction de Green sans interactions et celle avec interactions [5].Nous finissons le chapitre en introduisant la fonction spectrale comme l'extension de la densité d'états au-delà du régime des fermions libres.

- Dans le Chapitre 6, nous étudions l'influence de la courbure de Berry de l'état normal sur une phase supraconductrice dans une variante du modèle des fermions de Dirac massifs. À cette fin, nous commencons par réduire ce modèle à deux bandes à un modèle effectif à une bande en faisant usage de la substitution de Peierls généralisée ainsi que de la transformation de Foldy-Wouthuysen. Deux termes additionnels apparaissent alors dans le modèle effectif. Le premier est un couplage spin-orbite émergent où la courbure de Berry prend le rôle d'un spin, i.e. d'un axe d'hélicité. Quant au second, il s'agit d'un terme de Darwin émergent, venant avec la valeur absolue de la courbure de Berry. Avec l'aide de ce modèle effectif à une bande, nous abordons ensuite le problème à deux corps. En utilisant les coordonnées relatives et de centre de masse, nous trouvons un Hamiltonien à deux corps nous permettant de revisiter le problème de Cooper et la théorie BCS. Ce faisant, nous trouvons une interaction effective affectée par

[5] techniquement, leur inverse

les corrections en courbure de Berry. Des simplifications supplémentaires montrent que le couplage spin-orbite émergent ne contribue pas au problème tandis que le terme de Darwin renormalise l'interaction d'appariement, la rendant plus faible. Le courbure de Berry de l'état normal affaiblit alors l'interaction d'appariement, et à fortiori l'état supraconducteur, à travers le terme de Darwin émergent. Nous procédons ensuite par étendre ce résultat pour un dopage arbitraire, suggérant une façon de tester expérimentalement nos résultats. Enfin, nous allons au-delà de l'appariement *s-wave* et montrons que notre résultat reste le même tant que la parité de l'appariement est fixée.

- Dans le Chapitre 7, nous étudions l'influence de la métrique quantique de l'état normal sur l'état supraconducteur. L'objectif de ce chapitre est d'étudier théoriquement le comportement du poids suprafluide dans les interfaces d'oxide (111), et particulièrement l'interface LAO/STO. Nous commencons par établir le modèle de liaison forte pour cette interface, à partir duquel nous extrayons des modèles de basse énergie, sans spin et avec spin. Le modèle de basse énergie avec spin comporte un cône de Dirac isotrope au point Γ, suggérant une forte métrique quantique autour de ce dernier. Nous utilisons ensuite ces modèles de basse énergie afin d'établir le comportement qualitatif du poids suprafluide, en fonction du potentiel chimique. On anticipe alors que le poids géométrique se comporte en dôme en fonction du potentiel chimique, alors que la contribution conventionnelle se comporte linéairement. Des calculs numériques sur les modèles de basse énergie et de liaisons forte corroborent ce raisonnement. Nous finissons le chapitre par une discussion du poids suprafluide en fonction du dopage, afin de fournir une prédiction expérimentale. En se basant sur des observations expérimentales sur la dépendance du potentiel chimique sur le dopage, nous suggérons un scénario à deux dômes pour la supraconductivité dans les interfaces d'oxides (111). Le premier de ces dômes, à dopage faible, serait d'origine conventionelle alors que le second, à fort dopage, serait d'origine géométrique.

- Dans le Chapitre 8, nous commencons par récapituler les résultats des chapitres 6 et 7. Ces résultats suggèrent une compétition entre la courbure et la métrique de l'état normal envers la supraconductivité. De plus, des interprétations physique de l'effet du terme de Darwin sur la supraconductivité d'une part et sur le poids suprafluide géométrique d'autre part manquent à l'appel. Enfin, les calculs du Chapitre 6 ne sont valable que dans un modèle spécifique, quoique générique. Ce chapitre vise à apporter des réponses à ces questions, et ce basé sur l'interprétation de la géométrie quantique en termes de non-localité des fermions de Bloch que l'on a développé dans la première partie du manuscript. Nous commencons par donner une interprétation physique du poids suprafluide. Le fait que ce dernier, qui décrit le supertransport, comporte deux contributions suggère la présence de deux types de mouvements des paires de Cooper, et donc de supertransports associés. La contribution conventionnelle est alors associé à un mouvement global de centre de masse des fermions de Bloch composant les paires de Cooper. Quant à la contribution géométrique, celle-ci est associée aux mouvements de points-zéro de ces mêmes fermions de Bloch. Ceci expliquerait alors pourquoi la contribution géométrique subsiste dans les systèmes à bandes plates, car les mouvements de points-zéro sont toujours présents si le fermion de Bloch n'a pas de mouvement de centre de masse. De plus, le fait que la contribution géométrique est bornée par le bas par la valeur absolue de la

courbure de Berry s'explique naturellement par le fait que celle-ci guarantit un minimum de mouvement point-zéro, et donc de supertransport associé. Nous suivons ensuite par calculer la forme générale du terme de Darwin émergent en se basant sur la non-localité du fermion de Bloch. Ceci révèle que le terme de Darwin émergent est en fait relié à la métrique quantique de l'état normal, et non la courbure de Berry. Cette trouvaille est alors naturellement expliquée par l'interprétation du terme de Darwin émergent comme une conséquence de la non-localité typique du fermion de Bloch, et non celle minimale. En considérant l'exemple des fermions de Dirac massifs, nous voyons alors essentiellement le même terme de Darwin que nous avions trouvé dans le Chapitre 6. Ceci peut être expliqué par le fait que la géométrie quantique des fermions de Dirac massifs sature les inégalités de trace et de déterminants au points K et K', ce qui veut essentiellement dire que les non-localité des fermions de Dirac massifs typique et minimale coïncident. En se basant ensuite sur la forme générale du terme de Darwin émergent, nous calculons ensuite la renormalisation de l'interaction d'appariemment. Le fait que le terme de Darwin est en fait dû à la métrique quantique et non la courbure de Berry efface la possiblité d'une compétition courbure-métrique. Les deux effets que nous avons étudiés sont alors les deux faces de la même médaille, c'est-à-dire la non-localité (et donc l'émergence) du fermion de Bloch.

- Dans le Chapitre 9, nous montrons que les propriétés analytiques de la fonction de Green peuvent être utilisées afin de calculer les invariants topologiques $\mathbb{Z}_2$, dans les systèmes à deux bandes. Ce projet est basé sur la découverte récente que les zéros des éléments diagonaux de la fonction de Green, exprimée dans la base orbitalaire, peuvent être utilisées pour établir sur une phase est topologiquement non-triviale. Plus précisément, deux zéros associés à deux éléments diagonaux différents vont totalement traverser le gap de bandes dans des directions opposées entre deux points inversés de la zone de Brillouin. Nous commencons par revisiter le formalisme de ces zéros diagonaux, ce qui nous permet de fixer les notations et d'offrier des interprétations de ces zéros, ainsi que des relations qu'ils obéissent. Nous procédons ensuite par formuler une proposition dans les modèles à deux bandes nous permettant d'extraire les invariants $\mathbb{Z}_2$ des zéros diagonaux. Essentiellement, les croisements de zéros diagonaux séparent les TRIMs de parités opposées et les invariants $\mathbb{Z}_2$ sont ainsi obtenus en comptant le nombre de TRIMs d'un côté ou de l'autre de ces croisements. Nous prouvons ensuite la proposition, en expliquant intuitivement comment les zéros diagonaux sont reliés aux inversions de bandes. Nous considérons ensuite un modèle jouet des isolants topologique $\mathbb{Z}_2$ en trois dimensions, et prouvons qu'en effet les zéros diagonaux donnent les bonnes valeurs d'invariants topologique. Nous finissons le chapitre en formulant une conjecture dans un système avec un nombre arbitraire de bandes.

- Dans le Chapitre 10, nous proposons une extension du tenseur quantique géométrique au-delà du régime des fermions libres. Nous faisons ceci en revisitant le calcul de la formulation Hamiltonienne du tenseur et en y faisant apparaître la fonction de Green sans interactions. Le tenseur quantique géométrique généralisé (gQGT) est alors obtenu en remplaçant la fonction de Green sans interactions par son équivalent avec interactions. Nous mentionons ensuite brièvement certaines propriétés du gQGT. Premièrement, nous observons que la forme

du gQGT est similaire à l'information de Fisher classique, suggérant un lien subsistant avec l'information géométrique. Deuxièmement, nous mentionons que les zéros singuliers de la fonction de Green (ceux de son déterminant) apparaissent comme des singularités du gQGT. Troisièmement, développer le gQGT suggère la possibilité d'une géométrie quantique provenant de l'interaction électronique, autrement de la self-énergie. Nous finissons ensuite le chapitre en considérant l'exemple paradigmatique de l'élargissement Lorentzien de la fonction spectrale. La géométrie quantique, et le nombre de Chern généralisé associé, sont alors affaiblis par l'élargissement. Cet affaiblissement devient pertinent quand l'élargissement devient comparable au gap de bandes.

Outline of the manuscript

- In Chapter 1 we revisit the foundations of band theory, starting from the Hamiltonian of matter and the subsequent approximations that constitute the context of validity of the Bloch theorem. We then prove Bloch's theorem, introducing fundamental notions such as the Brillouin zone and the crystal momentum along the way. The main personal contribution to this chapter is the strong emphasis on the idea that the single-particle excitations described by the Bloch theorem are quasiparticles, dubbed Bloch fermions, that emerge from the electron-nuclei Coulomb interaction. We end the chapter by introducing the tight-binding method and considering the example of the honeycomb lattice. From the latter we extract the low-energy model of "gapped graphene" where the Bloch fermions appear as massive Dirac fermions.

- In Chapter 2, we extensively introduce and discuss the different aspects quantum geometry in band theory and beyond. We begin the chapter by deriving the different quantities of quantum geometry, that is the quantum geometric tensor as well as the Berry curvature and quantum metric. The latter then directly emerge from the part of the Bloch state that is a consequence of the electron-nuclei Coulomb interaction. We then discuss several properties of quantum geometry. The main part of the chapter is devoted to a series of six viewpoints, each revealing quantum geometry under different angles. The first viewpoint explains how quantum geometry also appears in the theory of quantum metrology, and the second then builds an analogy between quantum metrology and band theory. The result is that in low-energy models quantum geometry appears as the quantifier of the non-locality of the Bloch fermion, that is the quantum fluctuations of its position. The third viewpoint then interprets these quantum fluctuations as stemming from virtual interband transitions. The fourth viewpoint mentions the duality between the Berry curvature and the magnetic field, while the fifth introduces the Karplus-Luttinger drift velocity and the anomalous Hall effect. The Berry curvature then also appears as the helicity axis of the Bloch fermion's wavepacket. Finally, the sixth viewpoint mentions the mathematical side of quantum geometry, where vector bundles play a significant role. We then end the chapter by listing four different formulations of the quantum geometric tensor, and by considering the quantum geometry of massive Dirac fermions.

- In Chapter 3, we introduce the topological extension of band theory. We begin by building on the language of vector bundles to introduce how topology arises in band theory. We follow by mentioning the topological equivalence relation between Bloch Hamiltonians as the persistence of a band gap, and link this to the non-locality of the Bloch fermion. We then discuss the bulk-boundary correspondence. The rest of the chapter is devoted to the two main topological invariants in band theory: the Chern number and the $\mathbb{Z}_2$ topological invariant. The first one arises in systems without time-reversal symmetry, and signals an obstruction to smoothly defining the phase of the Bloch state accross the Brillouin zone. We then present a proof of the quantization of the Chern number where the latter appears as the sum of the winding numbers of the transition functions. We briefly discuss the history of the Chern number in band theory and mention the recent development on topological bounds. Finally, we compute the

half-Chern number of massive Dirac fermions. For the $\mathbb{Z}_2$ topological invariants, we summarize the papers of Fu, Kane and Mele that progressively led to their formulations of Z_2 topological insulators in time-reversal symmetric systems. We end the discussion by the Fu-Kane-Mele formula in inversion symmetric systems.

- In Chapter 4 we introduce the fundamentals of superconductivity, and particularly of BCS theory. We begin by discussing the history of superconductivity, from the liquefaction of gases by Faraday in 1823 to the advent of BCS theory in the 1950s. We follow by discussing the foundations of BCS theory through the Cooper problem as well as the BCS wavefunction and Hamiltonian. We then finish the chapter by suumarizing the mean-field theory of superconductivity, from the BCS variational approach to the Bogoliubov-de Gennes method. The aim of this chapter is to provide the theoretical framework of the second part of the manuscript, particularly Chapters 6 and 8, as well as introducing the BCS paradigm of superconductivity.

- In Chapter 5, we finish the first part of the manuscript by introducing the Green's function and its associated notions, in order to provide the theoretical framework of the third part of the manuscript, that is Chapters 9 and 10. We begin by discussing the general concept of a Green's function as the fundamental solution to a differential equation. We then introduce the single-particle Green's function as the fundamental solution of the Schrödinger equation associated to a single-particle Bloch Hamiltonian. We follow by introducing the self-energy as the difference between the (inverse) non-interacting and interacting single-particle Green functions. Finally, we introduce the spectral function as the generalization of the local density of states beyond the free-fermion limit.

- In Chapter 6, we study the influence of the normal state Berry curvature on the superconducting phase in a close variant of the massive Dirac fermions model. We begin by reducing the two-band model by an effective single-band model using both the generalized Peierls substitution and the Foldy-Wouthuysen transformation. Two additional terms appear in the effective model. The first one is an emergent spin-orbit coupling term where the Berry curvature appears as the helicity axis, i.e. the spin. The second one is an emergent Darwin term, driven by the modulus of the Berry curvature. Using the effective single-band model, we then tackle a two-body problem. Using the relative and center-of-mass coordinates, we then find a two-body Hamiltonian that we can directly use to revisit the Cooper problem and BCS theory. Doing so yields an effective interaction stemming from the Berry curvature corrections. Further simplification shows that the emergent spin-orbit coupling does not contribute and the Darwin term renormalizes the pairing interaction, making it weaker. The normal state Berry curvature thus weakens the pairing interaction, and thus superconductivity, through the emergent Darwin term. We then proceed by extending this result for arbitrary doping ranges, which suggests a way to experimentally test our predictions. Finally, we consider non s-wave pairings and show that the result holds as long as the parity of the pairing is fixed.

- In Chapter 7, we study the influence of the normal state quantum metric on the superconducting state. The goal of the chapter is to theoretically study the behaviour of the superfluid weight in (111) oriented oxide interfaces, and particularly the LAO/STO interface. We begin by stating

the tight-binding model for the interface, from which we then derive both spinless and spinful low-energy models. The spinful low-energy bands features isotropic Dirac cones, pointing to a strong quantum metric around the Γ point. We then use the low-energy models to qualitatively discuss the behaviour of the superfluid weight as a function of the chemical potential. The geometric superfluid weight is then expected to exhibit a dome behaviour while the conventional contribution is linear. Numerical calculations from the low-energy model and the tight-binding model corroborate the qualitative discussion. We then finish by discussing the gate voltage dependence of the superfluid weight, in order to be closer to experiments. Based on experimental observations of the gate voltage dependence of the chemical potential, our results suggest a two-dome scenario for the superconductivity in (111) oxide interfaces. The first dome is due to the conventional contribution while the second is due to the geometric contribution.

- In Chapter 8, we start by reflecting on the findings of Chapters 6 and 7. These results suggest a normal state curvature-metric competition towards superconductivity. Moreover, physical interpretations of the effect of the Darwin term on superconductivity and of the geometric superfluid weight are lacking. Lastly, our calculations in Chapter 6 were only limited to a specific model, however generic. Chapter 8 aims to solve these issues based on the non-local interpretation of quantum geometry we developed in the first part of the manuscript. First, we give a physical intepretation of the superfluid weight. The fact that the latter, which essentially describes supertransport, has two contributions suggests there are two types of movements, i.e. two sources of supertransport. The conventional contribution is associated with an overall movement of the Bloch fermions composing the Bloch wavepackets while the geometric contribution is associated to their zero-point motions. This also explains why the geometric superfluid weight is still present in flat-band systems, as in the latter the Bloch fermions stay still as a whole, but can still exhibit zero-point motion. Additionally, the fact that the geometric superfluid weight is bounded from below by the Berry curvature is also naturally explained by the fact that the Berry curvature essentially protects a minimal amount of zero-point motion, and thus of the associated supertransport. We then follow by deriving a general form for the emergent Darwin term based on the non-locality of the Bloch fermion. Doing so reveals that the driver of the Darwin term is in fact the quantum metric, and not the Berry curvature. This is also naturally explained by the interpretation of the Darwin term as emerging from the typical non-locality of the Bloch fermion, and not its minimal one. By considering the example of massive Dirac fermions, we see that its specific Darwin term is essentially the same as in Chapter 6. This stems from the fact that the quantum geometry of the massive Dirac fermions saturates the trace and determinant inequalities when taken exactly at the K and K' points, so the zero-point motions are minimal. Based on the general form of the Darwin term, we then derive the associated renormalization of the pairing interaction. The finding that the general Darwin term is due to the quantum metric and not the Berry curvature erases the possibility of the curvature-metric competition, as the two effects we studied (Darwin term and superfluid weight) are two sides of the same coin, that is the non-locality and emergence of the Bloch fermion.

- In Chapter 9, we show that the analytic properties of the Green's function can be used to com-

pute $\mathbb{Z}_2$ topological invariants in two-band systems. This project is based on the recent discovery that the zeroes of the diagonal elements of the Green's function, when expressed in the orbital basis, can be used to detect if a phase is topological or not. Specifically, two zeroes associated with different diagonal elements will fully cross the band gap in opposite directions between two inverted points in the Brillouin zone. We start by reviewing the formalism of these diagonal zeroes, which allows us to change the notations and offer interpretations of the diagonal zeroes and the different relations they obey. We then proceed by formulating a proposition allowing us to extract the values of the $\mathbb{Z}_2$ topological invariants from the diagonal zeroes. Essentially, the crossings of the diagonal zeroes separate the TRIMs with opposite parity eigenvalues, and the invariants are then readily obtained by counting the number of TRIMs on either side. We follow by proving the proposition, thereby naturally showing how diagonal zeroes relate to band inversions. We then consider an explicit toy model for three-dimensional $\mathbb{Z}_2$ topological insulators and show that the diagonal zeroes indeed give the right invariants. We then finish by formulating a conjecture extending the result to N-band systems.

- In Chapter 10, we propose an extension of the quantum geometric tensor beyond free-fermion systems using the Green's function. We do so by revisiting the derivation of the Hamiltonian formulation of the QGT and by expressing the latter in terms of the non-interacting Green's function. The generalised QGT (gQGT) is then obtained by replacing the non-interacting Green's function by its interacting counterpart. We then briefly reflect on some of the properties of the gQGT. First, we notice that the gQGT has a similar form as the classical Fisher information matrix, thereby suggesting a persisting link with information geometry. Then, we mention that the singular zeroes of the Green's function (i.e. that of its determinant) appear as singularities in the gQGT. Finally, expanding the gQGT shows the possibility of correlation-driven quantum geometry, coming from the self-energy. We then finish by considering the paradigmatic case of a Lorentzian broadening of the spectral function. The quantum geometry, and the associated generalised Chern number, are then weakened by the broadening. This weakening only becomes significant when the broadening becomes comparable to the band gap.

Notations

Sets

- $\mathbb{Z}$ denotes the set of *relative* integers, ranging from $-\infty$ to $+\infty$ (both not included).
- $\mathbb{N} = \left\{n \in \mathbb{Z} \,\middle|\, n \geq 0\right\}$ is the set of *natural* integers.
- If $\mathbb{K}$ denotes a field - typically $\mathbb{N}$, $\mathbb{Z}$, $\mathbb{Q}$, $\mathbb{R}$ or $\mathbb{C}$ - then $\mathbb{K}^* = \mathbb{K} \setminus \{0\}$.
- For $a, b \in \mathbb{Z}$ with $b \geq a$, $[\![a, b]\!] = \left\{n \in \mathbb{Z} \,\middle|\, a \leq n \leq b\right\}$.
- For $N \in \mathbb{N}^*$, $\mathcal{M}_N(\mathbb{C})$ is the set of complex square matrices of size N.
- For $N \in \mathbb{N}^*$, $\mathsf{U}(N) = \left\{U \in \mathcal{M}_N(\mathbb{C}) \,\middle|\, U^\dagger U = UU^\dagger = \mathbb{1}\right\}$ is the set of unitary matrices of size N.
- For $k \in \mathbb{N} \cup \{+\infty\}$ and A, B two sets, $\mathcal{C}^k(A, B)$ is the set of k-times continuously differentiable functions $f : A \to B$. By convention, $\mathcal{C}^k(A) = \mathcal{C}^k(A, A)$.
- For an operator H, $\mathrm{Sp}\, H$ is the *spectrum* of H, its set of eigenvalues.

Functions and relations

- Θ denotes the Heaviside function.
- For a set A, $\mathbb{1}_A : A \to \{0, 1\}$ is the indicator function of A.
- $\mathbb{1}$ is the identity operator.
- For a matrix A, A^t denotes its transpose matrix.
- For an operator A, the superoperator ad_A, called the adjoint action of A, is defined as $\mathrm{ad}_A = [A, \cdot]$
- For $x \in \mathbb{R}_+^*$, $\ln x$ denotes the natural logarithm of x.
- For $n, m, p \in \mathbb{Z}$ three integers, $n \equiv m \ \ [p]$ means that n and m are congruent modulo p.

Contents

Part I

Theoretical framework

1 - Foundations of band theory and the tight-binding approach

The objective of this chapter is twofold. First, we summarize the approximations that lead to the Bloch theorem and band theory, allowing us to be relatively self-contained and to fix sound notations in the process. We also discuss standard concepts like the Brillouin zone and crystal momentum, and establish the tight-binding method, for the same purposes. Second, the main personal contribution to this chapter is the strong emphasis on the emergent character of the Bloch state, and the Bloch fermion it represents. Indeed, we argue that the cell-periodic Bloch state differentiates the Bloch fermion from the elementary electron, and it is precisely from this difference that band quantum geometry and topology arise. Although the use of the term *quasiparticle* is usually reserved for states emerging from the electron-electron Coulomb interaction, we will also refer to the Bloch fermion as a quasiparticle, that instead emerges from the electron-nuclei Coulomb interaction. We will also refer to the quasiparticle character of the Bloch fermion as its *quasiness*.

The additional reason for the emphasis on this subtlety is that while it is better to have it in mind when interpreting quantum geometry, as we will see in Chapter 2, the subtlety becomes *necessary* when considering electronic interactions. More precisely, putting an interaction between electrons and Bloch fermions is not always equivalent physically. This is the effect of band quantum geometry on electronic correlations, that we discuss in the second part of the thesis, in the example of superconductivity.

1.1 . Hamiltonian of matter and its reduction to band theory

Let us first introduce the *Hamiltonian of matter*, and discuss the hierarchy of approximations leading to band theory. A solid is composed of electrons and atomic nuclei (itself composed of protons and neutrons). We will consider their kinetic energies, and the Coulomb interactions involved in such an assembly.

We denote the position and momentum operators of the j-th electron as $\hat{\boldsymbol{r}}_j$ and $\hat{\boldsymbol{p}}_j$, respectively. Treating the atomic nuclei as a single object, the position and momentum operators of the J-th atomic nuclei are $\hat{\boldsymbol{R}}_J$ and $\hat{\boldsymbol{P}}_J$, respectively[1]. The Hamiltonian describing the assembly of the nuclei and the electrons will then have two types of terms.

On one side, we have the free kinetic energies of the nuclei and that of the electrons, giving the following term,

$$\hat{T} = \hat{T}_e + \hat{T}_n = \sum_j \frac{\hat{\boldsymbol{p}}_j^2}{2m_e} + \sum_J \frac{\hat{\boldsymbol{P}}_J^2}{2M_J}. \tag{1.1}$$

The electrons all have the same mass $m_e \simeq 9.1 \times 10^{-31}$kg, while the nuclei can have different masses M_J, depending on their nature.

On the other side, we have the Coulomb interactions present in the problem. We write the

[1]We use capital indices for the nuclei.

Coulomb potential as

$$V_c(\boldsymbol{v}) = \frac{e^2}{4\pi\epsilon_0\|\boldsymbol{v}\|}, \tag{1.2}$$

where ϵ_0 is the vacuum permittivity. Here we have three such potentials: one between two nuclei, one between an electron and a nucleus as well as another between two electrons. The interaction term of the Hamiltonian of matter then reads

$$\hat{V} = \hat{V}_{nn} + \hat{V}_{en} + \hat{V}_{ee} \tag{1.3a}$$

$$= \frac{1}{2}\sum_{J_1 J_2} Z_{J_1} Z_{J_2} V_c\big(\hat{\boldsymbol{R}}_{J_1} - \hat{\boldsymbol{R}}_{J_2}\big) - \sum_{jJ} Z_J V_c\big(\hat{\boldsymbol{r}}_j - \hat{\boldsymbol{R}}_J\big) + \frac{1}{2}\sum_{j_1 j_2} V_c\big(\hat{\boldsymbol{r}}_{j_1} - \hat{\boldsymbol{r}}_{j_2}\big), \tag{1.3b}$$

where Z_J denotes the atomic number of the J-th nucleus. The $1/2$ factor is there to prevent double-counting. Our Hamiltonian of interest is then [8]

$$\hat{H} = \hat{T} + \hat{V} = \hat{T}_e + \hat{T}_n + \hat{V}_{nn} + \hat{V}_{en} + \hat{V}_{ee}. \tag{1.4}$$

In the field of quantum matter, it can be called the *Hamiltonian of matter*. But as its use is much more general than solids (molecular/atomic physics, quantum chemistry,...), it bears other names in different fields, for example the *molecular Hamiltonian* in atomic and molecular physics. The exponential complexity of the problem makes the direct resolution of the associated Schrödinger equation completely hopeless for more than a few dozen particles[2]. But we can get around this problem by further specializing, i.e. approximating, the Hamiltonian of matter.

1.1.1 . Born-Oppenheimer approximation

The first step is to implement the Born-Oppenheimer approximation [9], which uses the fact that the electrons are significantly lighter than the atomic nuclei. Indeed, as mentioned before an electron weighs $m_e \simeq 9.1 \times 10^{-31}$kg. On the other hand, protons and neutrons have a mass on the order of 10^{-27}kg. Therefore, any movement of the nuclei will be extremely slow compared to an electron's movement. The kinetic energies are then such that $\langle\psi|\,\hat{T}_n\,|\psi\rangle \ll \langle\psi|\,\hat{T}_e\,|\psi\rangle$ for any physical state $|\psi\rangle$. Focusing on the electrons' dynamics, the first step of the Born-Oppenheimer approximation then considers the atomic nuclei to be *fixed*. In the following, we refer to this approximation as the first Born-Oppenheimer approximation.

For the Hamiltonian $\hat{H}$, that means two things. First, the nuclei's kinetic energy becomes negligible, we then consider $\hat{T}_n$ to be zero. Second, since the atomic nuclei are all fixed, their position operator $\hat{\boldsymbol{R}}_J$ will, as a function of time, return the same result $\boldsymbol{R}_J$. Consequently, the Coulomb repulsion $\hat{V}_{nn}$ becomes a constant energy and as such can be discarded. The Hamiltonian $\hat{H}$ under the first Born-Oppenheimer approximation then becomes

$$\hat{H} = \hat{T}_e + \hat{V}_{en} + \hat{V}_{ee}. \tag{1.5}$$

The study of $\hat{H}$ beyond the first Born-Oppenheimer approximation, i.e. when the nuclei have dynamics, brings about the study of *phonons* [10]. We see in Chapter 4 that phonons constitute the key to conventional superconductivity.

[2] At least on classical computers

1.1.2 . Infinite and crystalline solid

Under the first Born-Oppenheimer approximation, all the nuclei are thus fixed. However, more approximations are needed before we can reach band theory.

One step is to assume the solid to be *infinite*, in that the array of nuclei has no end. Physically, we zoom deeply into the bulk of the material, enough to eliminate any influence from the surface. The resulting situation is that of a discrete and infinite arrangement of points in the space. Such arrangement is called a *lattice*.

The next step is to approximate the lattice as a *crystal*[3]. A lattice is said to be in a crystalline phase iff there exists a subset of points in the lattice from which the latter can be generated through a paving process. This subset is referred to as the *basis* of the lattice [11]. The parametrization of the crystal is then done as follows.

1. One lattice site of the basis is chosen as the origin of the lattice.
2. The *Bravais lattice* of the origin is then generated as

$$\boldsymbol{R_n} = \sum_{j=1}^{d} n_d \boldsymbol{a}_d, \qquad \boldsymbol{n} = (n_1, \dots, n_d) \in \mathbb{Z}^d, \tag{1.6}$$

   where the linearly independent $\boldsymbol{a}_d$ are the *primitive vectors* of the Bravais lattice and d is the spatial dimension. The vectors $\boldsymbol{R_n}$ are the *Bravais lattice vectors*. The number of possible Bravais lattices depends on the spatial dimension. Noteworthy examples are 5 for $d = 2$, 14 for $d = 3$ and 64 for $d = 4$ [12, 13, 14].
3. The Bravais lattices of the other sites of the basis, called the *inequivalent sites*, is then generated from the origin's Bravais lattice via a translation by $\boldsymbol{\delta}_\alpha$. The inequivalent sites then form *sublattices* of the lattice.
4. For each lattice site with position $\boldsymbol{r}$, there now exists $(n_1, \dots, n_d) \in \mathbb{Z}^d$ and a $\boldsymbol{\delta}_\alpha$ such that $\boldsymbol{r} = \boldsymbol{R_n} + \boldsymbol{\delta}_\alpha$. The crystal is thus fully parametrized.

It is important to notice that the choices of basis and primitive vectors is not unique.

One particular example is the honeycomb lattice pictured in Fig.1.1, relevant for many two-dimensional materials and interfaces, which we will encounter in Chapter 7. Its basis, as shown in Fig.1.1, is composed of one blue site and of the red site above it. One possible parametrization is [11]

$$\boldsymbol{a}_1 = \frac{\sqrt{3}}{2} a \boldsymbol{e}_x + \frac{3}{2} a \boldsymbol{e}_y, \quad \boldsymbol{a}_2 = -\frac{\sqrt{3}}{2} a \boldsymbol{e}_x + \frac{3}{2} a \boldsymbol{e}_y, \quad \boldsymbol{\delta}_1 = a \boldsymbol{e}_y, \tag{1.7}$$

with a the interatomic distance, of the order of 1.4Å in graphene [11].

The Coulomb interaction between the electrons and the atomic nuclei then becomes

$$\hat{V}_{en} = -\sum_{jJ} Z_J V_c\big(\hat{\boldsymbol{r}}_j - \boldsymbol{R}_J\big) = -\sum_{j} \sum_{\alpha, \boldsymbol{n}} Z_\alpha V_c\big(\hat{\boldsymbol{r}}_j - \boldsymbol{R_n} - \boldsymbol{\delta}_\alpha\big). \tag{1.8}$$

This interaction between the electrons and the nuclei (or ions) is commonly called the *crystalline potential*.

[3] We will use these words interchangeably in the following

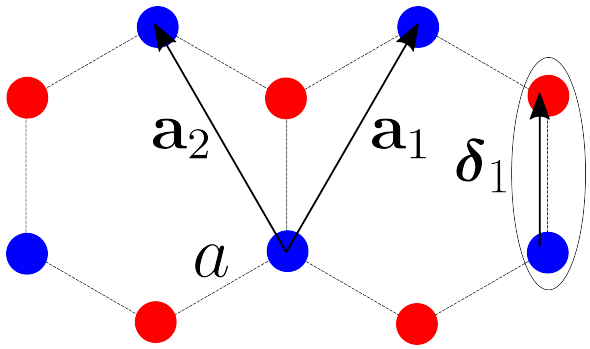

Figure 1.1: Parametrization of the honeycomb lattice in two dimensions. One blue atom is taken as the origin, from which the triangular Bravais lattice is generated, with the vectors $\boldsymbol{a}_1$ and $\boldsymbol{a}_2$. The opposite triangular Bravais lattice, that of the red atoms, is then obtained by a translation of $\boldsymbol{\delta}_1$ from the blue atoms. The basis of the honeycomb lattice is taken to be the original blue site and the red site above it.

Disorder The crystalline limit being an idealization, most solids are not actually in a crystalline phase. Among the latter are the *disordered* phases. As a solid is an arrangement of atoms on lattice sites, the disorder can happen either on the sites themselves or on the atoms. As such, we can distinguish two main types of disorder [15]. The first type is called *structural* disorder, as shown in Fig.1.2b. The arrangement of lattice sites then deviates from the crystalline phase, either by an irregularity of their mutual distance, or by vacancies. An extreme example of such disordered phases is amorphous materials. The second type of disorder is on the arrangement of atoms residing on the lattice sites, sometimes dubbed *substitutional* or *chemical* disorder [15].

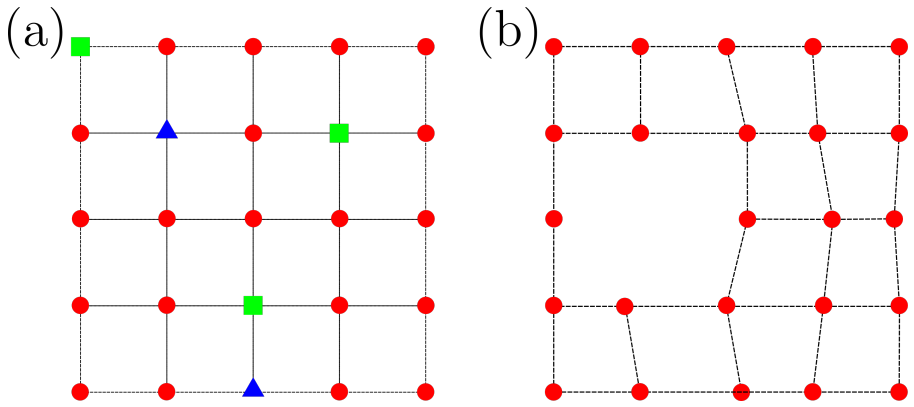

Figure 1.2: Two different types of disorders. (a) Substitutional disorder: Aperiodicity of the arrangement of nuclei on the sites. (b) Structural disorder: Aperiodicity of the sites, where the nuclei reside. Remade from Ref. [15].

1.1.3 . Independent electrons

At this stage, the Hamiltonian of matter reads

$$\hat{H} = \sum_j \left[\frac{\hat{\boldsymbol{p}}_j^2}{2m_e} - \sum_{\alpha,\boldsymbol{n}} Z_\alpha V_c\big(\hat{\boldsymbol{r}}_j - \boldsymbol{R}_{\boldsymbol{n}} - \boldsymbol{\delta}_\alpha\big) + \frac{1}{2}\sum_i V_c(\hat{\boldsymbol{r}}_j - \hat{\boldsymbol{r}}_i) \right] = \sum_j \hat{H}_j. \tag{1.9}$$

We can then define an Hamiltonian $\hat{H}_j$ for each electron j which consists of three terms. The first term is its kinetic energy, the second its Coulomb interaction with the lattice it lives in, and the last term is its Coulomb interaction with the other electrons. Contrary to what this writing may imply, $\hat{H}$ is not (yet) a separable Hamiltonian. This is precisely due to the Coulomb interaction between electrons. Because of this term, the Hamiltonians of two electrons $\hat{H}_i$ and $\hat{H}_j$ will not commute. That in turn implies that the eigenstates of $\hat{H}$ will not be the tensor product of the eigenstates of all the $\hat{H}_j$. In that sense the electrons are *correlated*, and the electron-electron Coulomb interaction is also referred to as *electronic correlations*.

The final approximation we make is to neglect these electron correlations, so that electrons are independent from one another and the Hamiltonians $\hat{H}_i$ and $\hat{H}_j$ mutually commute. If $|\psi\rangle$ and $|\psi_j\rangle$ are the respective eigenstates of $\hat{H}$ and $\hat{H}_j$, we then have

$$\big[\hat{H}_i, \hat{H}_j\big] = 0 \Rightarrow |\psi\rangle \sim \bigotimes_j |\psi_j\rangle\,, \tag{1.10}$$

where the product state has to be antisymmetrized, to obey Pauli's principle. Our task in the next section will be to determine the $|\psi_j\rangle$. The Hamiltonian on any electron j finally reads

$$\hat{H}_j = \frac{\hat{\boldsymbol{p}}_j^2}{2m_e} - \sum_{\alpha,\boldsymbol{R}_n} Z_\alpha V_c\big(\hat{\boldsymbol{r}}_j - \boldsymbol{R}_{\boldsymbol{n}} - \boldsymbol{\delta}_\alpha\big). \tag{1.11}$$

Since the Hamiltonian has the same form for every electron, we will drop the index j in the following.

1.2 . Bloch theorem and the emergence of Bloch fermions

The Hamiltonian $\hat{H}$ we focus on is given by

$$\hat{H} = \frac{\hat{\boldsymbol{p}}^2}{2m_e} + V(\hat{\boldsymbol{r}}), \tag{1.12}$$

where V is the crystalline potential, given by

$$V(\hat{\boldsymbol{r}}) = -\sum_{\alpha,\boldsymbol{n}} Z_\alpha V_c\big(\hat{\boldsymbol{r}} - \boldsymbol{R}_{\boldsymbol{n}} - \boldsymbol{\delta}_\alpha\big). \tag{1.13}$$

Again, Eq. (1.12) represents one electron living in, and interacting with, a perfect crystal. Our goal here is to find the eigenstates of this Hamiltonian.

1.2.1 . Translation invariance

The crucial property that will allow us to find these eigenstates is the translation invariance of $\hat{H}$, as written in Eq. (1.12). Consider the operator that translates the electron by a Bravais lattice vector $\boldsymbol{R_m}$, formally defined as follows.

Definition 1.2.1 (Bravais translation operator)**.** *Let $\boldsymbol{m} \in \mathbb{Z}^d$ and $|\boldsymbol{r}\rangle$ be the state representing the event "electron at position $\boldsymbol{r}$". The Bravais translation operator $\mathcal{T}_{\boldsymbol{m}}$ is defined as*

$$\mathcal{T}_{\boldsymbol{m}} |\boldsymbol{r}\rangle = |\boldsymbol{r} + \boldsymbol{R_m}\rangle . \tag{1.14}$$

The Bravais translation operators then obey the following properties.

Property 1.2.1 (Properties of $\mathcal{T}_{\boldsymbol{m}}$)**.** *Let $\boldsymbol{n}, \boldsymbol{m} \in \mathbb{Z}^d$.*

1. *Additivity: $\mathcal{T}_{\boldsymbol{n}}\mathcal{T}_{\boldsymbol{m}} = \mathcal{T}_{\boldsymbol{n}+\boldsymbol{m}}$.*
2. *Inverse operator: $\mathcal{T}_{\boldsymbol{m}}^{-1} = \mathcal{T}_{-\boldsymbol{m}}$.*
3. *Unitarity: $\mathcal{T}_{\boldsymbol{m}}^{\dagger} = \mathcal{T}_{\boldsymbol{m}}^{-1} = \mathcal{T}_{-\boldsymbol{m}}$.*
4. *Commutation with position operator: For any function f, $\mathcal{T}_{\boldsymbol{m}} f(\hat{\boldsymbol{r}}) = f\big(\hat{\boldsymbol{r}} - \boldsymbol{R_m}\big)\mathcal{T}_{\boldsymbol{m}}$.*

We prove these properties in appendix A.1. The operator $\hat{\boldsymbol{p}}$ commutes with the translation operator, and the crystalline potential behaves as

$$\mathcal{T}_{\boldsymbol{m}} V(\hat{\boldsymbol{r}}) = -\sum_{\alpha,\boldsymbol{n}} Z_\alpha \mathcal{T}_{\boldsymbol{m}} V_c\big(\hat{\boldsymbol{r}} - \boldsymbol{R_n} - \boldsymbol{\delta}_\alpha\big) = -\sum_{\alpha,\boldsymbol{n}} Z_\alpha V_c\big(\hat{\boldsymbol{r}} - \boldsymbol{R_n} - \boldsymbol{\delta}_\alpha - \boldsymbol{R_m}\big)\mathcal{T}_{\boldsymbol{m}}. \tag{1.15}$$

Eq. (1.6) implies that $\boldsymbol{R_n} + \boldsymbol{R_m} = \boldsymbol{R_{n+m}}$. By a relabelling $\boldsymbol{n} \mapsto \boldsymbol{p} = \boldsymbol{n} + \boldsymbol{m}$ of the sum over $\mathbb{Z}^d$, we then have

$$\mathcal{T}_{\boldsymbol{m}} V(\hat{\boldsymbol{r}}) = -\left[\sum_{\alpha}\sum_{\boldsymbol{n}\in\mathbb{Z}^d} Z_\alpha V_c\big(\hat{\boldsymbol{r}} - \boldsymbol{R_{n+m}} - \boldsymbol{\delta}_\alpha\big)\right]\mathcal{T}_{\boldsymbol{m}} \tag{1.16a}$$

$$= -\left[\sum_{\alpha}\sum_{\boldsymbol{p}\in\mathbb{Z}^d} Z_\alpha V_c\big(\hat{\boldsymbol{r}} - \boldsymbol{R_p} - \boldsymbol{\delta}_\alpha\big)\right]\mathcal{T}_{\boldsymbol{m}} = V(\hat{\boldsymbol{r}})\mathcal{T}_{\boldsymbol{m}}. \tag{1.16b}$$

We have thus shown that

$$\big[\mathcal{T}_{\boldsymbol{m}}, \hat{H}\big] = 0, \tag{1.17}$$

i.e. that $\hat{H}$ is invariant under translations by a Bravais lattice vector. Importantly the Hamiltonian $\hat{H}$ is not invariant under translation by a full lattice vector $\boldsymbol{R_m}+\boldsymbol{\delta}_\beta$, and it is in that sense the atoms forming the basis are inequivalent. The fact that $\hat{H}$ commutes with the Bravais translation operator $\mathcal{T}_{\boldsymbol{m}}$ means that both are simultaneously diagonalizable, so we can find a common orthonormal eigenbasis for both operators. Practically, this means that we can find the eigenstates of $\hat{H}$ by finding those of the Bravais translation operators $\mathcal{T}_{\boldsymbol{m}}$! Note that the Bravais translation operators, as unitary operators, are diagonalizable with a priori complex eigenvalues.

1.2.2 . Bloch theorem

In appendix A.3, we prove the Bloch theorem concerning the expression of the eigenstates of $\hat{H}$. In doing so, we introduce the notion of *reciprocal lattice*.

Definition 1.2.2 (Reciprocal lattice vectors)**.** *Let $j \in [\![1, d]\!]$. We then define $\boldsymbol{b}_j \in \mathbb{R}^d$ by*

$$\forall i \in [\![1, d]\!], \quad \boldsymbol{b}_j \cdot \boldsymbol{a}_i = 2\pi\delta_{ij}. \tag{1.18}$$

The vectors $\boldsymbol{b}_j$ are called the reciprocal primitive lattice vectors. With $\boldsymbol{n} \in \mathbb{Z}^d$ we also have

$$\boldsymbol{G}_{\boldsymbol{n}} = \sum_{j=1}^{d} n_j \boldsymbol{b}_j, \tag{1.19}$$

the reciprocal Bravais lattice vectors.

In appendix A.2 we prove their existence, provide general expressions in the two and three dimensional cases, and mention some examples. We will elaborate on the notion of reciprocal space in section 1.2.3.

Appendix A.3 proves that the eigenstates take the form of an exponential factor times a state whose wavefunction has the periodicity of the Bravais lattice vectors. This result is known as the *Bloch theorem*. In general there are multiple eigenvectors, which we then index by $n \in \mathbb{N}$.

Theorem 1.2.1 (Bloch Theorem)**.** *The eigenstates of the Hamiltonian $\hat{H}$, written in Eqs. (1.12,1.13), depend on an index $n \in \mathbb{N}$ as well as a parameter $\boldsymbol{k}$ and take the form*

$$|\psi_n(\boldsymbol{k})\rangle = e^{i\boldsymbol{k}\cdot\hat{\boldsymbol{r}}} \, |u_n(\boldsymbol{k})\rangle \,, \tag{1.20}$$

with $|u_n(\boldsymbol{k})\rangle$ such that

$$\forall \boldsymbol{m} \in \mathbb{Z}^d, \quad u_n(\boldsymbol{k}, \boldsymbol{r} + \boldsymbol{R}_{\boldsymbol{m}}) = u_n(\boldsymbol{k}, \boldsymbol{r}) = \langle \boldsymbol{r} | u_n(\boldsymbol{k}) \rangle \,. \tag{1.21}$$

$|\psi_n(\boldsymbol{k})\rangle$ is called the Bloch state while $|u_n(\boldsymbol{k})\rangle$ is the cell-periodic Bloch state [16].

We can further elaborate on the physical meaning of the Bloch theorem, and why the eigenstates have this form. Indeed, remember that the Hamiltonian $\hat{H}$, as written in Eq. (1.12), consists of two terms. The first is the electron's kinetic energy, and alone describes a free electron. The second term is the crystalline potential $V(\hat{\boldsymbol{r}})$, the Coulomb interaction between the electron and its environment, the atomic lattice.

Similarly, the Bloch states can also be cut in two parts. The first is the exponential factor $\exp(i\boldsymbol{k} \cdot \hat{\boldsymbol{r}})$. If the electron would be free, and $\hat{H} = \hat{\boldsymbol{p}}^2/2m_e$, then its wavefunction would be $e^{i\boldsymbol{k}\cdot\boldsymbol{r}}$ with $\boldsymbol{p} = \hbar\boldsymbol{k}$ the momentum. Identifying the parameter $\boldsymbol{k}$ from Bloch's theorem as a wavenumber (an analogy we discuss in section 1.2.3), the factor $e^{i\boldsymbol{k}\cdot\hat{\boldsymbol{r}}}$ in the Bloch state then appears as a consequence of the free-electron part of the Hamiltonian $\hat{H}$. The second part is the cell-periodic Bloch state $|u_n(\boldsymbol{k})\rangle$. The latter is a direct consequence of the crystalline potential, and marks the difference between the physics of the free electron and that of the electron living in a crystal, a many-body system. From that

point of view, the cell-periodic Bloch state also marks the difference between the Bloch state and the underlying electron.

The Bloch state is thus a mix of the electron and of its environment. Remembering that the crystalline potential is an interaction between the electron and the nuclei of the crystal lattice, the Bloch state then appears as an *emergent* state, a result of the coupling between the electron and the crystal. Imagining the physical "thing" associated to the Bloch state as a *Bloch fermion*, the Bloch fermion then appears as a *quasiparticle* resulting from the electron-nuclei interaction. And the cell-periodic Bloch state $|u_n(\boldsymbol{k})\rangle$ marks its quasiness.

The significance of the cell-periodic Bloch state, and thus the quasiness of the Bloch fermion, has not always been recognized, as can be seen from Félix Bloch's own words [17, 18]:

> "*When I started to think about it, I felt that the main problem was to explain how the electrons could sneak by all the ions in a metal so as to avoid a mean free path of the order of atomic distances. [...] To make my life easy, I began by considering wave functions in a one-dimensional periodic potential. By straight Fourier analysis I found to my delight that the wave differed from a plane wave of free electron* ***only*** *by a periodic modulation.*"

The spotlight was then more on the resemblance of the Bloch fermion to the electron than on its difference. However, as we will see in Chapters 2 and 3, the origin of geometric and topological properties in band theory precisely originate from the cell-periodic Bloch states, i.e. the difference between Bloch fermions and the bare electron. This observation has consequences when adding back the electron-electron interaction. As we will see in the example of superconductivity, putting an interaction between Bloch fermions and between electrons is not always physically equivalent.

1.2.3 . Reciprocal space

Parameter $\boldsymbol{k}$ The parameter $\boldsymbol{k}$ appearing in Bloch's theorem can be given a physical meaning. The exponential factor makes it clear that it may be seen as coming from a momentum $\boldsymbol{p}_c = \hbar\boldsymbol{k}$. And indeed one can prove, using $\hat{\boldsymbol{p}} = -i\hbar\partial_{\boldsymbol{r}}$, that the average velocity reads [13]

$$\langle\psi_n(\boldsymbol{k})|\,\hat{\boldsymbol{v}}\,|\psi_n(\boldsymbol{k})\rangle = \frac{1}{m_e}\langle\psi_n(\boldsymbol{k})|\,\hat{\boldsymbol{p}}\,|\psi_n(\boldsymbol{k})\rangle = \frac{1}{\hbar}\partial_{\boldsymbol{k}}\epsilon_n(\boldsymbol{k}). \tag{1.22}$$

As mentioned in Ref. [13], the full resemblance of $\boldsymbol{p}_c$ with the momentum $\boldsymbol{p}$ arises when considering the equations of motion of the Bloch Hamiltonian under an external electromagnetic field.

However, the parameter $\boldsymbol{k}$ cannot be fully identified as a momentum. The momentum is a good quantum number (i.e. a conserved quantity) only if the Hamiltonian is invariant under continuous translations. This continuous symmetry results, by Noether's theorem, in a conserved momentum, which is therefore a good quantum number. Here, because of the crystalline potential the Hamiltonian is invariant only under *discrete* translations. As such, the quantity $\boldsymbol{k}$ is only conserved up to a discrete amount, the latter depending on the discrete translations under which $\hat{H}$ is invariant. Because $\hat{H}$ commutes with translations by a Bravais lattice vector $\boldsymbol{R_m}$, the quantity $\boldsymbol{k}$ is only conserved up to a reciprocal Bravais lattice vector $\boldsymbol{G_n}$.

Nevertheless, it is in many ways helpful to think of $\hbar\boldsymbol{k}$ as an extension of the concept of momentum, and a quantity characteristic of the discrete translational symmetry of $\hat{H}$, just as the true momentum is for continuously symmetric systems [13]. The parameter $\boldsymbol{k}$ is often called the crystalline momentum, or the quasimomentum.

Brillouin Zone Because of this discrete conservation of the crystalline momentum $\boldsymbol{k}$, its space, called the reciprocal space, also forms a lattice, the reciprocal lattice. As stipulated in definition 1.2.2, the reciprocal lattice is spanned by the reciprocal primitive lattice vectors $\boldsymbol{b}_j$, from which the reciprocal Bravais lattice vectors $\boldsymbol{G}_{\boldsymbol{n}}$ are spanned. Focusing on $\boldsymbol{n} \in \mathbb{Z}^d$ with $n_j = 0, 1$ gives a primitive unit cell of the reciprocal lattice. However, a specific, and maybe different, primitive unit cell is considered when discussing the crystalline momentum. This primitive unit cell is called the *Brillouin zone* (BZ). It is defined as the set of $\boldsymbol{k}$ points closer to the central point $\boldsymbol{G}_0$, called the Γ point, than to any other reciprocal lattice point [8, 12, 13, 17]. Mathematically, one may write

$$\text{BZ} = \left\{ \boldsymbol{k} \in \mathbb{R}^d \;\middle|\; \forall \boldsymbol{n} \in \mathbb{Z}^d \setminus \{0\},\ \|\boldsymbol{k}\| \leq \|\boldsymbol{k} - \boldsymbol{G}_{\boldsymbol{n}}\| \right\}. \tag{1.23}$$

Practically, the Brillouin zone is constructed as the area drawn by the intersection of all the bisections of the Γ point with the nearest reciprocal lattice points. This is the Wigner-Seitz construction. For example, a triangular Bravais lattice has a honeycomb Brillouin Zone, as pictured in Fig.1.3. Of special interest in the BZ are the high-symmetry points. In the honeycomb lattice, these special points are the Γ, K and M points.

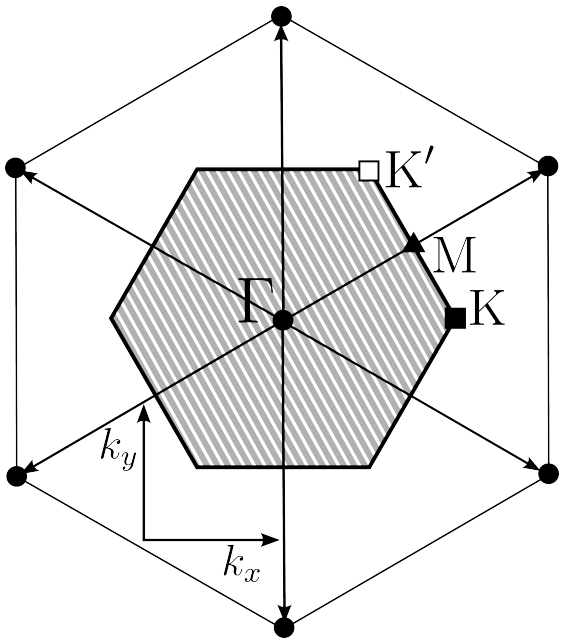

Figure 1.3: Brillouin zone of the honeycomb lattice in the two-dimensional reciprocal space, adapted from Ref. [19]. The black dots represent reciprocal Bravais lattice points, with the center one being the Γ point. Lines are then drawn between the Γ point and the nearest reciprocal lattice points. Drawing the bisecting lines of these lines then shapes the Brillouin Zone of the Bravais lattice, here the hexagonal shaded area.

Time-Reversal Invariant Momenta As we will see in chapters 3 and 9, another class of $\boldsymbol{k}$ points of interest in the Brillouin zone are those for which $-\boldsymbol{k}$ differs from $\boldsymbol{k}$ by a reciprocal Bravais lattice

vector. By the definition of the Brillouin Zone, and in Fig.1.3, we see that these points are where the bisecting lines cross the lines separating the Γ point from the nearest reciprocal lattice vectors. The latter are of the form $\boldsymbol{G_n}$ with $\boldsymbol{n} \in \{-1, 0, 1\}^d$. By symmetry of the $-\boldsymbol{k} \sim \boldsymbol{k}$ relation, we can omit the $n_j = -1$ case. This also avoids to multiply count equivalent points. In equations, the points are determined by

$$\exists \boldsymbol{n} \in \{0, 1\}^d \text{ s.t. } \boldsymbol{k} = -\boldsymbol{k} + \boldsymbol{G_n} \Leftrightarrow \boldsymbol{k} = \frac{1}{2}\boldsymbol{G_n} = \sum_{j=1}^{d} \frac{n_j}{2}\boldsymbol{b}_j. \tag{1.24}$$

These points are referred to as the *time-reversal invariant momenta* (TRIM), since the time-reversal operation is correlated with a $\boldsymbol{k} \mapsto -\boldsymbol{k}$ operation. In dimension d, there are 2^d TRIM points. In the honeycomb lattice, the four TRIM points are the Γ point and the three M points.

1.2.4 . Bloch Hamiltonian

Consider a Bloch state $|\psi_n(\boldsymbol{k})\rangle$ with eigenvalue $\epsilon_n(\boldsymbol{k})$. The eigenvalue problem of the Hamiltonian $\hat{H}$ then reads

$$\hat{H}\,|\psi_n(\boldsymbol{k})\rangle = \epsilon_n(\boldsymbol{k})\,|\psi_n(\boldsymbol{k})\rangle \Leftrightarrow \hat{H}e^{i\boldsymbol{k}\cdot\hat{\boldsymbol{r}}}\,|u_n(\boldsymbol{k})\rangle = \epsilon_n(\boldsymbol{k})e^{i\boldsymbol{k}\cdot\hat{\boldsymbol{r}}}\,|u_n(\boldsymbol{k})\rangle \tag{1.25a}$$

$$\Leftrightarrow e^{-i\boldsymbol{k}\cdot\hat{\boldsymbol{r}}}\hat{H}e^{i\boldsymbol{k}\cdot\hat{\boldsymbol{r}}}\,|u_n(\boldsymbol{k})\rangle = \epsilon_n(\boldsymbol{k})\,|u_n(\boldsymbol{k})\rangle\,. \tag{1.25b}$$

We can then further introduce the crystalline momentum by defining a $\boldsymbol{k}$-dependent Hamiltonian,

$$\hat{H}(\boldsymbol{k}) = e^{-i\boldsymbol{k}\cdot\hat{\boldsymbol{r}}}\hat{H}e^{i\boldsymbol{k}\cdot\hat{\boldsymbol{r}}}, \tag{1.25c}$$

called the *Bloch Hamiltonian*. Hereafter, we will consider the latter as our working Hamiltonian. Its eigenstates are the cell-periodic Bloch states $|u_n(\boldsymbol{k})\rangle$. This way we isolate the emergent part of the Bloch state. The eigenvalue problem

$$\hat{H}(\boldsymbol{k})\,|u_n(\boldsymbol{k})\rangle = \epsilon_n(\boldsymbol{k})\,|u_n(\boldsymbol{k})\rangle \tag{1.26}$$

is the core of *band theory*, where each $\boldsymbol{k}$-dependent solution is referred to as a *band*. $\boldsymbol{n} \in \mathbb{N}$ is the band index, while $\epsilon_n(\boldsymbol{k})$ is called the band dispersion. We will refer to the pair $(\epsilon_n, |u_n\rangle)$ as a band. Finally, we will use a common abuse of language in referring to the $|u_n(\boldsymbol{k})\rangle$ as Bloch states. The set of bands constituting the eigenstructure of the Bloch Hamiltonian is called the *band structure* of $\hat{H}(\boldsymbol{k})$.

1.3 . Tight-binding approach

How does one practically determine the band structure of a crystal ? Several methods are available. One example is the tight-binding method, relying on the linear combination of atomic orbitals (LCAO) [8]. Each atom is a priori formed by an infinite amount of orbitals, but only has a finite amount of electrons. Assuming no high-energy process happens so that the electrons occupy higher orbitals, one can then apply standard chemistry rules to determine what orbitals are actually occupied.

This way we can determine which orbitals form the solid through covalent bonding and which ones do not. The ones that do not are then called *conduction orbitals*, as they are the ones available to harbor conduction electrons. For example in graphene, the p_x and p_y orbitals form the honeycomb

lattice and the p_z orbital is the conduction orbital. We can then imagine the situation as follows. On each inequivalent atom α (i.e. on each sublattice), and spin σ, we consider a set of orbitals β. Let $|\alpha\beta\sigma\rangle$ be the quantum state of the orbital β on the sublattice α with spin σ. Remember that the Hamiltonian we consider, that written in Eq. (1.12), we have one electron living in the lattice. The electron will therefore always occupy one of the states $|\alpha\beta\sigma\rangle$. We can then imagine that the relevant Hilbert space for the problem is the one spanned by the states $|\alpha\beta\sigma\rangle$. Restricting to this Hilbert space is equivalent to assuming the following closure relation,

$$\sum_{\alpha\beta\sigma} |\alpha\beta\sigma\rangle \langle\alpha\beta\sigma| = \mathbb{1}. \tag{1.27}$$

The Bloch state $|u_n(\boldsymbol{k})\rangle$ can then be written as

$$|u_n(\boldsymbol{k})\rangle = \sum_{\alpha,\beta,\sigma} u_n^{(\alpha\beta\sigma)}(\boldsymbol{k}) |\alpha\beta\sigma\rangle , \tag{1.28}$$

with $u_n^{(\alpha\beta\sigma)}(\boldsymbol{k}) \in \mathbb{C}$. This approximation where the eigenstate is written as a linear superposition of the atomic orbitals is aptly named the LCAO method, since as we see below, the state $|\alpha\beta\sigma\rangle$ is a superposition of all the orbital wavefunctions of the orbital and spin (β, σ) centered at the sites $\boldsymbol{R_n} + \boldsymbol{\delta}_\alpha$. It is widely used in quantum chemistry and atomic physics [8].

To simplify the notion, we index all the possible combinations of spin, orbital and sublattices indices by $j \in [\![1, N]\!]$, with N equal to the product of the number of sublattices, the number of orbitals and the number of spins considered. We now have

$$|u_n(\boldsymbol{k})\rangle = \sum_{j=1}^{N} u_n^{(j)}(\boldsymbol{k}) |\alpha_j\beta_j\sigma_j\rangle . \tag{1.29}$$

As N is practically always finite, this approach has the very practical advantage of reducing the calculation of the band structure to a linear algebra problem ! The Bloch Hamiltonian can then be represented in this basis by a N by N complex matrix,

$$\hat{H}(\boldsymbol{k}) = \sum_{i,j=1}^{N} h_{ij}(\boldsymbol{k}) |\alpha_i\beta_i\sigma_i\rangle \langle\alpha_j\beta_j\sigma_j| , \quad h_{ij}(\boldsymbol{k}) = \langle\alpha_i\beta_i\sigma_i| \hat{H}(\boldsymbol{k}) |\alpha_j\beta_j\sigma_j\rangle \in \mathbb{C}. \tag{1.30}$$

As mentioned earlier, the state $|\alpha_i\beta_i\sigma_i\rangle$ represents the event in which the electron occupies the orbital β_i on the sublattice α_i with spin σ_i. Due to the crystalline nature of the solid, the orbital β_i will be present at each site of the form $\boldsymbol{R_n} + \boldsymbol{\delta}_{\alpha_i}$. Introducing $\phi_{\beta_i\sigma_i}(\boldsymbol{r} - \boldsymbol{R_n} - \boldsymbol{\delta}_{\alpha_i})$ the wavefunction of the electron in orbital β_i with spin σ_i centered on the site $\boldsymbol{R_n} + \boldsymbol{\delta}_{\alpha_i}$, we have

$$|\alpha_i\beta_i\sigma_i\rangle = \frac{1}{\sqrt{\mathcal{N}}} \sum_{\boldsymbol{n}} \int_{\mathbb{R}^d} \mathrm{d}\boldsymbol{r} \phi_{\beta_i\sigma_i}(\boldsymbol{r} - \boldsymbol{R_n} - \boldsymbol{\delta}_{\alpha_i}) |\boldsymbol{r}\rangle , \tag{1.31}$$

with $\mathcal{N}^{-1/2}$ a normalization factor. The wavefunctions $\phi_{\beta_i\sigma_i}(\boldsymbol{r} - \boldsymbol{R_n} - \boldsymbol{\delta}_{\alpha_i})$ typically exhibit exponential localization around their center. The electron is thus (typically) exponentially localized around the

lattice site. There comes the *tight-binding approximation*, where we say that the electron is purely on-site, i.e. infinitely tightly-bound to the nuclei, and moves in the crystal by tunneling between sites. The state $|\alpha_i\sigma_i\beta_i\rangle$ then becomes

$$|\alpha_i\sigma_i\beta_i\rangle = \frac{1}{\sqrt{\mathcal{N}}}\sum_{\boldsymbol{n}} \left|\phi_{\beta_i\sigma_i}\left(\boldsymbol{R_n}+\boldsymbol{\delta}_{\alpha_i}\right)\right\rangle. \tag{1.32}$$

The coefficients of the Bloch Hamiltonian can then be expanded as follows,

$$h_{ij}(\boldsymbol{k}) = \langle\alpha_i\beta_i\sigma_i|\,\hat{H}(\boldsymbol{k})\,|\alpha_j\beta_j\sigma_j\rangle = \frac{1}{\mathcal{N}}\sum_{\boldsymbol{n},\boldsymbol{m}} \left\langle\phi_{\beta_i\sigma_i}\left(\boldsymbol{R_n}+\boldsymbol{\delta}_{\alpha_i}\right)\right| e^{-i\boldsymbol{k}\cdot\hat{\boldsymbol{r}}}\hat{H}e^{i\boldsymbol{k}\cdot\hat{\boldsymbol{r}}}\left|\phi_{\beta_j\sigma_j}\left(\boldsymbol{R_m}+\boldsymbol{\delta}_{\alpha_j}\right)\right\rangle \tag{1.33a}$$

$$= \frac{1}{\mathcal{N}}\sum_{\boldsymbol{n},\boldsymbol{m}} e^{-i\boldsymbol{k}\cdot(\boldsymbol{R_n}-\boldsymbol{R_m})}e^{-i\boldsymbol{k}\cdot(\boldsymbol{\delta}_{\alpha_i}-\boldsymbol{\delta}_{\alpha_j})}\left\langle\phi_{\beta_i\sigma_i}\left(\boldsymbol{R_n}+\boldsymbol{\delta}_{\alpha_i}\right)\right|\hat{H}\left|\phi_{\beta_j\sigma_j}\left(\boldsymbol{R_m}+\boldsymbol{\delta}_{\alpha_j}\right)\right\rangle. \tag{1.33b}$$

Let us introduce the following notation for the matrix elements,

$$t_{ij,\boldsymbol{nm}} = \frac{1}{\mathcal{N}}\left\langle\phi_{\beta_i\sigma_i}\left(\boldsymbol{R_n}+\boldsymbol{\delta}_{\alpha_i}\right)\right|\hat{H}\left|\phi_{\beta_j\sigma_j}\left(\boldsymbol{R_m}+\boldsymbol{\delta}_{j}\right)\right\rangle. \tag{1.34}$$

Using second quantization notations where $|\phi_i\rangle \sim c_i^\dagger$, the Bloch Hamiltonian now reads

$$\hat{H}(\boldsymbol{k}) = \sum_{i,j=1}^{N} h_{ij}(\boldsymbol{k})c_i^\dagger c_j, \qquad h_{ij}(\boldsymbol{k}) = \sum_{\boldsymbol{n},\boldsymbol{m}} t_{ij,\boldsymbol{nm}}e^{-i\boldsymbol{k}\cdot(\boldsymbol{R_n}+\boldsymbol{\delta}_{\alpha_i}-\boldsymbol{R_m}-\boldsymbol{\delta}_{\alpha_j})}. \tag{1.35}$$

The parameter $t_{ij,\boldsymbol{nm}}$ represents the energy associated with the electron tunneling[4] (i.e. hopping) from the site $\boldsymbol{R_n}+\boldsymbol{\delta}_{\alpha_i}$ to the site $\boldsymbol{R_m}+\boldsymbol{\delta}_{\alpha_j}$. They are referred to as the tight-binding, or hopping, parameters. From Eq. (1.34) and $\hat{H}^\dagger = \hat{H}$, we see that

$$t^*_{ij,\boldsymbol{mn}} = \frac{1}{\mathcal{N}}\left\langle\phi_{\beta_j\sigma_j}\left(\boldsymbol{R_n}+\boldsymbol{\delta}_{\alpha_j}\right)\right|\hat{H}\left|\phi_{\beta_i\sigma_i}\left(\boldsymbol{R_n}+\boldsymbol{\delta}_{\alpha_i}\right)\right\rangle = t_{ji,\boldsymbol{mn}}. \tag{1.36}$$

This relation translates the so-called *reciprocity* of the hoppings, in that two opposite hoppings are associated with the same energy magnitude, but with opposing phases. We can show that the reciprocity of the hopping parameters is equivalent to the hermiticity of the Bloch Hamiltonian. Indeed, we have $h_{ij}(\boldsymbol{k})^* = h_{ji}(\boldsymbol{k})$ iff

$$\sum_{\boldsymbol{n},\boldsymbol{m}} t^*_{ij,\boldsymbol{nm}}e^{i\boldsymbol{k}\cdot(\boldsymbol{R_n}+\boldsymbol{\delta}_{\alpha_i}-\boldsymbol{R_m}-\boldsymbol{\delta}_{\alpha_j})} = \sum_{\boldsymbol{n},\boldsymbol{m}} t_{ji,\boldsymbol{nm}}e^{-i\boldsymbol{k}\cdot(\boldsymbol{R_n}+\boldsymbol{\delta}_{\alpha_j}-\boldsymbol{R_m}-\boldsymbol{\delta}_{\alpha_i})} \tag{1.37a}$$

$$\Leftrightarrow \sum_{\boldsymbol{n},\boldsymbol{m}} t^*_{ij,\boldsymbol{nm}}e^{i\boldsymbol{k}\cdot(\boldsymbol{R_n}+\boldsymbol{\delta}_{\alpha_i}-\boldsymbol{R_m}-\boldsymbol{\delta}_{\alpha_j})} = \sum_{\boldsymbol{nm}} t_{ji,\boldsymbol{nm}}e^{i\boldsymbol{k}\cdot(\boldsymbol{R_m}+\boldsymbol{\delta}_{\alpha_i}-\boldsymbol{R_n}-\boldsymbol{\delta}_{\alpha_j})} \tag{1.37b}$$

$$\Leftrightarrow \sum_{\boldsymbol{n},\boldsymbol{m}} (t^*_{ij,\boldsymbol{nm}} - t_{ji,\boldsymbol{mn}})e^{i\boldsymbol{k}\cdot(\boldsymbol{R_n}-\boldsymbol{R_m})} = 0. \tag{1.37c}$$

Recognizing the latter as a Fourier transform, the unicity of the coefficients yields

$$\hat{H}(\boldsymbol{k})^\dagger = \hat{H}(\boldsymbol{k}) \;\Leftrightarrow\; t^*_{ij,\boldsymbol{nm}} = t_{ji,\boldsymbol{mn}}. \tag{1.38}$$

[4] Hence the notation t.

Interestingly, some open and/or interacting systems can effectively be described by tight-binding models where the hoppings are non-reciprocal (also called asymetrical), bringing interest to the study of non-Hermitian models [20, 21, 22, 23].

The reciprocity implies that the on-site energy $t_{ii,\boldsymbol{nn}}$ is always real. Additional symmetries, like time-reversal of crystalline symmetries, can also allow the tight-binding parameters to be real.

Judging from Eq. (1.35), a large amount of tight-binding parameters are *a priori* involved. Practically, since the orbital wave-functions typically decay exponentially away from their center, their overlap between sites also gets much weaker as the sites become more distant. One therefore only focuses on the nearest-neighboor hoppings, and adds further hoppings if necessary.

Finally, the value of the hopping parameters is typically determined from a comparison between density functional theory calculations and experimental (e.g. ARPES[5]) measurements.

Using the invariance of $\hat{H}$ under Bravais translations, an alternative expression for the coefficients h_{ij} is

$$h_{ij}(\boldsymbol{k}) = e^{-i\boldsymbol{k}\cdot(\boldsymbol{\delta}_{\alpha_i}-\boldsymbol{\delta}_{\alpha_j})} \sum_{\boldsymbol{p}} t_{ij,\boldsymbol{p}} e^{i\boldsymbol{k}\cdot\boldsymbol{R}_{\boldsymbol{p}}}, \tag{1.39}$$

where $\boldsymbol{p} = \boldsymbol{m} - \boldsymbol{n}$ and

$$t_{ij,\boldsymbol{p}} = \frac{1}{\mathcal{N}} \left\langle \phi_{\beta_i\sigma_i}(\boldsymbol{\delta}_{\alpha_i}) \right| \hat{H} \left| \phi_{\alpha_j\sigma_j}\left(\boldsymbol{R}_{\boldsymbol{p}} + \boldsymbol{\delta}_{\alpha_j}\right) \right\rangle . \tag{1.40}$$

This expression shows that the hopping parameters only depend on the distance over which the hopping happens.

The tight-binding method offers an insight in the emergence of the Bloch state. Indeed, restoring the sublattice, orbital and spin indices, we have

$$|u_n(\boldsymbol{k})\rangle = \sum_{\alpha\beta\sigma} u_n^{(\alpha\beta\sigma)}(\boldsymbol{k}) \, |\alpha\beta\sigma\rangle . \tag{1.41}$$

Since the $|\alpha\beta\sigma\rangle$ are product states themselves[6], the Bloch state thus originates from the entanglement of the degrees of freedom, i.e. of all the different states an electron can occupy within a unit cell. This is coherent with the fact that band topology, originating from the Bloch state $|u_n(\boldsymbol{k})\rangle$, is linked with short-range entanglement patterns.

1.4 . Example: Honeycomb lattice, massive Dirac fermions

As a practical example, consider the *gapped graphene* model, which will be our toy model throughout the thesis. This spinless model is on a two-dimensional honeycomb lattice with one orbital per site. It is then a two-band model, because of the two triangular sublattices. Without loss of generality, we take the blue and red sublattices, pictured in Fig.1.1, to be $|\phi_1\rangle$ and $|\phi_2\rangle$, respectively. We then have $\boldsymbol{\delta}_{\alpha_1} = 0$ and $\boldsymbol{\delta}_{\alpha_2} = a\boldsymbol{e}_y = \boldsymbol{\delta}$.

In this basis, the Bloch Hamiltonian is then represented by the following matrix,

$$\hat{H}(\boldsymbol{k}) = \begin{pmatrix} h_{11}(\boldsymbol{k}) & h_{12}(\boldsymbol{k}) \\ h_{12}(\boldsymbol{k})^* & h_{22}(\boldsymbol{k}) \end{pmatrix} . \tag{1.42}$$

[5] Angle-Resolved Photo-Emission Spectroscopy

[6] $|\alpha\beta\sigma\rangle = |\alpha\rangle \otimes |\beta\rangle \otimes |\sigma\rangle$

h_{11} and h_{12} both represent intra-sublattice hoppings. The two leading contributions are the on-site energies $t_{ii,00}$, and the next-nearest neighbor hopping. We will ignore the latter, so that $h_{11}(\boldsymbol{k}) = t_{11,00} = \epsilon_A$ and $h_{22}(\boldsymbol{k}) = t_{22,00} = \epsilon_B$, both real quantities.

The inter-sublattice hopping is dominated by the nearest-neighbor hopping, which we focus on here. These hoppings are pictured in Fig.1.4 For simplicity, and since all three hoppings are equidis-

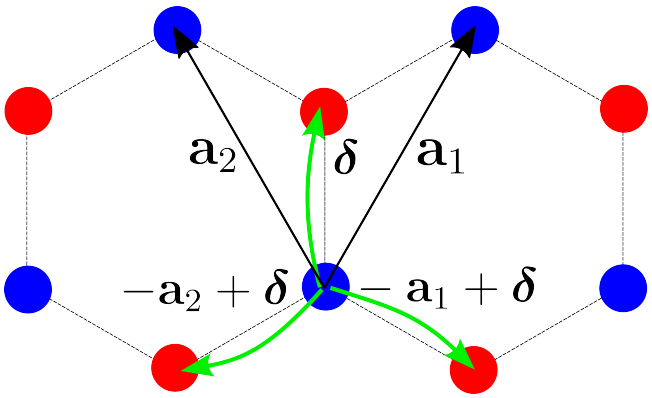

Figure 1.4: Nearest-neighbor hoppings in the honeycomb lattice, in green.

tant, we consider the nearest-neighbor hoppings to be of equal amplitude $-t$, which we choose to be real. Note the presence of the minus sign, a result of computational calculations [11].

The coefficient h_{12}^* represents hopping from the blue to red sublattices, and from Eq. (1.34) we have

$$h_{12}(\boldsymbol{k})^* = -te^{-i\boldsymbol{k}\cdot\boldsymbol{\delta}} - te^{-i\boldsymbol{k}\cdot(-\boldsymbol{a}_1+\boldsymbol{\delta})} - te^{-i\boldsymbol{k}\cdot(-\boldsymbol{a}_2+\boldsymbol{\delta})} = -te^{-i\boldsymbol{k}\cdot\boldsymbol{\delta}}\left(1 + e^{i\boldsymbol{k}\cdot\boldsymbol{a}_1} + e^{i\boldsymbol{k}\cdot\boldsymbol{a}_2}\right) = -te^{-i\boldsymbol{k}\cdot\boldsymbol{\delta}}\gamma_{\boldsymbol{k}}. \quad (1.43)$$

The Bloch Hamiltonian now reads

$$\hat{H}(\boldsymbol{k}) = \begin{pmatrix} \epsilon_A & -te^{i\boldsymbol{k}\cdot\boldsymbol{\delta}}\gamma_{\boldsymbol{k}}^* \\ -te^{-i\boldsymbol{k}\cdot\boldsymbol{\delta}}\gamma_{\boldsymbol{k}} & \epsilon_B \end{pmatrix}. \quad (1.44)$$

A general property of two-by-two Hermitian matrices is they can be composed as a sum of the three Pauli matrices $\sigma_{x,y,z}$, and the identity matrix σ_0, the coefficients being real. Such a decomposition reads

$$\hat{H}(\boldsymbol{k}) = h_0(\boldsymbol{k})\sigma_0 + \boldsymbol{h}(\boldsymbol{k})\cdot\boldsymbol{\sigma} = \begin{pmatrix} h_0(\boldsymbol{k}) + h_z(\boldsymbol{k}) & h_x(\boldsymbol{k}) - ih_y(\boldsymbol{k}) \\ h_x(\boldsymbol{k}) + ih_y(\boldsymbol{k}) & h_0(\boldsymbol{k}) - h_z(\boldsymbol{k}) \end{pmatrix}, \quad (1.45)$$

with $(h_0, \boldsymbol{h}) \in \mathbb{R} \times \mathbb{R}^3$. In the present case, we identify

$$h_0(\boldsymbol{k}) = \frac{\epsilon_A + \epsilon_B}{2}, \quad h_x(\boldsymbol{k}) = -t\cos(k_y)\,\mathrm{Re}\,\gamma_{\boldsymbol{k}}, \quad h_y(\boldsymbol{k}) = t\sin(k_y)\,\mathrm{Im}\,\gamma_{\boldsymbol{k}}, \quad h_z(\boldsymbol{k}) = \frac{\epsilon_A - \epsilon_B}{2}, \quad (1.46)$$

where we make use of the common abuse of notation $\boldsymbol{k} \mapsto \boldsymbol{k}a$.

The component h_0 may be ignored as it as no physical relevance, other than shifting the Fermi level. The h_z component is more interesting. In the case of graphene where the two sublattices are chemically identical (carbon), we have $\epsilon_A = \epsilon_B$ and therefore $h_z = 0$. In that case the system is inversion symmetric, as the two sublattices are related by spatial inversion. But in other cases, such as

hexagonal boron nitride (hBN) and transition metal dichalcogenides (TMDC), the two sublattices are not chemically equivalent. This fact breaks inversion symmetry, and induces an imbalance quantified by h_z, which we hereafter call Δ.

The model then finally reads

$$H(\boldsymbol{k}) = \begin{pmatrix} \Delta & -te^{i\boldsymbol{k}\cdot\boldsymbol{\delta}}\gamma_{\boldsymbol{k}}^* \\ -te^{-i\boldsymbol{k}\cdot\boldsymbol{\delta}}\gamma_{\boldsymbol{k}} & -\Delta \end{pmatrix}, \tag{1.47}$$

whose band dispersions are readily found to be

$$\epsilon_1(\boldsymbol{k}) = -\sqrt{\Delta^2 + t^2|\gamma_{\boldsymbol{k}}|^2}, \;\; \epsilon_2(\boldsymbol{k}) = \sqrt{\Delta^2 + t^2|\gamma_{\boldsymbol{k}}|^2}. \tag{1.48}$$

By convention, we label the eigenvalues in increasing order. As in Ref. [11], let us introduce $\lambda = \pm$ the band index such that $\epsilon_1(\boldsymbol{k}) = \epsilon_-(\boldsymbol{k})$ and $\epsilon_2(\boldsymbol{k}) = \epsilon_+(\boldsymbol{k})$.

Low-energy model Of special interest is the band structure near the $\boldsymbol{K}$ and $\boldsymbol{K'}$ points, situated at $+4\pi/3\sqrt{3}$ and $-4\pi/3\sqrt{3}$, respectively. At these points we have

$$\gamma_{\boldsymbol{K}(\boldsymbol{K'})} = 1 + \exp\left(\pm i\frac{4\pi}{3\sqrt{3}}\frac{\sqrt{3}}{2}\right) + \exp\left(\mp i\frac{4\pi}{3\sqrt{3}}\frac{\sqrt{3}}{2}\right) = 1 + 2\cos\left(\frac{2\pi}{3}\right) = 0. \tag{1.49}$$

At these points we therefore have $\epsilon_\pm(\boldsymbol{k}) = \pm|\Delta|$, the lowest difference possible between the two. This is why $|\Delta|$ is commonly referred to as a *band gap*. It is also interesting to study the behaviour of the Bloch fermions near these points. First, let $\xi = \pm 1$ such that $\xi\boldsymbol{K}$ refers to the $\boldsymbol{K}$ ($\boldsymbol{K'}$) point if $\xi_= + 1$ ($\xi = -1$). Close to these points we then have

$$\gamma_{\boldsymbol{k}} = \gamma_{\xi\boldsymbol{K}} + \boldsymbol{k}\cdot\partial_{\boldsymbol{k}}\gamma_{\boldsymbol{k}}\big|_{\xi\boldsymbol{K}} + \mathcal{O}(k^2). \tag{1.50}$$

Computing

$$\partial_{k_\mu}\gamma_{\boldsymbol{k}} = \partial_{k_\mu}(1 + e^{i\boldsymbol{k}\cdot\boldsymbol{a}_1} + e^{i\boldsymbol{k}\cdot\boldsymbol{a}_2}) = ia_{1,\mu}e^{i\boldsymbol{k}\cdot\boldsymbol{a}_1} + ia_{2,\mu}e^{i\boldsymbol{k}\cdot\boldsymbol{a}_2}, \tag{1.51}$$

we get

$$\gamma_{\boldsymbol{k}} = ie^{i\xi\boldsymbol{K}\cdot\boldsymbol{a}_1}\boldsymbol{k}\cdot\boldsymbol{a}_1 + ie^{i\xi\boldsymbol{K}\cdot\boldsymbol{a}_2}\boldsymbol{k}\cdot\boldsymbol{a}_2 = ie^{\xi 2i\pi/3}\boldsymbol{k}\cdot\boldsymbol{a}_1 + ie^{-\xi 2i\pi/3}\boldsymbol{k}\cdot\boldsymbol{a}_2 \tag{1.52a}$$

$$= i\frac{\sqrt{3}}{2}k_x\left(e^{\xi 2i\pi/3} - e^{-\xi 2i\pi/3}\right) + i\frac{3}{2}k_y\left(e^{\xi 2i\pi/3} + e^{-\xi 2i\pi/3}\right) = i\frac{\sqrt{3}}{2}k_x\cdot 2i\xi\frac{\sqrt{3}}{2} + i\frac{3}{2}k_y\cdot 2\frac{-1}{2} \tag{1.52b}$$

$$= -\xi\frac{3}{2}k_x - i\frac{3}{2}k_y = -\frac{3}{2}(\xi k_x + ik_y). \tag{1.52c}$$

The remaining factor to consider is the phase $e^{i\boldsymbol{k}\cdot\boldsymbol{\delta}}$. To first order it will contribute to the Bloch Hamiltonian through $\exp(i\xi\boldsymbol{K}\cdot\boldsymbol{\delta})$ which is trivial for the two K points we considered. This phase factor is different for the other points but we will consider the standard convention here [24]. The tight-binding model near the $\xi\boldsymbol{K}$ points now becomes a *low-energy model*[7]

$$\hat{H}(\boldsymbol{k}) = \begin{pmatrix} \Delta & \hbar v(\xi k_x - ik_y) \\ \hbar v(\xi k_x + ik_y) & -\Delta \end{pmatrix} = \hbar v\xi k_x\sigma_x + \hbar v k_y\sigma_y + \Delta\sigma_z, \tag{1.53}$$

[7] Generically, a low-energy model stems from the Taylor expansion of a tight-binding model around a specific point of interest, typically close to the Fermi level, at a lowest point of the band dispersion. Hence the name "low-energy model".

where we have defined

$$v = \frac{3ta}{2\hbar}, \tag{1.54}$$

which has the dimension of a velocity. For graphene, we have $t \simeq 3$eV and $a \simeq 1.42$Å[11] which yields $v \simeq 10^6$ meters per second. The band dispersions read

$$\epsilon_\lambda(\boldsymbol{k}) = \lambda\sqrt{\Delta^2 + \hbar^2 v^2 k^2} = \lambda|\Delta|\sqrt{1 + \lambda\!\!\!^{-2}_c k^2}, \tag{1.55}$$

with $k^2 = k_x^2 + k_y^2$, and where we have defined the length $\lambda\!\!\!^{-}_c = \hbar v/|\Delta|$. The band dispersions then behave quadratically directly near the $\boldsymbol{K}$ and $\boldsymbol{K'}$ points and linearly away from that (when $\lambda\!\!\!^{-}_c k \gg 1$).

Since the band dispersions have their low points in the vicinity of the $\boldsymbol{K}$ and $\boldsymbol{K'}$ points, these regions are referred to as the *valleys* of the Brillouin zone.

The Bloch fermions corresponding to the low-energy model may then be interpreted as *massive Dirac fermions*, of mass m such that $|\Delta| = mv^2$. The velocity v is called the Dirac velocity and the length $\lambda\!\!\!^{-}_c$ is the reduced Compton length. In the massless case ($\Delta = 0$), the band dispersions exhibit Dirac cones at the $\boldsymbol{K}$ and $\boldsymbol{K'}$ points.

In the following chapters we will see that the analogy goes deeper.

2 - Geometrical band theory

We now turn our attention to what will be the main object of study of this thesis, band quantum geometry. Reflecting its organization in four main sections, the objective of this chapter is fourfold. First, following the original approach of Provost and Vallée [25], we derive the geometric quantities associated with a general parameter-dependent quantum state. This allows to showcase the generality of quantum geometry. Second, we list several properties of the quantum geometric tensor, which we will all use throughout the thesis.

Third, we deliberately spend a considerable amount of time listing and elaborating the different viewpoints available on quantum geometry. These viewpoints aim at giving a general overview on quantum geometry, in band theory and beyond. Special emphasis is put on the first three viewpoints, which in the author's opinion gives the most physical and intuitive vision of quantum geometry. The second viewpoint is a personal contribution to the matter. Finally, we list several formulations of the quantum geometric tensor which offer alternative and simpler ways to compute band quantum geometry.

This chapter will therefore hopefully offer a sound practical, technical and conceptual basis for the rest of the thesis.

2.1 . Formal motivation

One important observation in the Bloch theorem is that while for the states $|\psi_n(\boldsymbol{k})\rangle$ we have

$$\big\langle \psi_m(\boldsymbol{k'})\big|\psi_n(\boldsymbol{k})\big\rangle = \delta_{nm}\delta^d(\boldsymbol{k}-\boldsymbol{k'}), \tag{2.1}$$

the same cannot, *a priori*, be said about the states $|u_n(\boldsymbol{k})\rangle$. When two of them are taken at the same crystalline momentum, we can show that

$$\langle u_m(\boldsymbol{k})|u_n(\boldsymbol{k})\rangle = \langle \psi_m(\boldsymbol{k})|\, e^{i\boldsymbol{k}\cdot\hat{\boldsymbol{r}}}e^{-i\boldsymbol{k}\cdot\hat{\boldsymbol{r}}}\,|\psi_n(\boldsymbol{k})\rangle = \langle \psi_m(\boldsymbol{k})|\psi_n(\boldsymbol{k})\rangle = \delta_{mn}. \tag{2.2}$$

But for two different values of the crystalline momentum

$$\big\langle u_m(\boldsymbol{k'})\big|u_n(\boldsymbol{k})\big\rangle = \int_{\mathbb{R}^d} \mathrm{d}\boldsymbol{r} e^{-i(\boldsymbol{k}-\boldsymbol{k'})\cdot\boldsymbol{r}}\psi_m(\boldsymbol{k'},\boldsymbol{r})^*\psi_n(\boldsymbol{k},\boldsymbol{r}), \tag{2.3}$$

which has *a priori* no reason to be zero. This can also be observed from the fact that the states $|u_n(\boldsymbol{k})\rangle$ are the eigenstates of the Bloch Hamiltonian, which depends on $\boldsymbol{k}$. So for each value of $\boldsymbol{k}$, the spectral theorem ensures that the states $|u_n(\boldsymbol{k})\rangle$ have zero mutual overlap. But for two different values of the crystalline momentum, $\hat{H}(\boldsymbol{k})$ and $\hat{H}(\boldsymbol{k'})$ are different operators, with different applications of the spectral theorem. This fact is explored in more depth in section 2.4.6.

That being said, can we still say things about the overlap of a Bloch state $|u_n\rangle$ at different values of $\boldsymbol{k}$? Doing so amounts to ask how $|u_n(\boldsymbol{k})\rangle$ changes when its parameter $\boldsymbol{k}$ changes. In other words, how far apart are $|u_n(\boldsymbol{k})\rangle$ and $|u_n(\boldsymbol{k'})\rangle$?

2.2 . Parametric derivations of the quantum geometric tensor

As the problem of distance in a parameter dependent quantum space is more general than band theory, we will take a more general stance. Consider a Hilbert space $\mathscr{H}$ and $\mathcal{M} \subset \mathbb{R}^N$ the space of N real parameters on which the states of $\mathscr{H}$ vary. A distance is generated by a metric, corresponding to infinitesimal changes in the parameters. We present a derivation of the quantum geometric tensor while searching for a natural notion of metric between quantum states at different parameter values, largely based on Refs. [25, 26]. This allows us to introduce the different quantities of geometrical band theory. We then present an alternative derivation directly based on the overlap $\langle\psi(\boldsymbol{s})|\psi(\boldsymbol{s}+\mathbf{d}\boldsymbol{s})\rangle$. Finally, we describe the special case of band theory.

Naive attempt A natural notion of distance would thus be reached by considering $|\psi(\boldsymbol{s})\rangle \in \mathscr{H}$ with $\boldsymbol{s} \in \mathcal{M}$, vary $\boldsymbol{s}$ infinitesimally and compare the resulting state with $|\psi(\boldsymbol{s})\rangle$ using the scalar product $\langle\cdot|\cdot\rangle$ which provides $\mathscr{H}$ with its complex vector space structure.

Doing so gives

$$\|\psi(\boldsymbol{s}+\mathbf{d}\boldsymbol{s})-\psi(\boldsymbol{s})\|^2 = \langle\partial_\mu\psi\,\mathrm{d}s_\mu|\partial_\nu\psi\,\mathrm{d}s_\nu\rangle = \langle\partial_\mu\psi|\partial_\nu\psi\rangle\,\mathrm{d}s_\mu\mathrm{d}s_\nu, \tag{2.4}$$

with $\partial_\mu = \partial_{s_\mu}$ and where we make use of Einstein's summation convention.

Local U(1) invariance One could then assume that $\langle\partial_\mu\psi|\partial_\nu\psi\rangle$ is a suitable metric, but there comes a subtlety. Quantum Mechanics has a local U(1) gauge invariance, i.e. all the states in $\mathscr{H}$ differing only by a phase factor represent the same *physical* state. Consequently, while the Hilbert space $\mathscr{H}$ is the space of all states, the projective space $\mathscr{H}/\mathrm{U}(1)$ is the space of all *physical* states. We can define it as follows. Consider two states $|\psi_1(\boldsymbol{s})\rangle, |\psi_2(\boldsymbol{s})\rangle \in \mathscr{H}$, and introduce the equivalence relation

$$|\psi_1(\boldsymbol{s})\rangle \sim |\psi_2(\boldsymbol{s})\rangle \quad\Leftrightarrow\quad \exists\varphi(\boldsymbol{s})\in\mathbb{R} \text{ s.t. } |\psi_2(\boldsymbol{s})\rangle = e^{i\varphi(\boldsymbol{s})}\,|\psi_1(\boldsymbol{s})\rangle\,. \tag{2.5}$$

Thus, all states differing only by a U(1) element $e^{i\varphi(\boldsymbol{s})}$ are equivalent under the relation $\sim$. The set of all equivalence classes under the relation $\sim$ defines the projective space $\mathscr{H}/\mathrm{U}(1)$. So while $\langle\partial_\mu\psi|\partial_\nu\psi\rangle$ may be a suitable metric for $\mathscr{H}$, what we would really want is a metric on this projective space. One way to see if $\langle\partial_\mu\psi|\partial_\nu\psi\rangle$ is also a good metric on $\mathscr{H}/\mathrm{U}(1)$ is to consider two states such that $|\psi_2(\boldsymbol{k})\rangle = e^{i\varphi(\boldsymbol{s})}\,|\psi_1(\boldsymbol{s})\rangle$ and see if $\langle\partial_\mu\psi|\partial_\nu\psi\rangle$ is invariant under this local U(1) transformation. Indeed, the two states represent the same point in $\mathscr{H}/\mathrm{U}(1)$. A good metric on this space must therefore be the same for two states equivalent under the relation $\sim$. We therefore expand $\langle\partial_\mu\psi_2|\partial_\mu\psi_2\rangle$ as follows,

$$\langle\partial_\mu\psi_2|\partial_\nu\psi_2\rangle = \Big[\,\langle\psi_1|\,e^{-i\varphi}(-i\partial_\mu\varphi) + \langle\partial_\mu\psi_1|\,e^{-i\varphi}\Big]\Big[e^{i\varphi}i\partial_\nu\varphi\,|\psi_1\rangle + e^{i\varphi}\,|\partial_\nu\psi_1\rangle\,\Big] \tag{2.6a}$$

$$= \langle\partial_\mu\psi_1|\partial_\nu\psi_1\rangle - i\partial_\mu\varphi\,\langle\psi_1|\partial_\nu\psi_1\rangle - i\partial_\nu\varphi\,\langle\psi_1|\partial_\mu\psi_1\rangle + \partial_\mu\varphi\partial_\nu\varphi. \tag{2.6b}$$

The quantity $\langle\partial_\mu\psi|\partial_\nu\psi\rangle$ is thus not invariant under a local U(1) gauge transform, and does not constitute a suitable metric for the projective space $\mathscr{H}/\mathrm{U}(1)$.

Quantum Geometric Tensor There is however a way to fall back on our feet. Introducing $\mathcal{A}_\mu^\psi(\boldsymbol{s}) = i\,\langle\psi(\boldsymbol{s})|\partial_\mu\psi(\boldsymbol{s})\rangle$, we can reexpress $\langle\partial_\mu\psi_2|\partial_\nu\psi_2\rangle$ as

$$\langle\partial_\mu\psi_2|\partial_\nu\psi_2\rangle = \langle\partial_\mu\psi_1|\partial_\nu\psi_1\rangle - \mathcal{A}_\nu^{\psi_1}\partial_\mu\varphi - \mathcal{A}_\mu^{\psi_1}\partial_\nu\varphi + \partial_\mu\varphi\partial_\nu\varphi \tag{2.7a}$$

$$= \langle\partial_\mu\psi_1|\partial_\nu\psi_1\rangle + \big(\mathcal{A}_\mu^{\psi_1} - \partial_\mu\varphi\big)\big(\mathcal{A}_\nu^{\psi_1} - \partial_\nu\varphi\big) - \mathcal{A}_\mu^{\psi_1}\mathcal{A}_\nu^{\psi_1}. \tag{2.7b}$$

$\mathcal{A}_\mu^\psi \in \mathbb{R}$ is called the *Berry connection*[1][11, 16]. We can then leverage the relation between $|\psi_1\rangle$ and $|\psi_2\rangle$ to get

$$\mathcal{A}_\mu^{\psi_2} = i\,\langle\psi_2|\partial_\mu\psi_2\rangle = i\,\langle\psi_1|\,e^{-i\varphi}\partial_\mu\big[e^{i\varphi}\,|\psi_1\rangle\,\big] = -\partial_\mu\varphi + i\,\langle\psi_1|\partial_\mu\psi_1\rangle = \mathcal{A}_\mu^{\psi_1} - \partial_\mu\varphi, \tag{2.8}$$

which thereby yields

$$\langle\partial_\mu\psi_2|\partial_\nu\psi_2\rangle - \mathcal{A}_\mu^{\psi_2}\mathcal{A}_\nu^{\psi_2} = \langle\partial_\mu\psi_1|\partial_\nu\psi_1\rangle - \mathcal{A}_\mu^{\psi_1}\mathcal{A}_\nu^{\psi_1}. \tag{2.9}$$

Let us then define the *quantum geometric tensor* (QGT)

$$Q_{\mu\nu}^\psi(\boldsymbol{s}) = \langle\partial_\mu\psi(\boldsymbol{s})|\partial_\nu\psi(\boldsymbol{s})\rangle - \mathcal{A}_\mu^\psi(\boldsymbol{s})\mathcal{A}_\mu^\psi(\boldsymbol{s}), \tag{2.10}$$

which is a quantity invariant under a local $\mathrm{U}(1)$ gauge transformation. As such, it can be a suitable metric for the projective space $\mathscr{H}/\mathrm{U}(1)$. We can rewrite it as follows,

$$Q_{\mu\nu}^\psi = \langle\partial_\mu\psi|\,\big[\mathbb{1} - |\psi\rangle\,\langle\psi|\,\big]\,|\partial_\nu\psi\rangle\,. \tag{2.11}$$

Quantum metric We saw that our naive choice of infinitesimal in Eq. (2.4) is flawed because it is not locally $\mathrm{U}(1)$ gauge invariant. But from there we could still construct an object satisfying this demand, the QGT. But to what notion of distance does the QGT correspond ? An intermediary result is the fact that only the real part of the QGT contributes to the infinitesimal distance. Indeed, using $Q_{\mu\nu}^{\psi*} = Q_{\nu\mu}^\psi$ we have

$$2i\,\mathrm{Im}\,Q_{\mu\nu}^\psi \mathrm{d}s_\mu \mathrm{d}s_\nu = Q_{\mu\nu}^\psi \mathrm{d}s_\mu \mathrm{d}s_\nu - Q_{\mu\nu}^{\psi*}\mathrm{d}s_\mu\mathrm{d}s_\nu = Q_{\mu\nu}^\psi \mathrm{d}s_\mu\mathrm{d}s_\nu - Q_{\nu\mu}^\psi \mathrm{d}s_\mu\mathrm{d}s_\nu \tag{2.12a}$$

$$= Q_{\mu\nu}^\psi \mathrm{d}s_\mu\mathrm{d}s_\nu - Q_{\mu\nu}^\psi \mathrm{d}s_\mu\mathrm{d}s_\nu = 0, \tag{2.12b}$$

by symmetry of $\mathrm{d}s_\mu\mathrm{d}s_\nu$ under $\mu \leftrightarrow \nu$. So the real part of the QGT is the only contributor to the actual metric on $\mathscr{H}/\mathrm{U}(1)$. We therefore introduce

$$g_{\mu\nu}^\psi(\boldsymbol{s}) = \mathrm{Re}\,Q_{\mu\nu}^\psi(\boldsymbol{s}) = \mathrm{Re}\,\langle\partial_\mu\psi(\boldsymbol{s})|\,\big[\mathbb{1} - |\psi(\boldsymbol{s})\rangle\,\langle\psi(\boldsymbol{s})|\,\big]\,|\partial_\mu\psi(\boldsymbol{s})\rangle \tag{2.13}$$

the *quantum metric* [25, 27]. As a metric on a projective complex variety, it is also referred to as the Fubini-Study metric [28, 29]. As we will see in section 2.4.1, it is a central quantity in quantum metrology where it is known as the quantum Fisher information.

[1] Since the norm of $|\psi(\boldsymbol{s})\rangle$ is always equal to 1, it is a constant with respect to $\boldsymbol{s}$, which implies that $\langle\partial_\mu\psi(\boldsymbol{s})|\psi(\boldsymbol{s})\rangle = -\langle\psi(\boldsymbol{s})|\partial_\mu\psi(\boldsymbol{s})\rangle$. Thus $\langle\psi(\boldsymbol{s})|\partial_\mu\psi(\boldsymbol{s})\rangle$ is purely imaginary and $\mathcal{A}_\mu^\psi$ is real.

Meaning of distance As for the infinitesimal distance, we have

$$g^{\psi}_{\mu\nu}\mathrm{d}s_\mu\mathrm{d}s_\nu = Q^{\psi}_{\mu\nu}\mathrm{d}s_\mu\mathrm{d}s_\nu = \langle\partial_\mu\psi\mathrm{d}s_\mu|\left[\mathbb{1}-|\psi\rangle\langle\psi|\right]|\partial_\nu\psi\mathrm{d}s_\nu\rangle \tag{2.14a}$$

$$= \left[\langle\psi(\boldsymbol{s}+\mathbf{d}\boldsymbol{s})| - \langle\psi(\boldsymbol{s})|\right]\left[\mathbb{1}-|\psi(\boldsymbol{s})\rangle\langle\psi(\boldsymbol{s})|\right]\left[|\psi(\boldsymbol{s}+\mathbf{d}\boldsymbol{s})\rangle - |\psi(\boldsymbol{s})\rangle\right] \tag{2.14b}$$

$$= \cdots = 1 - |\langle\psi(\boldsymbol{s})|\psi(\boldsymbol{s}+\mathbf{d}\boldsymbol{s})\rangle|^2. \tag{2.14c}$$

So the distance associated to the quantum metric $g^{\psi}_{\mu\nu}$ measures the distinguishability of a state between two neighboring parameter values. By the Cauchy-Schwartz inequality,

$$|\langle\psi(\boldsymbol{s})|\psi(\boldsymbol{s}+\mathbf{d}\boldsymbol{s})\rangle|^2 \leq \langle\psi(\boldsymbol{s})|\psi(\boldsymbol{s})\rangle\langle\psi(\boldsymbol{s}+\mathbf{d}\boldsymbol{s})|\psi(\boldsymbol{s}+\mathbf{d}\boldsymbol{s})\rangle = 1, \tag{2.15}$$

which implies that $g^{\psi}_{\mu\nu}(\boldsymbol{s})\mathrm{d}s_\mu\mathrm{d}s_\nu \in [0,1]$. Consider the two limiting cases. If the distance is zero, then the Cauchy-Schwartz inequality states that the two states must be colinear, i.e. proportional to one another. Since the states are normalized,

$$\exists\varphi(\boldsymbol{s})\in\mathbb{R} \text{ s.t. } |\psi(\boldsymbol{s}+\mathbf{d}\boldsymbol{s}\rangle = e^{i\varphi(\boldsymbol{s})}|\psi(\boldsymbol{s}\rangle), \tag{2.16}$$

i.e. they represent the same element in $\mathscr{H}/\mathrm{U}(1)$.

At the contrary, if the distance is one, then the overlap is zero meaning that $|\psi(\boldsymbol{s}+\mathbf{d}\boldsymbol{s})\rangle$ is orthogonal to $|\psi(\boldsymbol{s})\rangle$, indicating a drastic change is the state $|\psi\rangle$ upon $\boldsymbol{s}\mapsto\boldsymbol{s}+\mathbf{d}\boldsymbol{s}$. From a quantum metrology perspective, the quantum metric generates the infinitesimal fidelity (the modulus of the overlap), and quantifies the loss of information about the state $|\psi(\boldsymbol{s})\rangle$ when slightly changing its parameters. If the distance is zero, then the state is fully equivalent to what it was and no information was lost. But on the contrary if the distance is one then the new state looks like nothing like the old one and all information about the latter was lost.

In the perspective of condensed matter physics, this is reminiscent of a critical point, as we mention in section 2.4.

Berry curvature While it does not contribute to the infinitesimal distance, the imaginary part of the QGT is still interesting. First, we rewrite it as follows,

$$2i\,\mathrm{Im}\,Q^{\psi}_{\mu\nu} = Q^{\psi}_{\mu\nu} - Q^{\psi}_{\nu\mu} = \langle\partial_\mu\psi|\partial_\nu\psi\rangle - \mathcal{A}^{\psi}_\mu\mathcal{A}^{\psi}_\nu - \langle\partial_\nu\psi|\partial_\mu\psi\rangle + \mathcal{A}^{\psi}_\mu\mathcal{A}^{\psi}_\nu \tag{2.17a}$$

$$= \langle\partial_\mu\psi|\partial_\nu\psi\rangle - \langle\partial_\nu\psi|\partial_\mu\psi\rangle = \partial_\mu\langle\psi|\partial_\nu\psi\rangle - \langle\psi|\partial_\mu\partial_\nu\psi\rangle - \partial_\nu\langle\psi|\partial_\mu\psi\rangle + \langle\psi|\partial_\nu\partial_\mu\psi\rangle\,. \tag{2.17b}$$

In practice, we will consider quantum states that, apart from specific parameter values, will always be at least of class $\mathcal{C}^2$ with respect to its parameters $\boldsymbol{s}$. For Bloch states, we show in chapter 3 that apart from phase singularities in their components, which give rise to band topology, they are mostly analytic over the Brillouin zone within the tight-binding method. So considering that $|\psi(\boldsymbol{s}\rangle)$ is of class $\mathcal{C}^2$, we can freely permute its derivatives and therefore find

$$2i\,\mathrm{Im}\,Q^{\psi}_{\mu\nu} = \partial_\mu\langle\psi|\partial_\nu\psi\rangle - \partial_\nu\langle\psi|\partial_\mu\psi\rangle = -i\big(\partial_\mu\mathcal{A}^{\psi}_\nu - \partial_\nu\mathcal{A}^{\psi}_\mu\big) \tag{2.18a}$$

$$\Leftrightarrow\quad \mathrm{Im}\,Q^{\psi}_{\mu\nu} = -\frac{1}{2}\big(\partial_\mu\mathcal{A}^{\psi}_\nu - \partial_\nu\mathcal{A}^{\psi}_\mu\big) = -\frac{1}{2}\mathcal{B}^{\psi}_{\mu\nu}, \tag{2.18b}$$

where $\mathcal{B}^{\psi}_{\mu\nu}$ is the *Berry curvature* [11, 16, 27].

Finally, the quantum geometric tensor reads

$$Q^{\psi}_{\mu\nu}(\boldsymbol{s}) = \langle \partial_\mu \psi(\boldsymbol{s})| \left[\mathbb{1} - |\psi(\boldsymbol{s})\rangle \langle \psi(\boldsymbol{s})|\right] |\partial_\nu \psi(\boldsymbol{s})\rangle = g^{\psi}_{\mu\nu}(\boldsymbol{s}) - \frac{i}{2}\mathcal{B}^{\psi}_{\mu\nu}(\boldsymbol{s}), \tag{2.19}$$

with $g^{\psi}_{\mu\nu}$ the quantum metric and $\mathcal{B}^{\psi}_{\mu\nu}$ the Berry curvature being real quantities.

Infinitesimal overlap Consider $|\psi(\boldsymbol{s})\rangle \in \mathscr{H}$ with $\boldsymbol{s} \in \mathcal{M}$. To second order,

$$\langle \psi(\boldsymbol{s})|\psi(\boldsymbol{s}+\mathbf{d}\boldsymbol{s})\rangle = 1 + \langle \psi(\boldsymbol{s})|\partial_\mu \psi(\boldsymbol{s})\rangle \, \mathrm{d}s_\mu + \frac{1}{2}\langle \psi(\boldsymbol{s})|\partial_\mu\partial_\nu \psi(\boldsymbol{s})\rangle \, \mathrm{d}s_\mu \mathrm{d}s_\nu \tag{2.20a}$$

$$= 1 - i\mathcal{A}^{\psi}_{\mu}(\boldsymbol{s})\mathrm{d}s_\mu + \frac{1}{2}\langle \psi(\boldsymbol{s})|\partial_\mu\partial_\nu \psi(\boldsymbol{s})\rangle \, \mathrm{d}s_\mu \mathrm{d}s_\nu, \tag{2.20b}$$

using $\langle \psi(\boldsymbol{s})|\psi(\boldsymbol{s})\rangle = 1$. Let us now also denote

$$\langle \psi(\boldsymbol{s})|\psi(\boldsymbol{s}+\mathbf{d}\boldsymbol{s})\rangle = \mathcal{F}_\psi(\boldsymbol{s}) e^{i\Phi_\psi(\boldsymbol{s})}, \tag{2.21}$$

with $\mathcal{F}_\psi(\boldsymbol{s}) \in \mathbb{R}_+$ the modulus of the overlap. In appendix B.1 we show that to second order the modulus reads as in Eq. (2.14c),

$$\mathcal{F}^2_\psi = |\langle \psi(\boldsymbol{s})|\psi(\boldsymbol{s}+\mathbf{d}\boldsymbol{s})\rangle|^2 = 1 - g^{\psi}_{\mu\nu}\mathrm{d}s_\mu \mathrm{d}s_\nu, \tag{2.22}$$

making the $\boldsymbol{s}$ dependences implicit. As for the phase, we also show in appendix B.1 that to leading order we have

$$\Phi_\psi = -\mathcal{A}^{\psi}_{\mu}\mathrm{d}s_\mu = -\boldsymbol{\mathcal{A}}^{\psi}\cdot\mathbf{d}\boldsymbol{s}. \tag{2.23}$$

The infinitesimal overlap is thus obtained as

$$\langle \psi(\boldsymbol{s})|\psi(\boldsymbol{s}+\mathbf{d}\boldsymbol{s})\rangle = \left(1 - \frac{1}{2}g^{\psi}_{\mu\nu}(\boldsymbol{s})\mathrm{d}s_\mu \mathrm{d}s_\nu\right) e^{-i\boldsymbol{\mathcal{A}}^{\psi}(\boldsymbol{s})\cdot\mathbf{d}\boldsymbol{s}}. \tag{2.24}$$

Schematically, the real part of the QGT influences the modulus of the overlap while the imaginary part influences its phase [26].

Distance between rays The QGT can also be directly derived from a different notion of distance. As we mentioned, quantum states are physically different only if they are not related by a local $\mathrm{U}(1)$ transformation. This means that physically we care more about quantum rays than quantum states. A notion of distance between quantum rays thus sounds more natural. This is achieved by the following [25]. For $|\psi_1\rangle, |\psi_2\rangle \in \mathscr{H}$ where the $\boldsymbol{s}$ dependences are implicit, consider

$$d(\psi_1,\psi_2) = \inf_{\varphi_1,\varphi_2\in\mathbb{R}} \left\| e^{i\varphi_1}|\psi_1\rangle - e^{i\varphi_2}|\psi_2\rangle \right\|^2 = 2 - 2|\langle \psi_1|\psi_2\rangle|. \tag{2.25a}$$

For $\psi_1 = \psi(\boldsymbol{s})$ and $\psi_2 = \psi(\boldsymbol{s}+\mathbf{d}\boldsymbol{s})$, we then readily find

$$d(\psi(\boldsymbol{s}),\psi(\boldsymbol{s}+\mathbf{d}\boldsymbol{s})) = g^{\psi}_{\mu\nu}(\boldsymbol{s})\mathrm{d}s_\mu \mathrm{d}s_\nu \tag{2.26}$$

Band theory In band theory the Hilbert space we consider is that of the Bloch states, and its parameter space is the Brillouin zone (BZ). We have derived several geometric quantities. The first one was the Berry connection. For a Bloch state $|u_n(\boldsymbol{k})\rangle$, we will simply denote

$$\mathcal{A}_\mu^{u_n}(\boldsymbol{k}) = \mathcal{A}_\mu^n(\boldsymbol{k}) = i\,\langle u_n(\boldsymbol{k})|\partial_\mu u_n(\boldsymbol{k})\rangle\,. \tag{2.27}$$

The Berry curvature is the curl of the Berry connection, and reads

$$\mathcal{B}_{\mu\nu}^n(\boldsymbol{k}) = \partial_\mu \mathcal{A}_\nu^n(\boldsymbol{k}) - \partial_\nu \mathcal{A}_\mu^n(\boldsymbol{k}) = i\big(\,\langle\partial_\mu u_n(\boldsymbol{k})|\partial_\nu u_n(\boldsymbol{k})\rangle - \langle\partial_\nu u_n(\boldsymbol{k})|\partial_\mu u_n(\boldsymbol{k})\rangle\,\big). \tag{2.28}$$

And the quantum geometric tensor becomes

$$Q_{\mu\nu}^n(\boldsymbol{k}) = \langle\partial_\mu u_n(\boldsymbol{k})|\left[\mathbb{1} - |u_n(\boldsymbol{k})\rangle\,\langle u_n(\boldsymbol{k})|\right]|\partial_\nu u_n(\boldsymbol{k})\rangle = g_{\mu\nu}^n(\boldsymbol{k}) - \frac{i}{2}\mathcal{B}_{\mu\nu}^n(\boldsymbol{k}). \tag{2.29}$$

The quantum metric and the Berry curvature form the *quantum geometry* of the band $(\epsilon_n, |u_n\rangle)$. Notice that both the quantum metric and Berry curvature have the dimension of a surface, and the Berry connection has the dimension of a length. We shall see that we can indeed interpret these quantities as such.

2.3 . Properties of the quantum geometric tensor

The QGT obeys a list of properties. When needed, they are proven in appendix B.2.

Hermicity The quantum geometric tensor $Q^n \in \mathcal{M}_d(\mathbb{C})$ is Hermitian. Indeed, as we have shown before,

$$Q_{\mu\nu}^{n*} = \langle\partial_\mu u_n|\left[\mathbb{1} - |u_n\rangle\,\langle u_n|\right]|\partial_\nu u_n\rangle^* = \langle\partial_\nu u_n|\left[\mathbb{1} - |u_n\rangle\,\langle u_n|\right]|\partial_\mu u_n\rangle = Q_{\nu\mu}^n, \tag{2.30}$$

i.e. $Q^{n\dagger} = Q^n$. From Eq. (2.29), the quantum metric and Berry curvature obey

$$g_{\nu\mu}^n = g_{\mu\nu}^n \quad \mathcal{B}_{\nu\mu}^n = -\mathcal{B}_{\mu\nu}^n, \tag{2.31}$$

i.e. $g^{nt} = g^n$ and $\mathcal{B}^{nt} = -\mathcal{B}^n$. The quantum metric thus appears as the symmetric part of the QGT while the Berry curvature is its antisymmetric part.

U(N) gauge dependence By construction, the QGT is invariant under local U(1) gauge transformations. However, there is another class of transformations under which it is not. Consider a Bloch Hamiltonian written $H(\boldsymbol{k})$ in a finite basis of N states $|\phi_j\rangle$, for example an orbital basis of a tight-binding model. Now apply a local U(N) transformation using $U(\boldsymbol{k}) \in$ U(N). This corresponds to a change of basis $|\phi_j\rangle \mapsto U(\boldsymbol{k})\,|\phi_j\rangle$. The Bloch Hamiltonian and states are transformed as

$$H'(\boldsymbol{k}) = U(\boldsymbol{k})^\dagger H(\boldsymbol{k}) U(\boldsymbol{k}), \quad \big|u_n'(\boldsymbol{k})\big\rangle = U(\boldsymbol{k})\,|u_n(\boldsymbol{k})\rangle\,. \tag{2.32}$$

It is shown in appendix B.2 that the QGT transforms as $Q_{\mu\nu}^n \mapsto Q_{\mu\nu}^{n\prime}$ where

$$\begin{aligned} Q_{\mu\nu}^{n\prime} = Q_{\mu\nu}^n &+ \langle u_n|\left(\partial_\mu U^\dagger\right)U\left[\mathbb{1} - |u_n\rangle\,\langle u_n|\right]|\partial_\nu u_n\rangle + \langle\partial_\mu u_n|\left[\mathbb{1} - |u_n\rangle\,\langle u_n|\right]U^\dagger\partial_\nu U\,|u_n\rangle \\ &+ \langle u_n|\left(\partial_\mu U^\dagger\right)U\left[\mathbb{1} - |u_n\rangle\,\langle u_n|\right]U^\dagger\partial_\nu U\,|u_n\rangle\,. \end{aligned} \tag{2.33a}$$

If U does not depend on $\boldsymbol{k}$, then its derivatives vanish and $Q^{n\prime}_{\mu\nu} = Q^{n}_{\mu\nu}$. It is then invariant under global U(N) transformations. However, if U depends on $\boldsymbol{k}$, then the QGT actually changes upon the U(N) transformation. As such it is not invariant under local U(N) transformations. The fact that the QGT is only invariant under global transformations is understandable when remembering that it is a geometric notion.

Consider a simple line in a three dimensional space, pictured in Fig.2.1. On one side apply a global rotation R to it, and see that the shape of the line (i.e. its geometry) does not change. Now on the other side apply a local rotation $R(\boldsymbol{r})$ to it, such that the rotation becomes increasingly stronger as you go through the line. The result, as seen in Fig.2.1b, shows a distorted shape since one end of the line was much more rotated than the other. The geometry of the line is thus invariant under global rotations, but not under local ones. Note that we can equivalently see this as a distortion of the axes (x, y, z).

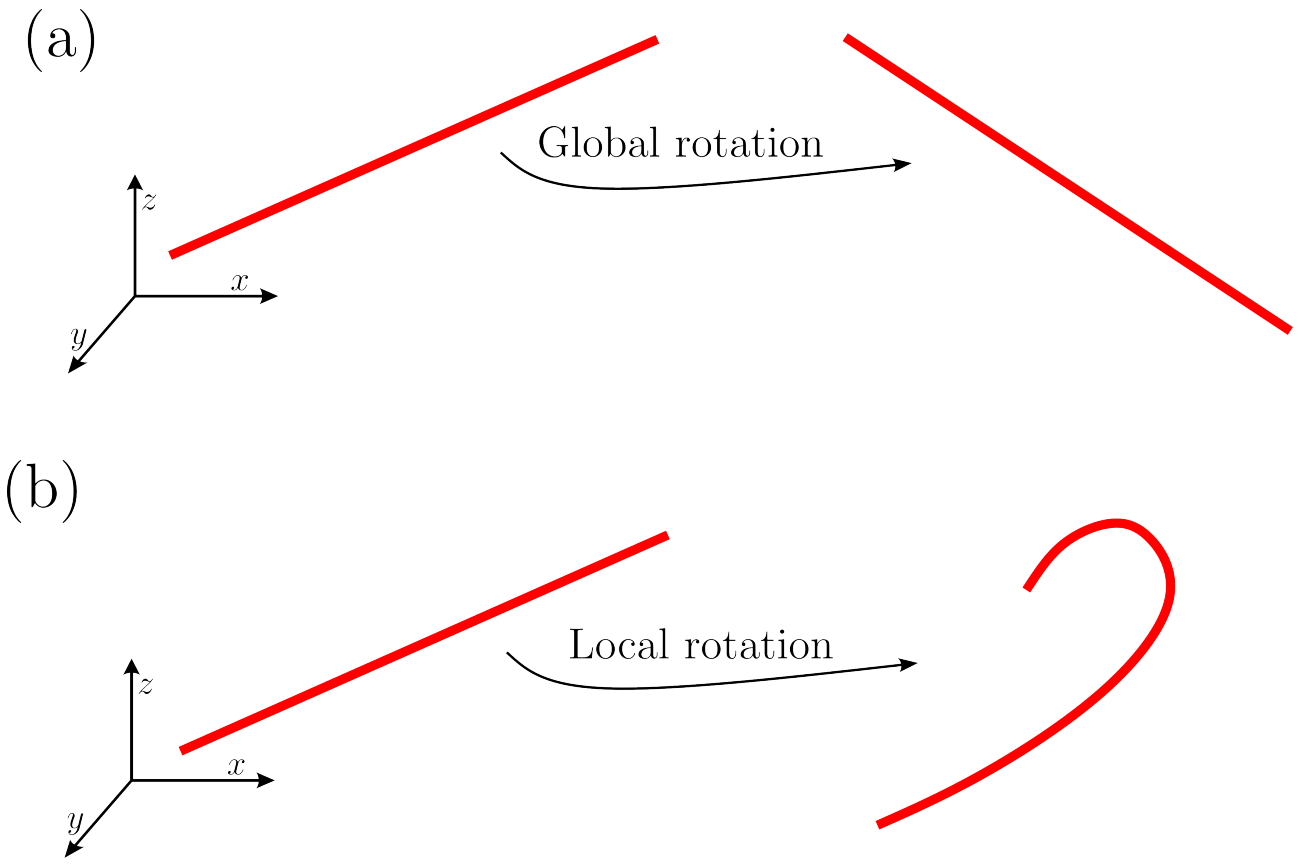

Figure 2.1: Example of global invariance but local dependence of geometry, with a line in the three-dimensional space. (a) The line is globally rotated in the three-dimensional space. Its shape, i.e. its geometry, is invariant. (b) The line is *locally* rotated. Points at the right end of the line get much more rotated than those at the left end. The result is a distorted shape, i.e. geometry.

Positive Semi-definiteness The infinitesimal distance associated to the quantum metric is

$$g^n_{\mu\nu}(\boldsymbol{k})\mathrm{d}k_\mu \mathrm{d}k_\nu = 1 - |\,\langle u_n(\boldsymbol{k})|u_n(\boldsymbol{k}+\mathbf{d}\boldsymbol{k})\rangle\,|^2. \tag{2.34}$$

Applying the Cauchy-Schwartz inequality gives

$$|\,\langle u_n(\boldsymbol{k})|u_n(\boldsymbol{k}+\mathbf{d}\boldsymbol{k})\rangle\,|^2 \leq \langle u_n(\boldsymbol{k})|u_n(\boldsymbol{k})\rangle\,\langle u_n(\boldsymbol{k}+\mathbf{d}\boldsymbol{k})|u_n(\boldsymbol{k}+\mathbf{d}\boldsymbol{k})\rangle = 1, \tag{2.35}$$

and implies that

$$g^n_{\mu\nu}(\boldsymbol{k})\mathrm{d}k_\mu \mathrm{d}k_\nu = \mathbf{d}\boldsymbol{k}^{\mathrm{t}} g^n \mathbf{d}\boldsymbol{k} \geq 0. \tag{2.36}$$

As such the metric g^n is positive semidefinite. And since $\mathbf{d}\boldsymbol{k}^{\mathrm{t}} g^n \mathbf{d}\boldsymbol{k} = \mathbf{d}\boldsymbol{k}^{\mathrm{t}} Q^n \mathbf{d}\boldsymbol{k}$, the quantum geometric tensor is also positive semidefinite. From that point of view, if $\mathscr{H}$ is the Hilbert space spanned by the orbital basis, then the manifold[2] $(\mathscr{H}, Q^n)$ is a pseudo-Riemannian manifold[3] [30].

If we consider the manifold $\left(\mathscr{H}/\mathrm{U}(1), Q^n\right)$, then since we have shown that $\mathbf{d}\boldsymbol{k}^{\mathrm{t}} g^n \mathbf{d}\boldsymbol{k}$ is zero iff $|u_n(\boldsymbol{k})\rangle$ and $|u_n(\boldsymbol{k}+\mathbf{d}\boldsymbol{k})\rangle$ are the same element of $\mathscr{H}/\mathrm{U}(1)$, we can exclude the latter case. Therefore, $\left(\mathscr{H}/\mathrm{U}(1), Q^n\right)$ is a Riemannian manifold [25].

Most importantly, the positive semidefiniteness of Q^n and g^n implies that both have real positive eigenvalues, i.e. their determinants and traces are positive. Analytically,

$$\det Q^n \geq 0, \;\; \det g^n \geq 0, \;\; \mathrm{Tr}\, Q^n = \mathrm{Tr}\, g^n = \sum_{\mu=1}^{d} g^n_{\mu\mu} \geq 0. \tag{2.37}$$

Two-dimensional inequality In two dimensions, we can write the QGT as

$$Q^n = \begin{pmatrix} g^n_{xx} & g^n_{xy} - \frac{i}{2}\mathcal{B}^n_{xy} \\ g^n_{xy} + \frac{i}{2}\mathcal{B}^n_{xy} & g^n_{yy} \end{pmatrix}, \tag{2.38}$$

so that its determinant reads

$$\det Q^n = g^n_{xx} g^n_{yy} - g^{n2}_{xy} - \frac{1}{4}|\mathcal{B}^n_{xy}|^2 = \det g^n - \frac{1}{4}|\mathcal{B}^n_{xy}|^2. \tag{2.39}$$

The positive definiteness thereby implies that

$$\sqrt{\det g^n} = \sqrt{g^n_{xx} g^n_{yy} - g^{n2}_{xy}} \geq \frac{1}{2}|\mathcal{B}^n_{xy}|, \tag{2.40}$$

where we can take the square root of $\det g^n$ because of the positive semi-definiteness of the quantum metric. It may be of importance to note that this analysis is true in any two-dimensional plane (μ, ν) if we are in more than two dimensions.[4] From this we can derive two other inequalities of interest. First, we have

$$\sqrt{g^n_{xx} g^n_{yy}} \geq \sqrt{g^n_{xx} g^n_{yy} - g^{n2}_{xy}} \geq \frac{1}{2}|\mathcal{B}^n_{xy}|. \tag{2.41}$$

[2] Or equivalently $(\mathscr{H}, g^n)$

[3] Another name is "Lorentzian manifold"

[4] This stems from Sylvester's criterion, which states that a matrix is positive semi-definite iff its determinant and that of *all* its principal submatrices are positive. Taking the case of a two by two submatrix in the plane of interest then yields the inequality.

Second, using Young's inequality we have

$$\frac{1}{2}\operatorname{Tr} g^n = \frac{g^n_{xx}}{2} + \frac{g^n_{xx}}{2} \geq \sqrt{g^n_{xx} g^n_{yy}} \geq \frac{1}{2}|\mathcal{B}^n_{xy}|. \tag{2.42}$$

We thus have three inequalities,

$$\sqrt{\det g^n} \geq \frac{1}{2}|\mathcal{B}_{xy}|, \quad \operatorname{Tr} g^n \geq |\mathcal{B}^n_{xy}|, \quad \sqrt{g^n_{xx} g^n_{yy}} \geq \frac{1}{2}|\mathcal{B}^n_{xy}|. \tag{2.43}$$

The first two inequalities are of special interest in the field of fractional Chern insulators (FCI), a phase analogous to the fractional quantum Hall phase, but that does not need a magnetic field. The inequalities in this field are respectively called the determinant and trace conditions. The interest is that their saturation is a condition for the stabilization of the FCI phase [28, 31, 32].

Berry's sum rule From Eq. (2.107), the Berry curvature can be expressed as

$$2i\mathcal{B}^n_{\mu\nu} = \sum_{\substack{m=1 \\ m\neq n}}^{N} \frac{\langle u_n|\,\partial_\mu H\,|u_m\rangle\,\langle u_m|\,\partial_\nu H\,|u_n\rangle - \langle u_n|\,\partial_\nu H\,|u_m\rangle\,\langle u_m|\,\partial_\mu H\,|u_n\rangle}{(\epsilon_n - \epsilon_m)^2}, \tag{2.44}$$

with N the number of bands. Let $A \in \mathcal{M}_N(\mathbb{R})$ defined by

$$A_{nm} = \frac{\langle u_n|\,\partial_\mu H\,|u_m\rangle\,\langle u_m|\,\partial_\nu H\,|u_n\rangle - \langle u_n|\,\partial_\nu H\,|u_m\rangle\,\langle u_m|\,\partial_\mu H\,|u_n\rangle}{(\epsilon_n - \epsilon_m)^2}. \tag{2.45}$$

A is clearly an antisymmetric matrix, i.e. $A_{mn} = -A_{nm}$. Therefore

$$2i\sum_{n=1}^{N}\mathcal{B}^n_{\mu\nu} = \sum_{n=1}^{N}\sum_{\substack{m=1 \\ m\neq n}}^{N} A_{nm} = \sum_{\substack{n,m=1 \\ m\neq n}}^{N} A_{nm}. \tag{2.46}$$

Summing the Berry curvatures of each band at a fixed $\boldsymbol{k}$ is equivalent to summing all the coefficients of A except its diagonal elements. We can therefore decompose the sum in the strictly upper and lower triangular parts of A. The two are then related by an exchange $n \leftrightarrow m$, and gives

$$2i\sum_{n=1}^{N}\mathcal{B}^n_{\mu\nu} = \sum_{\substack{n,m=1 \\ m>n}}^{N} A_{nm} + \sum_{\substack{n,m=1 \\ m<n}}^{N} A_{nm} = \sum_{\substack{n,m=1 \\ m<n}}^{N} (A_{nm} + A_{mn}) = 0, \tag{2.47a}$$

i.e.

$$\sum_{n=1}^{N}\mathcal{B}^n_{\mu\nu}(\boldsymbol{k}) = 0. \tag{2.48}$$

We call Eq. (2.48) the *Berry sum rule*. A mathematical result states that a matrix is of trace zero iff it can be written as a commutator [33, 34]. We can then imagine a matrix with coefficients $\mathcal{B}^{nm}_{\mu\nu}$ such that its diagonal elements are the $\mathcal{B}^n_{\mu\nu}$. This matrix could then be written as a commutator. We show its explicit form in section 2.4.2.

Time-reversal and spatial inversion The last property of the QGT we will mention is its behavior towards time-reversal and spatial inversion. We consider a model without spin-orbit coupling, so that we can index the spinful bands by (n, σ).

Time-reversal Under time-reversal it can be shown that quantum metric and Berry curvature transform as [11, 35]

$$g_{\mu\nu}^{n,\sigma}(\boldsymbol{k}) \mapsto g_{\mu\nu}^{n,-\sigma}(-\boldsymbol{k}), \;\; \mathcal{B}_{\mu\nu}^{n,\sigma}(\boldsymbol{k}) \mapsto -\mathcal{B}_{\mu\nu}^{n,-\sigma}(-\boldsymbol{k}). \tag{2.49}$$

In a time-reversal symmetric system, we thus have

$$g_{\mu\nu}^{n,-\sigma}(-\boldsymbol{k}) = g_{\mu\nu}^{n,\sigma}(\boldsymbol{k}), \;\; \mathcal{B}_{\mu\nu}^{n,-\sigma}(-\boldsymbol{k}) = -\mathcal{B}_{\mu\nu}^{n,\sigma}(\boldsymbol{k}). \tag{2.50}$$

Spatial inversion Under spatial inversion, one can show that

$$g_{\mu\nu}^{n,\sigma}(\boldsymbol{k}) \mapsto g_{\mu\nu}^{n,\sigma}(-\boldsymbol{k}), \;\; \mathcal{B}_{\mu\nu}^{n,\sigma}(\boldsymbol{k}) \mapsto \mathcal{B}_{\mu\nu}^{n,\sigma}(-\boldsymbol{k}), \tag{2.51}$$

which means that in an inversion symmetric[5] system we have

$$g_{\mu\nu}^{n,\sigma}(-\boldsymbol{k}) = g_{\mu\nu}^{n,\sigma}(\boldsymbol{k}), \;\; \mathcal{B}_{\mu\nu}^{n,\sigma}(-\boldsymbol{k}) = \mathcal{B}_{\mu\nu}^{n,\sigma}(\boldsymbol{k}). \tag{2.52}$$

One important consequence of these relations is that in a spinless system that has both symmetries the Berry curvature is identically zero, meaning that at least one of the two has to be broken in order to get a non-trivial Berry curvature.

2.4 . Viewpoints on quantum geometry

After the preceding technical discussion on quantum geometry and the geometric tensor, we now aim to give a conceptual intuition on it. This section remains rather general and formal, but a specific example is briefly discussed in Sec.2.6.

As quantum geometry is at the intersection, and at the forefront, of multiple fields of research [36] (e.g. quantum matter physics and quantum information theory), it seems that a unified understanding of quantum geometry is still out of reach. Instead, quantum geometry may be better understood through a series of *viewpoints*. Each viewpoint will translate one aspect of what quantum geometry is, and hopefully through the collection of these viewpoints our understanding of it will deepen.

This approach is directly inspired by A. Grothendieck in Ref. [37] [6]

[5] Another name is *centrosymmetric*

[6] Original text: *"Ainsi, le point de vue fécond n'est autre que cet "oeil" qui à la fois nous fait découvrir, et nous fait reconnaître l'unité dans la multiplicité de ce qui est découvert. [...] Mais comme son nom même le suggère, un "point de vue" en lui-même reste parcellaire. Il nous révèle un des aspects d'un paysage ou d'un panorama, parmi une multiplicité d'autres également valables, également "réels". C'est dans la mesure où se conjuguent les points de vue complémentaires d'une même réalité, où se multiplient nos "yeux", que le regard pénètre plus avant dans la connaissance des choses. Plus la réalité que nous désirons connaître est riche et complexe, et plus aussi il est important de disposer de plusieurs "yeux" pour l'appréhender dans toute son ampleur et dans toute sa finesse."*

"*Thus, the fruitful point of view is none other than that 'eye' which both makes us discover, and recognise the unity in the multiplicity of what is discovered. [...] But as its very name suggests, a 'point of view' in itself remains fragmentary. It reveals one aspect of a landscape or panorama, among a multiplicity of other equally valid, equally 'real' aspects. It is by combining complementary points of view of the same reality, by multiplying our 'eyes', that our gaze penetrates further into our knowledge of things. The richer and more complex the reality we wish to understand, the more important it is to have several 'eyes' to grasp it in all its breadth and finesse.*"

A unified and "linear" understanding of quantum geometry may be reached this way.[7] We present six such viewpoints. In the first one, we take a more general stance and review some aspects of quantum information theory and metrology related to the estimation of parameters in a multiparameter quantum system. This point of view will make it possible, in addition to talking about quantum geometry in a broader context, to establish certain relationships between quantum geometry and the generators of the parameters on which the quantum states depend. The second point of view is essentially an application of the first to the context of band theory, where the quantum geometry appears as a consequence of the non-locality of the Bloch fermion. The third viewpoint offers an explanation of the non-locality of the Bloch fermion as a consequence of its quasiness (its difference with the elementary electrons), and particularly of virtual interband transitions.

The fourth viewpoint summarizes the duality between the Berry curvature and the magnetic field. The fifth viewpoint concerns the Karplus-Luttinger drift velocity and the anomalous Hall effect, where the Berry curvature appears as an axis of self-rotation of the wavepacket of the Bloch fermion. Finally, the sixth viewpoint mentions the mathematical languages in which band theory can be translated.

2.4.1 . Viewpoint 1: Quantum metrology and multiparameter estimation theory

A central challenge in quantum metrology is to devise experimental protocols where the parameters measured are done so with the best precision possible. As it turns out, quantum geometry is a central tool in this endeavour. Following Ref. [38], we begin by briefly reviewing the classical case of multiparameter estimation through the classical quantum Fisher information matrix (CFIM). We then review how the quantum Fisher information matrix (QFIM) is constructed from its classical counterpart, and review its relation to the QGT in the case of pure states. Finally, we review how the QFIM relates to the parameter generators, and see that the QGT appears as their covariance matrix.

Classical multiparameter estimation Consider an experiment where one tries to estimate (or rather infer) N physical quantities $(\theta_1, \dots, \theta_N) = \boldsymbol{\theta} \in \mathbb{R}^N$ from a set of observed data $\boldsymbol{x} \in \mathbb{R}^N$. The goal of estimation theory is to consider the error of experiments and find the best precision possible for the estimation of $\boldsymbol{\theta}$. Note that here $\boldsymbol{\theta}$ will have the exact same role as the parameters $\boldsymbol{s}$ which

[7] From Ref. [37]:"*Et il arrive, parfois, qu'un faisceau de points de vue convergents sur un même et vaste paysage, par la vertu de cela en nous apte à saisir l'Un à travers le multiple, donne corps à une chose nouvelle ; à une chose qui dépasse chacune des perspectives partielles, de la même façon qu'un être vivant dépasse chacun de ses membres et de ses organes. Cette chose nouvelle, on peut l'appeler une vision. La vision unit les points de vue déjà connus qui l'incarnent, et elle nous en révèle d'autres jusque-là ignorés, tout comme le point de vue fécond fait découvrir et appréhender comme partie d'un même Tout, une multiplicité de questions, de notions et d'énoncés nouveaux.*"

appeared in Sec.2.2, and also will appear to be an analog of the crystal momentum $\boldsymbol{k}$. However, we choose to keep the notations of the corresponding fields, in order to keep the local coherence of the notations with their respective fields of origin.

We consider the approach of Fisher estimation where the parameters $\boldsymbol{\theta}$ are unknown but not random [38]. Considering the probability density $p(\boldsymbol{\theta}|\boldsymbol{x})$ (the probability of having the values $\boldsymbol{\theta}$ when observing $\boldsymbol{x}$) known, the parameters $\boldsymbol{\theta}$ may be inferred through a random variable called the estimator $\hat{\boldsymbol{\theta}}$, which is a function of $\boldsymbol{x}$ only. An important example is the maximum likelihood estimator $\hat{\boldsymbol{\theta}} = \arg\max_{\boldsymbol{\theta}} p(\boldsymbol{\theta}|\boldsymbol{x})$. Assuming an unbiased estimator, its covariance matrix $\mathrm{Cov}(\hat{\boldsymbol{\theta}}) \in \mathcal{M}_N(\mathbb{R})$ is defined as

$$\mathrm{Cov}(\hat{\boldsymbol{\theta}}) = \mathbb{E}\big[(\hat{\boldsymbol{\theta}} - \mathbb{E}[\hat{\boldsymbol{\theta}}])^t(\hat{\boldsymbol{\theta}} - \mathbb{E}[\hat{\boldsymbol{\theta}}])\big], \quad \mathbb{E}[\mathcal{O}(\boldsymbol{x})] = \int_{\mathbb{R}^N} \mathrm{d}\boldsymbol{x} p(\boldsymbol{\theta}|\boldsymbol{x})\mathcal{O}(\boldsymbol{x}). \tag{2.53}$$

We then define the classical Fisher information matrix (CFIM) $I(\boldsymbol{\theta})$ as [38, 39, 40]

$$I_{\mu\nu}(\boldsymbol{\theta}) = \int_{\mathbb{R}^N} \mathrm{d}\boldsymbol{x} p(\boldsymbol{\theta}|\boldsymbol{x})^{-1}\partial_{\theta_\mu} p(\boldsymbol{\theta}|\boldsymbol{x})\partial_{\theta_\nu} p(\boldsymbol{\theta}|\boldsymbol{x}) = \mathbb{E}\big[\partial_{\theta_\mu} \ln p(\boldsymbol{\theta}|\boldsymbol{x})\partial_{\theta_\nu} \ln p(\boldsymbol{\theta}|\boldsymbol{x})\big], \tag{2.54}$$

assuming some regularity conditions on $\ln p(\boldsymbol{\theta}|\boldsymbol{x})$. The classical Cramér-Rao bound is then established as

$$\mathrm{Cov}(\hat{\boldsymbol{\theta}}) \geq I(\boldsymbol{\theta})^{-1}. \tag{2.55}$$

The inverse of the Fisher information therefore gives the minimum uncertainty, i.e. the maximum precision, attainable in the estimation of $\boldsymbol{\theta}$. We can then go one step further and link the problem of parameter estimation to the field of information geometry, the field that studying probabilities in a geometric fashion [38, 41]. Indeed, one might want to get an idea of how two statistical distributions $p(\boldsymbol{\theta}_1|\boldsymbol{x})$ and $p(\boldsymbol{\theta}_2|\boldsymbol{x})$ differ from one another. This way we introduce the idea of *statistical distance*. Chentsov's theorem [41, 42] then ensures that the Fisher information matrix is the only metric on this manifold that satisfies certain statistical conditions. This geometrical point of view is very fertile, in that for example the optimization of an experimental protocole now corresponds to looking for the geodesics associated to the CFIM. This is also true in the quantum case.

Quantum Fisher Information Matrix Here we show that the quantum extenstion of the Fisher information reduces to the quantum geometric tensor in the case of pure states. In the quantum case, there are N parameters $\boldsymbol{\theta} \in \mathbb{R}^N$ that we want to measure *simultaneously*. The first step is to have a probe system, represented by a density matrix ρ_0. Then the probe system is prepared for the experiment, represented by a unitary parametrization by $U(\boldsymbol{\theta})$, such that the parametrized density matrix reads

$$\rho(\boldsymbol{\theta}) = U(\boldsymbol{\theta})^\dagger \rho_0 U(\boldsymbol{\theta}). \tag{2.56}$$

The extension of the CFIM to the quantum case can be done as follows [38]. Proceeding as in Refs. [38, 43], consider that the parameters that are actually measured are $\boldsymbol{x} \in \mathbb{R}^N$ through the Hermitian operator $\hat{E}(\boldsymbol{x})$, which is such that

$$\int_{\mathbb{R}^N} \hat{E}(\boldsymbol{x})\mathrm{d}\boldsymbol{x} = \mathbb{1}. \tag{2.57}$$

Using Born's rule the probability density $p(\boldsymbol{\theta}|\boldsymbol{x})$ is given by

$$p(\boldsymbol{\theta}|\boldsymbol{x}) = \mathrm{Tr}\Big[\hat{E}(\boldsymbol{x})\rho(\boldsymbol{\theta})\Big]. \tag{2.58}$$

One thus considers the associated CFIM. The quantum Fisher information matrix (QFIM) $\mathcal{F}(\boldsymbol{\theta})$ is then defined as the maximum CFIM over all possible measurements.[8] Analytically,

$$\mathcal{F}(\boldsymbol{\theta}) = \max_{\hat{E}} I(\boldsymbol{\theta}). \tag{2.59}$$

The maximisation yields [44]

$$\mathcal{F}_{\mu\nu}(\boldsymbol{\theta}) = \mathrm{Tr}[L_\mu L_\nu \rho(\boldsymbol{\theta})], \tag{2.60}$$

where L_μ is a Hermitian superoperator called the symmetric logarithmic derivative (SLD), defined by[9]

$$\partial_\mu \rho(\boldsymbol{\theta}) = \frac{1}{2}\{L_\mu, \rho(\boldsymbol{\theta})\}, \tag{2.61}$$

where $\partial_\mu = \partial_{\theta_\mu}$. Note that the SLD priori depends on $\boldsymbol{\theta}$. Additionally, it is also common to only consider the symmetric part of $\mathcal{F}$ in order to ensure it is a real quantity, as in Ref. [40]. With our definition its components may be complex but it is a Hermitian matrix.

The QFIM is of special interest for us when the parametrized density matrix is pure, i.e. $\rho(\boldsymbol{\theta}) = |\psi(\boldsymbol{\theta})\rangle \langle\psi(\boldsymbol{\theta})|$ such that $\rho^2 = \rho$. Using this we have

$$\partial_\mu \rho^2 = \partial_\mu \rho\rho + \rho\partial_\mu\rho = \partial_\mu\rho \quad \Rightarrow \quad L_\mu = 2\partial_\mu\rho = 2\,|\partial_\mu\psi\rangle\langle\psi| + 2\,|\psi\rangle\langle\partial_\mu\psi|\,. \tag{2.62}$$

Injecting the SLD into the QFIM then yields

$$\mathcal{F}_{\mu\nu} = 4\,\langle\partial_\mu\psi|\,[\mathbb{1} - |\psi\rangle\langle\psi|]\,|\partial_\nu\psi\rangle = 4Q^\psi_{\mu\nu}. \tag{2.63}$$

For pure states, the QFIM then reduces to the QGT !

Coming back to the general case, the quantum Cramér-Rao bound can be derived as

$$\mathrm{Cov}(\hat{\boldsymbol{\theta}}) \geq \mathcal{F}(\boldsymbol{\theta})^{-1}, \tag{2.64}$$

for an estimator $\hat{\boldsymbol{\theta}}$. The particularity of the multiparameter quantum case is that the Cramér-Rao bound can be unattainable. In fact, the weak commutativity condition [45] states that the multiparameter quantum Cramér-Rao bound is saturated iff

$$\forall \mu,\nu \in [\![1,N]\!], \;\; \mathrm{Tr}\left\{[L_\mu, L_\nu]\rho(\boldsymbol{\theta})\right\} = 2i\,\mathrm{Im}\,\mathcal{F}_{\mu\nu}(\boldsymbol{\theta}) = 0. \tag{2.65}$$

If ρ is pure then this relation amounts to

$$\forall \mu,\nu \in [\![1,N]\!], \;\; \mathcal{B}^\psi_{\mu\nu}(\boldsymbol{\theta}) = 0, \tag{2.66}$$

i.e. the bound is saturable (and saturated) iff the Berry curvature is zero. Conversely, a non-zero Berry curvature makes the bound not saturable ! This fact may be understood deeper by invoking the quantum generators of the parameters $\boldsymbol{\theta}$.

[8] I.e. the CFIM giving the best Cramér-Rao bound over all possible measurements

[9] It is also important to note that there is actually a family of QFIM that obey the maximization of the CFIM. See Ref. [38] for examples.

Quantum multiparameter estimation and parameter generators Some references for the link between estimation theory and the parameter generators are Refs. [39, 40, 46, 47, 48, 49, 50, 51].

The quantum generator G_μ of the parameter θ_μ may be implicitly defined by the von-Neumann equation

$$\partial_\mu \rho(\boldsymbol{\theta}) = i[G_\mu, \rho(\boldsymbol{\theta})], \tag{2.67}$$

where the factor i ensures the hermiticity of the generators.[10] Consider an infinitesimal evolution $\boldsymbol{\theta} \mapsto \boldsymbol{\theta} + \mathbf{d}\boldsymbol{\theta}$ of the parameters. The density matrix then reads to first order

$$\rho(\boldsymbol{\theta} + \mathbf{d}\boldsymbol{\theta}) = U(\boldsymbol{\theta} + \mathbf{d}\boldsymbol{\theta})^\dagger \rho_0 U(\boldsymbol{\theta} + \mathbf{d}\boldsymbol{\theta}) = \big[U(\boldsymbol{\theta}) + \partial_\mu U(\boldsymbol{\theta}) \mathrm{d}\theta_\mu\big]^\dagger \rho_0 \big[U(\boldsymbol{\theta}) + \partial_\mu U(\boldsymbol{\theta}) \mathrm{d}\theta_\mu\big] \tag{2.68a}$$

$$= \rho + \big(\rho U^\dagger \partial_\mu U + \partial_\mu U^\dagger U \rho\big) \mathrm{d}\theta_\mu + \mathcal{O}\big(\mathbf{d}\boldsymbol{\theta}^2\big), \tag{2.68b}$$

where we have made the $\boldsymbol{\theta}$ dependences implicit, and made use of Einstein's summation convention. Now we can use that fact that $U(\boldsymbol{\theta})$ is unitary to show that $\partial_\mu U^\dagger U = (U^\dagger \partial_\mu U)^\dagger = -U^\dagger \partial_\mu U$, such that

$$\mathrm{d}\rho = \rho(\boldsymbol{\theta} + \mathbf{d}\boldsymbol{\theta}) - \rho(\boldsymbol{\theta}) = \big[- U^\dagger \partial_\mu U, \rho(\boldsymbol{\theta})] \mathrm{d}\theta_\mu = i\big[iU^\dagger \partial_\mu U, \rho(\boldsymbol{\theta})\big] \mathrm{d}\theta_\mu. \tag{2.69}$$

The generator can thus be written as $G_\mu = iU^\dagger \partial_\mu U = -i\partial_\mu U^\dagger U$. Now let us come back to the case where $\rho(\boldsymbol{\theta})$ is a pure state, such that $\rho(\boldsymbol{\theta}) = |\psi(\boldsymbol{\theta})\rangle \langle\psi(\boldsymbol{\theta})|$. Using Eq. (2.33) and the fact that $\rho_0 = |\psi_0\rangle \langle\psi_0|$ is $\boldsymbol{\theta}$-independent yields

$$\mathcal{F}_{\mu\nu} = 4Q^\psi_{\mu\nu} = 4 \langle\psi_0| \partial_\mu U^\dagger U \big[\mathbb{1} - |\psi_0\rangle \langle\psi_0|\big] U^\dagger \partial_\nu U |\psi_0\rangle \tag{2.70a}$$

$$= 4 \langle\psi_0| (-i\partial_\mu U^\dagger U) \big[\mathbb{1} - |\psi_0\rangle \langle\psi_0|\big] iU^\dagger \partial_\nu U |\psi_0\rangle = 4 \langle\psi_0| G_\mu \big[\mathbb{1} - |\psi_0\rangle \langle\psi_0|\big] G_\nu |\psi_0\rangle \tag{2.70b}$$

$$= 4\big(\langle\psi_0| G_\mu G_\nu |\psi_0\rangle - \langle\psi_0| G_\mu |\psi_0\rangle \langle\psi_0| G_\nu |\psi_0\rangle \big) = 4 \mathrm{Cov}_{|\psi_0\rangle}(G_\mu, G_\nu). \tag{2.70c}$$

The QFIM, and QGT, are then directly related to the quantum fluctuations of the parameter generators! Two special cases are the diagonal components and the Berry curvature,

$$\mathcal{F}_{\mu\mu} = 4g^\psi_{\mu\mu} = 4 \langle\psi_0| G_\mu^2 |\psi_0\rangle - \langle\psi_0| G_\mu |\psi_0\rangle^2 = 4\sigma^2_\psi(G_\mu) \tag{2.71a}$$

$$\mathcal{B}^\psi_{\mu\nu} = -2 \,\mathrm{Im}\, Q^\psi_{\mu\nu} = i \langle\psi_0| [G_\mu, G_\nu] |\psi_0\rangle . \tag{2.71b}$$

The non-attainability of the quantum Cramér-Rao bound then stems from the non-commutativity between different parameter generators. In such situations, the parameters are said to be *incompatible*, and some trade-off has to be made in order to maximise the QFIM for some parameters.

2.4.2 . Viewpoint 2: Position operator and non-locality

Here, we apply the first viewpoint to band theory, and specifically the Bloch Hamiltonian, to show that band quantum geometry, at least in a low-energy regime, stems from the non-locality of the Bloch fermion. In chapter 1, we defined the Bloch Hamiltonian as

$$H(\boldsymbol{k}) = e^{-i\boldsymbol{k}\cdot\hat{\boldsymbol{r}}} H e^{i\boldsymbol{k}\cdot\hat{\boldsymbol{r}}}, \tag{2.72}$$

[10] Which follows from the hermiticity of the density matrix

with its eigenstates being $|u_n(\boldsymbol{k})\rangle = e^{-i\boldsymbol{k}\cdot\hat{\boldsymbol{r}}}|\psi_n(\boldsymbol{k})\rangle$. Building on the first viewpoint, we may build an analogy between band theory and quantum estimation theory. Defining $U(\boldsymbol{k}) = \exp(-i\boldsymbol{k}\cdot\hat{\boldsymbol{r}})$, we have

$$H(\boldsymbol{k}) = U(\boldsymbol{k})HU(\boldsymbol{k})^\dagger, \quad |u_n(\boldsymbol{k})\rangle = U(\boldsymbol{k})|\psi_n(\boldsymbol{k})\rangle\,. \tag{2.73}$$

The crystalline momentum $\boldsymbol{k}$ plays the role of the estimated parameters $\boldsymbol{\theta}$, and $U(\boldsymbol{k})$ is the unitary parametrization. The state $|u_n(\boldsymbol{k})\rangle$ then appears as the parametrized state while $|\psi_n(\boldsymbol{k})\rangle$ is the probe state, up to the fact that the latter also depends on $\boldsymbol{k}$. However, as will we see their orthogonality at different crystalline momenta will make the analogy work for the QGT. The analogy is summarized in Table 2.1. Using Eq. (2.33) on $|u_n(\boldsymbol{k})\rangle = U(\boldsymbol{k})|\psi_n(\boldsymbol{k})\rangle$, we find[11]

	Quantum estimation theory	Band theory
Probe state	$\|\psi_0\rangle$	$\|\psi_n(\boldsymbol{k})\rangle$
Parameters to estimate	$\boldsymbol{\theta}$	$\boldsymbol{k}$
Unitary parametrization	$U(\boldsymbol{\theta})$	$U(\boldsymbol{k}) = \exp\big(-i\boldsymbol{k}\cdot\hat{\boldsymbol{r}}\big)$
Parametrized state	$\|\psi(\boldsymbol{\theta})\rangle$	$\|u_n(\boldsymbol{k})\rangle$

Table 2.1: Analogy between band theory and quantum estimation theory

$$Q^n_{\mu\nu} = \langle\psi_n|\, iU^\dagger\partial_\mu U\big[\mathbb{1} - |\psi_n\rangle\langle\psi_n|\big]iU^\dagger\partial_\nu U\,|\psi_n\rangle = \mathrm{Cov}_{|\psi_n\rangle}\left(\hat{R}_\mu, \hat{R}_\nu\right), \tag{2.75}$$

The quantum geometric tensor of the n-th band is the covariance matrix of the operator $\hat{R}_\mu = iU^\dagger\partial_\mu U$. In the case of quantum estimation theory, we identified this operator as the generator of θ_μ. From the form of $U(\boldsymbol{k})$ one might be tempted to say that the generator of k_μ is the position operator $\hat{r}_\mu$, however things are more complicated than that. We may explicit the generator using the identity [40, 52],

$$\partial_\lambda e^{\hat{A}} = \int_0^1 e^{(1-s)\hat{A}}\partial_\lambda\hat{A}e^{s\hat{A}}\mathrm{d}s = \sum_{n=0}^{+\infty}\frac{(-1)^n}{(n+1)!}\,\mathrm{ad}^n_{\hat{A}}\,\partial_\lambda\hat{A}, \tag{2.76}$$

where ad_A is the superoperator defined by $\mathrm{ad}_A(B) = [A, B]$, and $\mathrm{ad}^n_A B = \big[A, \mathrm{ad}^{n-1}_A B\big]$. In our case we have $U = e^{\hat{A}}$ with $\hat{A} = -i\boldsymbol{k}\cdot\hat{\boldsymbol{r}}$ and $\partial_\mu\hat{A} = -i\hat{r}_\mu$, such that

$$\partial_\mu U = U\int_0^1 e^{-is\boldsymbol{k}\cdot\hat{\boldsymbol{r}}}(-i\hat{r}_\mu)e^{-is\boldsymbol{k}\cdot\hat{\boldsymbol{r}}}\mathrm{d}s = \sum_{n=0}^{+\infty}\frac{(-1)^n}{(n+1)!}\,\mathrm{ad}^n_{-i\boldsymbol{k}\cdot\hat{\boldsymbol{r}}}(-i\hat{r}_\mu), \tag{2.77}$$

[11] The spectral theorem applied to H gives $\langle\psi_n(\boldsymbol{k})|\psi_m(\boldsymbol{k'})\rangle = \delta_{nm}\delta^d(\boldsymbol{k}-\boldsymbol{k'})$, which implies that for $m \neq n$ we have

$$\begin{aligned}\langle\psi_n(\boldsymbol{k})|\partial_\mu\psi_m(\boldsymbol{k})\rangle &= \langle\psi_n(\boldsymbol{k})|\lim_{h\to0}\frac{1}{h}\big(\,|\psi_m(\boldsymbol{k}+h\boldsymbol{e}_\mu)\rangle - |\psi_m(\boldsymbol{k})\rangle\,\big)\\ &= \lim_{h\to0}\frac{1}{h}\big(\,\langle\psi_n(\boldsymbol{k})|\psi_m(\boldsymbol{k}+h\boldsymbol{e}_\mu)\rangle - \langle\psi_n(\boldsymbol{k})|\psi_m(\boldsymbol{k})\rangle\,\big) = 0.\end{aligned}$$

This way it is shown that the other three terms of Eq. (2.33) vanish.

which can be simplified as

$$iU^\dagger \partial_\mu U = \hat{R}_\mu = \int_0^1 e^{-is\boldsymbol{k}\cdot\hat{\boldsymbol{r}}} \hat{r}_\mu e^{is\boldsymbol{k}\cdot\hat{\boldsymbol{r}}} \mathrm{d}s = \sum_{n=0}^{+\infty} \frac{i^n}{(n+1)!} \mathrm{ad}^n_{\boldsymbol{k}\cdot\hat{\boldsymbol{r}}} \hat{r}_\mu. \tag{2.78}$$

So in general the operator $\hat{R}_\mu$ may not be identified as the position operator $\hat{r}_\mu$. However things are different when considering low-energy models. Indeed low-energy models, like the massive Dirac fermions model, are concentrated around a particular point in the Brillouin zone, which serves a zero value of $\boldsymbol{k}$. So if we define a low-energy-model as a $k \ll 1$ regime, then similarly to Ref. [44] the leading term is

$$\hat{R}_\mu \underset{k\ll 1}{\simeq} \hat{r}_\mu \quad \Rightarrow \quad Q^n_{\mu\nu}(\boldsymbol{k}) \underset{k\ll 1}{\simeq} \mathrm{Cov}_{|\psi_n(\boldsymbol{k})\rangle}\left(\hat{r}_\mu, \hat{r}_\nu\right). \tag{2.79}$$

While this may appear as a crude approximation, we will see multiple times throughout the thesis that it gives an intuitive interpretation of some physical consequences of quantum geometry, and can even serve as a guide to their generalization.

Let us now go in the low-energy regime where $k \ll 1$ and consider $Q^n_{\mu\nu} = \mathrm{Cov}_{|\psi_n\rangle}\left(\hat{r}_\mu, \hat{r}_\nu\right)$. First notice that the states $|\psi_n(\boldsymbol{k})\rangle$ are the actual Bloch states, so they are the ones, contrary to the $|u_n(\boldsymbol{k})\rangle$, that physically represent the Bloch fermion. Therefore the expression of Eq. (2.79) translates physical properties of the Bloch fermions (for example a Dirac fermion in graphene [11]). The QGT is then related to the quantum fluctutations of the Bloch fermion's position. In other words, the QGT quantifies the *non-locality* of the Bloch fermion. The quantum fluctuations, when imagined over time, represent its *zero-point motions*. The relation between the QGT and its divergent scaling at quantum phase transitions (QPT) is also an interesting fact to bring here [39, 53]. Indeed, if the QGT really represents the zero-point motion of the Bloch fermions, then its divergence could mean that the Bloch fermions becomes infinitely non-localized, all of them would overlap thereby resulting in a critical state that is instable towards QPTs, possibly topological.

Applying this relationship to the quantum metric and the Berry curvature gives

$$g^n_{\mu\mu}(\boldsymbol{k}) = \sigma_{|\psi_n(\boldsymbol{k})\rangle}(\hat{r}_\mu)^2 = \langle\psi_n(\boldsymbol{k})|\, \hat{r}^2_\mu \,|\psi_n(\boldsymbol{k})\rangle - \langle\psi_n(\boldsymbol{k})|\, \hat{r}_\mu \,|\psi_n(\boldsymbol{k})\rangle^2, \tag{2.80a}$$

$$\mathcal{B}^n_{\mu\nu}(\boldsymbol{k}) = i\,\langle\psi_n(\boldsymbol{k})|\,[\hat{r}_\mu, \hat{r}_\nu]\,|\psi_n(\boldsymbol{k})\rangle\,. \tag{2.80b}$$

The (diagonal) quantum metric then is the squared standard deviation of the position operator while the Berry curvature is its commutator. In each direction μ, the typical length over which the wavepacket of the Bloch fermion (hereafter called the Bloch wavepacket) quantum fluctuates is given by $\sqrt{g^n_{\mu\mu}}$. In a two-dimensional plane (μ, ν) the situation is as depicted in Fig.2.2. The typical area of zero-point motion of the Bloch fermion in the plane (μ, ν) is then given by $\mathcal{A}^n_{\mathrm{typ},\mu\nu} = \pi\sqrt{g^n_{\mu\mu} g^n_{\nu\nu}}$.

By noticing that these formulations of the quantum metric and Berry curvature are actually the two sides of the Robertson-Schrödinger uncertainty relation, we can write

$$\sigma_{|\psi_n(\boldsymbol{k})\rangle}(\hat{r}_\mu)\sigma_{|\psi_n(\boldsymbol{k})\rangle}(\hat{r}_\nu) \geq \frac{1}{2}\left|\,\langle\psi_n(\boldsymbol{k})|\,[\hat{r}_\mu, \hat{r}_\nu]\,|\psi_n(\boldsymbol{k})\rangle\,\right| \quad \Leftrightarrow \quad \sqrt{g^n_{\mu\mu}(\boldsymbol{k}) g^n_{\nu\nu}(\boldsymbol{k})} \geq \frac{1}{2}|\mathcal{B}^n_{\mu\nu}(\boldsymbol{k})|, \tag{2.81}$$

which is the third inequality we found in Eq. (2.43). The Berry curvature then appears as the consequence, and quantifier, of the *minimal* amount of zero point-motion ensured by the non-commutativity

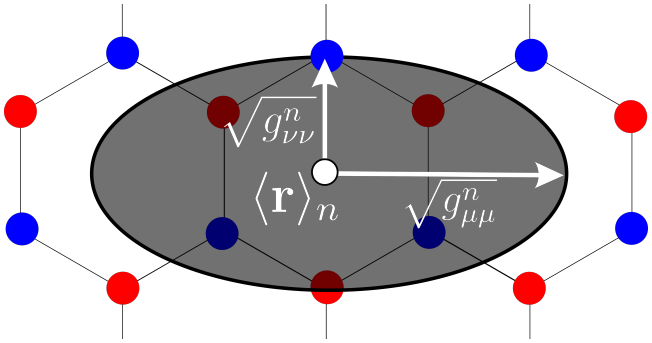

Figure 2.2: Typical Bloch wavepacket in a two-dimensional plane (μ, ν), here pictured in the honeycomb lattice. The area of the typical Bloch wavepacket at a given crystalline momentum $\boldsymbol{k}$ is $\mathcal{A}_{\text{typ},\mu\nu}(\boldsymbol{k}) = \pi\sqrt{g^n_{\mu\mu}(\boldsymbol{k})g^n_{\nu\nu}(\boldsymbol{k})}$.

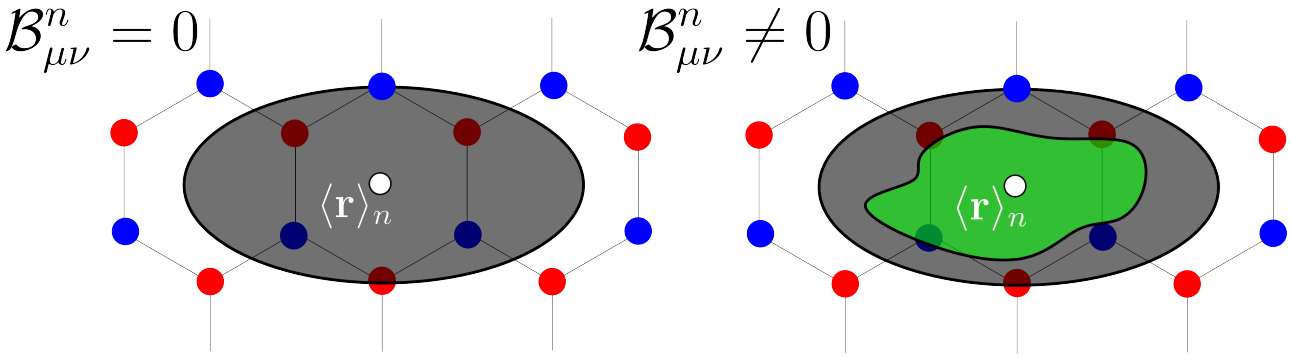

Figure 2.3: Bloch wavepacket in the plane (μ, ν) in the case of zero (left) and non-zero (right) Berry curvature. If the Berry curvature is zero, the wavepacket can be purely localized. Contrarily, if the Berry curvature is non-zero, the uncertainty principle ensures a minimal area of zero-point motion (/quantum fluctuations) pictured in green. At a given crystalline momentum $\boldsymbol{k}$, the minimal area is given by $\mathcal{A}_{\text{min},\mu\nu}(\boldsymbol{k}) = \frac{1}{2}|\mathcal{B}^n_{\mu\nu}(\boldsymbol{k})|$.

of the position operator in the Bloch state. Reformulating the uncertainty principle in terms of area, the typical area of zero-point motion is bounded from below by the Berry curvature as

$$\mathcal{A}_{\text{typ},\mu\nu} \geq \mathcal{A}^n_{\text{min},\mu\nu} = \frac{\pi}{2}|\mathcal{B}^n_{\mu\nu}|. \tag{2.82}$$

The situation is then as depicted in Fig.2.3.

2.4.3 . Viewpoint 3: Quasiness of Bloch fermions and virtual interband transitions

Using the closure relation we can write the QGT as

$$Q^n_{\mu\nu} = \langle \partial_\mu u_n | \left[\mathbb{1} - |u_n\rangle \langle u_n| \right] |\partial_\nu u_n\rangle = \sum_{m \neq n} \langle \partial_\mu u_n | u_m \rangle \langle u_m | \partial_\nu u_n \rangle . \tag{2.83}$$

This formulation of the QGT makes apparent the fact that *geometric properties only arise in multiband systems*. This is consistent with what we observed in the framework of tight-binding models. In this

formalism, the Bloch state ($|u_n\rangle$) is a superposition of all the possible states an electron can have within the unit cell. As the number of such states equals the number of bands, a single band system correspond to a unit cell where an electron can only have one state. The superposition therefore does not happen and the Bloch fermion is simply the elementary electron. We thus come back to the fact that geometric and topological properties arise from the quasiness of Bloch fermions. Consequently, the presence of several bands is necessary for geometric (and *a fortiori* topological) properties to emerge.

We can also infer from this that the different branches of Bloch fermions (i.e. the different bands) "feel" each other, even though band theory is formulated within the adiabatic approximation [27] so no interband transitions occur. Geometric and topological properties are thus associated with *virtual* interband transitions [11, 16].

Finally, following Ref. [54] we can link this viewpoint with the non-local properties of Bloch fermions, as discussed earlier. In relativistic quantum mechanics, the existence of the electron is accompanied by that of its antiparticle, the positron. A particularity of such situations is that the electron undergoes quantum fluctuations as erratic electron-positron annihilation and creation occur, and a photon travels in between.

The electron is therefore not purely localizable, specifically not on lengthscales smaller than the distance between its annihilation and recreation. Such lengthscale can be estimated as follows[54]. Using the uncertainty principle the typical time between the annihilation and the recreation of an electron is $\Delta t \sim \hbar/\Delta E \sim \hbar/mc^2$. Since the photon in the vacuum travels at the speed of light c, the distance of travel of the virtual electron-positron pair is $\lambda\!\!\!^{-}_c \sim c\Delta t \sim \hbar/mc$. $\lambda\!\!\!^{-}_c$ is called the (reduced) Compton wavelength, and gives the order of magnitude of the lengthscale below which an electron is localizable. More pratically, it is the length below which relativistic effects are no longer negligible in quantum mechanics, and the use of quantum field theory becomes necessary.

In a band structure we can draw a similar scenario. A Bloch fermion undergoes virtual interband transitions that render it unlocalizable, or *blurred*, under a certain lengthscale, the latter being a geometric quantity. This quantity is the Berry curvature if we consider the *minimal* lengthscale in which these virtual interband transitions occur, or it can be the square root of the quantum metric if we consider the *typical* lengthscale over which the virtual transitions occur.

As observed in Sec.2.6, the analogy is direct when considering the gapped graphene model, where Bloch fermions are identified as massive Dirac fermions. The Bloch fermions thus exhibit an emergent relativistic character, because of their quasiness.

2.4.4 . Viewpoint 4: Duality between the Berry curvature and the magnetic field

The original derivation of the Berry curvature was based on the adiabatic approximation [11, 55]. Consider a time evolution problem in band theory, formalized by a path $\mathcal{C}$ in the Brillouin zone with a time-dependent crystalline momentum $\boldsymbol{k}(t)$, with $t \in [0, T]$. The initial condition is that the state $|\psi(t)\rangle$ is in the Bloch state, i.e. $|\psi(t=0)\rangle = |u_n(\boldsymbol{k}(t=0)\rangle$. The adiabatic approximation then amounts to say that at all times the state $|\psi(t)\rangle$ physically represents the n-th Bloch fermion, i.e. no interband transitions occur. "Physically" here means that $|\psi(t)\rangle$ is U(1)-equivalent to $|u_n(\boldsymbol{k}(t))\rangle$, i.e. generally we have

$$|\psi(t)\rangle = e^{i\gamma(t)}\,|u_n(\boldsymbol{k}(t))\rangle\,. \tag{2.84}$$

As any quantum state, the state $|\psi(t)\rangle$ obeys the Schrödinger equation

$$i\hbar\frac{\mathrm{d}}{\mathrm{d}t}|\psi(t)\rangle = H(\boldsymbol{k}(t))\,|\psi(t)\rangle\,. \tag{2.85}$$

Plugging in the U(1)-equivalence and the band eigenproblem, we get

$$i\hbar i\dot{\gamma}\,|u_n(\boldsymbol{k}(t))\rangle + i\hbar\dot{\boldsymbol{k}}\cdot|\partial_{\boldsymbol{k}}u_n(\boldsymbol{k}(t))\rangle = \epsilon_n(\boldsymbol{k}(t))\,|u_n(\boldsymbol{k}(t))\rangle\,. \tag{2.86}$$

Projecting on $\langle u_n(\boldsymbol{k}(t))|$, we then get

$$-\hbar\dot{\gamma} + i\hbar\dot{\boldsymbol{k}}\cdot\langle u_n(\boldsymbol{k}(t))|\partial_{\boldsymbol{k}}u_n(\boldsymbol{k}(t))\rangle = \epsilon_n(\boldsymbol{k}(t)) \tag{2.87a}$$

$$\Leftrightarrow\ \dot{\gamma} = -\frac{1}{\hbar}\epsilon_n(\boldsymbol{k}(t)) - \dot{\boldsymbol{k}}\cdot\boldsymbol{\mathcal{A}}^n(\boldsymbol{k}(t)). \tag{2.87b}$$

Integrating the latter over the whole time evolution then yields

$$\gamma(T)-\gamma(0) = -\frac{1}{\hbar}\int_0^T\epsilon_n(\boldsymbol{k}(t))\mathrm{d}t - \int_0^T\boldsymbol{\mathcal{A}}^n(\boldsymbol{k}(t))\cdot\dot{\boldsymbol{k}}\mathrm{d}t \tag{2.88a}$$

$$= -\frac{1}{\hbar}\int_0^T\epsilon_n(\boldsymbol{k}(t))\mathrm{d}t - \int_{\boldsymbol{k}(0)}^{\boldsymbol{k}(T)}\boldsymbol{\mathcal{A}}^n(\boldsymbol{k})\cdot\mathbf{d}\boldsymbol{k} \tag{2.88b}$$

$$= -\frac{1}{\hbar}\int_0^T\epsilon_n(\boldsymbol{k}(t))\mathrm{d}t - \int_{\mathcal{C}}\boldsymbol{\mathcal{A}}^n(\boldsymbol{k})\cdot\mathbf{d}\boldsymbol{k} = \Phi_d + \Phi_g. \tag{2.88c}$$

The first term Φ_d is called the dynamical phase, while the second one Φ_g is the *geometric phase*. When $\mathcal{C}$ is a closed path in the Brillouin zone, the geometric phase

$$\Phi_g(\mathcal{C}) = -\oint_{\mathcal{C}}\boldsymbol{\mathcal{A}}^n(\boldsymbol{k})\cdot\mathbf{d}\boldsymbol{k} \tag{2.89}$$

is called the *Berry phase*. The collection of the three quantities: Berry curvature, Berry connection and Berry phase, is sometimes referred to as the *Berryology* of a band structure [16, 56, 57]. The geometric phase strongly resembles the Aharonov-Bohm phase, given by [11]

$$\Gamma(P) = \frac{e}{\hbar}\oint_P A(\boldsymbol{r})\cdot\mathbf{d}\boldsymbol{r}. \tag{2.90}$$

The two phases are actually analogous. The Aharonov-Bohm phase is the phase accumulated by a quantum state when subject to a magnetic field. Specifically, it concerns a time evolution that begins and ends at the same position, i.e. a closed loop in real space. As for the Berry phase, we have shown that it is the phase picked up by the Bloch state when undergoing a time evolution represented by a closed loop in momentum space. If the two phases are indeed analogous, then the crystalline momentum plays the role of the position, while the Berry connection and curvature respectively appear as the vector potential and the magnetic field. This is corroborated from the fact that the Berry curvature is the curl of the Berry connection. Since the analogy swaps the position space with its dual reciprocal space, we will refer to this analogy as a duality. The duality is summarized in Table 2.2. The duality acually goes much deeper, see Ref. [16] for an exhaustive description. One reason for the depth of the duality is that both sides can be formulated in the same mathematical language, that of gauge theory. See again Ref. [16] for a more thorough discussion on this topic.

Berryology	Magnetism
crystal momentum $\boldsymbol{k}$	position $\boldsymbol{r}$
Berry connection $\boldsymbol{\mathcal{A}}_n$	vector potential $\boldsymbol{A}$
Berry curvature $\mathcal{B}^n_{\mu\nu}$	Magnetic field $\boldsymbol{B}$
Berry Phase $\Phi_g(\mathcal{C})$	Aharonov-Bohm phase $\Gamma(P)$

Table 2.2: Duality between Berryology and magnetism

2.4.5 . Viewpoint 5: Karplus-Luttinger velocity and wavepacket self-rotation

We can use the duality between Berryology and magnetism as in inspiration to incorporate band quantum geometry in the equations of motion of a Bloch fermion. Indeed, one way to incorporate a magnetic field in the equations of motion is to shift the momentum operator as

$$\hat{\boldsymbol{p}} \longmapsto \hat{\boldsymbol{\Pi}} = \hat{\boldsymbol{p}} + e\boldsymbol{A}(\boldsymbol{r}). \tag{2.91}$$

This shift is called the Peierls substitution. Similarly, we can do a Peierls substitution for the Berry connection

$$\hat{\boldsymbol{r}} \longmapsto \hat{\boldsymbol{R}} = \hat{\boldsymbol{r}} + \boldsymbol{\mathcal{A}}(\boldsymbol{k}). \tag{2.92}$$

The latter is called the *generalized Peielrs substitution*[58, 59, 60, 61, 62, 63].[12] Consider now a Bloch fermion under an additional potential,

$$H_n = \epsilon_n(\boldsymbol{k}) + V(\boldsymbol{r}), \tag{2.93}$$

The potential V is any potential beyond the crystalline one. It can for example represent an external electric field applied to the crystal, or even represent inherent electric fields like the ones coming from electron-electron correlations. Applying the generalized Peierls substitution gives

$$H_n = \epsilon_n(\boldsymbol{k}) + V(\boldsymbol{R}) = \epsilon_n(\boldsymbol{k}) + V(\boldsymbol{r} + \boldsymbol{\mathcal{A}}_n(\boldsymbol{k})). \tag{2.94}$$

If we assume the Berry connection to be small, and the potential V to be regular enough, we can expand to first order and find

$$H_n = \epsilon_n(\boldsymbol{k}) + V(\boldsymbol{r}) + \boldsymbol{\mathcal{A}}_n(\boldsymbol{k}) \cdot \partial_{\boldsymbol{r}} V(\boldsymbol{r}) + \mathcal{O}\big(\mathcal{A}_n^2\big). \tag{2.95}$$

The additional term has the form of a dipolar force, where the Berry connection acts as a dipolar moment. This makes sense since the Bloch wave-packet is non-local and as it is charged it will have an electric dipole when subjected to an electric field. Another form is reached when choosing the symmetric gauge for the Berry connection,

$$\boldsymbol{\mathcal{A}}_n(\boldsymbol{k}) = \frac{1}{2}\boldsymbol{\mathcal{B}}_n(\boldsymbol{k}) \times \boldsymbol{k} \quad \Rightarrow \quad H_n = \epsilon_n(\boldsymbol{k}) + V(\boldsymbol{r}) + \frac{1}{2}\boldsymbol{\mathcal{B}}_n(\boldsymbol{k}) \times \boldsymbol{k} \cdot \partial_{\boldsymbol{r}} V(\boldsymbol{r}) + \mathcal{O}\big(\mathcal{A}_n^2\big). \tag{2.96}$$

[12] Note this is a slight abuse of language. A generalization must include the original case as a special case. A more appropriate nomenclature would refer to this as the *dual* Peierls substitution, and the collection of the two would be the *generalized* Peierls substitution.

The additional term then appears as an emergent spin-orbit coupling of the form $\boldsymbol{\sigma} \times \boldsymbol{E} \cdot \boldsymbol{p}$. Interestingly, the Berry curvature takes the role of a spin ! A more appropriate formulation is that the Berry curvature appears as a helicity axis for the Bloch wavepacket. The Berry curvature thus yields a self-rotation of the Bloch wavepacket in the presence of an electric field, a fact mentioned many times in the litterature [64, 65, 66, 67, 68, 69, 70]. An important consequence of this emergent spin-orbit coupling is found when examining the equations of motion. Temporarily promoting $\boldsymbol{r}$ and $\boldsymbol{k}$ to operators, and treating the Berry curvature as a scalar, we find

$$\dot{r}_\mu = \frac{1}{i\hbar}[r_\mu, H_n] = \frac{1}{i\hbar}[r_\mu, \epsilon_n] + \frac{1}{2i\hbar}\epsilon_{abc}[r_\mu, \mathcal{B}_{n,b}k_c\partial_{r_a}V] = \frac{1}{\hbar}\partial_\mu\epsilon_n + \frac{1}{2\hbar}\epsilon_{ab\mu}\mathcal{B}_{n,b}\partial_{r_a}V \tag{2.97a}$$

$$= \frac{1}{\hbar}\partial_\mu\epsilon_n - \frac{1}{2\hbar}\left(\boldsymbol{\mathcal{B}}_n \times \partial_{\boldsymbol{r}}V\right)_\mu. \tag{2.97b}$$

In Chapter 6, we discuss in more details the generalized Peierls substitution and the related equations of motion, notably in the presence of a magentic field. Beyond the usual group velocity $\hbar^{-1}\partial_{\boldsymbol{k}}\epsilon_n$, the Berry curvature produces an *anomalous velocity*, commonly called the *Karplus-Luttinger drift velocity* [71]. It is this velocity that gives rise to the intrinsic[13] anomalous quantum Hall effect [72, 73]. Note that the name "anomalous Hall effect" refers to any mechanism yielding a Hall effect without a magnetic field. Here, following the analogy between Berryology and magnetism, it then makes sense to suggest that the Berry curvature acts as an emergent magnetic field.

The situation is intuitively pictured in Fig.2.4 for the case of two-dimensional materials. In that case the Berry curvature is purely out-of-plane, and the self-rotation of the wavepacket then purely happens in-plane, if the electric field is. The Hall effect resulting from the Karplus-Luttinger velocity has elegantly been interpreted as a type of Magnus effect [74]. Indeed, as the non-local Bloch wavepacket self-rotates and evolves in a surrounding electric field, a Magnus-type force will make it drift in one direction or another, depending on its direction of rotation.

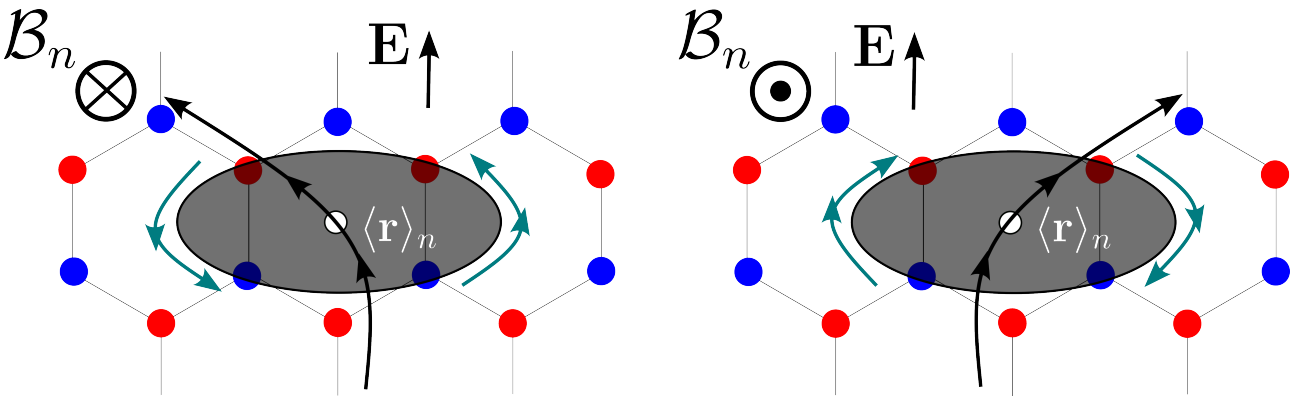

Figure 2.4: Illustration of the drift velocity and wavepacket self-rotation for two-dimensional materials, with an electric field along the x direction.

[13] One anomalous Hall effect results from impurities, with charge carriers getting scattered in different directions depending on their spin.

2.4.6 . Viewpoint 6: Vector bundles, gauge theory and geometric quantum mechanics

Band theory has a natural translation in mathematics, particularly in algebraic topology and differential geometry through the context of *vector bundles* [75]. See Refs. [16, 76, 77, 78] for more thorough discussions on the topic, as well as the works of Bruno Mera and Tomoki Ozawa [79, 80, 81]. The eigendecomposition of the Bloch Hamiltonian reads

$$H(\boldsymbol{k}) = \sum_{n=1}^{N} \epsilon_n(\boldsymbol{k}) \mathcal{P}_n(\boldsymbol{k}), \tag{2.98}$$

with $\mathcal{P}_n(\boldsymbol{k})$ the projector on the n-th band. Let $\mathscr{H}(\boldsymbol{k})$ be the Hilbert space spanned by the projectors $\mathcal{P}_n(\boldsymbol{k})$. Mathematically, one may write

$$\mathscr{H}(\boldsymbol{k}) = \bigcup_{n=1}^{N} \operatorname{Im} \mathcal{P}_n(\boldsymbol{k}), \tag{2.99}$$

with $\operatorname{Im} \mathcal{P}_n(\boldsymbol{k})$ the image of $\mathcal{P}_n(\boldsymbol{k})$ in $\mathbb{C}$, defined as

$$\operatorname{Im} \mathcal{P}_n(\boldsymbol{k}) = \left\{ \alpha \left| u_n(\boldsymbol{k}) \right\rangle , \ \alpha \in \mathbb{C} \right\} = \mathbb{C} \left| u_n(\boldsymbol{k}) \right\rangle . \tag{2.100}$$

We then have a *parametrized vector space*, i.e. a family of vector spaces parametrized here by the crystalline momentum in the Brillouin zone. As such, we need to consider a sort of formalism of parametrized linear algebra, which is essentially what the formalism of vector bundles offers.

Our example here is the *Bloch bundle* [16, 76, 82], defined by

$$\mathscr{B} = \left\{ \left(\boldsymbol{k}, \mathscr{H}(\boldsymbol{k})\right), \ \ \boldsymbol{k} \in \mathsf{BZ} \right\} = \bigoplus_{n=1}^{N} \left\{ \left(\boldsymbol{k}, \operatorname{Im} \mathcal{P}_n(\boldsymbol{k})\right), \ \ \boldsymbol{k} \in \mathsf{BZ} \right\} = \bigoplus_{n=1}^{N} \mathscr{B}_n. \tag{2.101}$$

Let us focus on the vector bundle of the n-th band $\mathscr{B}_n$. In the linguo of vector bundles, $\operatorname{Im} \mathcal{P}(\boldsymbol{k})$ for a fixed $\boldsymbol{k}$ is a *fiber* of the bundle $\mathscr{B}_n$, the Brillouin zone BZ is its *base space* and the Bloch state

$$\begin{array}{rccc} & \mathsf{BZ} & \longrightarrow & \bigcup\limits_{\boldsymbol{k} \in \mathsf{BZ}} \operatorname{Im} \mathcal{P}_n(\boldsymbol{k}) \\ |u_n\rangle : & \boldsymbol{k} & \longmapsto & |u_n(\boldsymbol{k})\rangle \end{array} \tag{2.102}$$

is a *section* of $\mathscr{B}_n$[14]. Note that here each $\mathscr{B}_n$ is a one-dimensional vector bundle (the dimension of its fibers), otherwise called a *(complex) line bundle* [83]. So schematically, we have a family of vector spaces that depend on some parameters. The space of thoses parameters is the base space, and one of these vector spaces at a fixed parameter value is a fiber.

A fundamental object of vector bundles is a connection. It arises from the need of defining a derivative over the parametrized vector space. For example, consider $\mathscr{B}_n$. Since $\operatorname{Im} \mathcal{P}_n(\boldsymbol{k})$ and $\operatorname{Im} \mathcal{P}_n(\boldsymbol{k} + \mathbf{d}\boldsymbol{k})$ represent different vector spaces, one cannot directly take the difference of $|u_n(\boldsymbol{k})\rangle$ and $|u_n(\boldsymbol{k} + \mathbf{d}\boldsymbol{k})\rangle$. We need an object to *connect* the two vector spaces, in order to define a proper notion of derivative, the latter being called a *connection*. The connection then allows to define the *covariant derivative*,

[14] Note that this is just an example. A general section s is a map from the base space BZ to the total space of $\mathscr{B}_n$. Here, $s(\boldsymbol{k}) = \alpha(\boldsymbol{k}) \left| u_n(\boldsymbol{k}) \right\rangle$

which may be found by searching for parallel transport. In the case of $\mathscr{B}_n$, the parallel transport condition for the covariant derivative D_μ^n may be written as

$$\left\langle u_n(\boldsymbol{k}) \middle| \mathsf{D}_\mu^n u_n(\boldsymbol{k}) \right\rangle = 0. \tag{2.103}$$

Writing the covariant derivative as $\mathsf{D}_\mu^n = \partial_\mu - f_{n,\mu}(\boldsymbol{k})$ with $f_{n,\mu}(\boldsymbol{k})$ the connection[15], we have

$$\left\langle u_n(\boldsymbol{k}) \middle| \mathsf{D}_\mu^n u_n(\boldsymbol{k}) \right\rangle = \langle u_n(\boldsymbol{k}) | \partial_\mu u_n(\boldsymbol{k}) \rangle - f_{n,\mu}(\boldsymbol{k}) \quad \Rightarrow f_{n,\mu}(\boldsymbol{k}) = \langle u_n(\boldsymbol{k}) | \partial_\mu u_n(\boldsymbol{k}) \rangle = -i\mathcal{A}_{n,\mu}(\boldsymbol{k}). \tag{2.104a}$$

The Berry connection then holds its name from the fact that it is a connection on the vector bundle $\mathscr{B}_n$, and we can write $i\mathsf{D}_\mu^n = i\partial_\mu - \mathcal{A}_{n,\mu}(\boldsymbol{k})$. The curvature 2-form associated to the Berry connection is the Berry curvature, which also explains where the latter holds its name form.

The whole Bloch bundle $\mathscr{B}$ turns out to be trivial [76], which implies that the sum of all the Berry curvatures at a fixed $\boldsymbol{k}$ must be zero. This is another way to show the Berry sum rule.

This language of vector bundles, and particularly gauge theory[16] turns out to also be a good mathematical translation of electromagnetism [84, 85]. Band theory and electromagnetism are thus two different "incarnations" of the same mathematics, which might explain the duality observed in the fourth viewpoint.

Finally, the quantum metric is also known as the Fubini-Study metric, as it constitutes a metric on a complex projective manifold. This fact places the quantum metric in a much larger context where a reformulation of quantum mechanics in terms of geometry has been proposed. This program was initially proposed in Ref. [86]. See Refs. [86, 87, 88, 89, 90, 91] for further discussion on the topic.

2.5 . Computing quantum geometry

There are various ways of computing band quantum geometry, which essentially amount to rewriting the QGT in various ways, each having its merits and downsides. We mention four ways to do so.

2.5.1 . States

The first uses the original formulation of the QGT we found, which we could call the *states formulation*,

$$Q_{\mu\nu}^n = \langle \partial_\mu u_n | \left[\mathbb{1} - |u_n\rangle \langle u_n| \right] |\partial_\nu u_n\rangle = \sum_{\substack{m=1 \\ m\neq n}}^{N} \langle \partial_\mu u_n | u_m \rangle \langle u_m | \partial_\nu u_n \rangle . \tag{2.105}$$

Then one computes the Bloch states $|u_n\rangle$ from the knowledge of the Bloch Hamiltonian, and from there computes the QGT using Eq. (2.105). While it is doable in simple models, such as two-band low-energy models, Eq. (2.105) rapidly becomes cumbersome for systems with more than two bands or models defined over the whole Brillouin zone. Even for two-dimensional low-energy models, one has to write the eigenstate in an ingenious way [11] so as to simplify the derivation of the normalization factor of the Bloch states.

[15] which we assume to be a scalar

[16] This has led some authors to refer to the Berry curvature as a field strength, and to denote it as $\mathcal{F}_{\mu\nu}$

2.5.2 . Projectors

Another formulation of the QGT is the *projector formulation*, shown in appendix B.3, is [92]

$$Q^n_{\mu\nu} = \mathrm{Tr}\left[\mathcal{P}_n \partial_\mu \mathcal{P}_n (\mathbb{1} - \mathcal{P}_n) \partial_\nu \mathcal{P}_n\right], \tag{2.106}$$

with $\mathcal{P}_n = |u_n\rangle \langle u_n|$. This expression has the merit of explicitly showing that the QGT is $\mathrm{U}(1)$-gauge invariant, as the projector clearly is. In fact, this formulation shows that any symmetry of the Hamiltonian leaves the QGT invariant. Indeed, all the symmetries of the Hamiltonian are also symmetries of the projectors. However the computation is still quite involved, even for simple models.

2.5.3 . Hamiltonian

The third formulation of the QGT we put forward is

$$Q^n_{\mu\nu} = \sum_{\substack{m=1 \\ m\neq n}}^{N} \frac{\langle u_n| \partial_\mu H |u_m\rangle \langle u_m| \partial_\nu H |u_n\rangle}{(\epsilon_n - \epsilon_m)^2}, \tag{2.107}$$

which we call the *Hamiltonian formulation*. This formulation is much more convenient than the first two. Indeed, the differentiation is now directly on the Hamiltonian which is much more tractable than the eigenstate or the projector. The downside we could put forward is that the number of calculation steps needed is still quite important, especially as the number of band grows.

2.5.4 . Bloch vector

The fourth and final formulation of the QGT we put forward has been proposed in Ref. [92].

Motivation from two-band models A two-band Bloch Hamiltonian can be composed as a sum of the four Pauli matrices as

$$H = h_0\sigma_0 + \boldsymbol{h}\cdot\boldsymbol{\sigma} = \begin{pmatrix} h_0 + h_z & h_x - ih_y \\ h_x + ih_y & h_0 - h_z \end{pmatrix}, \tag{2.108}$$

where all four coefficients are real. In the following we omit the $\boldsymbol{h}_0$ term. The two band dispersions are then given by $\epsilon_\lambda = \lambda|\boldsymbol{h}|$ with $\lambda = \pm 1$. One can then readily show that the projector $\mathcal{P}_\lambda$ is expressable as

$$\mathcal{P}_\lambda = \frac{1}{2}\left(\sigma_0 + \frac{1}{\epsilon_\lambda} H\right) = \frac{1}{2}\left(\sigma_0 + \boldsymbol{b}_\lambda \cdot \boldsymbol{\sigma}\right), \quad \boldsymbol{b}_\lambda = \lambda \frac{\boldsymbol{h}}{|\boldsymbol{h}|}. \tag{2.109}$$

In appendix B.3 we show that plugging this expression of $\mathcal{P}_\lambda$ yields

$$Q^\lambda_{\mu\nu} = \frac{1}{4}\partial_\mu \boldsymbol{b}_\lambda \cdot \partial_\nu \boldsymbol{b}_\lambda + \frac{i}{4}\boldsymbol{b}_\lambda \cdot \partial_\mu \boldsymbol{b}_\lambda \times \partial_\nu \boldsymbol{b}_\lambda. \tag{2.110}$$

This formulation of the QGT provides a remarkably simple (compared to other approaches) way to analytically compute band quantum geometry in a two-band model. The knowledge of the band dispersions and eigenstates is not necessary, just the right formulation of the Hamiltonian. The expressions for the quantum metric and Berry curvature can be further simplified as [92]

$$g^\lambda_{\mu\nu} = \frac{1}{4}\partial_\mu \boldsymbol{b}_\lambda \cdot \partial_\nu \boldsymbol{b}_\lambda = \frac{1}{4|\boldsymbol{h}|^2}\left[\partial_\mu \boldsymbol{h}\cdot\partial_\nu \boldsymbol{h} - \frac{(\boldsymbol{h}\cdot\partial_\mu \boldsymbol{h})(\boldsymbol{h}\cdot\partial_\nu \boldsymbol{h})}{|\boldsymbol{h}|^2}\right], \tag{2.111a}$$

$$\mathcal{B}^\lambda_{\mu\nu} = -\frac{1}{2}\boldsymbol{b}_\lambda \cdot \partial_\mu \boldsymbol{b}_\lambda \times \partial_\nu \boldsymbol{b}_\lambda = -\frac{\lambda}{2|\boldsymbol{h}|^3}\boldsymbol{h}\cdot\partial_\mu \boldsymbol{h}\times\partial_\nu \boldsymbol{h}. \tag{2.111b}$$

Extension to $N > 2$ bands The goal of Ref. [92] was to extend Eq. (2.110) to a general N band system. The space of N by N Hermitian matrices is spanned by the *generalized Gell-Mann matrices* $\boldsymbol{\lambda}$, of which there are $N^2 - 1$. The original Gell-Mann matrices, for the $N = 3$ case, are explicited in appendix F.5. We then write the Hamiltonian, omitting its traceful part, as

$$H = \boldsymbol{h} \cdot \boldsymbol{\lambda}, \tag{2.112}$$

where $\boldsymbol{h} \in \mathbb{R}^{N^2-1}$ is the *Hamiltonian vector*. We also define the *Bloch vector* $\boldsymbol{b}_n \in \mathbb{R}^{N^2-1}$ by

$$\mathcal{P}_n = \frac{1}{N}\big(\mathbb{1} + \boldsymbol{b}_n \cdot \boldsymbol{\lambda}\big). \tag{2.113}$$

The existence of the Bloch vector is ensured by the hermiticity of $N\mathcal{P}_n - \mathbb{1}$. Plugging the projector $\mathcal{P}_n$ into Eq. (2.106) then yields Eq. (2.110). One contribution of Ref. [92] was to show how we can construct the Bloch vector from the Hamiltonian vector.

2.6 . Example: Two-dimensional massive Dirac fermions

Recall the gapped graphene model

$$H = \begin{pmatrix} \Delta & \hbar v(\xi k_x - i k_y) \\ \hbar v(k_x + i k_y) & -\Delta \end{pmatrix} = |\Delta| \begin{pmatrix} \operatorname{sgn}\Delta & \lambda\!\!\!^{-}_c(\xi k_x - i k_y) \\ \lambda\!\!\!^{-}_c(\xi k_x + i k_y) & -\operatorname{sgn}\Delta \end{pmatrix}. \tag{2.114}$$

In appendix B.4, we show using the Bloch vector formulation that the quantum metric and Berry curvature of the two bands read

$$g^n_{\mu\nu}(\boldsymbol{k}) = \frac{\lambda\!\!\!^{-2}_c}{4} \frac{(1 + \lambda\!\!\!^{-2}_c k^2)\delta_{\mu\nu} - \lambda\!\!\!^{-2}_c k_\mu k_\nu}{(1 + \lambda\!\!\!^{-2}_c k^2)}, \quad \mathcal{B}_n(k) = -\frac{n\xi \operatorname{sgn}\Delta}{2} \frac{\lambda\!\!\!^{-2}_c}{(1 + \lambda\!\!\!^{-2}_c k^2)^{3/2}}. \tag{2.115}$$

The Berry curvatures of the two bands are opposite, as required by the Berry sum rule. Additionally, the two valleys exhibit opposite Berry curvatures, in accordance with the time-reversal symmetry of the model.

Let us take the values exactly at the point $k = 0$, where $\mathcal{B}_n(0) = -n\xi \operatorname{sgn}\Delta \lambda\!\!\!^{-2}_c/2$ and $g^n_{\mu\mu}(0) = \lambda\!\!\!^{-2}_c/4$. We thus have

$$\operatorname{Tr} g^n(0) = \frac{\lambda\!\!\!^{-2}_c}{2} = |\mathcal{B}_n(0)|, \quad \det g^n(0) = \sqrt{g^n_{xx}(0) g^n_{yy}(0)} = \frac{\lambda\!\!\!^{-2}_c}{4} = \frac{1}{2}|\mathcal{B}_n(0)|. \tag{2.116}$$

The inequalities of Eq. (2.43) are thus saturated at the $\boldsymbol{K}$ and $\boldsymbol{K'}$ points, and the Bloch wavepacket is minimally delocalized. The delocalization length is given by half of the Compton length, $\sqrt{g^n_{\mu\mu}(0)} = \lambda\!\!\!^{-}_c/2$. However, away from those points the inequalities are not saturated and a difference arises between minimal and typical delocalizations.

On a final note, we see that the analogy between the Bloch fermions of the gapped graphene (low-energy) model and massive Dirac fermions subsists. Indeed, as we mentioned in the viewpoint 2.4.3, massive Dirac electrons[17] in relativistic quantum mechanics exhibit a delocalization of the order of the Compton length due to virtual electron-positron annihilation and creation. Here due to virtual interband transitions, of which the higher is the 'electron' and the lower is the 'positron', the Bloch fermion exhibits a delocalization that is of the order of the Compton length.

[17] the actual ones

3 - Topological band theory

The existence of a *geometrical* band theory, associated with quantities *local* in reciprocal space, hints at a possible *topological* band theory, associated with *global* quantities in reciprocal space. This chapter introduces topological band theory, which will be of use in Chapters 9 and 10. We start by a general introduction to the topic, using the language of fiber bundles, in order to motivate the topological character of a band. We then motivate, and interpret, the topological equivalence relation between Bloch Hamiltonians, and we discuss the bulk-boundary correspondance.

Then, we focus on two topological invariants of interest in this thesis. First, we introduce the Chern number for time-reversal broken systems. We provide an explicit proof of its quantization, which also makes the resulting topological obstruction explicit. We follow by briefly discussing its relation with condensed matter physics and how the field of topological insulators came to be. We mention the recent development on topological bounds, and finally compute the valley Chern number in the gapped graphene model. Next, for time-reversal invariant systems, we discuss the history of the $\mathbb{Z}_2$ topological invariants, and mention its associated obstruction on the half Brillouin zone.

3.1 . Introduction

To introduce the topic, we may go back to viewpoint 6 on the language of vector bundles. For each band n we can construct a vector bundle $\mathscr{B}_n$ whose base space and fibers are the Brillouin zone and $\mathbb{C}\,|u_n(\boldsymbol{k})\rangle$, respectively. $\mathscr{B}_n$ is then a complex line bundle because its fibers are of dimension one over the complex numbers. The *total space* E_n of the bundle $\mathscr{B}_n$ is then defined as [93]

$$E_n = \bigcup_{\boldsymbol{k}\in \mathrm{BZ}} \{\boldsymbol{k}\} \times \mathbb{C}\,|u_n(\boldsymbol{k})\rangle\,. \tag{3.1}$$

The total space E_n is then a truly global property of the n-th band. The vector bundle $\mathscr{B}_n$ is then called *trivial* if the total space is homeomorphic[1] to a product space BZ $\times\, \mathcal{S}$ for some $\mathcal{S}$ which here will mostly be $\mathbb{C}$ (or rather $\mathrm{U}(1)$ if we stick to the projective bundle). The triviality of the bundle essentially amounts to defining a consistent smooth section throughout the base space. In our context, sticking to the projective bundle means that a general section will have the form $s(\boldsymbol{k}) = e^{i\varphi(\boldsymbol{k})}\,|u_n(\boldsymbol{k})\rangle$. Its consistence and smoothness then amounts to being able to define a smooth phase convention throughout the whole Brillouin zone.

If E_n is not homeomorphic to BZ $\times\, \mathcal{S}$, $\mathscr{B}_n$ is said to be *twisted*, and *topologically non-trivial*.[2] Its topological character is then quantified by a *topological invariant*, which classifies all the possible twists of the bundle $\mathscr{B}_n$. One such invariant for complex vector bundles is the first Chern number [11, 16, 76, 94, 95].

[1] A homeomorphism is a continuous bijection between two topological spaces, whose inverse is also continuous.

[2] Another way to phrase it that the bundle is trivial if it is topologically equivalent to a bundle where the base space can be separated from the fibers. If it is not the case, then the base space and the fibers are sort of entangled, analogously to quantum states, where the latter cannot be written as a product state.

While the bundle of all bands is necessarily trivial, transport properties will only be affected by the *occupied* bands, such that the important bundle for them is the valence bundle [82]. This is where the difference between a metal and an insulator becomes fundamental. In an insulator, a band is either fully occupied or not at all, so that we can properly define a valence bundle. However, in a metal only some parts of some bands are occupied and the valence bundle cannot be properly defined.[3]

The classification of different topologies present in insulators, according to their dimensionality and basic symmetries, is commonly referred to as the *tenfold way* [96, 97], or the Altland-Zirnbauer classification [98].

The study of topological properties of a band structure (i.e. a band topology) then forms topological band theory. While a variety of topological invariants have been put forward in band theory, such as the Hopf [26, 99], Stiefel-Whitney [100] or Euler [101] invariants[4], we will only focus on the arguably two main invariants of topological band theory, the Chern number and the $\mathbb{Z}_2$ topological invariants.

3.2 . Topological equivalence relation

The bands of a Bloch Hamiltonian may thus exhibit non-trivial topology with respect to its crystal momentum dependence. In that sense, two Bloch Hamiltonians are topologically equivalent iff they can be smoothly transformed into one another. They share the same value of topological invariant and are then said to be in the same topological phase. In practice, the Bloch Hamiltonian will depend on parameters other than the crystal momentum, e.g. hopping parameters, spin-orbit coupling strength, strain,... . Gathering these parameters in a vector $\boldsymbol{\lambda}$, the Bloch Hamiltonian can be written as $H(\boldsymbol{k}, \boldsymbol{\lambda})$. Plotting the different values of the topological invariants in the space of the vector $\boldsymbol{\lambda}$ then yields the *topological phase diagram* of the Bloch Hamiltonian.

The topological equivalence relationship between two Bloch Hamiltonians may be reformulated in a more intuitive way, with the following heuristic argument.

As mentioned in Chapter 2, divergences of the quantum Fisher information have become a hallmark of quantum phase transitions [53]. Since band quantum geometry is the direct origin of band topology, it seems natural to intuit that topological (quantum) phase transitions are signaled by a divergence of the quantum geometric tensor. The origin of these divergences is best seen in the Hamiltonian formulation of the QGT,

$$Q^n_{\mu\nu} = \sum_{\substack{m=1 \\ m\neq n}}^{N} \frac{\langle u_n | \partial_\mu H | u_m \rangle \langle u_m | \partial_\nu H | u_n \rangle}{(\epsilon_n - \epsilon_m)^2}. \tag{3.2}$$

As the numerator is typically well-behaved, the quantum geometric tensor diverges if (and only if) some ϵ_m crosses ϵ_n, i.e when a band crossing happens. Then, two Bloch Hamiltonians are topologically equivalent iff they is a transformation between the two that does not induce a band crossing along the way.[5]

[3] More technically, the base space is not the same for all the bands

[4] A common practice is to name these phases and materials according to their invariants, e.g. Chern insulators, $\mathbb{Z}_2$ topological insulators, Hopf topological insulators, etc...

[5] and that does not break a symmetry protecting the topological phase

We may get a more physical picture using the second and third viewpoints in Chapter 2. As the value of the QGT is linked to the extent of quantum fluctuation of the Bloch fermion's position, a divergence implies that the Bloch wavepacket becomes infinitely extended. All Bloch fermions of the n-th band exhibit infinite quantum fluctuations and overlap with each other[6]. This situation is very reminiscent of a critical point, i.e. of a phase transition, here topological.

Therefore, if one starts at a value of parameters $\boldsymbol{\lambda}_1$ such that the n-th band of the Bloch Hamiltonian $H(\boldsymbol{k}, \boldsymbol{\lambda}_1)$ is isolated from the others, and then changes the parameters to a value $\boldsymbol{\lambda}_c$ where $\epsilon_n(\boldsymbol{k}, \boldsymbol{\lambda}_c)$ crosses some other band, then a topological phase transition happens. The Bloch fermions become infinitely fluctuating, overlapping with each other and being extremely sensible to a phase transition. The Bloch fermions would then rearrange themselves with a new parameter value $\boldsymbol{\lambda}_2$, in a different topological phase.

3.3 . Bulk-boundary correspondence: Edge states

Arguably the most important consequence of having a non-trivial topological invariant is the presence of *robust*[7] *conducting edge states*, the latter being often considered as a defining feature of topological insulators [102].

Since band theory is formulated purely in the bulk, the correspondence between the topological invariant of the band structure and the conducting edge states is called the *bulk-boundary correspondence*. It may be formally understood as an application of the Atiyah-Singer index theorem [103, 104]. When the material has surfaces in a certain number of directions, the corresponding operators k_μ are not good quantum numbers anymore but maybe replaced in the Bloch Hamiltonian by $k_\mu = -i\partial_{r_\mu}$. The Bloch Hamiltonian then becomes a differential operator, onto which we may apply the Atiyah-Singer index theorem which states that the topological index of a (certain type of) differential operator equals its analytical index. Here we may see the topological index of the Bloch Hamiltonian as its bulk topological invariant, while the analytical index is the number of solutions to the set of PDE[8] defined by the eigenproblem of the Bloch Hamiltonian. The simplest example of such a problem gives the Jackiw-Rebbi edge state in Dirac materials [105]. Since these solutions represent edge states at the interface, where the PDE is important, we thus have that the number of edge states on the interface is equal to the bulk topological invariant of the Bloch Hamiltonian.

A more heuristic argument may be put forward. Consider one material with a certain topological invariant $\mathcal{I}_1$, and now interface it with another material which has a different topological invariant $\mathcal{I}_2$, for example zero for the vacuum. Now consider the two materials as one (sort of). Since the two materials harbor different values of the topological invariant $\mathcal{I}$, a path between the two necessarily involves a topological phase transition at the interface. But as we argued, a topological phase transition is necessarily accompanied by a gap closing. Consequently, the interface is metallic, and the two

[6] Although independent when electronic correlations are neglected

[7] The reasoning being that perturbations on the material may be seen as deformations of the Bloch Hamiltonian. Any such perturbation that does not close the gap with the neighbouring bands or break a protecting symmetry will thus not affect the presence of these conducting edge states. This is the so-called *topological robustness* of edge states.

[8] Partial Differential Equation

materials harbor conducting edge states.

3.4 . Time-reversal broken systems: Chern number

Here we consider two-dimensional materials. The Chern number associated to the n-th band is defined as

$$\mathcal{C}_n = \frac{1}{2\pi}\int_{\mathrm{BZ}} \mathcal{B}_n(\boldsymbol{k})\mathrm{d}^2\boldsymbol{k} = \frac{1}{2\pi}\int_{\mathrm{BZ}} \boldsymbol{\nabla}\times\boldsymbol{\mathcal{A}}_n(\boldsymbol{k})\cdot\mathbf{d}\boldsymbol{S}, \tag{3.3}$$

with $\mathbf{d}\boldsymbol{S} = (\mathrm{d}k_y\mathrm{d}k_z, \mathrm{d}k_x\mathrm{d}k_z, \mathrm{d}k_x\mathrm{d}k_y)$. Notice that if the Bloch Hamiltonian is time-reversal symmetric, then the Berry curvature is odd in the crystal momentum and the Chern number $\mathcal{C}_n$ must vanish.[9]

3.4.1 . Quantization and obstruction on the BZ

An alternative way to show that the Chern number is quantized is by relating it to transition functions, and interpreting it as an obstruction to the application of Stokes theorem [35, 106, 107, 108, 109, 110]. From the definition of the Chern number, one may be tempted to apply Stokes theorem and find

$$\mathcal{C}_n = \frac{1}{2\pi}\int_{\mathrm{BZ}} \boldsymbol{\nabla}\times\boldsymbol{\mathcal{A}}_n(\boldsymbol{k})\cdot\mathbf{d}\boldsymbol{S} = \frac{1}{2\pi}\oint_{\partial\mathrm{BZ}} \boldsymbol{\mathcal{A}}_n(\boldsymbol{k})\cdot\mathbf{d}\boldsymbol{k} = \frac{1}{2\pi}\Phi_g(\partial\mathrm{BZ}), \tag{3.4}$$

where ∂BZ is the boundary of the Brillouin zone. However, Stokes theorem requires that the Berry connection $\mathcal{A}_n$ is of class $\mathcal{C}^1$ over the surface of integration, here the Brillouin zone. Interestingly, one can prove that in this case, the Chern number is necessarily zero [107, 108]. This is directly seen from Eq. (3.4). Indeed, since the Brillouin zone obeys periodic boundary conditions, as soon as we reach the boundary we end up on the other side of it. In other words, the Brillouin zone is a closed set, and has the behavior of a torus. Such spaces have no boundary, i.e. $\partial\mathrm{BZ} = \varnothing$. Then we necessarily have $\Phi_g(\partial\mathrm{BZ}) = 0$ and $\mathcal{C}_n = 0$.

An alternative way to prove this, following Ref. [107], is by partitioning the Brillouin zone in two subsets $\mathcal{S}_1$ and $\mathcal{S}_2$ and applying Stokes theorem on both terms. This way we get

$$\mathcal{C}_n = \frac{1}{2\pi}\oint_{\partial\mathcal{S}_1} \boldsymbol{\mathcal{A}}_n(\boldsymbol{k})\cdot\mathbf{d}\boldsymbol{k} + \frac{1}{2\pi}\oint_{\partial\mathcal{S}_2} \boldsymbol{\mathcal{A}}_n(\boldsymbol{k})\cdot\mathbf{d}\boldsymbol{k}. \tag{3.5}$$

Using the fact that the two boundaries will have opposite $\mathbf{d}\boldsymbol{k}$ along their common frontier, a change of variable shows that $\oint_{\partial\mathcal{S}_2} \sim -\oint_{\partial\mathcal{S}_1}$ and thus

$$\mathcal{C}_n = \frac{1}{2\pi}\oint_{\partial\mathcal{S}_1} \boldsymbol{\mathcal{A}}_n(\boldsymbol{k})\cdot\mathbf{d}\boldsymbol{k} - \frac{1}{2\pi}\oint_{\partial\mathcal{S}_1} \boldsymbol{\mathcal{A}}_n(\boldsymbol{k})\cdot\mathbf{d}\boldsymbol{k} = 0. \tag{3.6}$$

Consequently, having $\mathcal{A}_n \in \mathcal{C}^1(\mathrm{BZ})$ implies that the Chern number is trivial, necessarily. By contraposition, having a non-trivial Chern number implies that there is a part of the Brillouin zone where the Berry connection has "singularities", i.e. where it is not continuously differentiable. In that sense, the non-tiviality of the Chern number signals an obstruction to applying Stokes theorem [35]. One natural question is the origin of these singularities, which can be found in the gauge freedom of the Berry connection. Indeed, as in electromagnetism with the magnetic field, the Berry curvature is the

[9] Indeed, it can be seen from the definition of the BZ in Eq. (1.23) that is it symmetric around the Γ point.

actual observable and a class of Berry connections give rise to the same Berry curvature. Specifically, any function of the form $\mathcal{A}_n - \boldsymbol{\nabla} f$ yields the same rotational, i.e. the same Berry curvature. A bit of manipulation then directly shows

$$\boldsymbol{\mathcal{A}}_n(\boldsymbol{k}) - \boldsymbol{\nabla} f(\boldsymbol{k}) = i\big[\, \langle u_n(\boldsymbol{k})|\, e^{-if(\boldsymbol{k})}\big]\boldsymbol{\nabla}\big[e^{if(\boldsymbol{k})}\, |u_n(\boldsymbol{k})\rangle\,\big] = i\, \langle v_n(\boldsymbol{k})|\boldsymbol{\nabla} v_n(\boldsymbol{k})\rangle\,, \tag{3.7}$$

with $|v_n(\boldsymbol{k})\rangle = e^{if(\boldsymbol{k})}\, |u_n(\boldsymbol{k})\rangle$. The gauge freedom of the Berry connection thus corresponds to the U(1)-gauge freedom of the Bloch state $|u_n(\boldsymbol{k})\rangle$. The fact that the Berry connection has singularities in the Brillouin zone now stems from the impossibility of defining a smooth choice of phase (i.e. U(1) gauge) across the whole Brillouin zone. It thus makes sense that the Chern number quantifies such obstructions, as we have seen that this impossibility is the origin of the non-triviality of the fiber bundle associated to the band.

We can dwell on this relation to show the quantization of the Chern number. A common assumption [35, 106, 107, 108] is to assume that the singularities of the Berry connection are isolated points[10] $\boldsymbol{k}_\alpha$.

A fundamental property of fiber bundles[11] is that they are locally trivial. At every point of the base space there exists a neighborhood in which the fiber bundle is separable as a product space. For us, it means that at each point $\boldsymbol{k}_\alpha$ where the Berry connection is singular, there exists a $\delta > 0$ such that on the disk $\mathcal{D}_\alpha$ with width δ, the fiber bundle is trivializable. The situation is then as pictured in Fig.3.1.

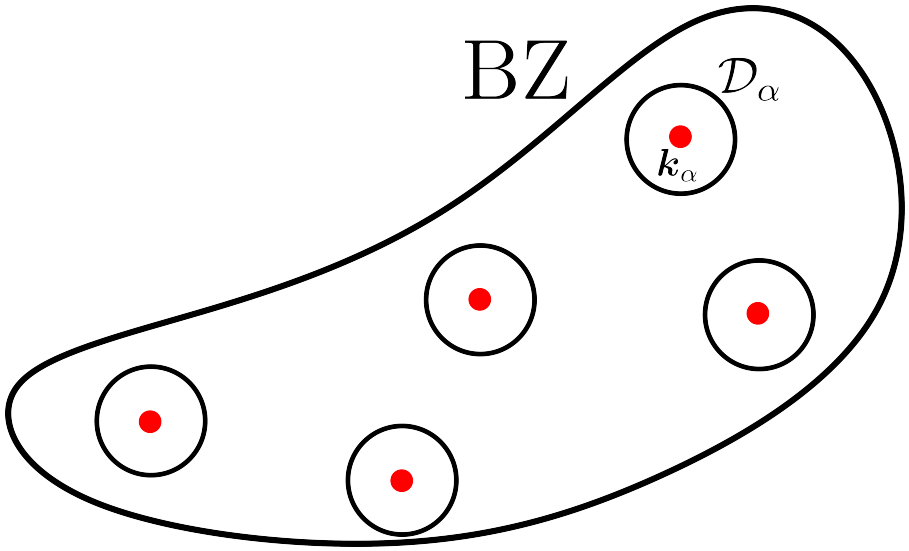

Figure 3.1: Isolated singularity points $\boldsymbol{k}_\alpha$ in the Brillouin zone.

This *local trivializability* means that there exists a f such that $\boldsymbol{\mathcal{A}}_{n\alpha} = \boldsymbol{\mathcal{A}}_n - \boldsymbol{\nabla} f$ is of class $\mathcal{C}^1$ in $\mathcal{D}_\alpha$.

[10] This is at least true within the tight-binding method. Indeed, in this method the Bloch Hamiltonian consists of cosine and sine functions, such that the components of the Bloch state are rational functions of these sine and cosine. As such their poles and zeros (which are the sources of phase singularities) only come in discrete points.

[11] A fiber bundle is a more general structure than a vector bundle, in that the fiber need not be a vector space [111]. However for our needs, the distinction is not relevant.

There is thus always a good $\mathrm{U}(1)$-gauge choice locally in the Brillouin zone. The Chern number can then be written as

$$2\pi\mathcal{C}_n = \sum_\alpha \int_{\mathcal{D}_\alpha} \boldsymbol{\nabla} \times \boldsymbol{\mathcal{A}}_n \cdot \mathbf{d}\boldsymbol{S} + \int_{\mathrm{BZ}\setminus\bigcup_\alpha \mathcal{D}_\alpha} \boldsymbol{\nabla} \times \boldsymbol{\mathcal{A}}_n \cdot \mathbf{d}\boldsymbol{S}. \tag{3.8}$$

By definition of $\mathcal{D}_\alpha$ we can directly apply Stokes theorem on the second term, whose boundary is $-\bigcup_\alpha \partial\mathcal{D}_\alpha$, where the minus sign refers to the orientation of $\partial\mathcal{D}_\alpha$. By contrast, we cannot apply Stokes theorem on the first term as it is, since $\mathcal{A}_n$ is not $\mathcal{C}^1$ over $\mathcal{D}_\alpha$. But using the local trivializability we know there exists a function f_α such that $\boldsymbol{\mathcal{A}}_{n\alpha} = \boldsymbol{\mathcal{A}}_n - \boldsymbol{\nabla} f_\alpha$. These functions f_α are then called the *transition functions*, as they allow to transition locally to a smooth gauge. Using $\boldsymbol{\nabla} \times \boldsymbol{\mathcal{A}}_n = \boldsymbol{\nabla} \times \boldsymbol{\mathcal{A}}_{n\alpha}$, we can apply Stokes theorem on the first term, which yields

$$2\pi\mathcal{C}_n = \sum_\alpha \int_{\mathcal{D}_\alpha} \boldsymbol{\nabla} \times \boldsymbol{\mathcal{A}}_{n\alpha} \cdot \mathbf{d}\boldsymbol{S} + \oint_{-\bigcup_\alpha \partial\mathcal{D}_\alpha} \boldsymbol{\mathcal{A}}_n \cdot \mathbf{d}\boldsymbol{k} = \sum_\alpha \oint_{\partial\mathcal{D}_\alpha} \boldsymbol{\mathcal{A}}_{n\alpha} \cdot \mathbf{d}\boldsymbol{k} - \sum_\alpha \oint_{\partial\mathcal{D}_\alpha} \boldsymbol{\mathcal{A}}_n \cdot \mathbf{d}\boldsymbol{k} \tag{3.9a}$$

$$= \sum_\alpha \oint_{\partial\mathcal{D}_\alpha} (\boldsymbol{\mathcal{A}}_{n\alpha} - \boldsymbol{\mathcal{A}}_\alpha) \cdot \mathbf{d}\boldsymbol{k} = -\sum_\alpha \oint_{\partial\mathcal{D}_\alpha} \boldsymbol{\nabla} f_\alpha \cdot \mathbf{d}\boldsymbol{k}. \tag{3.9b}$$

The Chern number is thus the sum of the winding numbers of the transition functions around the singularities ! Since a winding number is always quantized, the Chern number is as well !

Now the final question to be asked is can we make sense out of these transition functions ? In other words, can we actually construct them out of the Bloch state $|u_n(\boldsymbol{k})\rangle$? We can answer this by further finding the origin of the singularities at the point $\boldsymbol{k}_\alpha$. The phase singularities arise from the zeros of the Bloch state components $u_n^{(j)}$ as a function of $\boldsymbol{k}$ [107, 108]. In the case where only one such component $u_n^{(j)}$ is zero at $\boldsymbol{k}_\alpha$, we can gauge out its phase[12] $\phi_n^{(j)}$ in order to remove the phase singularity. In the case the gauge taken is $|v_n\rangle = \exp(-i\phi_n^{(j)})\,|u_n\rangle$ and the transition function is simply $f_\alpha = -\phi_n^{(j)}$. The singularity at $\boldsymbol{k}_\alpha$ will thus contribute to the Chern number through the winding number of $u_n^{(j)}$. In the case where multiple coefficients are simultaneously zero, the situation is more complex and the construction of the transition function may depend on the specific model considered.

3.4.2 . Brief history

The field of topological insulators finds its origins with the discovery of the (integer) quantum Hall effect (IQHE) in 1980 [112, 113]. The transverse Hall conductance of a two-dimensional system was found to be quantized when subjected to a large out-of-plane magnetic field. The connection between the quantization and the Chern number only came a couple years later with the celebrated TKNN paper [114] and the work of Barry Simon [77].[13] The Hall conductance is then proportional to the sum of the Chern numbers of all the occupied bands. This is readily derived from the semi-classical equation of motion as follows. The current associated to the n-th band reads

$$\boldsymbol{j}_n = \int_{\mathrm{BZ}} (-e)\dot{\boldsymbol{r}} \frac{\mathrm{d}^2\boldsymbol{k}}{(2\pi)^2} = -\frac{e}{\hbar}\int_{\mathrm{BZ}} \boldsymbol{\nabla}\epsilon_n \frac{\mathrm{d}^2\boldsymbol{k}}{(2\pi)^2} + \frac{e}{\hbar}\boldsymbol{E} \times \int_{\mathrm{BZ}} \boldsymbol{\mathcal{B}}_n \frac{\mathrm{d}^2\boldsymbol{k}}{(2\pi)^2}. \tag{3.10}$$

[12] Such that $u_n^{(j)} = |u_n^{(j)}|e^{i\phi_n^{(j)}}$

[13] Specifically, Ref. [114] showed the Hall conductance is quantized by rewriting in a form that makes the Chern number appear, but they did not make the connection to the latter. The contribution of Ref. [77] was to explicit the connection between the TKNN form, the Chern number and the work of M.V. Berry.

The first term vanishes by the periodicity of the band dispersion. In a two-dimensional system the Berry curvature is purely out-of-plane, say the z direction. The current then becomes

$$\boldsymbol{j}_n = \frac{e}{h}\boldsymbol{E} \times \mathcal{C}_n \boldsymbol{e}_z = \frac{e}{h}\mathcal{C}_n\big(E_y, -E_x, 0\big). \tag{3.11}$$

The Hall conductance tensor σ is then defined by $\boldsymbol{j} = \sigma \boldsymbol{E}$ where $\boldsymbol{j}$ is the sum of all the currents of the occupied bands n. Picturing a typical Hall measurement setup where $\boldsymbol{E} = E_x \boldsymbol{e}_x$, we find

$$\boldsymbol{j}_n = j_{n,y}\boldsymbol{e}_y = -\frac{e}{h}\mathcal{C}_n E_x \quad \Rightarrow \quad \sigma_{xy} = \frac{e}{h}\sum_{n\in \text{occ}} \mathcal{C}_n \in \frac{e}{h}\mathbb{Z}. \tag{3.12}$$

For a more thorough discussion on quantum Hall effects, see Ref. [115]. The next milestone came in 1988 with the Haldane model [116]. It was then realized that a magnetic field was not needed for a quantized Hall conductance, and that one could get such a state in crystalline systems.[14] Thus was born the field of topological insulators [117].

3.4.3 . Topological bounds

A notable recent development related to the Chern number is its appearance in several *topological bounds*, where the Chern number appears as a lower bound to several physical observables. The first example was in superconductivity through the superfluid weight [29], and more recent examples include electron-phonon coupling [118], optical absorption [119] and the structure factor [120]. These bounds broadly stem from the three inequalities we derived in Eq. (2.43). Usually they involve the integrated trace of the quantum metric over the Brillouin zone. Using Eq. (2.43), we indeed have

$$\int_{\text{BZ}} \operatorname{Tr} g^n \mathrm{d}^2\boldsymbol{k} \geq \int_{\text{BZ}} |\mathcal{B}^n| \mathrm{d}^2\boldsymbol{k} \geq 2\pi |\mathcal{C}_n|. \tag{3.13}$$

We can similarly put a lower bound on the average typical area of zero-point motion over the Brillouin zone,

$$\langle \mathcal{A}_{\text{typ}} \rangle_{\text{BZ}} = \frac{1}{\mathcal{A}_{\text{BZ}}}\int_{\text{BZ}} \pi \sqrt{g^n_{xx} g^n_{yy}}\, \mathrm{d}^2\boldsymbol{k} \geq \frac{1}{2\mathcal{A}_{\text{BZ}}}\int_{\text{BZ}} \pi |\mathcal{B}^n| \mathrm{d}^2\boldsymbol{k} \geq \frac{\pi |\mathcal{C}_n|}{2\mathcal{A}_{\text{BZ}}}, \tag{3.14a}$$

with $\mathcal{A}_{\text{BZ}}$ the area of the Brillouin zone. We will interpret one such bound in Chapter 8 from the fact that the Berry curvature guarantuees a minimum amount of zero-point motion of the Bloch fermion, and therefore a minimal amount of transport.

3.4.4 . Example: Valley Chern number in massive Dirac fermions

As the tight-binding model we derived in section 1.47 is time-reversal symmetric, the Chern number must be zero. However, we can still have *sub*-Chern numbers, corresponding to integrations over certain parts of the Brillouin zone. We can for example introduce *valley* Chern numbers $\mathcal{C}_{n\xi}$, specific to a certain valley. The ones of the honeycomb lattice may be derived from the low-energy model of massive Dirac fermions, where the integration over k in done over $\mathbb{R}^2$. Such an integration yields

$$\mathcal{C}_{n\xi} = -\frac{n\xi \operatorname{sgn}\Delta}{2}\int_0^{+\infty} \frac{\lambda\!\!\!^{-2}_c k}{(1+\lambda\!\!\!^{-2}_c k^2)^{3/2}} \mathrm{d}k = \frac{n\xi \operatorname{sgn}\Delta}{2}\Big[\big(1+\lambda\!\!\!^{-2}_c k^2\big)^{-1/2}\Big]_0^{+\infty} = -\frac{n\xi \operatorname{sgn}\Delta}{2}. \tag{3.15}$$

[14] Specifically, it is an extension of Eq. (1.47) where *complex* second nearest-neighbor hoppings are added. Their phase is what gives rise to the non-trivial topology. One origin of such a phase is a magnetic field, but it is not necessary. Indeed, any time-reversal breaking mechanism can suffice.

We first see that the sum of the valley Chern numbers over the bands, and that over the valleys, go indeed to zero as required by the Berry sum rule and time-reversal symmetry respectively.

We also see that the valley Chern number is not quantized, and is in fact a half-integer [11]. This further shows that the valley Chern number is not an actual Chern number, but rather a half-Chern number.

3.5 . Time-reversal invariant systems: $\mathbb{Z}_2$ topological invariants

As we have briefly dicussed, the notion of topological insulator went initially in pair with the Chern number. And as we have also seen, time-reversal symmetry enforces the triviality of the Chern number. One might thus think that time-reversal invariant systems harbor no topology. But a couple decades after the discovery of the IQHE, this thought was proven wrong with the discovery of $\mathbb{Z}_2$ topological insulators. Although the latter has been formulated in numerous ways, see Ref. [121] for an exhaustive list, we will stick to the works of Fu, Kane and Mele [122, 123, 124, 125, 126].[15]

3.5.1 . Origins

In Ref. [122], authors studied the effect of atomic and Rashba spin-orbit couplings (SOC) in graphene, thus creating the *Kane-Mele model*. By varying the relative strength of the Rashba and atomic SOC, λ_R and Δ_{so} respectively, the band gap induced by SOC closes and reopens. They then argued that the resulting gapped phase is topologically distinct from the former one. First, without the Rashba SOC the Kane-Mele model amounts to two copies of the Haldane model with opposite hopping phases, such that time-reversal symmetry is obeyed. Additionally, the phase holds quantized spin Hall conductance (when $\lambda_R = 0$) and exhibits helical edge states. Such a phenomena was then called the *quantum spin Hall effect* (QSHE).[16] They then showed that the edge states are robust to weak interactions and disorder. The QSHE has all the markings of a topologically non-trivial phase. Ref. [122] thus shows that topological order exists beyond the Chern number.

The goal of Ref. [123] was then to find the invariant that characterizes this topological phase. It was found that the QSHE phase is differentiated from the ordinary phase by a $\mathbb{Z}_2$ invariant.[17] In the simple case of a single Kramers pair,[18] the invariant is the parity of the number of times the Kramers partners are orthogonal in the Brillouin zone. This condition can be reformulated as the number modulo 2 of zeros of the Pfaffian $\mathrm{Pf}[\langle u_n(\boldsymbol{k})|\,\mathcal{T}\,|u_m(\boldsymbol{k})\rangle]$ with $\mathcal{T}$ the time-reversal operator, which is directly generalizable to the general case of N Kramers pairs.

3.5.2 . Time-reversal polarization

While an expression for the $\mathbb{Z}_2$ invariant was derived, its physical and formal meaning was still quite obscure. Ref. [124] then solved this problem by rephrasing the $\mathbb{Z}_2$ invariant in terms of the difference in polarization between two Kramers partners. This difference is called the time-reversal

[15] which remarkably were all published within a span of two years, between 2005 and 2007.

[16] A subtlety is that when $\lambda_R \neq 0$, the spin Hall conductance is not quantized anymore, but the helical edge states are still present, and robust. The QSHE is therefore a quantum effect, but not quantized.

[17] i.e. an invariant that only takes two values, typically zero or one.

[18] For a proof and discussion on Kramers theorem, see Ref. [11] for example.

polarization, and is noted P_θ. The $\mathbb{Z}_2$ invariant then takes the form

$$(-1)^\nu = \prod_{i=1}^{4} \frac{\sqrt{\det w(\Gamma_i)}}{\mathrm{Pf}\, w(\Gamma_i)} = \prod_{i=1}^{4} \mathrm{sgn}\,\mathrm{Pf}\, w(\Gamma_i), \tag{3.16}$$

where ν is related to the P_θ. $w_{nm}(\boldsymbol{k}) = \langle u_n(-\boldsymbol{k})|\,\mathcal{T}\,|u_m(\boldsymbol{k})\rangle$ is the *sewing matrix*, and the Γ_i are the four TRIMs of the square lattice. The square root of $\det w$ can be taken since one can continuously choose its sign over the Brillouin zone, a fact guaranteed by time-reversal symmetry and the vanishing Chern number. The most remarkable fact about this formula is that it only involves specific points in the Brillouin zone, and therefore does not explicitely appear as a global quantity over the Brillouin zone. Why this is the case will become clear when considering the transverse gauge in inversion symmetric systems.

3.5.3 . Three-dimensional $\mathbb{Z}_2$ topological insulators

With the basic theory of $\mathbb{Z}_2$ band topology laid out, the main open question was the experimental realization of the $\mathbb{Z}_2$ topological insulating phase. While the original motivation was graphene, the SOC band gap was thought to be realistically too small [125, 127, 128]. And indeed, it was recently measured to be of the order of 40μeV [129]. It was therefore needed to come up with other candidate materials. It is then that the direction shifted from two-dimensional materials to three-dimensional ones [127]. Ref. [125] then adressed the extension of $\mathbb{Z}_2$ band topology to three dimensions and applied the latter to a tight-binding model, in order to identify candidate materials. In two-dimensions, the $\mathbb{Z}_2$ invariant written in Eq. (3.16) involves the product of

$$\delta(\Gamma_i) = \frac{\sqrt{\det w(\Gamma_i)}}{\mathrm{Pf}\, w(\Gamma_i)} \tag{3.17}$$

at each of the four TRIMs Γ_i. In three dimensions there are $2^3 = 8$ distinct TRIMs. As mentioned in Chapter 1, the eight TRIMs are of the form

$$\boldsymbol{\Gamma} = \frac{n_1}{2}\boldsymbol{b}_1 + \frac{n_2}{2}\boldsymbol{b}_2 + \frac{n_3}{2}\boldsymbol{b}_3, \tag{3.18}$$

with $n_j \in \{0,1\}$. They are pictured in Fig.3.2 for the cubic lattice. Let us introduce $\mathsf{T}_0 = \{0,1\}^3$ the set of all eight TRIMs and $\mathsf{T}_j = \{(n_1,n_2,n_3) \in \mathsf{T}_0 \mid n_j = 1\}$. Visually, the eight points form the dashed red cube sketched in Fig.3.2, while the sets T_1,T_2 and T_3 are formed by four TRIMs obtained by the projection of the cube in the x, y and z directions respectively. They correspond to the planes in green, red and blue in Fig.3.2, respectively. Fu and Kane, based on arguments of $\mathrm{U}(1)$-gauge invariance, then argued that there are four separate topological invariants, given by the products of $\delta(\boldsymbol{\Gamma})$ over the sets T_j for $j \in \{0,1,2,3\}$, respectively. One then finds four invariants $(\nu_0,\nu_1,\nu_2,\nu_3)$ by

$$(-1)^{\nu_j} = \prod_{\boldsymbol{\Gamma}\in\mathsf{T}_j} \delta(\boldsymbol{\Gamma}), \quad j \in \{0,1,2,3\}. \tag{3.19}$$

The invariant ν_0 was shown in Ref. [125] to be different from the other three. Indeed, as it involves the product over all eight TRIMs, it is truly a three-dimensional quantity and can be shown to be robust against disorder. On the contrary, the invariants (ν_1,ν_2,ν_3) involve the product of TRIMs in

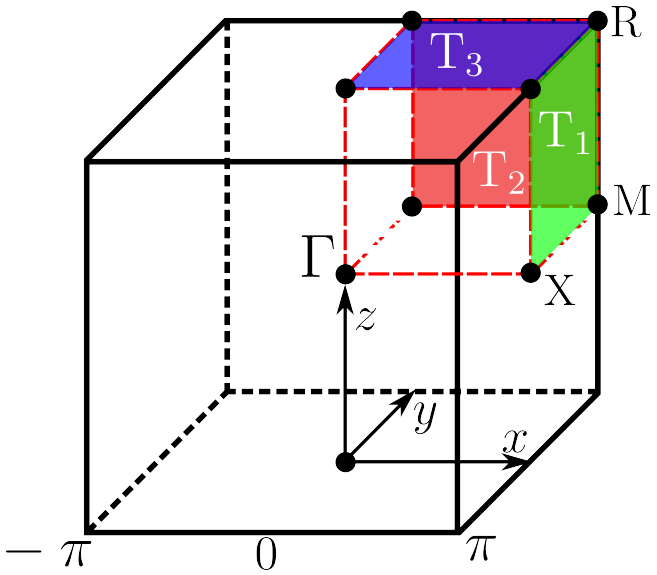

Figure 3.2: Brillouin zone of the cubic lattice, and its eight distinct TRIMs, forming the dotted points and dashed red cube.

the same two-dimensional plane. They were then shown in Ref. [125] to be quickly destroyed by disorder and were associated with a stacking of two-dimensional QSHI[19] planes in their associated directions. As such, the invariant ν_0 is referred to as the *strong* $\mathbb{Z}_2$ topological invariant while the other three (ν_1, ν_2, ν_3) are the *weak* invariants. A phase in which $\nu_0 = 0$ but at least one weak invariant is non-zero is a *weak topological insulating (WSI)* phase while $\nu_0 = 1$ corresponds to a *strong topological insulating (STI)* phase.

In order to make the distinction explicit, we adopt the notation $(\nu_0; \nu_1\nu_2\nu_3)$ to label the $\mathbb{Z}_2$ topology of a time-reversal invariant system.

Finally, a tight-binding model for the diamond lattice was considered and shown to exhibit the WSI and STI phases, and bismuth based materials were identified as possible candidates for the three-dimensional $\mathbb{Z}_2$ topological phases.

3.5.4 . Fu-Kane-Mele formula in inversion symmetric systems

One significant drawback of Eq. (3.19) is that the derivation of the factors $\delta(\Gamma)$ turns out to be quite involved. As we mentioned before, one needs to be in a gauge in which the sewing matrix w is continuously defined over the Brillouin zone. While the existence of this gauge is ensured by time-reversal symmetry, its practical construction turned out to be a complicated task in general.

The purpose of Ref. [126] was then to show that Eq. (3.19) is greatly simplified when the system in invariant under spatial inversion. Introducing P the parity operator, its action on the Bloch states reads

$$P\,|u_n(\boldsymbol{k})\rangle = e^{i\phi_n(\boldsymbol{k})}\,|u_n(-\boldsymbol{k})\rangle\,, \tag{3.20}$$

[19] Quantum Spin Hall Insulator

which means that at a TRIM $\mathbf{\Gamma}$, where $\mathbf{\Gamma} \sim -\mathbf{\Gamma}$, we have

$$P\left|u_n(\mathbf{\Gamma})\right\rangle = e^{i\phi_n(\mathbf{\Gamma})}\left|u_n(\mathbf{\Gamma})\right\rangle, \tag{3.21}$$

i.e. $e^{i\phi_n(\mathbf{\Gamma})} \in \operatorname{Sp} P$. But, since $P^\dagger = P$, we must have $e^{i\phi_n(\mathbf{\Gamma})}$ real, i.e. $e^{i\phi_n(\mathbf{\Gamma})} = \pm 1 = \xi_n(\mathbf{\Gamma})$. $\xi_n(\mathbf{\Gamma})$ is the *parity eigenvalue* of the n-th band at the TRIM $\mathbf{\Gamma}$. The main result of Ref. [126] is that the factors $\delta(\mathbf{\Gamma})$ are, in a special gauge, directy expressable in terms of the parity eigenvalues, as

$$\delta(\mathbf{\Gamma}) = \prod_{n=1}^{N_{\text{occ}}} \xi_{2n}(\mathbf{\Gamma}), \tag{3.22}$$

where N_{occ} is the number of occupied Kramers pairs and the product is taken over one partner of each Kramers pair, hence the index $2n$. The four invariants then become

$$(-1)^{\nu_j} = \prod_{\Gamma \in \mathsf{T}_j} \prod_{n=1}^{N_{\text{occ}}} \xi_{2n}(\Gamma), \tag{3.23}$$

which is much more accessible in practical calculations. We will refer to Eq. (3.23) as the *Fu-Kane-Mele (FKM) formula* for $\mathbb{Z}_2$ topological invariants.

The special gauge which allows to derive the FKM formula is the *transverse gauge*. As we have seen in Chapter 2, the Berry curvature is odd and even in the presence time-reversal and inversion symmetries, respectively. In the presence of both, it thus vanishes identically. A vanishing Berry curvature then implies that

$$\boldsymbol{\nabla} \times \boldsymbol{\mathcal{A}}_n(\boldsymbol{k}) = 0 \quad \Rightarrow \quad \boldsymbol{\mathcal{A}}_n(\boldsymbol{k}) = \boldsymbol{\nabla} f(\boldsymbol{k}), \tag{3.24}$$

for some function $f(\boldsymbol{k})$. It can then be gauged out by the $\mathrm{U}(1)$ transform $\left|u_n(\boldsymbol{k})\right\rangle \mapsto \exp(-if(\boldsymbol{k}))\left|u_n(\boldsymbol{k})\right\rangle$. This choice of gauge is what is referred to as the transverse gauge, in which we thus have $\boldsymbol{\mathcal{A}}_n(\boldsymbol{k}) = 0$. The singularities we thus saw for the Chern number seem to be completely wiped out in the transverse gauge. The subtlety here is that the tranverse gauge is actually not possible in *all* of the Brillouin zone.[20] Indeed, Kramers theorem ensures that every band dispersion crosses that of its Kramers partner at the TRIMs. Such degeneracies can also be seen as a type of singularity from which non-trivial topology arises. This point will be made clear in Chapter 9. The sources of topology in the Brillouin zone are thus confined to the TRIMs, which thereby explains why the $\mathbb{Z}_2$ topological invariants are solely determined by the behaviour of the band structure at the TRIMs.

In Chapter 9, we show that in two-band models the $\mathbb{Z}_2$ invariants can be determined by the analytic properties of the Green's function. We will also take the opportunity to explicit the relationship of the $\mathbb{Z}_2$ invariants with the notion of *band inversion*.

On a final note, Ref. [126] notes that the value of the factors $\delta(\mathbf{\Gamma})$ do not necessarily come from the spin-orbit coupling. While spin-orbit coupling was the initial motivation and key element leading to the discovery of $\mathbb{Z}_2$ topology, the latter can exist in any band structure, regardless of the presence of spin-orbit coupling. Additionally, Ref. [126] further identified Bismuth and Antimony based materials as candidates for $\mathbb{Z}_2$ topological phases.

[20] Nous sommes en 2007 après Jésus-Christ. Toute la zone de Brillouin est occupée par la jauge transverse… Toute ? Non ! Un village d'irréductibles TRIM résiste encore et toujours à l'envahisseur. (Il est tard…)

3.5.5 . $\mathbb{Z}_2$ topological invariant as an obstruction on the half-BZ

Finally, we mention that the $\mathbb{Z}_2$ topological invariant can also be seen as an obstruction to the definition of sections of the fiber bundle, but on the half-BZ [76, 97, 126].

As time-reversal maps one half of the BZ to the other, TRS implies that one half of the BZ compensates the potential obstruction on the other. One can therefore focus on only one half of the Brillouin zone, and actually show that the $\mathbb{Z}_2$ invariant is linked to a violation of Stokes theorem on this half-BZ.

4 - Superconductivity

The second part of the thesis, i.e. Chapters 6,7 and 8, explores the interplay between quantum geometry and superconductivity. As such, we now briefly introduce superconductivity, focusing mainly on introducing BCS theory. We start by discussing the history of superconductivity, from the 19th century up to the developments that led to the celebrated paper by Bardeen, Cooper and Schrieffer in 1957 [130], but also the Cooper problem in 1956 [131]. This discussion mainly relies on Refs. [3, 4, 5, 6] We follow by introducing the foundations of BCS theory, particularly the Cooper problem, the BCS Hamiltonian and wavefunction. Finally, we discuss the mean-field theory of the BCS Hamiltonian and summarize its main results.

4.1 . Brief history of superconductivity

Below we describe the history of superconductivity, from the 19th century and the development of low-temperature physics up until the 1950s and BCS theory. This part is not relevant for the scientific results presented in this manuscript and may thus be skipped.

4.1.1 . Genesis: Low-temperature physics [3]

The history of superconductivity is closely linked to that of low-temperature physics, which can be traced back to the beginning of the 19th century, with Michael Faraday. In the winter of 1823, on the suggestion of his mentor Sir Humphry Davy, Faraday experimented on chlorine gas, and managed to liquefy it. A substance known only as gas at the time, could be liquefied. From then on, Faraday studied and liquefied other gases, like ammonia or carbon dioxide. However, certain gases resisted his efforts and remained in the gaseous phase. These include hydrogen, nitrogen and oxygen. As such, he referred to them as *permanent gases*, whose liquefaction then became an open question. Progress emerged in the 1860s when Thomas Andrews formulated precise conditions needed for liquefaction to occur. The understanding then came that Faraday could not liquefy the permanent gases because he could not reach the pressures needed to raise their boiling temperature to a relatively ambient value.

A breakthrough came in 1877 when, simultaneously, Cailletet (in France) and Pictet (in Switzerland) liquefied oxygen using two different methods. Cailletet used a method based on a rapid variation of pressure[1], while Pictet relied on a 'cascade' of liquefaction. With the liquefaction of oxygen, Cailletet and Pictet launched a 'race' to liquefy the remaining permanent gases and attain ever lower temperatures, thus lauching the field of *low-temperature physics*, or *cryogenics* [132]. The first significant improvement was brought in 1883 by Polish scientists Wróblewski and Olszewski in Kraków when they successfully liquefied oxygen and nitrogen in their stable phases (Cailletet only liquefied the latter in the so-called dynamic phase, close to the boiling point). By then, only one permanent gas remained, hydrogen. More specifically, it was the only *known* one. Indeed, observations of the Sun's spectrum in

[1]The principle of cooling a gas by rapid expansion, which actually dates back to 1852, is known as the Joule-Thomson effect, named after James Prescott Joule and William Thomson (Lord Kelvin) [3].

the 1890s revealed the existence of another element, helium. The goal now was to liquefy both hydrogen and helium. The death of Wróblewski in 1888 while studying hydrogen practically put the Polish duo out of the race. Actually, the race was to be made between two main competitors, in England and the Netherlands[2].

The first contender, from England, was Sir James Dewar. Based at the Royal Institution as the Fullerian Professor of chemistry, he caught up with the Polish duo in 1886 by producing solid oxygen. Troubled by the fact that the glassware containing the liquefied gases tended to frost, making the liquids hardly visible, Dewar set out to remedy the problem. In 1892 he then invented the Dewar flask[3], an invaluable invention for low-temperature physics, and the furthering of his quest to liquefy the permanent gases. His work finally paid off in 1898 with the liquefaction of hydrogen, at a temperature he later estimated to 20 Kelvin, followed a year later by its solidification at 14 Kelvin. However, helium remained a gas.

The second contender, this time from the Netherlands, is Heike Kamerlingh Onnes. Onnes' interest for low-temperature physics reportedly comes from the influence of Van Der Waals [3]. Upon the observation that the ideal gas law was inadequate for real gases, in that for example it did not predict that gases could be liquefied, the latter set out to formulate a more precise law. His work then resulted in the celebrated Van der Waals equation of state in 1873, from which the boiling temperature of a gas could be derived for any pressure. Motivated by these theoretical advances, Onnes set out to test the predictions of the Van der Waals equation by studying the behaviour of gases at very low temperatures. To this end he founded his laboratory in Leiden, where he was appointed as a professor in 1881. His advantage in the race for helium came from his insight that advances in cryogenics could only come from high standards in the quality of the experimental machines, glassware and technicians, which led him to found several schools to train the needed craftsmen. This tedious work paid off in 1906 when he could liquefy hydrogen, only in much larger quantities than Dewar could produce, and with a much more reliable equipment. Finally, Onnes and his team were able to liquefy helium in 1908 [133], at around 4.2 Kelvin. See Ref. [5] on a more detailed account of the work of Onnes leading to this achievement.

4.1.2 . Discovery of superconductivity [4, 5]

Studying the behaviour of the resistance of a material as a function of temperature had a practical interest, that of thermometry. Indeed, the need for precise thermometers led to the development and modelization of resistance thermometers, more reliable than their gas-based counterparts. A characterization of the resistance down to the absolute zero was then appealing in order to get reliable thermometers in the lowest temperatures. Beyond that, the behavior of the resistance of metals at the lowest temperatures also held interest on its own. We may go back to 1857, where Adam Arndtsen argued from his measurements that the resistance $W(T)$ could be expressed as $W(T) = W_0(1 + aT + bT^2)$ with W_0 the resistance at $T = 0°C$. He then hypothesized that the quadratic term is only relevant for alloys and iron, while the linear coefficient had the same value for all perfectly pure (i.e. elemental) metals. This work caught the attention of Rudolf Clausius, who noted

[2]For further information on their competition and cooperation, see the correspondance between Onnes and Dewar at https://www.lorentz.leidenuniv.nl/history/KOL_archive/.

[3]Now colloquially known as a 'Dewar', or a 'Thermos flask' for everyday uses.

in 1860 that the linear coefficient of Arnsdten and the expansion coefficient of permanent gases had very close values. In the 1860s, the work of Matthiessen and René Benoit showed that the quadratic term was more important than previously thought.

As mentioned before, this subject got a practical dimension with the appearance of resistance thermometers, particularly with platinum and gold. This technology was first imagined by Siemens, and then significantly improved upon in 1885 by the work of Hugh Callendar, under the supervision of J.J Thomson. These thermometers were much more reliable and convenient than the gas-based ones available at the time. Their characterization relied on the accurate fitting of the resistance versus temperature. Platinum held special interest because of its quasi linear behavior in a wide range of temperature, and purifiability.

Meanwhile, Dewar had acquired a large quantity of cryogenic liquid, namely oxygen and ethylene, which he then put to use by studying various properties of matter at these low-temperatures, starting with resistivity. In collaboration with John A. Fleming, he measured the resistivity of various materials down to -200° C. The results, published in 1892, show, among other things, that the resistivity of pure metals significantly decreases with temperature and that the latter was extremely sensitive to the presence of impurities. Contrarily, alloys and impure metals showed significantly weaker decreases in the same range of temperature. These results were in accordance with Matthiessen's rule, formulated in 1860, stating that the increase of resistivity coming from impurities was independent of temperature.

The next notable development came again from Callendar who, in 1899, mentioned that the extrapolation of his experimental data suggested that the resistivity of platinum vanishes at -240.2° C, before arguing that it should rather saturate at a value given by the amount of impurity, in accordance with Mathiessen's rule. Nevertheless, it may have been the first time that the idea of a vanishing resistance beyond the absolute zero was put forward. As for Dewar, his following work convinced him in 1901 that perfectly pure metals have a vanishing resistance at the absolute zero, but the presence of impurities would result in a residual resistivity.

On the theoretical side, the discovery of the electron and of cathode rays stimulated theoreticians to elaborate a theory of conduction of metals in terms of electrons. Notable theoreticians working on this were Lorentz, Thomson, Paul Drude and Riecke. Drude put forwart his now celebrated model in 1900, in direct analogy with the kinetic theory of gases, thereby suggesting the idea of an electron gas in metals. The theory predicted a resistivity linear in the temperature. While the Drude model was already known not to be valid at low temperature, its extrapolation to the absolute zero yields a vanishing resistance at the latter. An alternate point of view on the matter was put forward by Kelvin in 1901, where he argued that at a temperature close to absolute zero, the electrons should all condense on the atoms, thus rendering the metal a perfect insulator (a superinsulator, so to speak). This point of view may be inspired from the kinetic theory of gases, a theoretical milestone at the time, whose intuition would suggest that the gas of electron would simply seize all movements, and thus stop conducting altogether.

Therefore, three competing predictions existed for the resistance of metal at absolute zero. First, experiments done thus far showed that a perfect pure metal should exhibit a vanishing resistance, in accordance with the extrapolation of the Drude model. Second, Matthiessen's rule suggests that, since impurities will always be present and that Dewar showed the resistvitiy was extremely suscep-

tible to their presence, the metal should have a residual constance resistance at zero temperature. Third, Kelvin's arguments suggested the metal should become a superinsulator in such a limit. It may be relevant to mention that while the experiments didn't suggest this thus far, Onnes had, at some point, the same opinion as Lord Kelvin.

It was in this context that Onnes, in 1910, having liquefied helium, set out to measure the resistivity of metals down to a couple of Kelvins. He first tried on platinum and gold where he saw a saturation of the resistance down to $1.5°$K. However, the inevitable presence of impurities, especially in platinum wires, made it difficult to formulate a definitive conclusion. To settle this problem, Mercury appeared as a solution. Indeed, as it is a liquid at ambient temperature, it could be distilled again and again until the desired purity is achieved. Finally, on the 8th of April in the year 1911, Onnes and his assistants[4] observed the sudden drop of resistance of mercury just below 4.2 Kelvin, as pictured by Onnes in Fig.4.1 and as noted in his notebook, "Mercury['s resistance] is practically zero". Interestingly, further

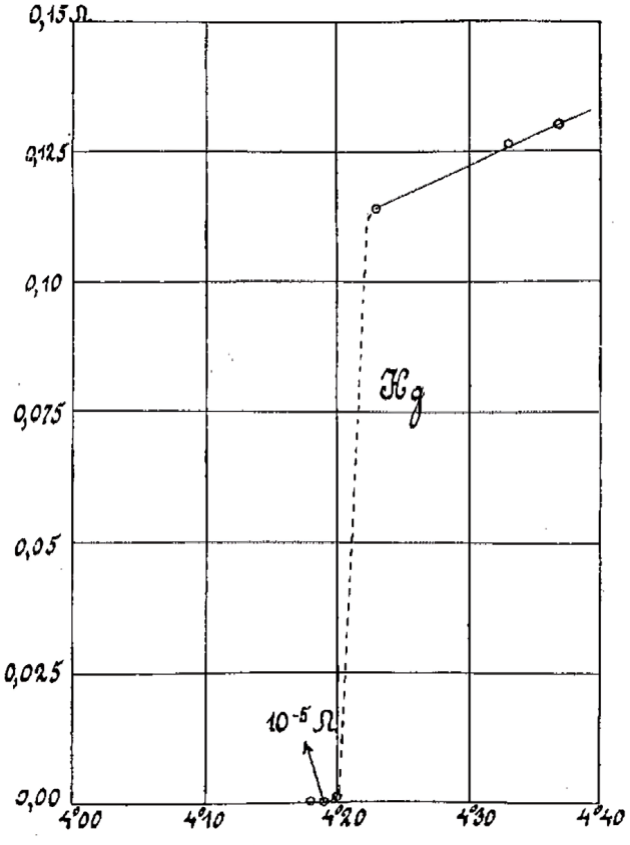

Figure 4.1: Sudden drop of resistance of a Mercury wire, below the experimental sensitivity of Onnes' equipment. This particular, historic, graph corresponds to a later experiment done on the 20th of October in 1911.

[4]Notably Gilles Holst, who did the inital measurement

experiments showed that the presence of impurities did not change the picture[5], and all the time spent caring about purity could have been saved, in the words of Onnes himself.

In 1914, as Onnes perceived the interest of superconductors in the making of strong magnets, discovered that a small magnetic field killed the superconducting state, thereby discovering the notion of critical field[6].

4.1.3 . Theoretical failures [4, 6]

Initially, Onnes' discovery did not raise many eyebrows, for example at the Solvay meeting of 1911. The situation changed when Onnes set out to measure how small was the resistance of the superconducting state, he was eventually unable to do so, as he consistently found that the persistent current in the superconductor showed no decay whatsoever[7]. This fact, shown in a conference by Onnes in 1914, struck many physicists, notably Erhenfest and Planck, and the news of ever running currents in superconductors spread internationally [4].

In Ref. [6], a number of failed theories of superconductivity are outlined, and it is shown that a great number of notable theoreticians of the 20th century tried to explain this phenomena. Among them are J.J. Thomson, Planck, Bohr, Born, Heisenberg, Einstein[8], Bloch, Brillouin, Feynman[9], Kronig, Landau, and others. All of these failures showed that the current theories could not account for superconductivity, and that this was an interacting many-body problem.

To further argue this [5], we may point out the links, already mentioned earlier, between the specific heat and the resistivity. Indeed measurements done by Nernst led him to build a bridge between the two quantities. The specific heat was the subject of heavy work at the beginning of the 20th century, notably from Einstein, Planck and Nernst, when the classical theory failed to explain its behavior at low-temperatures. A significant subject of discussion in the Solvay meeting of 1911, it was clear that only the quantum theory unearthed by Planck could solve the issue, as shown by Einstein in his celebrated model of Planck vibrators.[10] Using the bridge built by Nernst, this may have instilled the idea that only a quantum theory could explain superconductivity.

4.1.4 . Experimental clues, and theoretical advances [4, 6]

Notwithstanding the theoretical failures to explain superconductivity, experimental clues gradually came between the discovery of Onnes up until 1950. As argued by Cooper in Ref. [6], we may put forward five of them.

The first and second ones are the discoveries of Onnes that on one side, the resistance disappears suddenly below a critical temperature, and that above a critical magnetic field, the superconducting

[5] A fact we now know as Anderson's theorem

[6] At least for type I superconductors, i.e. elemental ones. The situation is more complicated in alloys, as demonstrated by Shubnikov in the 1930s, who thus discovered type II superconductors, a fact later theoretically explained by Ginzburg, Landau and especially Abrikosov

[7] He could also greatly improve the sensitivity of his resistivity experiments, and showed in 1926 with Tuyn that the residual resistivity was smaller than $10^{-13}R(4.2K)$, i.e. smaller than a ten-trillionth of the normal state resistivity.

[8] For a deeper discussion on the role of Einstein in superconductivity and in condensed matter physics, see Refs. [134, 135]

[9] See Ref. [136] for a deeper discussion of his relation with superconductivity

[10] Now referred to as phonons

phase is destroyed.

The third one is the pivotal discovery of Meissner and Ochsenfeld in 1933, that the superconductor expells any magnetic field in its interior [137]. Above all, this discovery showed that a superconductor is more than a super-conductor (or rather a perfect conductor). Indeed, as argued in 1919 by Lippmann, the magnetic field inside a perfect conductor cannot change. This is readily derived using Faraday's law and Ohm's law [4],

$$\boldsymbol{J} = \sigma \boldsymbol{E} \;\; \Rightarrow \;\; \boldsymbol{E} = \frac{1}{\sigma}\boldsymbol{J} \;\; \Rightarrow \;\; \boldsymbol{\nabla} \times \boldsymbol{E} = \frac{1}{\sigma}\boldsymbol{\nabla} \times \boldsymbol{J} = -\partial_t \boldsymbol{B} \xrightarrow[\sigma \to \infty]{} 0. \tag{4.1}$$

The argument is thus as follows. Picture a metal at room temperature under an applied magnetic field. The metal will then adopt the surrounding magnetic field. Now cool the metal so that it becomes a perfect conductor. Lippman's argument then tells us that the magnetic field stays the same, and it thus still present in the material. Imagine now the opposite, where a metal is brought to the perfect conducting phase but no magnetic field is applied, so that $\boldsymbol{B} = 0$ inside the material. And now apply a magnetic field. Lippmann's rule then implies that we still have $\boldsymbol{B} = 0$ inside the conductor. The order in which the experiment is done thus influences the properties of the perfect conductor. As such, it does not represent a (equilibrium) thermodynamic phase, since its state depends on its memory. The Meissner-Ochsenfeld effect shows that a superconductor is not just a perfect conductor in that we *always* have $\boldsymbol{B} = 0$ inside the superconductor, no matter what happened before the advent of the superconducting phase.

The superconducting phase thus appeared as a thermodynamic phase, a fact which inspired several theoreticians, starting by Gorter and Casimir in the following year, who proposed their *ad-hoc* two-fluid model, a thermodynamic approach. In 1935, the London brothers published their celebrated equations [138], a now fundamental theoretical tool for superconductivity. Finally, we may mention Landau and Ginzburg, who applied Landau's theory to superconductors, leading to the also celebrated Ginzburg-Landau theory [139].

The fourth experimental clue was the behavior of the specific heat, measured in 1932-1933 by Kok and Keesom [4]. The specific heat was shown to exhibit a continuous jump at the critical temperature as well as an exponential decrease in the superconducting phase (i.e. when $T < T_c$). This meant two things. First, it was also evidence that superconductivity was a thermodynamic phase, and specifically, the jump at T_c implied that the superconducting transition was a phase transition of second order. Second, the exponential decrease of the specific heat in the superconducting phase pointed to the existence of a gap in the single-particle excitation spectrum, as mentioned by Cooper [6]. This was corroborated in 1946 by radiation measurements of Glover and Thinkam [4]. The presence of the gap turned out to be a main focus for BCS in the development of their subsequent theory.

Finally, the discovery of the isotope effect in 1950 significantly narrowed the possible origins of superconductivity. Independently discovered by two teams whose articles were published on the same day[11] [140, 141]. The two teams measured the critical temperature of mercury for several of its isotopes, and found an empirical law that the critical temperature was inversely proportional to the square root of the isotope's mass, i.e. $T_c \propto M^{-1/2}$. This law also followed from a theory independently developed by Fröhlich a couple of weeks earlier [142]. The isotope effect clearly indicated that electron-

[11] Additionally in the same journal

phonon coupling was the source of superconductivity. Couple this with the theory based on the Bose-Einstein condensation of electron pairs developed by Schafroth a couple years later [143, 144], and you have the gist of BCS theory's background.[12]

4.1.5 . Final steps: BCS [6]

The main clues and intuition there, now the theory was just waiting to be derived. We now summarize this development, from Bardeen, Cooper, Schrieffer and Pines. The latter is thoroughly covered by BCS in Ref. [6] and Pines in Ref. [4].

While John Bardeen had already worked on superconductivity in the late 1930s, he only came back to it in 1950, after his work on semiconductors. With David Pines, a newly appointed assistant professor, they showed in 1955 within the random-phase approximation that the electron-phonon coupling could overwhelm the Coulomb repulsion for electron whose difference of energy is smaller than a typical phonon energy [145]. Therefore, such electrons could experience a net attractive interaction.

After that, Pines left the group and Bardeen, looking for a postdoc competent in the latest quantum field theory techniques (in order to handle the many-body interacting problem), recruited Leon Cooper to work on their attempts at superconductivity. Despite much attempts at a perturbative treatment through Feynman diagrams in the fall of 1955, Cooper remained unsuccessful. Unable to treat the many-body problem, he focused instead on a two-electron problem. He considered two electrons in a metal, close enough to the Fermi level, so that he would be in the validity regime of the results of Bardeen and Pines, subject to an attractive interaction. This is the so-called *Cooper problem*. He could then show that no matter the strength of the attractive interaction, the two electrons inevitably form a bound state, a *Cooper pair*. The Fermi surface was thus unstable towards the formation of such pairs, a phenomenon dubbed the *Cooper instability*. His results were published in 1956 [131].

Now that the single pair problem was settled, the issue was to build a many-body problem from this. Specifically, the goal was to build a many-body wavefunction, with the insights offered by Cooper. This was the task of a graduate student called Robert Schrieffer[13]. After six unsuccessful months, and an encouragement from Bardeen, finally came up with the celebrated BCS wavefunction.

With the BCS wavefunction now built, now the task was to prove that the resulting theory explained the known facts about superconductors we enumerated earlier[14]. After months of tedious and intense work from the trio, the BCS theory was worked out, and indeed explained the behaviour of superconductors.[15] The results were published in 1957 [130], and remarkably fitted the experimental data. The theory was immediately widely accepted, and the trio won the Nobel prize in 1972[16]

To this day, although entire classes of superconductors where the BCS theory does not fit have been discovered (cuprates, pnictides, nickelates,...), it remains the paradigm for superconductivity.

[12] Specifically, Schafroth assumed pairs that are closely packed, in order to make his calculations tractable. This would today correspond to the BEC end of the BCS-BEC crossover

[13] Whose office was in a shared office called the 'Institute for Retarded Studies'

[14] Plus some additional ones like nuclear magnetic resonance, radiation and penetration depth measurements

[15] That is those known at the time, of course

[16] One of eight Nobel prizes for superconductivity and its close cousin, superfluidity !

4.2 . Foundations of BCS theory

We now summarize the foundations of BCS theory, namely the Cooper problem as well as how to intuitively construct the BCS Hamiltonian and wavefunction.

4.2.1 . Cooper problem

We largely follow the standard Thinkam textbook [7]. Consider two electron with energies ϵ_1 and ϵ_2 relative to the Fermi level ϵ_F, subject to an interaction V. If ψ is the wavefunction of the two-electron problem, then the stationary Schrödinger equation reads

$$-\frac{\hbar^2}{2m}(\nabla_1^2+\nabla_2^2)\psi + V\psi = (\epsilon+2\epsilon_F)\psi, \tag{4.2}$$

with $\epsilon = \epsilon_1+\epsilon_2$. Placing ourselves in the rest frame, we can write

$$\psi(\boldsymbol{\rho}) = \sum_{\boldsymbol{k}} g_{\boldsymbol{k}} e^{i\boldsymbol{k}\cdot\boldsymbol{\rho}}, \tag{4.3}$$

with $\boldsymbol{\rho}$ the relative position of the two electrons. The weight $g_{\boldsymbol{k}}$ can be interpreted as the probability amplitude of having the electron 1 at momentum $\boldsymbol{k}$ and the second one at the opposite momenta $-\boldsymbol{k}$. We can also decompose the two-body interaction V in momentum space, as

$$V = \sum_{\boldsymbol{k},\boldsymbol{k'}} V_{\boldsymbol{k}\boldsymbol{k'}}, \tag{4.4}$$

such that the Schrödinger equation can be rewritten as

$$(\epsilon+2\epsilon_F)g_{\boldsymbol{k}} = \sum_{\boldsymbol{k'}} V_{\boldsymbol{k}\boldsymbol{k'}} g_{\boldsymbol{k'}}. \tag{4.5}$$

Using the results of Fröhlich, Bardeen and Pines, we assume that $V_{\boldsymbol{k}\boldsymbol{k'}}$ is non-zero only for energies close enough to the Fermi level, within ϵ_F and $\epsilon_F+\hbar\omega_D$ with $\hbar\omega_D$ the Debye energy. This defines a set $\mathcal{D}$ of momenta $\boldsymbol{k}$. Furthermore, using the same results, we take the interaction to be constant, at $-V<0$ in its non-trivial range. The Schrödinger equation can then be further arranged into

$$\frac{1}{V} = \sum_{\boldsymbol{k}\in\mathcal{D}} \frac{1}{\hbar^2k^2/m - (\epsilon+2\epsilon_F)}. \tag{4.6}$$

A usual move is then to move to an integral over energies using the density of states ρ. Defining $\xi = \hbar^2k^2/2m$ and ρ, we then get

$$\frac{1}{V} = \int_{\epsilon_F}^{\epsilon_F+\hbar\omega_D} \rho(\xi)\frac{1}{2\xi-(\epsilon+2\epsilon_F)}\mathrm{d}\xi = \int_0^{\hbar\omega_D} \rho(\epsilon_F+\xi)\frac{1}{2\xi-\epsilon}\mathrm{d}\xi. \tag{4.7}$$

Assuming $\epsilon_F \gg \hbar\omega_D$ and that the density of states varies slowly enough over the range of integration, we approximate by its value at the Fermi level, such that

$$\frac{1}{V} = \rho(\epsilon_F)\int_0^{\hbar\omega_D}\frac{1}{2\xi-\epsilon_F}\mathrm{d}\xi = \frac{\rho(\epsilon_F)}{2}\ln\left|1-\frac{2\hbar\omega_D}{\epsilon}\right|. \tag{4.8}$$

Remember that we defined ϵ to be the energy of the two electron *together* relative to the Fermi level. Therefore, a bound state would correspond to $\epsilon_<0$. Searching for such a solution finally yields

$$\epsilon = -\frac{2\hbar\omega_D}{1+\exp(2/\rho(\epsilon_F)V)} \simeq -2\hbar\omega_D e^{-2/\lambda}, \tag{4.9}$$

with $\lambda = \rho(\epsilon_F)V$ the BCS coupling constant. We have thus proved the existence of a bound state solution to the pair problem. Since this is the lowest energy solution, this also proves the Cooper instability. An interesting fact is the non-analytic dependence of ϵ the binding energy of the pair as a function of the BCS coupling constant, which shows that superconductivity is indeed a non-perturbative phenomenon.

4.2.2 . BCS Hamiltonian

We now briefly go through simple arguments leading to the BCS Hamiltonian in its standard form. We consider the original formulation in which BCS assumes a single-band model, such that

$$H_{\text{BCS}} = \sum_{\boldsymbol{k}\sigma}(\epsilon(\boldsymbol{k})-\mu)c^\dagger_{\boldsymbol{k}\sigma}c_{\boldsymbol{k}\sigma} + \sum_{\boldsymbol{k}\boldsymbol{k}'} V_{\boldsymbol{k}\boldsymbol{k}'}c^\dagger_{\boldsymbol{k}'\uparrow}c^\dagger_{-\boldsymbol{k}'\downarrow}c_{\boldsymbol{k}\uparrow}c_{-\boldsymbol{k}\downarrow}, \tag{4.10}$$

with μ the chemical potential. The first term is simply the kinetic terms of the underlying electrons forming the normal state. For the interaction term, we can justify its form as follows. A general form, again assuming a single-band model, would take any momentum and spin content into account. If the two electrons have momenta $\boldsymbol{k}$ and $\boldsymbol{q}$, then the Cooper pair would in general exhibit a finite center-of-mass momentum $\boldsymbol{K} = \boldsymbol{k}+\boldsymbol{q}$, resulting in a kinetic energy associated with the latter. One then sees that the energy of the Cooper pair is the lowest when $\boldsymbol{K} = 0$, i.e. when the pairing happens between electrons of opposite momenta. The possibility of a non-zero center-of-mass momentum for Cooper pairs is the subject of *FFLO superconductivity* [146, 147] and of *pair-density waves* [148], which results in a spatial modulation of the Cooper pair wavefunction.

Additionally, the two electrons will generally have spins σ_1 and σ_2. Another possible source of energy is angular momentum, which leads to the two electrons having opposite spin, so that the Cooper pair hos zero total spin.

Therefore, the electrons that cost the least amount of energy to pair are the ones with opposite momenta and spins. Unless their formation is strictly forbidden by some symmetry, then it will be these that form first. This so-called s-wave superconductivity is by far the most common type of superconductivity. One therefore arrives at the BCS Hamiltonian stated in Eq. (4.10).

4.2.3 . BCS wavefunction

For intuitively constructing the BCS wavefunction, we may start by introducing the "pairon" operator $b^\dagger_{\boldsymbol{k}} = c^\dagger_{\boldsymbol{k}\uparrow}c^\dagger_{-\boldsymbol{k}\downarrow}$. The interaction term can then be written as

$$-\sum_{\boldsymbol{k}\boldsymbol{k}'} V_{\boldsymbol{k}\boldsymbol{k}'}b^\dagger_{\boldsymbol{k}'}b_{\boldsymbol{k}}, \tag{4.11}$$

which, in a sense, is a quadratic term. It describes the scattering of a Cooper pair at a momentum $\boldsymbol{k}$ to another momentum $\boldsymbol{k}'$, but it is not a scattering between two Cooper pairs. In that sense, the Cooper pairs themselves are not interacting, and can be conceived as *statistically independent*. Indeed,

such terms would involve at least four pairon operators, i.e. eight electronic operators, which is not the case here. We can use this observation to heuristically construct the BCS wavefunction $|\psi_{\text{BCS}}\rangle$. This state represents a certain probability P, and a given configuration of Cooper pairs, notably in momentum space. From the statistical independence of the Cooper pairs at different momenta, we may infer that the probability be should be of the form

$$P = \prod_{\boldsymbol{k}} P(\boldsymbol{k}), \tag{4.12}$$

where $P(\boldsymbol{k})$ is essentially the probability of having a Cooper pair at momentum $\boldsymbol{k}$. Using the correspondence between probability theory and quantum mechanics, this hints at the possibility that the state $|\psi_{\text{BCS}}\rangle$ has the form

$$|\psi_{\text{BCS}}\rangle = \prod_{\boldsymbol{k}} |\psi(\boldsymbol{k})\rangle\,, \tag{4.13}$$

with $|\psi(\boldsymbol{k})\rangle$ representing the Cooper pair at momentum $\boldsymbol{k}$.

Evidently, at each $\boldsymbol{k}$, we either have a Cooper pair, or we don't. Let $u_{\boldsymbol{k}}$ be the probability amplitude of *not* having a Cooper pair at momentum $\boldsymbol{k}$ and $v_{\boldsymbol{k}}$ be the probability amplitude that we do. We then naturally have $|u_{\boldsymbol{k}}|^2 + |v_{\boldsymbol{k}}|^2 = 1$. Then, again using the analogy between probabilities and quantum states, the state $|\psi(\boldsymbol{k})\rangle$ could take the following form,

$$|\psi(\boldsymbol{k})\rangle = u_{\boldsymbol{k}} |\phi_0\rangle + v_{\boldsymbol{k}} b^\dagger_{\boldsymbol{k}} |\phi_0\rangle\,, \tag{4.14}$$

where $|\phi_0\rangle$ is a vacuum state, e.g. the Fermi sea. The BCS wavefunction thus takes the form

$$|\psi_{\text{BCS}}\rangle = \prod_{\boldsymbol{k}} \left(u_{\boldsymbol{k}} + v_{\boldsymbol{k}} c^\dagger_{\boldsymbol{k}\uparrow} c^\dagger_{-\boldsymbol{k}\downarrow}\right) |\phi_0\rangle\,. \tag{4.15}$$

A slightly alternative form may be found by fixing the U(1)-gauge as $u_{\boldsymbol{k}} \in \mathbb{R}$. Then, with $\phi(\boldsymbol{k})$ the relative phase between the two coefficients, we have

$$|\psi_{\text{BCS}}\rangle = \prod_{\boldsymbol{k}} \left(u_{\boldsymbol{k}} + v_{\boldsymbol{k}} e^{i\phi(\boldsymbol{k})} c^\dagger_{\boldsymbol{k}\uparrow} c^\dagger_{-\boldsymbol{k}\downarrow}\right) |\phi_0\rangle\,, \tag{4.16}$$

where $v_{\boldsymbol{k}} \in \mathbb{R}$. This construction was in essence the one originally done by BCS [130].

4.3 . Mean-field theory of superconductivity [7]

We now summarize the main methods and results of the mean-field theory of superconductivity.

4.3.1 . Variational method

The original treatment of BCS was ot exactly a mean-field theory in the modern sense of it, other than the fact that the BCS wavefunction has a Hartree flavor to it. Specifically, they treated the probability amplitudes $u_{\boldsymbol{k}}$ and $v_{\boldsymbol{k}}$ as *variational parameters*. Their idea was that the actual groundstate would be the one that minimizes the energy. The variational condition was then [130]

$$\delta \langle \psi_{\text{BCS}}| H_{\text{BCS}} |\psi_{\text{BCS}}\rangle = 0. \tag{4.17}$$

First, the expectation value can be expressed as [7]

$$\langle\psi_{\text{BCS}}|\, H_{\text{BCS}}\, |\psi_{\text{BCS}}\rangle = 2\sum_{\boldsymbol{k}} \xi_{\boldsymbol{k}} v_{\boldsymbol{k}}^2 + \sum_{\boldsymbol{k}'\boldsymbol{k}} V_{\boldsymbol{k}\boldsymbol{k}'} u_{\boldsymbol{k}'} v_{\boldsymbol{k}'} u_{\boldsymbol{k}} v_{\boldsymbol{k}}, \tag{4.18}$$

with $\xi_{\boldsymbol{k}} = \epsilon_{\boldsymbol{k}} - \mu$, assuming a standard spin degenerate band structure. Now introducing $\theta_{\boldsymbol{k}}$ such that $(u_{\boldsymbol{k}}, v_{\boldsymbol{k}}) = (\cos\theta_{\boldsymbol{k}}, \sin\theta_{\boldsymbol{k}})$, we have

$$\langle\psi_{\text{BCS}}|\, H_{\text{BCS}}\, |\psi_{\text{BCS}}\rangle = \sum_{\boldsymbol{k}} \xi_{\boldsymbol{k}}\big(1+\cos(2\theta_{\boldsymbol{k}})\big) + \frac{1}{4}\sum_{\boldsymbol{k}\boldsymbol{k}'} V_{\boldsymbol{k}\boldsymbol{k}'} \sin(2\theta_{\boldsymbol{k}})\sin(2\theta_{\boldsymbol{k}'}). \tag{4.19}$$

The variational condition now states that the derivative of the expectation value with respect to $\theta_{\boldsymbol{k}}$ is zero. Expliciting the derivative then leads to the following self-consistency equation,

$$\tan(2\theta_{\boldsymbol{k}}) = \frac{1}{2\xi_{\boldsymbol{k}}}\sum_{\boldsymbol{k}'} V_{\boldsymbol{k}\boldsymbol{k}'}\sin(2\theta_{\boldsymbol{k}'}). \tag{4.20}$$

We now introduce a new change of variables,

$$\Delta_{\boldsymbol{k}} = -\frac{1}{2}\sum_{\boldsymbol{k}'} V_{\boldsymbol{k}\boldsymbol{k}'}\sin(2\theta_{\boldsymbol{k}'}), \quad E_{\boldsymbol{k}} = \sqrt{\xi_{\boldsymbol{k}}^2 + \Delta_{\boldsymbol{k}}^2}, \tag{4.21}$$

where $\Delta_{\boldsymbol{k}}$ will be seen as the superconducting gap and $E_{\boldsymbol{k}}$ is the energy associated to a Cooper pair. The self-consistency equation becomes

$$\Delta_{\boldsymbol{k}} = -\frac{1}{2}\sum_{\boldsymbol{k}'} V_{\boldsymbol{k}\boldsymbol{k}'}\frac{\Delta_{\boldsymbol{k}'}}{E_{\boldsymbol{k}'}}. \tag{4.22}$$

Eq. (4.22) is called the *gap equation*, a central object of the mean-field theory of superconductivity.

Finally, specifying the BCS interaction yields that $\Delta_{\boldsymbol{k}} = \Delta\Theta(|\xi_{\boldsymbol{k}}| - \hbar\omega_D)$, such that the gap equation can be reduced to

$$\frac{1}{\lambda} = \int_0^{\hbar\omega_D} \frac{1}{\sqrt{\xi^2+\Delta^2}}\mathrm{d}\xi = \operatorname{arcsinh}\left(\frac{\hbar\omega_D}{\Delta}\right), \tag{4.23}$$

where again $\lambda = \rho(\epsilon_F)V$ is the BCS coupling constant, which is typically smaller than one.[17] The superconducting gap then finally reads

$$\Delta = \frac{\hbar\omega_D}{\sinh(1/\lambda)} \simeq 2\hbar\omega_D e^{-1/\lambda}, \tag{4.24}$$

an expression which again underscores the non-perturbative character of superconductivity. As for the critical temperature, the notion of temperature was incorporated through the free energy, whose minimization, and the condition $\Delta(T_c) = 0$, yields the following equation [130],

$$\frac{1}{\lambda} = \int_0^{\hbar\omega_D/2k_BT_c} \frac{\tanh x}{x}\mathrm{d}x. \tag{4.25}$$

[17] Making BCS theory a *weak-coupling* theory.

We show in appendix C.1 that in the usual regime where $\hbar\omega_D \gg k_B T_c$, the critical temperature reads

$$k_B T_c = 2\hbar\omega_D \frac{e^\gamma}{\pi} e^{-1/\lambda}, \tag{4.26}$$

where $\gamma \simeq 0.577$ is the Euler-Mascheroni constant. The remarkable consequence of this result is that the ratio between the superconducting gap (at zero temperature) and the critical temperature has a universal value,

$$\frac{\Delta}{k_B T_c} \simeq \frac{\pi}{e^\gamma} \simeq 1.76. \tag{4.27}$$

This relation has become a standard test to check if a superconductor is conventional or not (i.e. follows BCS theory).

4.3.2 . Bogoliubov-Valatin transformation

In 1958, the year following the publication of BCS theory, a much simpler method to handle the BCS Hamiltonian was developed by Bogoliubov [149]. Going back to Eq. (4.10), the mean-field approximation in this technique consider that the fluctuations of the pairon operator are small, so that they constitute a perturbative parameter. Doing so and introducing the order parameter

$$\Delta_{\boldsymbol{k}} = -\sum_{\boldsymbol{k'}} V_{\boldsymbol{k}\boldsymbol{k'}} \langle c_{-\boldsymbol{k}\downarrow} c_{\boldsymbol{k}\uparrow} \rangle, \tag{4.28}$$

one finds the *mean-field BCS Hamiltonian*

$$H = 2\sum_{\boldsymbol{k}} \left[\sum_\sigma \xi_{\boldsymbol{k}} c^\dagger_{\boldsymbol{k}\sigma} c_{\boldsymbol{k}\sigma} - \Delta_{\boldsymbol{k}} c^\dagger_{\boldsymbol{k}\uparrow} c^\dagger_{-\boldsymbol{k}\downarrow} - \Delta^*_{\boldsymbol{k}} c_{-\boldsymbol{k}\downarrow} c_{\boldsymbol{k}\uparrow} \right] + \text{cst}, \tag{4.29}$$

where the constant is related to the condensation energy, the difference in energy between the superconducting and normal state. One thus obtains a Hamiltonian bilinear in the fermionic operators, which can thus be diagonalized by a linear transformation. The latter is called the *Bogoliubov-Valatin transformation*, and represents the so-called Bogoliubons. Further calculations shows the same results as derived by BCS in the variational method. This method shows that the mean-field method doubles the amount of bands with respect to the normal state, and the Bogoliubons can be seen as a mixture of electrons and holes, composing the so-called Nambu space.

4.3.3 . Modern Bogoliubov-de Gennes (BdG) method

The generalization of the Bogoliubov method in the case where the normal state can have multiple internal degrees of freedom (sublattice, orbital,...) and general spin content is called the Bogoliubov-de Gennes method, where the mean-field Hamiltonian in a suitable Nambu space reads

$$\mathcal{H}_{\text{BdG}} = \begin{pmatrix} H(\boldsymbol{k}) & \hat{\Delta}(\boldsymbol{k}) \\ \hat{\Delta}(\boldsymbol{k})^\dagger & -H(-\boldsymbol{k})^* \end{pmatrix}. \tag{4.30}$$

$H(\boldsymbol{k})$ is the spinless normal state Hamiltonian and $\hat{\Delta}(\boldsymbol{k})$ is the order parameter matrix, defined similarly as in the single-band case.

5 - Green's function

Green's functions feature prominently in Chapters 9 and 10. Indeed, in Chapter 9, we show that the Green's function can provide information about the topological phases of non-interacting models. In contrast, Chapter 10 aims to formulate a natural generalization of the quantum geometric tensor beyond the free-fermion limit, using Green's functions.

The objective of this chapter is to introduce the most fundamental quantities from Green's functions that we make use of. We thus start by introducing the general principle of a Green's function, as the fundamental solution of a differential equation. We then proceed to the special case where the differential equation is the Schrödinger equation, with a single-particle Hamiltonian, thus giving rise to the single-particle Green's function. Based on the latter, we introduce the spectral function, which extends the notion of density of states beyond single-particle Hamiltonians. Finally we introduce, through the Dyson equation, the self-energy and the interacting Green's function. Standard references for Green's functions in quantum many-body physics include Refs. [150, 151, 152, 153, 154]. References more inclined towards the mathematical field of partial differential equations include Refs. [155, 156, 157, 158].

5.1 . General idea of a Green's function

Consider a system described by several variables $\boldsymbol{x}$, and a differential operator L represented as a polynomial of partial derivatives with respect to the different variables x_μ. Consider then two functions u and f related by the differential equation

$$Lu(\boldsymbol{x}) = f(\boldsymbol{x}). \tag{5.1}$$

The Green's function of the differential operator L is defined as the function $G(\boldsymbol{x}, \boldsymbol{s})$ such that

$$LG(\boldsymbol{x}, \boldsymbol{s}) = \delta(\boldsymbol{x} - \boldsymbol{s}). \tag{5.2}$$

If the coefficients of L are independent of $\boldsymbol{x}$, then the differential equation is said to be translation invariant, and we have $G(\boldsymbol{x}, \boldsymbol{s}) = G(\boldsymbol{x} - \boldsymbol{s})$. The main interest of the Green's function is that from its knowledge we can construct a solution of Eq. (5.1). Indeed, as L acts only on $\boldsymbol{x}$ we have

$$L \int G(\boldsymbol{x}, \boldsymbol{s}) f(\boldsymbol{s}) \mathrm{d}\boldsymbol{s} = \int LG(\boldsymbol{x}, \boldsymbol{s}) f(\boldsymbol{s}) \mathrm{d}\boldsymbol{s} = \int \delta(\boldsymbol{x} - \boldsymbol{s}) f(\boldsymbol{s}) \mathrm{d}\boldsymbol{s} = f(\boldsymbol{x}). \tag{5.3a}$$

Therefore, $u : \boldsymbol{x} \mapsto \int G(\boldsymbol{x}, \boldsymbol{s}) f(\boldsymbol{s}) \mathrm{d}\boldsymbol{s}$ is a solution of Eq. (5.1). In that sense, the Green's function is a *fundamental solution* of its associated differential equation.

5.2 . Single-particle Green's function

For quantum systems, the differential equation we care about is the Schrödinger equation, where the (single) variable $\boldsymbol{x}$ is time t. Denoting $\boldsymbol{s} = t'$, the Green's function of the Schrödinger equation is

defined by

$$\big(i\hbar\partial_t - H\big)G(t,t') = \delta(t-t'). \tag{5.4}$$

Since H does not typically depend on time, we have $G(t,t') = G(t-t')$. As we have observed in Chapter 2, band quantum geometric and topological properties only occur in multiband systems. As such, consider the following single-particle Hamiltonian

$$H(\boldsymbol{k}) = \sum_{\alpha,\beta=1}^{N} h_{\alpha\beta}(\boldsymbol{k}) c^\dagger_{\boldsymbol{k}\alpha} c_{\boldsymbol{k}\beta}, \tag{5.5}$$

written in a finite-dimensional basis, for example in a tight-binding calculation. We show in appendix D.1 that the following Green's function

$$G_{\alpha\beta}(t,t',\boldsymbol{k}) = -\frac{i}{\hbar}\Theta(t-t')\langle\big\{c_{\boldsymbol{k}\alpha}(t), c^\dagger_{\boldsymbol{k}\beta}(t')\big\}\rangle, \tag{5.6}$$

obeys the equation

$$\big(i\hbar\partial_t - H\big)G(t,t',\boldsymbol{k}) = \delta(t-t')\mathbb{1}, \tag{5.7}$$

where we drop the identity matrix $\mathbb{1}$ in the following. G is referred to as the *single-particle Green's function*. Its expression can be interpreted as follows. First, the average $\langle\cdot\rangle$ is typically the thermal average $\langle\mathcal{O}\rangle = \mathrm{Tr}\big[\mathcal{O}e^{-\beta H}\big]/Z$. The anticommutator gives rise to two terms. One is $\langle c_{\boldsymbol{k}\alpha}(t), c^\dagger_{\boldsymbol{k}\beta}(t')\rangle$, which corresponds to the creation of an electron with indices β at time t' followed by the annihilation of an electron with indices α at time t. The other term, $\langle c^\dagger_{\boldsymbol{k}\beta}(t') c_{\boldsymbol{k}\alpha}(t)\rangle$ describes the same event but happening backwards. Finally, the Heaviside factor $\Theta(t-t')$ ensures the causality of the Green's function.

We can additionally use the time-translation invariance to write $G(t,t',\boldsymbol{k}) = G(t-t',\boldsymbol{k})$, and by relabeling[1] $t-t' \mapsto t$, have

$$G_{\alpha\beta}(t,\boldsymbol{k}) = -\frac{i}{\hbar}\Theta(t)\langle\big\{c_{\boldsymbol{k}\alpha}(t), c^\dagger_{\boldsymbol{k}\beta}\big\}\rangle. \tag{5.8}$$

Having done this, we can now introduce the Fourier transform of the Green's function

$$\tilde{G}(\omega,\boldsymbol{k}) = \int_{-\infty}^{+\infty} G(t,\boldsymbol{k}) e^{i\omega t}\mathrm{d}t, \tag{5.9}$$

which, for simplicity, we denote as $G(\omega,\boldsymbol{k})$ in the following. We show in appendix D.2 that the Fourier transform of the single-particle Green's function reads

$$G(\omega,\boldsymbol{k}) = \lim_{\eta\to 0^+} \frac{1}{\hbar\omega\mathbb{1} - H(\boldsymbol{k}) + i\eta\mathbb{1}}, \tag{5.10}$$

where by an abuse of notation we have noted the matrix $h(\boldsymbol{k})$ as $H(\boldsymbol{k})$.

[1] Or equivalently setting $t' = 0$.

5.3 . Self-energy and Dyson equation

Going beyond the free-fermion limit, consider a single-particle Hamiltonian H_0 and an interaction term V such that the Hamiltonian is $H = H_0 + V$, where we make the $\boldsymbol{k}$ dependences implicit. We will thus have two Green functions, G_0 denoting the non-interacting one and G its interacting counterparts. A central object in the theory of interacting systems is the *self-energy* Σ, defined as

$$\Sigma = G_0^{-1} - G^{-1}. \tag{5.11}$$

The self-energy thus encodes the difference between the non-interacting and interacting systems. From the definition of the self-energy one can derive the *Dyson equation*,

$$G = G_0 + G_0 \Sigma G. \tag{5.12}$$

The Dyson equation is the basis of perturbation theory, particularly through the approach of Feynman diagrams.

The Fourier transform of the interacting Green's function reads

$$G(\omega, \boldsymbol{k}) = \lim_{\eta \to 0^+} \frac{1}{\hbar\omega \mathbb{1} - H_0(\boldsymbol{k}) - \Sigma(\omega, \boldsymbol{k}) + i\eta \mathbb{1}}, \tag{5.13}$$

where we reintroduced the $\boldsymbol{k}$ dependences. Note that, as $H_0(\boldsymbol{k})$, we will also in Chapter 10 represent the self-energy $\Sigma(\omega, \boldsymbol{k})$ as a matrix in the orbital, or band basis. Its off-diagonal elements therefore describe the hybridization between different orbitals or bands, respectively.

The big difference with the interacting Green's function is that the self-energy might not be a Hermitian matrix. Indeed, let us decompose the latter into its Hermitian and anti-Hermitian parts

$$\Sigma(\omega, \boldsymbol{k}) = \frac{1}{2}\Big(\Sigma(\omega, \boldsymbol{k}) + \Sigma(\omega, \boldsymbol{k})^\dagger\Big) + \frac{1}{2}\Big(\Sigma(\omega, \boldsymbol{k}) - \Sigma(\omega, \boldsymbol{k})^\dagger\Big) = \Sigma_{\mathsf{H}}(\omega, \boldsymbol{k}) + \Sigma_{\mathsf{AH}}(\omega, \boldsymbol{k}). \tag{5.14}$$

If only the Hermitian part $\Sigma_{\mathsf{H}}(\omega, \boldsymbol{k})$ plays a role, then the effect will be to renormalize the bands and Bloch states, but a well-defined band structure is still present. However, if the anti-Hermitian part is non-zero, then it will introduce dissipation into the system, and the band structure will not be well-defined.

5.4 . Spectral function

The last object we introduce in this chapter is the spectral function, a generalization of the notion of density of states, valid in the non-interacting limit. Considering a band structure described by

$$H_0(\boldsymbol{k}) = \sum_{n=1}^{N} \epsilon_n(\boldsymbol{k}) c^\dagger_{\boldsymbol{k}n} c_{\boldsymbol{k}n}, \tag{5.15}$$

the local density of states of the n-th band $\rho_n(\omega, \boldsymbol{k})$ is defined as

$$\rho_n(\omega, \boldsymbol{k}) = \delta\big(\hbar\omega - \epsilon_n(\boldsymbol{k})\big). \tag{5.16}$$

We can express the density of states purely in terms of the Green's function G_0. Indeed,

$$\langle u_n(\boldsymbol{k})|\, G_0(\omega,\boldsymbol{k})\, |u_n(\boldsymbol{k})\rangle = \lim_{\eta\to 0^+} \langle u_n(\boldsymbol{k})|\, \frac{1}{\hbar\omega\mathbb{1} - H_0(\boldsymbol{k}) + i\eta\mathbb{1}}\, |u_n(\boldsymbol{k})\rangle = \lim_{\eta\to 0^+} \frac{1}{\hbar\omega - \epsilon_n(\boldsymbol{k}) + i\eta} \tag{5.17a}$$

Making use of the Sokhotski–Plemelj formula with $\mathscr{P}$ the principal value [159], we get

$$\lim_{\eta\to 0^+} \frac{1}{\hbar\omega - \epsilon_n(\boldsymbol{k}) + i\eta} = \mathscr{P}\left[\frac{1}{\hbar\omega - \epsilon_n(\boldsymbol{k})}\right] - i\pi\delta\big(\hbar\omega - \epsilon_n(\boldsymbol{k})\big), \tag{5.18}$$

thereby implying

$$\rho_n(\omega,\boldsymbol{k}) = \delta\big(\hbar\omega - \epsilon_n(\boldsymbol{k})\big) = -\frac{1}{\pi}\,\mathrm{Im}\,\langle u_n(\boldsymbol{k})|\, G_0(\omega,\boldsymbol{k})\, |u_n(\boldsymbol{k})\rangle\,. \tag{5.19}$$

Replacing G_0 by its interacting counterpart G then yields the *spectral function*[2],

$$\mathcal{A}_n(\omega,\boldsymbol{k}) = -\frac{1}{\pi}\,\mathrm{Im}\,\langle u_n(\boldsymbol{k})|\, G(\omega,\boldsymbol{k})\, |u_n(\boldsymbol{k})\rangle\,. \tag{5.20}$$

While the spectral function does not actually define a local density of states, it can practically be seen as a related quantity.

A paradigmatic example of spectral function is in the case of *spectral broadening*, which occurs for the self-energy $\Sigma(\omega,\boldsymbol{k}) = -i\Gamma_n\mathbb{1}$, expressed in the band basis. In that case one may rapidly show that

$$\mathcal{A}_n(\omega,\boldsymbol{k}) = \frac{1}{\pi}\frac{\Gamma_n}{\big(\hbar\omega - \epsilon_n(\boldsymbol{k})\big)^2 + \Gamma_n^2}, \tag{5.21}$$

which thus appears as a Lorentzian peak of width Γ_n and centered at $\hbar\omega = \epsilon_n(\boldsymbol{k})$.

[2]Note that while we use a similar notation as for the Berry connection, this does not introduce ambiguity as we will not use both objects at the same time in this manuscript

Part II

Normal State quantum geometry and superconductivity

Introduction

In Chapter 4 we have seen that in the BCS paradigm of superconductivity, the superconducting phase is formed by Cooper pairs. These Cooper pairs are formed by electrons with energies near the Fermi level, subject to a net attractive interaction between electrons, thereby triggering a Cooper instability of the Fermi sea. However, there is a subtle caveat in this paradigm. A more precise statement would be that *Cooper pairs are formed by the charge carriers of the normal state*. While this may appear as nothing but a turgid and trivial change, it possesses a physical meaning.

We have argued in Chapter 1 that the states describing a perfect crystal, are the Bloch states, which *emerge* from the electron-nuclei Coulomb interaction. As emergent *quasiparticles*, the Bloch fermions have differences with the elementary electrons, which we encapsulated in the term *quasiness*. As seen in Chapter 2, an example of such a difference is band quantum geometry. If we consider the Bloch fermions to be the charge carriers of the normal state, then the quasiness of the Bloch fermions, and notably their quantum geometry, may impact the superconducting phase. We may thus formulate the following questions: *What if Cooper pairs are formed by Bloch fermions, instead of elementary electrons ? Does their quantum geometry, the normal state quantum geometry, affect the superconducting phase ? If so, how ?*

We may formulate a naive answer to this question. In the vast majority of superconductors, their normal state only has one band crossing the Fermi level. Exceptions to this, dubbed *multiband superconductors*, are but a few, with the notable example of MgB_2 [160, 161]. Aside from these exceptions, we may consider a superconductor whose normal state has a single band crossing the Fermi level. As the attractive interaction is only present for states close to the Fermi level, only a single band will be involved in the superconducting phase. We may thus naively want to project the Bloch Hamiltonian H_0 to the band of interest: $H_0 \longmapsto \tilde{H}_{0,n} = \epsilon_n |u_n\rangle \langle u_n|$. Then the usual BCS theory can be applied and the pairing of Bloch fermions reduces to the standard pairing of electrons, albeit with a different dispersion ϵ_n. However, from the expression of the QGT

$$Q^n_{\mu\nu} = \langle \partial_\mu u_n | \left(\mathbb{1} - |u_n\rangle \langle u_n| \right) |\partial_\nu u_n\rangle \,, \tag{5.22}$$

we see that for the QGT $\tilde{Q}^n_{\mu\nu}$ associated with $\tilde{H}_{0,n}$ we have $\mathbb{1} = |u_n\rangle \langle u_n|$, which implies $\tilde{Q}^n_{\mu\nu} = 0$. In other words, the projection to a single band $H_0 \longmapsto \epsilon_n |u_n\rangle \langle u_n|$ completely washes away its quantum geometry.[3]

The failure of this naive argument may be understood from the viewpoints presented in Chapter 2. From the third viewpoint described in Section 2.4.3, we know that the quantum geometry of a Bloch fermion, and thus its quasiness, relies on virtual interband transitions. That is to say, the different Bloch fermions are inherently linked to each other, and focusing on only one amounts to reducing it to an elementary electron, albeit with a different energy dispersion. Although one band is involved in the superconducting state, the presence of other bands in the normal state gives additional properties to the band in question, notably a quantum geometry. This *normal state quantum geometry* may thus *a priori* affect the superconducting state.

[3] This being said, we argue in Chapter 8 that there is a way to make this projection while keeping track of the quantum geometry of the band of interest

Finally, we may alternatively understand the problem using the Bogoliubov-de Gennes Hamiltonian, as depicted in Fig.5.1. We can then differentiate the pairing of electrons and that of Bloch

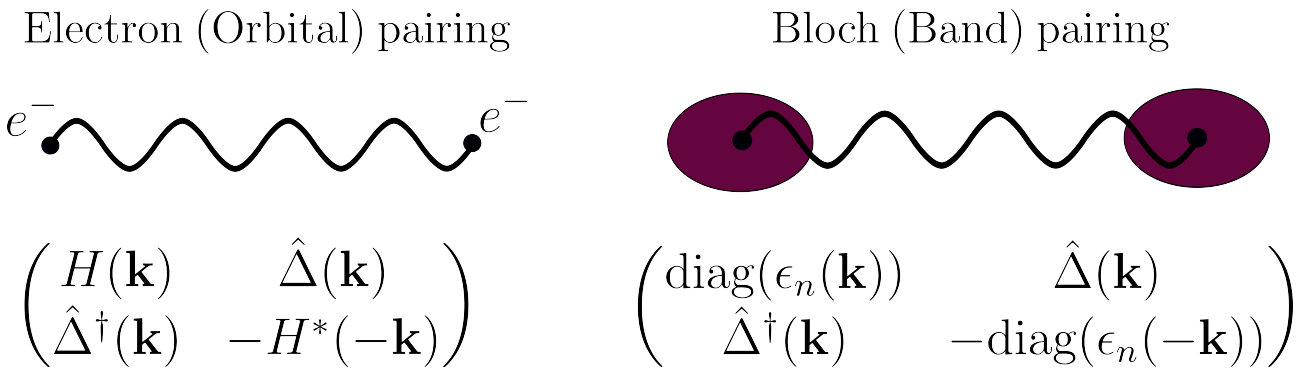

Figure 5.1: BdG Hamiltonians in both the orbital and band representations

fermions by writing the BdG Hamiltonian in two different ways. On one hand, if we consider pairing between different electrons, i.e. different orbitals, we then write the BdG Hamiltonian in the orbital basis, as pictured on the left of Fig.5.1. On the other hand, if we directly consider a pairing between Bloch fermions, we will then write the BdG Hamiltonian in the band basis, as pictured on the right of Fig.5.1. As they are related by a momentum dependent unitary transformation, the two representations may not yield the same quantum geometric and topological properties. In other words, putting the attractive interaction between electrons or Bloch fermions does not *a priori* represent the same physical situation. The relation between the two representations is discussed in more detail in Ref. [162], where it is shown that the difference gives rise to the geometric superfluid weight.

The goal of this part of the manuscript is to study the influence of the normal state quantum geometry on the superconducting state. This is done in three different projects. The first, presented in Chapter 6, studies the influence of the normal state Berry curvature in two-dimensional Dirac fermions. By applying a Foldy-Wouthuysen transformation and the generalized Peierls substitution, we can perturbatively reduce the two-band model to a single-band one while still keeping track of Berry curvature corrections. This allows us to revisit the Cooper problem as well as BCS theory. We find that the pairing interaction is weakened by the Berry curvature, due to an emergent Darwin term. We study how the critical temperature and superconducting gaps are changed, and finally propose an experimental test. In the second project, presented in Chapter 7, we compute the superfluid weight, where a contribution coming from the normal state quantum metric was discovered, in the case of (111) oxide interfaces. Based on a tight-binding modeling of the interface, we develop a low-energy model that allows us to directly compute the superfluid weight, and to qualitatively discuss its dependence on the chemical potential. Based on experimental data relating the chemical potential to the gate voltage, we argue that the interface displays a two-dome behavior. The first dome, at low gate-voltage, is due to the conventional contribution while the second, at higher gate-voltage, is due to the geometrical contribution. From Chapters 6 and 7, we may infer that there is a normal state curvature-metric competition towards superconductivity. Indeed, we have shown, in a relatively simple example, that the Berry curvature weakens superconductivity while the quantum metric has a good influence on it, as it offers another source of supercurrent. In Chapter 8 we aim to resolve

this matter, by finding a physical intuition for both the Berry curvature and quantum metric effects. We do so based on the first and second viewpoints, presented in Sections 2.4.1 and 2.4.2. We find an intuitive interpretation of the quantum metric superfluid weight, and generalize the renormalization of the pairing interaction. Remarkably, both effects appear to come from the quantum metric and are actually two sides of the same coin. Indeed, both effects stem from the non-locality of the Bloch fermion, thereby revealing the importance of its quasiness and the ambivalence of the effect of normal state quantum geometry on superconductivity.

Finally, we present some perspectives, and relate this part of the manuscript to the general problem of the effect of non-interacting quantum geometry on interacting phases. We emphasize that we do not investigate topological superconductivity [163], which is actually a larger subject. We further discuss relation of the normal state quantum geometry and topological superconductivity when discussing perspectives of our work, in Chapter 8.5. The results presented in Chapters 6 and 7 have been published in two scientific papers, namely Refs. [1, 2] respectively.

6 - Normal state Berry curvature in two-dimensional massive Dirac fermions

6.1 . Introduction

A large variety of superconducting materials, dubbed *conventional*, can be theoretically understood within BCS theory, described in Chapter 4. In the latter, the normal state considered is that of a single, partially filled band from which Cooper pairs are formed by a weak attraction, while other bands are discarded based on the premise that they are much more remote in energy than the typical energy scale set by the attractive interaction. As we also described in Chapter 4, conventional superconductivity stems from electron-phonon coupling. Within the weak-coupling limit, the typical energy scale for superconductivity is then a fraction of the Debye temperature $k_B T_D$ that is itself in the $10-100$ meV range, while the Fermi energy and the typical band gaps are on the order of ~ 1 eV [7]. This disparity between the two energy scales justifies to discard all other bands of the normal state, and tempts one to project them out, as argued in the introduction to Part II.

While the above-mentioned energy-scale consideration has remained unchallenged for a long time, the advent of topological band theory [16, 164] and its success in the theoretical description of a plethora of materials [165], such as topological insulators [121, 166], topological superconductors [35, 163], Weyl and Dirac semimetals [167], has shown that the coupling between energy bands is not only governed by energy scales but by more subtle geometric quantities, such as the Berry curvature or the quantum metric. Indeed as argued in the introduction of Part II, projecting the other bands out neglects the geometry of the band of interest. Several recent papers have investigated the role of the latter, namely in the presence of flat bands in which the quantum metric can be the dominant contribution to the superfluid weight [29, 168, 169, 170]. The Berry curvature has been theoretically shown to play a relevant role in a two-body problem that is closely related to the Cooper pair, namely in the physics of excitons. For example, in two-dimensional (2D) semiconducting transition-metal dichalcogenides (TMDC) [171], excitons – bound electron-hole pairs – are formed in the vicinity of the K and K' points of the first Brillouin zone, where the Berry curvature reaches its maximal value [172]. Experimentally, a first hint to the relevance of band-geometric effects came from the failure of the effective hydrogen model, which had been extremely successful before in the theoretical understanding of the measured exciton spectra [173, 174]. It was later shown that the Berry curvature affects the exciton spectra, contrary to the one-particle case, because it couples to the electric field that is generated by the attractive interaction between the electron and the hole forming the bound exciton state [59, 62, 63, 175]. This is a consequence of the intrinsic Dirac character of the low-energy charge carriers in these materials, which are commonly described in terms of a 2D massive Dirac equation [176, 177]. Excitons in 2D TMDC and potentially other bound pairs inherit then this Dirac character [178].

Based on the above-mentioned exciton example, it is therefore natural to consider that the Berry curvature might also affect the formation of the Cooper pair due to the mutual interaction between the two electrons. This is the main motivation of the present theoretical study, where we show that

the effective electron-electron interaction is generically weakened when one includes energy terms in the Hamiltonian that take into account the effect of the Berry curvature. We consider conventional BCS-type superconductivity in 2D materials, such as the above-mentioned 2D semiconducting TMDC for a moderate doping range. As discussed in Section 2.4.5, the Berryology of a band may be introduced via the generalized Peierls substitution $\boldsymbol{r} \mapsto \boldsymbol{r} + \mathcal{A}_n(\boldsymbol{k})$. This yields a dipole that interacts with the electric field, and this dipolar structure, which the Cooper pair inherits, is at the origin of the weakened Cooper pairing. More precisely, the projection yields two extra terms which affect the electron-electron interaction to the one-body Hamiltonian. One of them is reminiscent of the spin-orbit coupling if one interprets the Berry curvature in terms of a spin, and the second one corresponds to the Darwin term, which arises within a Dirac-fermion treatment of the two bands in the vicinity of the direct gap [179]. We show that the latter is responsible for a reduced effective BCS coupling constant that results in a smaller superconducting BCS gap, while the former spin-orbit-type term does not play a role in s-wave nor other types of pure singlet or triplet pairing.

The chapter is organized as follows. In Sec. 6.2, we briefly introduce the model we will consider. It is an extension of the model of massive Dirac fermions which we presented in Chapter 1, where spin-orbit coupling induced spin-valley locking induces additional complexity [176]. In Sec. 6.3, we briefly revisit, along the lines exposed in Ref. [63], the emergence of corrective terms to the one-body Hamiltonian of a charge projected to a single band. We present two complementary approaches: one based on the generalized Peierls substitution in Sec. 6.3.2 and one in Sec. 6.3.1 based on a treatment within the continuum two-band model of massive Dirac fermions in the vicinity of the direct gap, where the role of the Berry curvature is most prominent. This treatment is the basis of the two-body problem, which we present in Sec. 6.4. After some general considerations in Sec. 6.4.1, Sec. 6.4.2 shows how the Cooper pair and its binding energy are modified by the extra terms, while Sec. 6.5 presents the BCS theory of conventional s-wave-type superconductivity in the presence of the corrective terms due to the Berry curvature. In the calculations, we consider a Fermi level that is extremely close to the conduction-band bottom, and we discuss then the role of stronger doping on Cooper pairing and BCS superconductivity in Sec. 6.6. In Sec. 6.7, we briefly discuss how our theoretical picture of superconductivity in the presence of non-zero Berry curvature evolves in other pairing symmetries, be they singlet or triplet. Finally, in Section 6.8 is devoted to possible experimental implications of our theoretical studies. There, we compare the superconducting gap and the critical temperature in the absence and the presence of the weakened interaction due to the Berry curvature.

6.2 . Model of interest

The low-energy Hamiltonian we will consider is a $\boldsymbol{k} \cdot \boldsymbol{p}$ Hamiltonian coming from transition metal dichalcogenides [180]. The two-band model is written as [11]

$$H = \boldsymbol{h}(\boldsymbol{k}) \cdot \boldsymbol{\sigma} = |\Delta_\tau| \begin{pmatrix} \operatorname{sgn} \Delta_\tau & \lambda\!\!\!^{-}_\tau(\tau k_x - i k_y) \\ \lambda\!\!\!^{-}_\tau(\tau k_x + i k_y) & -\operatorname{sgn} \Delta_\tau \end{pmatrix}, \tag{6.1}$$

where $\tau = \xi\sigma$ is the product of the spin and valley indices, noted as σ and ξ, respectively. The fact that the model depends only on their product is a consequence of inversion symmetry breaking and atomic spin-orbit coupling [181]. Additionally, $\lambda\!\!\!^{-}_\tau = \hbar v/|\Delta_\tau|$ is the reduced Compton wave-

length and $\boldsymbol{h}(\boldsymbol{k}) = |\Delta_\tau|\big(\tau\lambda_\tau k_x, \lambda_\tau k_y, \operatorname{sgn}\Delta_\tau\big)$. H therefore represents a slightly more complex case of two-dimensional massive Dirac fermions. The energy spectrum is given by

$$\epsilon_{n\tau}(\boldsymbol{k}) = n|\Delta_\tau|\sqrt{1+\lambda_\tau^2 k^2}, \quad n = \pm 1. \tag{6.2}$$

$n = -1(+1)$ represents the valence (conduction) band, which are the analogs of positrons and electrons in high-energy physics, respectively. The dispersions in the two valleys are pictured in Fig.6.1. As for the quantum geometry, the calculation done in appendix B.4 still holds, and we thus have

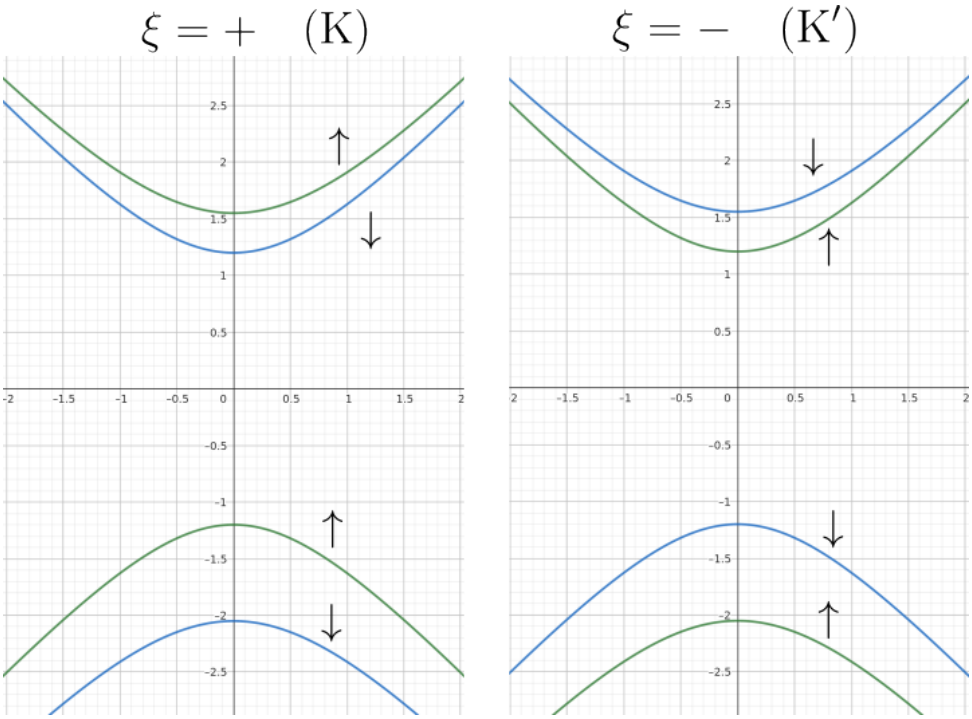

Figure 6.1: Band dispersions of two-dimensional massive Dirac fermions in the valleys K ($\xi = +1$) and K' ($\xi = -1$). For illustration, we include the spin splitting due to additional types of spin-orbit coupling [181].

$$g_{\mu\nu}^{n\tau} = \frac{\lambda_\tau^2}{4}\frac{(1+\lambda_\tau^2 k^2)\delta_{\mu\nu} - \lambda_\tau^2 k_\mu k_\nu}{(1+\lambda_\tau^2 k^2)^2}, \quad \mathcal{B}_{n\tau} = -\frac{n\tau\operatorname{sgn}\Delta_\tau}{2}\frac{\lambda_\tau^2}{(1+\lambda_\tau^2 k^2)^{3/2}}. \tag{6.3}$$

6.3 . Effective single-band Hamiltonian

BCS theory being traditionally formulated in a single-band manner, we aim here to find an effective single-band Hamiltonian that takes into account the Berry curvature. We will consider pairing in the conduction band.

6.3.1 . Pauli Hamiltonian

Consider the model written in Eq. (6.1) upon which we add an external potential $V(\boldsymbol{r})\sigma_0$,

$$H = |\Delta_\tau|\lambda\!\!\!^{-}_\tau k_x\sigma_x + |\Delta_\tau|\lambda\!\!\!^{-}_\tau k_y\sigma_y + \Delta_\tau\sigma_z + V(\boldsymbol{r})\sigma_0. \tag{6.4}$$

For now, we will consider the case where the pairing is happening near the bottom of the conduction band. We thus assume a regime where $\lambda\!\!\!^{-}_\tau k \ll 1$. This is equivalent to a quasi-classical regime, where a Foldy-Wouthuysen transformation can be used to pertubatively project out the valence band. We thus make use of this (time-independent) transformation, which will give us an effective single-band model in the form of a Pauli Hamiltonian. The transformed Hamiltonian H', via the Hermitian generator S, reads

$$H_P = e^{iS}He^{-iS} = \sum_{n=0}^{+\infty}\frac{i^n}{n!}\,\mathrm{ad}_S^n\,H, \tag{6.5}$$

with $\mathrm{ad}_S\,H = [S,H]$. S is then chosen such that $[S,\Delta_\tau\sigma_z]$ cancels the off-diagonal terms of H [179, 182], with $\lambda\!\!\!^{-}_\tau$ being the perturbative parameter. The expansion in nested commutators to second order then yields the Pauli Hamiltonian H_P, which in our case reads [179, 182]

$$H_P = \Delta_\tau + \frac{1}{2}\Delta_\tau\lambda\!\!\!^{-2}_\tau k^2 + V(\boldsymbol{r}) - \tau\,\mathrm{sgn}\,\Delta_\tau\frac{\lambda\!\!\!^{-2}_\tau}{4}(\boldsymbol{e}_z\times\boldsymbol{k})\cdot\partial_{\boldsymbol{r}}V + \frac{\lambda\!\!\!^{-2}_\tau}{8}\partial^2_{\boldsymbol{r}}V, \tag{6.6}$$

which indeed has the form of the Pauli Hamiltonian [179, 182]. We can make the Berry curvature of the conduction band appear explicitly through its value at $k=0$, $\boldsymbol{\mathcal{B}}_\tau(0) = \boldsymbol{\mathcal{B}}_{+\tau}(0) = -\tau\,\mathrm{sgn}\,\Delta_\tau\lambda\!\!\!^{-2}_\tau/2\boldsymbol{e}_z$,

$$H_P = \Delta_\tau + \frac{1}{2}\Delta_\tau\lambda\!\!\!^{-2}_\tau k^2 + V + \frac{1}{2}\big(\boldsymbol{\mathcal{B}}_{\boldsymbol{n}\tau}(0)\times\boldsymbol{k}\big)\cdot\partial_{\boldsymbol{r}}V + \frac{1}{4}|\mathcal{B}_\tau(0)|\partial^2_{\boldsymbol{r}}V. \tag{6.7}$$

Eq. (6.7) appears in similar forms in Refs. [59, 63]. The terms are readily interpreted analogously to the case of vacuum electrons [179, 182]. The first two terms and the third are the band dispersion $\epsilon_{+\tau}$ expanded to order $\mathcal{O}(\lambda\!\!\!^{-4}_\tau)$ and the potential V, respectively. The fourth term is an emergent spin-orbit coupling, where interestingly the Berry curvature appears as an emergent spin. This is coherent with Section 2.4.5 where we argued that the Berry curvature is an emergent helicity axis of the Bloch wavepacket, giving rise to a drift velocity responsible for anomalous Hall effects. And indeed we will see in Section 6.4 that this emergent spin-orbit coupling gives rise to Karplus-Luttinger drift velocities. The last term is the Darwin term, which can be interpreted following Sections 2.4.2 and 2.4.3. Due to erratic *virtual* interband transitions, the Bloch wavepacket cannot be localized on a length smaller than the length traveled by such transitions during their lifetime (as they are virtual, they have no physical meaning, and our theory does not apply to smaller lengthscales). Such a lengthscale is provided here by the Compton length $\lambda\!\!\!^{-}_\tau$. The Bloch wavepacket being non-local, the external potential V gets smeared by an emergent Darwin term. The interpretation is therefore fully analogous to the case of vacuum electrons.

Nevertheless while the interpretations are similar, the physical consequences may be different. Indeed for vacuum electrons, as with excitons [59, 63], V is usually taken to be the Coulomb repulsion, for which $\partial^2_{\boldsymbol{r}}V \propto \delta(\boldsymbol{r})$. Consequently, only wavefunctions $\psi(\boldsymbol{r})$ for which $\psi(\boldsymbol{r}) \neq 0$ are affected by the Darwin term. However here we will take V to be the pairing interaction, whose Laplacian is not the Dirac delta. Therefore, the s-wave pairing state will not *a priori* be the only one affected by the emergent Darwin term. And we will see in Section 6.7 that it is indeed the case.

6.3.2 . Generalized Peierls substitution

In this section we aim to provide a complementary insight into the corrective terms involving the Berry curvature of the conduction band, by using the generalized Peierls substitution.

Let us first recall how to incorporate the magnetic field to describe the dynamics of an electron in the n-th band $E_n(\boldsymbol{k})$ via the Peierls substitution (in the absence of a Berry curvature). Because the wave vector $\boldsymbol{k} = -i\partial_{\boldsymbol{r}}$ is not a gauge-invariant quantity, it needs to be replaced by its gauge-invariant form

$$\hbar\boldsymbol{k} \longrightarrow \boldsymbol{\Pi} = \hbar\boldsymbol{k} + e\boldsymbol{A}(\boldsymbol{r}), \tag{6.8}$$

in terms of the vector potential $\boldsymbol{A}(\boldsymbol{r})$ which yields the magnetic field, $\boldsymbol{B}(\boldsymbol{r}) = \partial_{\boldsymbol{r}} \times \boldsymbol{A}(\boldsymbol{r})$. We consider, here, electrons of charge $-e$ ($e > 0$). From a semi-classical point of view, one obtains the equations of motion

$$\dot{\boldsymbol{r}}_n = \boldsymbol{v}_n = \frac{1}{\hbar}\partial_{\boldsymbol{k}} E_n \qquad \text{and} \qquad \hbar\dot{\boldsymbol{k}} = -e\boldsymbol{v}_n \times \boldsymbol{B}, \tag{6.9}$$

where $\boldsymbol{r}_n$ and $\boldsymbol{v}_n$ are the average position and velocity, respectively, of the electron in the n-th band. One justification of the Peierls substitution is that the Hamiltonian thus obtained, $H(\boldsymbol{\Pi}) = E_n(\boldsymbol{\Pi})$, yields the same equations of motion if one uses the *quantum* Heisenberg equations of motion

$$i\hbar\dot{\Pi}_j = [\Pi_j, H(\boldsymbol{\Pi})], \tag{6.10}$$

with the help of the commutation relations $[\Pi_x, \Pi_y] = -i\hbar^2/l_B^2$, in terms of the magnetic length $l_B = \sqrt{\hbar/eB}$. Indeed, one then obtains

$$\dot{\Pi}_j = -\frac{\hbar}{l_B^2}\epsilon_{jl}\frac{\partial H}{\partial \Pi_l}, \tag{6.11}$$

where ϵ_{jl} is the antisymmetric Levi-Civita tensor. The quantum Hamiltonian $H(\boldsymbol{\Pi})$ yields therefore Heisenberg equations of motion that are the same as the semi-classical ones if we identify the (semi-classical) wave vector $\boldsymbol{k}$ with the gauge-invariant quantity $\boldsymbol{\Pi}/\hbar$, as it is precisely stipulated by the Peierls substitution.

The generalized Peierls substitution follows the same spirit when considering a system with a non-zero Berry curvature in the presence of a spatially varying potential $V(\boldsymbol{r})$, thus starting from the band energy $H_n = E_n(\boldsymbol{k}) + V(\boldsymbol{r})$. In this case, the semi-classical equations of motion read [16, 64]

$$\dot{\boldsymbol{r}}_n = \boldsymbol{v}_n = \frac{1}{\hbar}\partial_{\boldsymbol{k}} E_n + \frac{1}{\hbar}\partial_{\boldsymbol{r}} V(\boldsymbol{r}) \times \boldsymbol{\mathcal{B}}_n(\boldsymbol{k}) \tag{6.12}$$

$$\text{and} \qquad \hbar\dot{\boldsymbol{k}} = -\partial_{\boldsymbol{r}} V - e\boldsymbol{v}_n \times \boldsymbol{B}, \tag{6.13}$$

where $\boldsymbol{\mathcal{B}}_n(\boldsymbol{k}) = \partial_{\boldsymbol{k}} \times \mathcal{A}_n(\boldsymbol{k})$ is the Berry curvature of the n-th band in terms of its Berry connection $\mathcal{A}_n(\boldsymbol{k})$. Similarly to the case discussed above, one can obtain these equations of motion from a *quantum* Hamiltonian

$$H(\boldsymbol{\Pi}, \boldsymbol{R}) = E_n(\boldsymbol{\Pi}) + V(\boldsymbol{R}), \tag{6.14}$$

where we have replaced not only the wave vector by its gauge-invariant expression (6.8) but also the position by its expression projected onto the n-th band [16, 64, 183]

$$\boldsymbol{r} \longrightarrow \boldsymbol{R} = \boldsymbol{r} + \boldsymbol{\mathcal{A}}_n(\boldsymbol{k}), \tag{6.15}$$

which involves the Berry connection $\mathcal{A}_n(\boldsymbol{k})$. Similarly to the Peierls substitution (6.8), the position $\boldsymbol{r}$ on the right-hand-side of this expression should be interpreted as a reciprocal-space derivative $\boldsymbol{r} = i\partial_{\boldsymbol{k}}$. The replacement (6.15) may be viewed as a *generalized Peierls substitution* [58, 59, 60, 61, 63]. The semi-classical equations of motion are then retrieved as the Heisenberg equations of motion not only for $\boldsymbol{\Pi}$ but also for $\boldsymbol{R} = (X, Y)$ on the basis of the Hamiltonian (6.14) and the induced commutation relations $[X, Y] = i\mathcal{B}_n(\boldsymbol{k})$ [63].

Let us now discard the magnetic field, which we have only discussed in order to remind the reader of the Peierls substitution and to justify its generalized form, and expand the Hamiltonian (6.14) to lowest order in the Berry connection. This expansion is legitimate as long as the external potential $V(\boldsymbol{r})$ varies slowly on a length scale that is set, in orders of magnitude, by the Berry connection and that can be related to the Compton length, as we discuss below. The Hamiltonian then becomes

$$H = E_n(\boldsymbol{k}) + V(\boldsymbol{r}) + \boldsymbol{\mathcal{A}}_n(\boldsymbol{k}) \cdot \partial_{\boldsymbol{r}} V(\boldsymbol{r}). \tag{6.16}$$

The last generated term is interesting. First, it can be interpreted as the energy of an electric dipole $-e\boldsymbol{\mathcal{A}}_n(\boldsymbol{k})$ in an electric field $\boldsymbol{E}(\boldsymbol{r}) = \partial_{\boldsymbol{r}} V(\boldsymbol{r})/e$. We therefore call this term the *Berry dipole term*. Second, this term can be understood as an effective spin-orbit coupling if we use the *symmetric gauge* for the Berry connection

$$\boldsymbol{\mathcal{A}}_n(\boldsymbol{k}) = \frac{1}{2}\boldsymbol{\mathcal{B}}_n(\boldsymbol{k}) \times \boldsymbol{k}, \tag{6.17}$$

in which case the corrective term reads

$$\boldsymbol{\mathcal{A}}_n(\boldsymbol{k}) \cdot \partial_{\boldsymbol{r}} V(\boldsymbol{r}) = \frac{1}{2}\big(\boldsymbol{\mathcal{B}}_n(\boldsymbol{k}) \times \boldsymbol{k}\big) \cdot \partial_{\boldsymbol{r}} V(\boldsymbol{r}). \tag{6.18}$$

The Berry dipole then harbors a similar form as the emergent spin-orbit coupling term obtained in Eq. (6.7). The Berry curvature thus once more appears as an *emergent spin*, even though it is often viewed as an *emergent magnetic field*.

6.3.3 . Effective Hamiltonian

Following sections 6.3.1 and 6.3.2, we adopt the following single-band effective Hamiltonian for the conduction band,

$$H = \Delta_\tau + \frac{1}{2}\Delta_\tau \lambda_\tau^2 k^2 + V + \frac{1}{2}\big(\boldsymbol{\mathcal{B}}_\tau(\boldsymbol{k}) \times \boldsymbol{k}\big) \cdot \partial_{\boldsymbol{r}} V + \frac{1}{4}|\mathcal{B}(0)|\partial_{\boldsymbol{r}}^2 V, \tag{6.19}$$

where we have taken the spin-orbit coupling term coming the generalized Peierls substitution.

6.4 . Two-body problem

We now consider two Bloch fermions, with spin-valley locked indices $\tau_1 = \xi_1\sigma_1$ and $\tau_2 = \xi_2\sigma_2$, as well as positions $\boldsymbol{r}_1, \boldsymbol{r}_2$ and momentum $\boldsymbol{k}_1, \boldsymbol{k}_2$. For simplicity we consider $\tau_1 = \tau_2 = \tau$, i.e. Bloch fermions with both equal spin and opposite valleys or opposite spin and equal valleys. On top of that, the two Bloch fermions are subject to a potential V depending only on their relative position $\boldsymbol{\rho} = \boldsymbol{r}_1 - \boldsymbol{r}_2$, as is the case for the BCS potential. The two-body Hamiltonian then reads

$$H_2 = 2\Delta_\tau + \Delta_\tau \lambda_\tau^2 \frac{k_1^2 + k_2^2}{2} + V(\boldsymbol{\rho}) + \frac{1}{2}\Big(\boldsymbol{\mathcal{B}}_\tau(\boldsymbol{k}_1) \times \boldsymbol{k}_1 + \boldsymbol{\mathcal{B}}_\tau(\boldsymbol{k}_2) \times \boldsymbol{k}_2\Big) \cdot \partial_{\boldsymbol{\rho}} V + \frac{1}{2}|\mathcal{B}(0)|\partial_{\boldsymbol{\rho}}^2 V. \tag{6.20}$$

We will consider the two-body problem in two steps. We will begin by studying the general case, notably through its Heisenberg equations of motion and we follow up with the special case where the two bodies have opposite momenta, i.e. the Cooper problem.

6.4.1 . General case

Motivated by the fact hat the potential V only depends on $\boldsymbol{\rho}$, we introduce the relative and center-of-mass (CoM) coordinates,

$$\text{Relative}: \quad \boldsymbol{\rho} = \boldsymbol{r}_1 - \boldsymbol{r}_2, \qquad \boldsymbol{k} = \frac{\boldsymbol{k}_1 - \boldsymbol{k}_2}{2}, \tag{6.21a}$$

$$\text{CoM}: \quad \boldsymbol{R} = \frac{\boldsymbol{r}_1 + \boldsymbol{r}_2}{2}, \qquad \boldsymbol{K} = \boldsymbol{k}_1 + \boldsymbol{k}_2. \tag{6.21b}$$

Converting Eq. (6.20) in this frame yields

$$H_2 = 2\Delta_\tau + \Delta_\tau \frac{\lambda\!\!\!^{-2}_\tau}{4} K^2 + \Delta_\tau \lambda\!\!\!^{-2}_\tau k^2 + \frac{1}{4}\Big(\boldsymbol{\Lambda}^+_\tau(\boldsymbol{K},\boldsymbol{k}) \times \boldsymbol{K}\Big) \cdot \partial_{\boldsymbol{\rho}} V + \frac{1}{2}\Big(\boldsymbol{\Lambda}^-_{\tau_1\tau_2}(\boldsymbol{K},\boldsymbol{k}) \times \boldsymbol{k}\Big) \cdot \partial_{\boldsymbol{\rho}} V + \frac{1}{2}|\mathcal{B}(0)|\partial^2_{\boldsymbol{\rho}} V, \tag{6.22}$$

where

$$\boldsymbol{\Lambda}^\pm_\tau(\boldsymbol{K},\boldsymbol{k}) = \boldsymbol{\mathcal{B}}_\tau\left(\frac{\boldsymbol{K}+2\boldsymbol{k}}{2}\right) \pm \boldsymbol{\mathcal{B}}_\tau\left(\frac{\boldsymbol{K}-2\boldsymbol{k}}{2}\right). \tag{6.23}$$

It is interesting to notice that, when moving to CoM/relative coordinates, the Berry dipole term splits into two dipoles acting on the Bloch pair. One is associated with its *center-of-mass motion* and the *sum* of the two Berry curvatures and the other is associated with its *relative motion* and the *difference* of the two Berry curvatures. To gain further insight into the physical meaning of these two terms, we can calculate the Heisenberg equations of motion,

$$\dot{\boldsymbol{K}} = 0, \qquad \dot{\boldsymbol{R}} = \frac{\lambda\!\!\!^{-2}_\tau}{2\hbar}\boldsymbol{K} + \frac{1}{4\hbar}\partial_{\boldsymbol{\rho}} V \times \boldsymbol{\Lambda}^+_\tau(\boldsymbol{K},\boldsymbol{k}), \tag{6.24a}$$

$$\dot{\boldsymbol{k}} = -\frac{1}{\hbar}\partial_{\boldsymbol{\rho}} H_2, \quad \dot{\boldsymbol{\rho}} = \frac{\lambda\!\!\!^{-2}_\tau}{\hbar}\boldsymbol{k} + \frac{1}{2\hbar}\partial_{\boldsymbol{\rho}} V \times \boldsymbol{\Lambda}^-_\tau(\boldsymbol{K},\boldsymbol{k}). \tag{6.24b}$$

The CoM momentum is a conserved quantity, owing to the fact that H_c does not depend on $\boldsymbol{R}$. We also see that the two dipoles induce two Karplus-Luttinger-type velocities: Λ_+, which is associated to the CoM dipole, generates a drift velocity of the CoM coordinate, and Λ^-, which is associated with the relative dipole, yields another drift velocity of the relative coordinate of the Bloch pair.

It is interesting to note that, from both the Hamiltonian in Eq. (6.22) and the equations of motion in Eq. (6.24b), we see that the Berry curvature indeed plays a dynamical role once potential gradients are present.[1] Electron-electron interactions are a possible source of such potential gradients. In the next section, we explore the special case where the potential V is that of the BCS interaction, thus corresponding to the Cooper problem in the two-body case.

[1] Other than the crystalline potential

6.4.2 . Cooper problem

We are now in a position to study the effect of the Berry curvature on a Cooper pair, the building block of superconductors. To do so, we revisit the Cooper problem following the lines of Ref. [131] and standard textbooks [7]. We then set $K = 0$, i.e. we consider the rest frame, so that our two-body Hamiltonian (6.20) now reads

$$H_2 = 2\Delta_\tau + \lambda_\tau^2 k^2 + V(\boldsymbol{\rho}) + \frac{1}{2}\big(\boldsymbol{\Lambda}_\tau^-(\boldsymbol{k}) \times \boldsymbol{k}\big) \cdot \partial_{\boldsymbol{\rho}} V + \frac{1}{2}|\mathcal{B}(0)|\partial_{\boldsymbol{\rho}}^2 V, \tag{6.25}$$

where we have

$$\boldsymbol{\Lambda}_\tau^-(\boldsymbol{k}) = \boldsymbol{\mathcal{B}}_\tau(\boldsymbol{k}) - \boldsymbol{\mathcal{B}}_\tau(-\boldsymbol{k}) = -\frac{\tau \operatorname{sgn}\Delta_\tau}{2}\left[\frac{\lambda_\tau^2}{(1+\lambda_\tau^2\boldsymbol{k}^2)^{3/2}} - \frac{\lambda_\tau^2}{(1+\lambda_\tau^2(-\boldsymbol{k})^2)^{3/2}}\right]\boldsymbol{e}_z = 0. \tag{6.26}$$

Therefore in the case we considered, where $\tau_1 = \tau_2 = \tau$, the Berry dipole terms of both Bloch fermions compensate each other and the relative Berry dipole vanishes. However one could have a non-zero relative Berry dipole if $\tau_1 \neq \tau_2$, i.e. inter-spin and intra-valley pairing or vice-versa, where we would have

$$\boldsymbol{\Lambda}_{\tau_1\tau_2}^-(\boldsymbol{k}) = \boldsymbol{\mathcal{B}}_{\tau_1}(\boldsymbol{k}) - \boldsymbol{\mathcal{B}}_{\tau_2}(-\boldsymbol{k}). \tag{6.27}$$

Consequently, the relative Berry dipole term only acts on Bloch pairs formed by either intra-valley and inter-spin pairings or inter-valley and intra-spin pairings. In the case where $\tau_1 = \tau_2$, the Berry curvature only appears through the Darwin term.

Let us now take a closer look at the wave function of the Cooper pair $\psi(\boldsymbol{\rho})$, which is a solution of $H_2\psi(\boldsymbol{\rho}) = E\psi(\boldsymbol{\rho})$. We then decompose ψ and V in a Fourier series

$$\psi(\boldsymbol{\rho}) = \sum_{\boldsymbol{k}} g_{\boldsymbol{k}} e^{i\boldsymbol{k}\cdot\boldsymbol{\rho}}, \tag{6.28}$$

$$V(\boldsymbol{\rho}) = \sum_{\boldsymbol{k}\boldsymbol{k}'} V_{\boldsymbol{k}\boldsymbol{k}'} e^{i(\boldsymbol{k}-\boldsymbol{k}')\cdot\boldsymbol{\rho}} \quad . \tag{6.29}$$

Physically, $g_{\boldsymbol{k}}$ is the probability amplitude of the Cooper pair being at momenta $(\boldsymbol{k}, -\boldsymbol{k})$ while the coefficient $V_{\boldsymbol{k}\boldsymbol{k}'}$ is the scattering amplitude of the Cooper pair from $(\boldsymbol{k}, -\boldsymbol{k})$ to $(\boldsymbol{k}', -\boldsymbol{k}')$. Following the steps of Ref. [7] we find a self-consistency equation for the coefficients $g_{\boldsymbol{k}}$, in terms of an *effective interaction* $V_{\boldsymbol{k}\boldsymbol{k}'}^{\text{eff}}$

$$\big[E - 2\epsilon_\tau(k)\big] g_{\boldsymbol{k}} = \sum_{\boldsymbol{k}'} V_{\boldsymbol{k}\boldsymbol{k}'}^{\text{eff}} g_{\boldsymbol{k}'}, \tag{6.30}$$

where

$$2\epsilon_\tau(k) = 2\Delta_\tau + \lambda_{\tau_1}^2 k^2. \tag{6.31}$$

The effective interaction is found to be

$$V_{\boldsymbol{k}\boldsymbol{k}'}^{\text{eff}} = \left[1 - \frac{1}{2}|\mathcal{B}(0)|\big(\boldsymbol{k} - \boldsymbol{k}'\big)^2\right] V_{\boldsymbol{k}\boldsymbol{k}'}. \tag{6.32}$$

The extension to the case where $\tau_1 \neq \tau_2$ yields

$$V_{\boldsymbol{k}\boldsymbol{k}'}^{\text{eff}} = \left[1 + \frac{i}{2}\big(\boldsymbol{\Lambda}_{\tau_1\tau_2}^-(\boldsymbol{k}) \times \boldsymbol{k}\big) \cdot \boldsymbol{k}' - \frac{1}{2}|\mathcal{B}(0)|\big(\boldsymbol{k} - \boldsymbol{k}'\big)^2\right] V_{\boldsymbol{k}\boldsymbol{k}'}. \tag{6.33}$$

This equation is one of the main results of this chapter. Qualitatively, we see that the two terms may compete with one another. The second term stems from the relative Berry dipole term and may increase or decrease the interaction potential and thus the strength of the Cooper pairing depending on the sign of $\mathbf{\Lambda}^{-}_{\tau_1\tau_2}$. As for the last (Darwin) term, it is negative irrespective of the spin-valley index, meaning that it tends to weaken the electron-electron interaction and thus the superconducting phase. On a more practical level, the above expressions tell us that the calculations for the energy of the Cooper pair in the presence of a Berry curvature are the same as in the conventional pairing case [7], but in terms of the effective interaction in Eq. (6.32).

Moving forward in the calculations, we find the following self-consistency equation on the interaction

$$\sum_{\boldsymbol{k}} \frac{\langle V^{\text{eff}}_{\boldsymbol{k}\boldsymbol{k}'}\rangle}{E - 2\epsilon_\tau(k)} = 1, \tag{6.34}$$

where we have defined the average

$$\langle \mathcal{O}(\boldsymbol{k}')\rangle = \frac{\sum_{\boldsymbol{k}'} \mathcal{O}(\boldsymbol{k}')g_{\boldsymbol{k}'}}{\sum_{\boldsymbol{k}'} g_{\boldsymbol{k}'}} \tag{6.35}$$

with respect to the weighting coefficients $g_{\boldsymbol{k}}$. The term $\langle V^{\text{eff}}_{\boldsymbol{k}\boldsymbol{k}'}\rangle$ may be rewritten as

$$\langle V^{\text{eff}}_{\boldsymbol{k}\boldsymbol{k}'}\rangle = \left(1 - \frac{1}{2}\big|\mathcal{B}(0)\big|\boldsymbol{k}^2\right)\langle V_{\boldsymbol{k}\boldsymbol{k}'}\rangle + \left(\big|\mathcal{B}(0)\big|\boldsymbol{k} + \frac{i}{2}\mathbf{\Lambda}^{-}_{\tau_1\tau_2}(\boldsymbol{k})\times\boldsymbol{k}\right)\cdot\langle \boldsymbol{k}' V_{\boldsymbol{k}\boldsymbol{k}'}\rangle - \frac{1}{2}\big|\mathcal{B}(0)\big|\langle \boldsymbol{k}'^2 V_{\boldsymbol{k}\boldsymbol{k}'}\rangle, \tag{6.36}$$

for arbitrary τ_1 and τ_2. We now specify $V_{\boldsymbol{k}\boldsymbol{k}'}$ to be the BCS potential, defined as

$$V_{\boldsymbol{k}\boldsymbol{k}'} = \begin{cases} -V < 0 & \text{if } \epsilon_F \le \epsilon_\tau(k), \epsilon_\tau(k') \le \epsilon_F + \hbar\omega_D \\ 0 & \text{otherwise,} \end{cases} \tag{6.37}$$

where ϵ_F is the Fermi energy and $\hbar\omega_D$ the Debye energy. We can compactly rewrite it as

$$V_{\boldsymbol{k}\boldsymbol{k}'} = -V\mathbb{1}_{\mathcal{D}}(\boldsymbol{k})\mathbb{1}_{\mathcal{D}}(\boldsymbol{k}') \tag{6.38}$$

where the set $\mathcal{D}$ is defined as

$$\mathcal{D} = \left\{\boldsymbol{k}\in\mathbb{R}^2 \;\middle|\; \epsilon_F \le \epsilon_\tau(k) \le \epsilon_F + \hbar\omega_D\right\}. \tag{6.39}$$

With this in mind, we write

$$\langle \boldsymbol{k}' V_{\boldsymbol{k}\boldsymbol{k}'}\rangle \propto \sum_{\boldsymbol{k}'\in\mathcal{D}} \boldsymbol{k}' V_{\boldsymbol{k}\boldsymbol{k}'} g_{\boldsymbol{k}'} \tag{6.40}$$

From Eq. (6.38) we see that $V_{\boldsymbol{k};-\boldsymbol{k}'} = V_{\boldsymbol{k}\boldsymbol{k}'}$. Moreover, for BCS s-wave superconductivity we have $g_{-\boldsymbol{k}'} = g_{\boldsymbol{k}'}$, so that $\boldsymbol{k}' V_{\boldsymbol{k}\boldsymbol{k}'} g_{\boldsymbol{k}'}$ is an odd function of $\boldsymbol{k}'$. Because summing an odd function over the set $\mathcal{D}$ gives zero[2], we have $\langle \boldsymbol{k}' V_{\boldsymbol{k}\boldsymbol{k}'}\rangle = 0$ so that *the Berry dipole term does not affect the Cooper pair*, even in the case $\tau_1 \neq \tau_2$,which is then solely affected by the Darwin term. Therefore, if we remember

[2]Since the set $\mathcal{D}$ is symmetric around the $k = 0$ point, summing an odd function over it amounts to integrating an odd function $f(k)$ in an interval of the form $[-a, a]$.

the competition between the dipolar and Darwin terms, this suggests that the effect of the Berry curvature is to weaken the Cooper pair.

Remember that $V^{\text{eff}}_{\boldsymbol{kk'}}$ is non-zero only for $\boldsymbol{k}, \boldsymbol{k'} \in \mathcal{D}$, and from the definition of $\mathcal{D}$ we rewrite the energy as $\epsilon_\tau(\boldsymbol{k}) = \epsilon_F + \eta_k \hbar\omega_D$ with $\eta_k \in [0,1]$. Furthermore, suppose that $\hbar\omega_D \ll \epsilon_F - \Delta_\tau$ so that the perturbation does not reach the bottom of the conduction band. From this and the expression of $\epsilon_\tau(k)$ we obtain

$$\big|\mathcal{B}_\tau(0)\big|k^2 = \frac{\epsilon_F - \Delta_\tau}{\Delta_\tau} + \eta_k \frac{\hbar\omega_D}{\Delta_\tau}. \tag{6.41}$$

Now, for many 2D materials (including any TMDC), the band gap is in the 1eV range (see e.g. Refs. [180, 184]) while for most crystals $\hbar\omega_D \sim 0.01$eV [185]. One therefore obtains a ratio $\hbar\omega_D/\Delta_\tau \sim 10^{-2}$, so that we may neglect the corresponding term and thus make the approximation

$$\big|\mathcal{B}_\tau(0)\big|k^2 \simeq \big|\mathcal{B}_\tau(0)\big|k_F^2 \qquad \big|\mathcal{B}_\tau(0)\big|k'^2 \simeq \big|\mathcal{B}_\tau(0)\big|k_F^2, \tag{6.42}$$

where the Fermi momentum k_F is defined by $\epsilon_\tau(k_F) = \epsilon_F$. With this and $\langle \boldsymbol{k'} V_{\boldsymbol{kk'}} \rangle = 0$, we finally obtain

$$\langle V^{\text{eff}}_{\boldsymbol{kk'}} \rangle = \big(1 - \big|\mathcal{B}_\tau(0)\big|k_F^2\big) \langle V_{\boldsymbol{kk'}} \rangle, \tag{6.43}$$

in line with our qualitative argument of a weakening of the electron-electron interaction induced by the Darwin term. With the BCS potential one finds $\langle V_{\boldsymbol{kk'}} \rangle = -V$, such that

$$\sum_{\boldsymbol{k}} \frac{1}{E - 2\epsilon_\tau(\boldsymbol{k})} = -\frac{1}{\big(1 - |\mathcal{B}_\tau(0)|k_F^2\big)V}. \tag{6.44}$$

As usual, the sum over the wave vector may be replaced by an integral over energy with the help of the density of states $\rho(\epsilon)$ and the BCS coupling constant $\lambda = V\rho(\epsilon_F)$. We finally find the binding energy of the Cooper pair

$$E_B = \frac{2\hbar\omega_D}{e^{2/\lambda_{\text{eff}}} - 1} \quad \text{with} \quad \lambda_{\text{eff}} = \big(1 - \big|\mathcal{B}_\tau(0)\big|k_F^2\big)\lambda, \tag{6.45}$$

which is the same as the conventional expression

$$E_B^{\text{BCS}} = \frac{2\hbar\omega_D}{e^{2/\lambda} - 1}, \tag{6.46}$$

where we have replaced λ by an effective (lower) coupling constant. If we set the Berry curvature to zero or if we set the band gap to be infinite, we recover the usual expression, as expected.

To summarize this subsection, we highlight two aspects. First, the effect of the Berry curvature on the Cooper pair reveals itself through a competition between two terms. On the one hand, the Berry dipole term, with its dipolar/spin-orbit form, induces a drift velocity analogous to the Karplus-Luttinger veloctity on the relative position of the electrons of the Cooper pair. It *could* in principle enhance the electron-electron interaction $V_{\boldsymbol{kk'}}$. On the other hand, the Darwin term yields a negative contribution and thus weakens the effective interaction. Second, the Berry dipole term's contribution to Cooper pairing turns out to be zero for s-wave superconductivity, and thus we are only left with a weakened electron-electron interaction due to the Darwin term. This is clearly seen in the expression of the

binding energy (6.45) Indeed, since the interaction V is lowered, so is the BCS coupling λ, thereby lowering the binding energy of the Cooper pair.

In conclusion, the Berry curvature makes the Cooper pairs less bound and thus more easily breakable, *e.g.* by thermal fluctuations. This means that the critical temperature (and the superconducting gap) are lowered as well, as we show explicitely in the following section, where we discuss the action of the Berry-curvature corrective terms in the BCS many-body approach.

6.5 . Many-body problem: Effective BCS theory

In the previous section, we found that the calculations in the Cooper problem with Berry curvature were the same as in its absence, but with an effective interaction. We therefore consider, in this part, the BCS Hamiltonian where we replace the interaction $V_{\boldsymbol{k}\boldsymbol{k}'}$ with the effective one $V^{\text{eff}}_{\boldsymbol{k}\boldsymbol{k}'}$ which is given in Eq. (6.32) and that accounts for the corrective terms due to the Berry curvature.

$$H = \sum_{\boldsymbol{k}\tau} \xi_{\boldsymbol{k}} c^\dagger_{\boldsymbol{k}\tau} c_{\boldsymbol{k}\tau} + \sum_{\boldsymbol{k}\boldsymbol{k}'} V^{\text{eff}}_{\boldsymbol{k}\boldsymbol{k}'} c^\dagger_{\boldsymbol{k}'\uparrow} c^\dagger_{-\boldsymbol{k}'\downarrow} c_{\boldsymbol{k}\uparrow} c_{-\boldsymbol{k}\downarrow} \tag{6.47}$$

where $\xi_{\boldsymbol{k}} = \epsilon_\tau(k) - \epsilon_F$, and the bare interaction (in the absence of Berry curvature corrections) is again $V_{\boldsymbol{k}\boldsymbol{k}'} = -V \mathbb{1}_{\mathcal{D}}(\boldsymbol{k}) \mathbb{1}_{\mathcal{D}}(\boldsymbol{k}')$ with this time $\mathcal{D} = \left\{ \boldsymbol{k} \in \mathbb{R}^2 \middle| \epsilon_F - \hbar\omega_D \leq \epsilon_\tau(k) \leq \epsilon_F + \hbar\omega_D \right\}$. We also keep the same groundstate. Since this Hamiltonian has the same form as the original BCS Hamiltonian, the same calculations hold as long as the interaction is not specified. We thus find the textbook gap equation [7]

$$\Delta_{\boldsymbol{k}} = -\frac{1}{2} \sum_{\boldsymbol{k}'} V^{\text{eff}}_{\boldsymbol{k}\boldsymbol{k}'} \frac{\Delta_{\boldsymbol{k}'}}{\sqrt{\Delta^2_{\boldsymbol{k}'} + \xi^2_{\boldsymbol{k}'}}} \tanh\left(\frac{\beta}{2} \sqrt{\Delta^2_{\boldsymbol{k}'} + \xi^2_{\boldsymbol{k}'}} \right), \tag{6.48}$$

with $\Delta_{\boldsymbol{k}} = -\sum_{\boldsymbol{k}'} V^{\text{eff}}_{\boldsymbol{k}\boldsymbol{k}'} \langle c^\dagger_{\boldsymbol{k}'\uparrow} c^\dagger_{-\boldsymbol{k}'\downarrow} \rangle$ and $\beta = (k_B T)^{-1}$. In terms of the auxiliary function

$$f_{\beta,\boldsymbol{k}}(\boldsymbol{k}') = \frac{\Delta_{\boldsymbol{k}'}}{\sqrt{\Delta^2_{\boldsymbol{k}'} + \xi^2_{\boldsymbol{k}'}}} \tanh\left(\frac{\beta}{2} \sqrt{\Delta^2_{\boldsymbol{k}'} + \xi^2_{\boldsymbol{k}'}} \right), \tag{6.49}$$

the self-consistent gap equation reads

$$\begin{aligned} \Delta_{\boldsymbol{k}} = &-\frac{1}{2} \left(1 - \frac{1}{2} \big| \mathcal{B}_\tau(0) \big| \boldsymbol{k}^2 \right) \sum_{\boldsymbol{k}'} V_{\boldsymbol{k}\boldsymbol{k}'} f_{\beta,\boldsymbol{k}}(\boldsymbol{k}') - \frac{1}{2} \left(\frac{i}{2} \boldsymbol{\Lambda}^-_{\tau_1\tau_2}(\boldsymbol{k}) \times \boldsymbol{k} + \big| \mathcal{B}_\tau(0) \big| \boldsymbol{k} \right) \cdot \sum_{\boldsymbol{k}'} \boldsymbol{k}' V_{\boldsymbol{k}\boldsymbol{k}'} f_{\beta,\boldsymbol{k}}(\boldsymbol{k}') \\ &- \frac{1}{2} \sum_{\boldsymbol{k}'} \frac{1}{2} \big| \mathcal{B}_\tau(0) \big| \boldsymbol{k}'^2 V_{\boldsymbol{k}\boldsymbol{k}'} f_{\beta,\boldsymbol{k}}(\boldsymbol{k}'). \end{aligned} \tag{6.50}$$

One can show that if the bare superconducting gap has a definite parity, then $\Delta_{\boldsymbol{k}}$ (so defined through the effective interaction) has the same parity. Therefore for BCS (s-wave) superconductivity we have $\Delta_{-\boldsymbol{k}} = \Delta_{\boldsymbol{k}}$. From equation (6.49), it is then clear that $f_{\beta,\boldsymbol{k}}(-\boldsymbol{k}') = f_{\beta,\boldsymbol{k}}(\boldsymbol{k}')$. And since $V_{\boldsymbol{k};-\boldsymbol{k}'} = V_{\boldsymbol{k};\boldsymbol{k}'}$, the function $\boldsymbol{k}' \longrightarrow \boldsymbol{k}' V_{\boldsymbol{k}\boldsymbol{k}'} f_{\beta,\boldsymbol{k}}(\boldsymbol{k}')$ is an odd function so that

$$\sum_{\boldsymbol{k}'} \boldsymbol{k}' V_{\boldsymbol{k}\boldsymbol{k}'} f_{\beta,\boldsymbol{k}}(\boldsymbol{k}') = \sum_{\boldsymbol{k}' \in \mathcal{D}} \boldsymbol{k}' V_{\boldsymbol{k}\boldsymbol{k}'} f_{\beta,\boldsymbol{k}}(\boldsymbol{k}') = 0, \tag{6.51}$$

and thus, again, the Berry dipole term does not affect the many-body result, which is consistent with the results obtained in the previous section. We then make the same approximate treatment [see Eqs. (6.42) and (6.43)] as for the Cooper pair problem and we find

$$\Delta_{\boldsymbol{k}} = -\frac{1}{2}\sum_{\boldsymbol{k'}} \big(1 - \big|\mathcal{B}_\tau(0)\big|k_F^2\big) V_{\boldsymbol{k}\boldsymbol{k'}} f_{\beta,\boldsymbol{k}}(\boldsymbol{k'}), \tag{6.52}$$

in agreement with our previous result. The Berry curvature reduces the attractive electron-electron interaction due to the Darwin term. We are now able to calculate the zero-temperature superconducting gap. At $T = 0$, the gap equation is

$$\Delta_{\boldsymbol{k}} = -\frac{1}{2}\big(1 - |\mathcal{B}_\tau(0)|k_F^2\big) \sum_{\boldsymbol{k'}} V_{\boldsymbol{k}\boldsymbol{k'}} \frac{\Delta_{\boldsymbol{k'}}}{\sqrt{\Delta_{\boldsymbol{k'}}^2 + \xi_{\boldsymbol{k'}}^2}}, \tag{6.53}$$

which becomes, with the use of $V_{\boldsymbol{k}\boldsymbol{k'}} = -V\mathbb{1}_{\mathcal{D}}(\boldsymbol{k})\mathbb{1}_{\mathcal{D}}(\boldsymbol{k'})$,

$$\Delta_{\boldsymbol{k}} = \mathbb{1}_{\mathcal{D}}(\boldsymbol{k})\frac{1}{2}\Big(1 - \big|\mathcal{B}(0)\big|k_F^2\Big) V \sum_{\boldsymbol{k}\in\mathcal{D}} \frac{\Delta_{\boldsymbol{k'}}}{\sqrt{\Delta_{\boldsymbol{k'}}^2 + \xi_{\boldsymbol{k'}}^2}}. \tag{6.54}$$

Thus $\Delta_{\boldsymbol{k}} = 0$ for $\boldsymbol{k} \notin \mathcal{D}$, and then one can show directly that $\Delta_{\boldsymbol{k}} = \Delta$ for $\boldsymbol{k} \in \mathcal{D}$. The former case is trivially satisfied since if $\boldsymbol{k} \notin \mathcal{D}$, the corresponding Bloch fermion is not subject to the attractive interaction so it cannot condense and participate in a SC state. The latter indicates that the gap is then isotropic for the Bloch fermions that are concerned by superconductivity. We may again follow the conventional derivation [7] and find the $T = 0$ superconducting gap

$$\Delta(T = 0) = \frac{\hbar\omega_D}{\sinh\big(1/\lambda_{\text{eff}}\big)} \quad \text{with} \quad \lambda_{\text{eff}} = \big(1 - |\mathcal{B}_\tau(0)|k_F^2\big)\lambda, \tag{6.55}$$

i.e. with the same effective coupling constant λ_{eff} as that obtained in the previous section [see Eq. (6.45)]. Comparing this to the bare BCS expression

$$\Delta^{\text{BCS}}(T = 0) = \frac{\hbar\omega_D}{\sinh\big(1/\lambda\big)} \tag{6.56}$$

we obtain the same result as in the Cooper pair problem, that is to say a lowering of the BCS coupling constant driven by the Berry curvature thereby lowering the $T = 0$ superconducting gap. This is also consistent with what we said about the consequences for the Cooper pairs. Indeed, since the superconducting gap is smaller, so is the energy of the quasiparticles in the superconductor. This makes them more sensitive to variations of energy, e.g. thermal fluctuations. In other words, the superconducting phase is weakened and thus more easily suppressed upon raising temperature.

Similarly, the expression for the critical temperature takes the form shown in Chapter 4 and Ref. [7],

$$T_c = 2\hbar\omega_D \frac{e^\gamma}{\pi} e^{-1/\lambda_{\text{eff}}} \tag{6.57}$$

and is identical to the standard one except for the fact that the coupling constant needs to be replaced by $\lambda \to \lambda_{\text{eff}}$ to take into account the extra terms due to the Berry curvature. Here, $\gamma \simeq 0.577$ is

the Euler-Mascheroni constant, and the approximation is valid if $2T_c \ll \hbar\omega_D/k_B = T_D$, and it is relatively reliable when $2T_c \lesssim T_D$. Notice finally, that the Berry curvature therefore does not affect the universality of the ratio between the superconducting gap and T_c in the weak-coupling limit,

$$\frac{\Delta(T=0)}{k_B T_c} \underset{\lambda \ll 1}{=} \frac{\pi}{e^\gamma} \simeq 1.76. \tag{6.58}$$

Indeed this ratio is independent of the (effective) coupling constant.

6.6 . Doping dependence: BCS coupling constant and critical temperature

Until now, we considered a low-doping limit, in which the Fermi level is close to the bottom of the conduction band. This allowed us to approximate the Berry curvature as $\mathcal{B}_\tau(k) \simeq \mathcal{B}_\tau(0)$. At larger doping, we first expect a weakening of the inter-band effects since the relevant physics will take place farther away from the other band. We should then expect to recover the usual one-band BCS results as the Fermi energy increases. The main thing to change would be our extra terms. The Berry dipole term (as derived from the generalized Peierls subsitution) does not rely on the low-energy expansion of the Dirac Hamiltonian, and we thus do not need to change it. The Darwin term is different: we have obtained it by expanding the Dirac Hamiltonian in the low-energy/non-relativistic limit. In this limit, the Berry curvature enters as $\left|\mathcal{B}_\tau(0)\right|$. Since the physics is controlled by states near the Fermi energy, we change $\left|\mathcal{B}_\tau(0)\right| \longrightarrow \left|\mathcal{B}_\tau(k_F)\right|$, *i.e.* the most important contribution of the Berry curvature is its value at the Fermi level. The effective coupling constant λ_{eff} takes then the form

$$\lambda_{\text{eff}} = \left(1 - \left|\mathcal{B}(k_F)\right| k_F^2\right)\lambda = \left(1 - \frac{\lambda_\tau^2 k_F^2}{2\left(1+\lambda_\tau^2 k_F^2\right)^{3/2}}\right)\lambda, \tag{6.59}$$

and we have

$$\text{Low-doping limit: } \frac{\lambda_{\text{eff}}}{\lambda} \underset{\lambda_\tau k_F \ll 1}{\sim} 1 - \frac{\lambda_\tau^2 k_F^2}{2}, \quad \text{High-doping limit: } \frac{\lambda_{\text{eff}}}{\lambda} \underset{\lambda_\tau k_F \gg 1}{\sim} 1 - \frac{1}{2\lambda_\tau k_F}, \tag{6.60}$$

for the different limiting cases. As a consistency check, we recover the previous result in the low-doping limit (indeed, $\lambda_\tau^2/2 = \left|\mathcal{B}_\tau(0)\right|$). In the high-doping limit, the effective coupling constant approaches its bare BCS value as the Fermi level goes to $+\infty$. This is consistent with our expectation of a decreased role of the corrective terms due to the Berry curvature and thus of the inter-band effects in this limit. The doping dependence of the coupling constant (i.e. on $\lambda_\tau k_F$) is depicted in Fig. 6.2. It is apparent that the effective coupling constant has a minimum that can be shown to occur at $\lambda_\tau k_F = \sqrt{2}$. Therefore the effect of the Berry curvature on conventional BCS type (s-wave) superconductivity is expected to be strongest in an intermediate doping regime in which the Fermi wave vector is on the order of the inverse effective Compton length. We then have

$$\min_{\lambda_\tau k_F} \frac{\lambda_{\text{eff}}}{\lambda} = 1 - \frac{1}{3\sqrt{3}} \simeq 81\%, \tag{6.61}$$

i.e. the maximal reduction is approximately 19%. It is interesting to note that while the ratio goes to 1 as the Fermi level goes to $+\infty$, the difference does not go to zero. Indeed,

$$\lim_{k_F \to +\infty} \left[\lambda_{\text{eff}} - \lambda\right] = -\frac{AV}{4\pi\Delta_\tau} \tag{6.62}$$

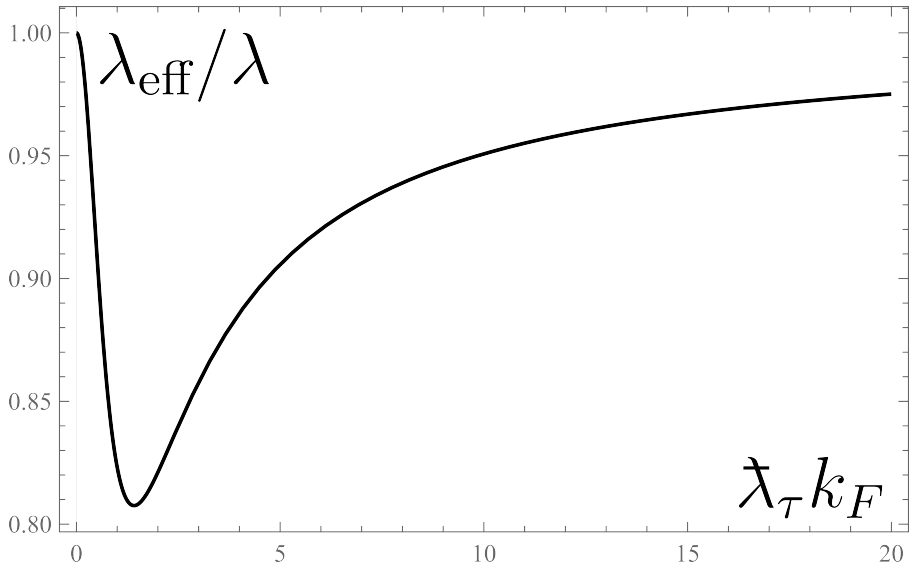

Figure 6.2: Ratio $\lambda_{\rm eff}/\lambda$ as a function of $\lambda\!\!\!^{-}_{\tau} k_F$.

with A the area of the Brillouin zone. Note that V represents, here, the interaction energy per unit area in reciprocal space so that the quantity AV itself is an energy and the coupling constant is dimensionless. While the reduction of the coupling constant seems rather limited, we must not forget that the critical temperature and the superconducting gap both depend exponentially on this coupling constant, so the effect could be quite substantial.

The central result of this chapter is Eq. (6.59). Indeed, from it ensues most of the results we had so far. Moreover, it could have several uses. First, doping could offer a way to experimentally observe the effects of a Berry curvature on a superconducting phase discussed in this paper. We present some possible paths for an experimental test of Berry-curvature effects on BCS superconductivity in Sec.6.8. Second, while this specific deformation of the coupling constant may not be true for other types of band structures, these could still exhibit other types of deformations depending on the corrective terms of the one-body problem. If Eq. (6.59) is true in other types of band structures, it can even be a way to detect the presence of a Berry curvature as well as its k-dependence.

6.7 . Beyond s-wave pairing

Now that we have studied the conventional s-wave case, let us see what happens with other types of superconductivity. As in the case for the s-wave case (see Sec. 6.4), we first revisit the modified Cooper problem from a more general point of view following Ref. [186]. We will then study the many-body BCS theory, this time following Refs. [187, 188].

6.7.1 . Cooper problem

In order to investigate superconducting order parameters beyond the s-wave case, we need to consider the angular-momentum dependence of the effective interaction. To this end, the two-electron

potential may be decomposed in the relative-angular momentum basis as [186]

$$V_{\boldsymbol{k}\boldsymbol{k}'} = \sum_{l=0}^{+\infty} V_l(\boldsymbol{k}, \boldsymbol{k}') \tag{6.63}$$

with $V_l(-\boldsymbol{k}, \boldsymbol{k}') = (-1)^l V_l(\boldsymbol{k}, \boldsymbol{k}') = V_l(\boldsymbol{k}, -\boldsymbol{k}')$. The integer l represents the angular momentum of the superconducting phase. It is even for singlet pairing and odd for triplet pairing. Let us pick a superconducting phase with fixed l, so that the pairing is either singlet or triplet. Then $V_{\boldsymbol{k}\boldsymbol{k}'} = V_l(\boldsymbol{k}, \boldsymbol{k}')$. The same is done to $g_{\boldsymbol{k}} = g_l(\boldsymbol{k})$ with also $g_l(-\boldsymbol{k}) = (-1)^l g_l(\boldsymbol{k})$. Equation (6.34) becomes therefore

$$\sum_{\boldsymbol{k}} \frac{\langle V_l^{\text{eff}}(\boldsymbol{k}, \boldsymbol{k}')\rangle_l}{E - 2\epsilon_{\tau_1\tau_2}(\boldsymbol{k})} = 1, \tag{6.64}$$

and we then proceed in the same way as before, expanding $\langle V_l^{\text{eff}}(\boldsymbol{k}, \boldsymbol{k}')\rangle_l$ and considering

$$\langle \boldsymbol{k}' V_l(\boldsymbol{k}, \boldsymbol{k}')\rangle_l \propto \sum_{\boldsymbol{k}'} \boldsymbol{k}' V_l(\boldsymbol{k}, \boldsymbol{k}') g_l(\boldsymbol{k}'). \tag{6.65}$$

If we then take $V_l(\boldsymbol{k}, \boldsymbol{k}')$ to be non-zero only within a thin layer of energy around the Fermi level, with the energy cut-off ϵ_l, one retrieves Eq. (6.39) but with $\mathcal{D}_l = \left\{\boldsymbol{k} \in \mathbb{R}^2 \middle| \epsilon_F \leq \epsilon_{\tau_1\tau_2}(\boldsymbol{k}) \leq \epsilon_F + \epsilon_l\right\}$. Because of the symmetry

$$\begin{aligned} V_l(\boldsymbol{k}, -\boldsymbol{k}')g_l(-\boldsymbol{k}') &= (-1)^l V_l(\boldsymbol{k}, \boldsymbol{k}')(-1)^l g_l(\boldsymbol{k}') \\ &= V_l(\boldsymbol{k}, \boldsymbol{k}')g_l(\boldsymbol{k}'), \end{aligned} \tag{6.66}$$

the function $\boldsymbol{k}' V_l(\boldsymbol{k}, \boldsymbol{k}')g_l(\boldsymbol{k}')$ is odd in $\boldsymbol{k}'$ so that the sum over the set $\mathcal{D}_l$ yields zero. Since this term carries the Berry dipole term, we can conclude that *the Berry dipole term does not contribute to the energy of the Cooper pair with pure singlet or triplet pairings*. Notice, however, that the Berry dipole term may nevertheless play a significant role in exotic superconductors that mix singlet and triplet pairing, as we sketch out in Sec. 6.7.3.

We then proceed with the same approximation as for the conventional s-wave case, which gives the effective interaction

$$\langle V_l^{\text{eff}}(\boldsymbol{k}, \boldsymbol{k}')\rangle_l = \left(1 - \left|\mathcal{B}(k_F)\right|k_F^2\right)\langle V_l(\boldsymbol{k}, \boldsymbol{k}')\rangle_l. \tag{6.67}$$

We also take the approach of Ref. [186] and take $V_l(\boldsymbol{k}, \boldsymbol{k}') = V_l(k, k')f(\hat{k}, \hat{k}')$ with $V_l(k, k') = -V_l \mathbb{1}_{\mathcal{D}_l}(\boldsymbol{k})\mathbb{1}_{\mathcal{D}_l}(\boldsymbol{k}')$. This approach gives a binding energy $E_{B,l}$ given by

$$E_{B,l} = \frac{2\epsilon_l}{e^{2/\lambda_{\text{eff}}} - 1} \tag{6.68}$$

with $\lambda_{\text{eff}} = \left(1 - \left|\mathcal{B}(k_F)\right|k_F^2\right)\lambda$, i.e. *the result obtained for the conventional Cooper problem extends to all purely singlet and triplet pairings*.

6.7.2 . Many-body problem: generalized BCS theory

We now briefly address the many-body problem from a more general point of view, using the generalized BCS theory presented in Refs. [188] and [187]. Its Hamiltonian is

$$H = \sum_{\boldsymbol{k}\tau} \xi_{\boldsymbol{k}} c^\dagger_{\boldsymbol{k}\tau} c_{\boldsymbol{k}\tau} + \frac{1}{2} \sum_{\substack{\sigma_1\sigma_2 \\ \sigma_3\sigma_4}} \sum_{\boldsymbol{k}\boldsymbol{k}'} V^{\sigma_1\sigma_2}_{\mathrm{eff},\boldsymbol{k}\boldsymbol{k}'^{\sigma_3\sigma_4}} c^\dagger_{\boldsymbol{k}\sigma_1} c^\dagger_{-\boldsymbol{k}\sigma_2} c_{-\boldsymbol{k}'\sigma_3} c_{\boldsymbol{k}'\sigma_4}, \tag{6.69}$$

with the effective interaction containing the Berry curvature corrections. The mean-field theory of this Hamiltonian gives rise to a 2×2 matrix $\widehat{\Delta}_{\boldsymbol{k}}$. As in the conventional case, one can prove that the dressed order parameter has the same parity as the bare one. Similarly to the Cooper problem, let us investigate a pairing that is either singlet or triplet. Then the gap equation has the form [187]

$$\Delta^{\sigma_1\sigma_2}_{\boldsymbol{k}} = -\sum_{\sigma_3\sigma_4} \sum_{\boldsymbol{k}'} V^{\sigma_2\sigma_1}_{\mathrm{eff},\boldsymbol{k}\boldsymbol{k}'^{\sigma_3\sigma_4}} \mathscr{I}^{\sigma_3\sigma_4}_\beta(\boldsymbol{k}'), \tag{6.70}$$

where $\mathscr{I}^{\sigma_3\sigma_4}_\beta(\boldsymbol{k}')$ is a kernel, explicited in Eq. (6.73) for unitary superconductors and in Appendix E.1 for the non-unitary triplet case. The expansion of the effective interaction yields

$$\begin{aligned}\Delta^{\sigma_1\sigma_2}_{\boldsymbol{k}} = &-\left(1 - \frac{1}{2}\left|\mathcal{B}_\tau(k_F)\right|\boldsymbol{k}^2\right) \sum_{\sigma_3\sigma_4} \sum_{\boldsymbol{k}'} V^{\sigma_2\sigma_1}_{\boldsymbol{k}\boldsymbol{k}'^{\sigma_3\sigma_4}} \mathscr{I}^{\sigma_3\sigma_4}_\beta(\boldsymbol{k}') \\ &- \left(\frac{i}{2}\boldsymbol{\Lambda}^-_{\tau_1\tau_2}(\boldsymbol{k}) \times \boldsymbol{k} + \left|\mathcal{B}_\tau(k_F)\right|\boldsymbol{k}\right) \cdot \sum_{\sigma_3\sigma_4} \sum_{\boldsymbol{k}'} \boldsymbol{k}' V^{\sigma_2\sigma_1}_{\boldsymbol{k}\boldsymbol{k}'^{\sigma_3\sigma_4}} \mathscr{I}^{\sigma_3\sigma_4}_\beta(\boldsymbol{k}') - \frac{1}{2}\left|\mathcal{B}_\tau(k_F)\right| \sum_{\sigma_3\sigma_4} \sum_{\boldsymbol{k}'} \boldsymbol{k}'^2 V^{\sigma_2\sigma_1}_{\boldsymbol{k}\boldsymbol{k}'^{\sigma_3\sigma_4}} \mathscr{I}^{\sigma_3\sigma_4}_\beta(\boldsymbol{k}'),\end{aligned} \tag{6.71}$$

where the summand of the $\boldsymbol{k}'$-linear term is

$$\sum_{\sigma_3\sigma_4} \boldsymbol{k}' V^{\sigma_2\sigma_1}_{\boldsymbol{k}\boldsymbol{k}'^{\sigma_3\sigma_4}} \mathscr{I}^{\sigma_3\sigma_4}_\beta(\boldsymbol{k}'). \tag{6.72}$$

We study two separate cases now. First, let us consider a unitary pairing, *i.e.* one for which $\widehat{\Delta}_{\boldsymbol{k}}\widehat{\Delta}^\dagger_{\boldsymbol{k}} \propto \sigma_0$. This entails all singlet pairings and unitary triplet pairings (those without spin polarization). In that case, the kernel $\hat{\mathscr{I}}_\beta(\boldsymbol{k}')$ is given by [187, 188]

$$\hat{\mathscr{I}}_\beta(\boldsymbol{k}') = \frac{\widehat{\Delta}_{\boldsymbol{k}'}}{2E_{\boldsymbol{k}'}} \tanh\left(\frac{\beta}{2}E_{\boldsymbol{k}'}\right). \tag{6.73}$$

Since the order parameter generally obeys $\widehat{\Delta}_{-\boldsymbol{k}} = -\widehat{\Delta}^\top_{\boldsymbol{k}}$ and $E_{-\boldsymbol{k}} = E_{\boldsymbol{k}}$, we have

$$\mathscr{I}^{\sigma_3\sigma_4}_\beta(-\boldsymbol{k}') = -\mathscr{I}^{\sigma_4\sigma_3}_\beta(\boldsymbol{k}'). \tag{6.74}$$

Furthermore, in order to respect the anticommutation relations of the fermionic operators, the interaction must obey $V^{\sigma_2\sigma_1}_{\boldsymbol{k};-\boldsymbol{k}'^{\sigma_3\sigma_4}} = -V^{\sigma_2\sigma_1}_{\boldsymbol{k}\boldsymbol{k}'^{\sigma_4\sigma_3}}$ [188]. With this, we have

$$\begin{aligned}\sum_{\sigma_3\sigma_4} -\boldsymbol{k}' V^{\sigma_2\sigma_1}_{\boldsymbol{k};-\boldsymbol{k}'^{\sigma_3\sigma_4}} \mathscr{I}^{\sigma_3\sigma_4}_\beta(-\boldsymbol{k}') &= -\sum_{\sigma_3\sigma_4} \boldsymbol{k}' V^{\sigma_2\sigma_1}_{\boldsymbol{k}\boldsymbol{k}'^{\sigma_4\sigma_3}} \mathscr{I}^{\sigma_4\sigma_3}_\beta(\boldsymbol{k}') \\ &= -\sum_{\sigma_3\sigma_4} \boldsymbol{k}' V^{\sigma_2\sigma_1}_{\boldsymbol{k}\boldsymbol{k}'^{\sigma_3\sigma_4}} \mathscr{I}^{\sigma_3\sigma_4}_\beta(\boldsymbol{k}')\end{aligned} \tag{6.75}$$

i.e. the latter is odd in $\boldsymbol{k'}$. If one takes the interaction to be non-zero in a thin layer of energy around the Fermi level with energy cutoff ϵ_c, the sum over the term that is linear in $\boldsymbol{k'}$ in Eq. (6.71) vanishes again, a situation encountered several times in this chapter. So the Berry dipole term does not change the gap and critical temperature for unitary pairings. As pointed out in appendix E.1, the latter is also valid for non-unitary triplet pairings. Therefore, *the Berry dipole term does not change the gap equation for pure singlet and triplet pairings*.

6.7.3 . Possible situations in which the Berry dipole term may become relevant

In view of the above results, one may then wonder if there is any possible effect of the Berry dipole term on superconductivity. What we proved so far is that it does not change the SC gap or T_c if the parity of the pairing is well defined. So a necessary condition for the Berry dipole term to actually contribute would be a superconducting phase without a fixed parity. We saw in the Cooper problem that the Berry dipole term drops out because the following sum is zero

$$\sum_{\boldsymbol{k'}} \boldsymbol{k'} V_{\boldsymbol{k}\boldsymbol{k'}} g_{\boldsymbol{k'}}. \tag{6.76}$$

If we decompose the two functions $V_{\boldsymbol{k}\boldsymbol{k'}}$ and $g_{\boldsymbol{k'}}$ in the sum of an even and an odd function

$$V_{\boldsymbol{k}\boldsymbol{k'}} = V^e_{\boldsymbol{k}\boldsymbol{k'}} + V^o_{\boldsymbol{k}\boldsymbol{k'}} \tag{6.77}$$

$$g_{\boldsymbol{k'}} = g^e_{\boldsymbol{k'}} + g^o_{\boldsymbol{k'}} \tag{6.78}$$

and interpret the e and o parts respectively as the singlet and triplet parts, we then have

$$V_{\boldsymbol{k}\boldsymbol{k'}} g_{\boldsymbol{k'}} = V^e_{\boldsymbol{k}\boldsymbol{k'}} g^e_{\boldsymbol{k'}} + V^o_{\boldsymbol{k}\boldsymbol{k'}} g^o_{\boldsymbol{k'}} + V^o_{\boldsymbol{k}\boldsymbol{k'}} g^e_{\boldsymbol{k'}} + V^e_{\boldsymbol{k}\boldsymbol{k'}} g^o_{\boldsymbol{k'}}. \tag{6.79}$$

While the first two terms disappear in Eq. (6.76) as they are even functions of $\boldsymbol{k'}$, the other two terms do *a priori* not disappear as they are odd functions of $\boldsymbol{k'}$. $V^o g^e$ may be interpreted as the interactions between triplet pairs in the presence of singlet pairs while $V^e g^o$ is the opposite.

These two terms may then be an opportunity for the Berry dipole term to have a non-zero contribution in the superconducting phase, *i.e.* if the latter shows coexistence between singlet and triplet pairs. We would then need a superconducting phase where none of the two dominates. Some materials have been proposed to exhibit two superconducting phases, each with a different parity, such as $CeRh_2As_2$ and bilayer-$NbSe_2$ [189, 190]. Notice furthermore that a very recent theoretical study argues that the observed superconducting phase in twisted bilayer graphene [191] might be due to an admixture of singlet and triplet pairs [192], and the Berry dipole term might then be a relevant parameter in the stabilization of this type of superconductivity.

Note that for both $CeRh_2As_2$ and bilayer-$NbSe_2$, and generally in non-centrosymmetric superconductors [193], a magnetic field is necessary to obtain a parity-mixed superconducting phase. To circumvent this issue, one could first implement the magnetic field in a BCS formalism for these systems, thereby absorbing it in an effective superconducting order parameter/interaction, which could then be used to our discussion here. This approach seems plausible since the coupling between the Berry curvature and the magnetic field appears in the equations of motion as the product of the two, so as a second term that could be neglected as long as the magnetic field necessary is not too high.

6.8 . Experimental proposal

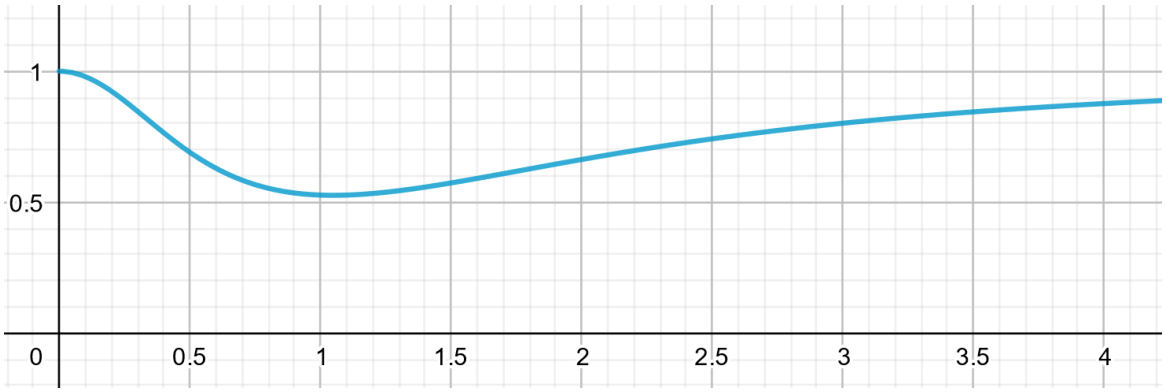

Figure 6.3: Ratio T_c/T_c^{BCS} as a function of $\lambda\!\!\!^{-}_{\tau} k_F \propto \sqrt{n_{2\text{D}}}$. Here, we have used $AV/2\pi\Delta_\tau \simeq 0.2$ for illustration.

.

As shown in Sec. 6.6, the Berry curvature has its strongest effect at Fermi wave vectors that are on the order of the inverse effective (Compton) length $\lambda\!\!\!^{-}_{\tau}$. Even if the relative reduction of the coupling constant is on the order of 19%, one needs to keep in mind that the experimentally measurable superconducting gap and critical temperature depend exponentially on the coupling constant. Indeed, the former is accessible by spectroscopic means, *e.g.* in scanning-tunneling spectroscopy, and the latter within resistive temperature-dependent measurements. Experimentally, it is likely impossible to change the Berry curvature *in situ* because this would require experimental access to the band parameters, such as the direct band gap in 2D TMDC. While one could hope to change it *e.g* under strain, also the phonon spectrum and the electron-phonon coupling would then change, possibly in an uncontrolled manner, thus excluding a direct measurement of the Berry-curvature effect in superconductivity.

However, one may compare the evolution of the Berry-curvature dependent superconducting gap or critical temperature, measured as a function of doping, to the *expected* behavior of these quantities. Direct comparison of the critical temperature T_c in Eq. (6.57), in terms of the effective coupling constant (6.45), yields the ratio

$$\frac{T_c}{T_c^{\text{BCS}}} = \exp\left(-\frac{2\pi\Delta_\tau}{AV} \frac{\left|\mathcal{B}_\tau(k_F)\right| k_F^2}{\left(1-\left|\mathcal{B}_\tau(k_F)\right| k_F^2\right)\sqrt{1+\lambda\!\!\!^{-2}_{\tau} k_F^2}} \right), \tag{6.80}$$

where T_c^{BCS} is the BCS critical temperature in the absence of Berry-curvature terms. We notice here the clear competition between the Berry curvature (through the gap) and superconductivity (through the attractive interaction V.). The ratio (6.80) is plotted in Fig. 6.3 as a function of the doping-dependent Fermi wave vector, $k_F = \sqrt{(4\pi/g)n_{2\text{D}}}$, in terms of the induced 2D electronic density $n_{2\text{D}}$. The factor g takes into account the degeneracy due to internal degrees of freedom, such as the valley and the spin. Notice that, in 2D TMDC with a prominent spin-orbit coupling, the valley and spin degrees of freedom are generically locked, as mentioned above. One would therefore expect $g = 2$ in these materials.

This is likely the case in the valence band, with a spin-orbit splitting on the order of ~ 100 meV, while it is only in the $\sim 1-10$ meV range in the conduction band. The reduction of the critical temperature is strongest at the minimum, which occurs at $\lambda\!\!\!^{-}_{\tau} k_F \simeq 1.05$. This corresponds to an electronic density of

$$n_{\mathsf{2D}} = \frac{g}{4\pi} k_F^2 \simeq 1.1 \frac{g}{4\pi} \lambda\!\!\!^{-2}_{\tau}. \tag{6.81}$$

We can then give an approximation of the minimum of the ratio as

$$\min_{k_F} \frac{T_c}{T_c^{\mathsf{BCS}}} \simeq \exp\left(-0.15 \frac{2\pi \Delta_\tau}{AV} \right). \tag{6.82}$$

6.9 . Conclusion

In conclusion, we have studied the effect of the Berry curvature on BCS-type superconductors in 2D electronic systems. We have shown that the two-body Hamiltonian for interacting electrons inherits terms that are linear in the Berry curvature and that are inherited from the single-electron band structure. In this case, the Berry curvature, which arises in the adiabatic limit when the electrons are restricted to a single band due to purely virtual transitions to the other bands, is coupled to electric potentials beyond the periodic one, which gives rise to the Bloch bands. While such potentials may arise due to external electric fields, they naturally arise when interactions between the electrons (or holes) are taken into account. Generically, the Berry curvature provides a dipolar structure to the charged pairs, and one of the terms emerging in the two-body Hamiltonian can indeed be interpreted as a dipole in an electric field. A second term emerges in the form of a Darwin term, in which the Berry curvature couples to the Laplacian of the electric potential. This term is best understood within a relativistic treatment of the (massive) Dirac Hamiltonian that mimics the two adjacent bands in a direct-gap semiconductor.

Following the lines of the usual BCS treatment of superconductivity in the weak-coupling limit, we have shown that the latter Darwin term generally lowers the BCS coupling constant. As a consequence, this lowers also the stability of the Cooper pair so that the superconducting gap and critical temperature are decreased. On the contrary, the dipolar term, which potentially has the power to increase superconductivity, does not affect the superconducting properties in an s-wave or any pure singlet or triplet superconductor because of their fixed parity. The dipolar term might then play a role in systems where superconducting phases of different parity coexist or where the superconducting order parameter does not have a fixed parity. This path might be explored in future work, but it is beyond the scope of our present work.

Interestingly, the gap-to-T_c ratio remains the same as in the conventional BCS theory in the weak-coupling limit, that we have considered here. Upon doping, the reduction of BCS superconductivity is strongest when the Fermi wave vector is on the order of the inverse effective Compton length, $k_F \sim \lambda\!\!\!^{-1}_{\xi\sigma}$, where the BCS coupling constant is lowered by 19%. Indeed, for stronger doping, the Fermi level is situated at wave vectors, where the Berry curvature rapidly tends to zero. Since the superconducting gap and the critical temperature both depend exponentially on the BCS coupling constant, the relatively weak reduction of the coupling constant is more prominent there. Our calculations show that the reduction of the doping-dependent superconducting gap and critical temperature depends then both on the band gap, which determines the value of the Berry curvature, as well

as on the effective electron-electron interaction. The experimental measurement of these quantities in 2D materials upon doping might then provide a test of our theoretical studies if compared to the expected evolution predicted by the usual BCS theory in the absence of Berry-curvature corrections.

7 - Normal state quantum metric in the (111) $LaAlO_3/SrTiO_3$ interface

7.1 . Background

Before discussing the impact of the normal state quantum metric in (111) oxide interfaces, we briefly introduce the latter as well as the superfluid weight.

7.1.1 . Oxide interfaces

In this chapter, we will consider a class of heterostructures known as *oxide interfaces*. The term "oxide" refers to transition metal oxides which, as their name implies, are compounds of transition metals and oxygen atoms. One class of transition metal oxides are perovskites with a chemical formula ABO_3, with A an alkaline or earth alkaline cation and B a transition metal ion [194]. One paradigmatic example of perovskite is $SrTiO_3$, which displays numerous properties ranging from paraelectric insulating phases [194] to a notoriously low-density superconducting phase under doping [195, 196].

A new range of phenomena were discovered when select transition metal oxides were interfaced with thin metallic, insulating, polar, ferroelectric or ferromagnetic oxide capping layers. In 2004, it was discovered in Ref. [197] that the interface between $LaAlO_3$ (LAO) and $SrTiO_3$ (STO) hosts a two-dimensional metallic state. This unexpected discovery, partly because both materials are insulators with band gaps at several electronvolts, attracted considerable interest. Over the following decade, the interest in the interface grew significantly with the discovery, amongst other phenomena, of superconductivity, large spin-orbit coupling and electric field tunability [198, 199]. The critical temperature of the superconducting phase is of the order of $100-200$mK [194, 199, 200, 201, 202], and the superconducting gap is of the order of $\Delta \simeq 40$μeV [202, 203].

Although the main orientation that was studied is the (001) interface, the (111) oriented interface also displays similar richness. In addition, as can be seen in Fig. 7.1, the interface can be seen as a honeycomb lattice, which would in a way make the (111) LAO/STO system a multiorbital version of graphene [204], with potential geometrical and topological properties. The two-dimensional electron gas at the (111) LAO/STO interface was shown in Ref. [205] to reside a few nanometers on the STO side.

7.1.2 . Superfluid weight

The conventional London equation relates $\boldsymbol{j}_s$, the supercurrent within the superconductor, to the external electrodynamic perturbation, which takes the form of a potential vector $\boldsymbol{A}$. The equation reads [7, 206]

$$\boldsymbol{j}_s = -\frac{ne^2}{m}\boldsymbol{A}. \tag{7.1}$$

However, this equation is only valid in the simplest cases. Indeed, in general the supercurrent and the electrodynamic perturbation may be related by a general tensor [207]

$$j_{s\mu}(\omega, \boldsymbol{q}) = K_{\mu\nu}(\omega, \boldsymbol{q})A_\nu(\omega, \boldsymbol{q}). \tag{7.2}$$

Within linear response theory, the tensor $K_{\mu\nu}$ appears as a current-current response function [207]. The *superfluid weight* is then defined, at the mean-field level, by the $\boldsymbol{q} \to 0$ limit of the static ($\omega = 0$) Meissner effect, i.e. [207]

$$D_{\mu\nu} = K_{\mu\nu}(\omega = 0, \boldsymbol{q} \to 0). \tag{7.3}$$

During the past decade, a significant number of papers have discussed the role of the normal-state quantum metric on the superconducting state [168, 169, 207]. It was found that the superfluid weight contains two terms. One is the well-known BCS contribution (see Ref. [208], for example), and the other is a geometric contribution which stems from interband couplings when the normal-state electronic structure involves several bands. In the isolated band limit, and in two-band models, this geometric contribution directly involves the normal state quantum metric [207].

For a band $(\epsilon_n, |u_n\rangle)$, expressions for both the *conventional* and *geometric* superfluid weights were derived in Ref. [207]. The conventional contribution reads

$$D^n_{\text{conv},\mu\nu} = \sum_{\boldsymbol{k}} \left[\frac{\tanh(\beta E_n/2)}{2} - \frac{\beta}{2\cosh(\beta E_n/2)} \right] \frac{\Delta^2}{E_n^2} \partial_\mu \epsilon_n \partial_\nu \epsilon_n, \tag{7.4}$$

while the geometric contribution in the isolated band limit reads

$$D^n_{\text{geom},\mu\nu} = 4\Delta^2 \sum_{\boldsymbol{k}} \frac{\tanh(\beta E_n/2)}{E_n} g^n_{\mu\nu}, \tag{7.5}$$

where Δ is the superconducting gap, $E_n = \sqrt{\Delta^2 + \epsilon_n^2}$ and $\beta^{-1} = k_B T$. The fact that the superfluid weight is composed of two terms, such that $D^n = D^n_{\text{conv}} + D^n_{\text{geom}}$, means that there are actually two sources of supertransport in superconductors, one of which being driven by the normal state quantum metric. Based on the second viewpoint of Chapter 2, we argue in Chapter 8 that the geometric contribution stems from the zero-point motions of the Bloch fermions, quantified by the normal state quantum metric. The conventional contribution on the other hand stems from the overall, i.e. group, velocity of the Bloch fermion, which disappears in the case of a flat band.

7.2 . Introduction

While we have shown that the normal state Berry curvature has an effect on the superconducting phase, the same is also true for the normal state quantum metric. Recent studies have theoretically pointed out the relevance of the quantum metric for the superfluid weight of flat-band models [29, 168, 169, 207, 209]. This chapter aims to study the impact of the normal state quantum geometry on superconductivity for (111)-oriented oxide interfaces, and more specifically for the $LaAlO_3$-$SrTiO_3$ (LAO/STO) heterostructure [198]. Let us point out that the results which we present here may be relevant for other materials, including other (111) oxide interfaces. The LAO/STO heterostructure hosts a two-dimensional electron gas (2DEG) on the STO side, confined to a few layers in the vicinity of the interface [205]. For the (111) interface, carriers in the 2DEG move on a honeycomb structure with three orbitals per site and, from that point of view, this may be seen as a three-orbital version of graphene [204].

Starting from a tight-binding (TB) modeling of the interface, we develop a low-energy model around the Γ point in two steps. First, we consider the spinless case for which the system has six bands. The dominance in energy of intra-orbital nearest-neighbor hoppings allows us to decouple the six bands into a bonding triplet and an anti-bonding triplet of bands. Focusing on the bonding triplet, we derive a low-energy three band model to quadratic order in $\mathbf{k}$. The latter presents two upper bands, degenerate at the Γ point, that represent the $|e_{\pm g}\rangle$ states. The other band is lower in energy, because of the trigonal crystal field, and represents the $|a_{1g}\rangle$ state. The three bands have isotropic and quadratic dispersions but the lowest band is significantly heavier than the other two. The latter presents a strong peak of the quantum metric, driven by inter-orbital nearest neighbor hoppings, which we refer to as *orbital mixing*. Second, we consider the spinful case in which a spin-orbit coupling term is taken into account. We then have a twelve-band TB model, from which we also derive a two-band low-energy model. The latter reveals an isotropic Dirac cone at the Γ point, which stems from the orbital mixing.

From the low-energy model, we can then draw a qualitative scenario for the chemical potential (μ) dependence of the conventional and geometric contributions to the superfluid weight [169, 207]. The conventional contribution is essentially linear in μ, because of the isotropy of the dispersion, and the geometric contribution presents a dome as a function of μ, since the Dirac cone produces a strong peak in the quantum metric.

Finally, we compare the results of the qualitative scenario to the experimental data, in the case of the LAO/STO interface. Taking into account thermal and disorder effects, we compute the superfluid weight both for the low-energy model, and the spinful TB model. In both cases, we find the correct order of magnitude for the superfluid weight (and the associated BKT temperature). The most significant difference between the two models is the value of μ below which the geometric contribution becomes dominant. In the low-energy model, the μ functional form of this quantity displays such a steep variation that it seems hardly possible to experimentally observe the regime when it dominates. In the spinful TB model, bands from the anti-bonding group, though $6-7$eVs away, contribute significantly to the quantum metric of the lowest Kramers' partners, producing a smoother variation of the geometric term and increasing the value of chemical potential below which the geometrical contribution dominates.

While the evolution of the superfluid weight is naturally discussed in terms of the chemical potential within a theoretical approach, experiments use the gate voltage V_g as a tuning parameter rather than μ. Oftentimes the variation of μ with V_g is monotonic both quantities are related by a monotonic function but Hall transport experiments [210, 211] have indicated that this is not the case for the LAO/STO (111) interfaces, where a non-monotonic dependence of the Hall carrier density on V_g has been observed. Assuming that the Hall carrier density is a monotonic function of the chemical potential, this suggests that the chemical potential is non monotonic in V_g. Taking this as an experimental fact, we then infer a qualitative dependence of the superfluid weight (and thus BKT temperature) on the gate voltage. The experimentally observed dome is explained by the conventional contribution and the non monotonic dependence of μ on V_g. As V_g is further increased, we expect a saturation effect followed by the appearance of a *second superconducting dome*, due purely to the geometric contribution to the superfluid weight.

The chapter is organized as follows. In Section 7.3, we present the tight-binding model, both in the spinless and spinful cases. In Section 7.4, we derive low-energy models and discuss their structure,

both in the spinless and the spinful cases. We then build on the spinful low-energy model to qualitatively discuss the dependence of the superfluid weight on the chemical potential. Finally, in Section 7.5 we make contact with experiments for the spinful case. We numerically compute the superfluid weight versus the chemical potential, for the low-energy model and then for the full TB model, and we discuss the extent to which the results that are obtained are consistent with the scenario presented in Section 7.4.

7.3 . Tight-binding model

7.3.1 . Crystal structure

We first introduce the relevant TB modeling of the (111) interface and discuss its various terms. The values of the relevant energy scales, presented in detail in Sec. 7.4, are mainly taken from Refs. [205, 211, 212, 213, 214]. The structure of the (111) oriented STO substrate is shown in Fig. . The two-

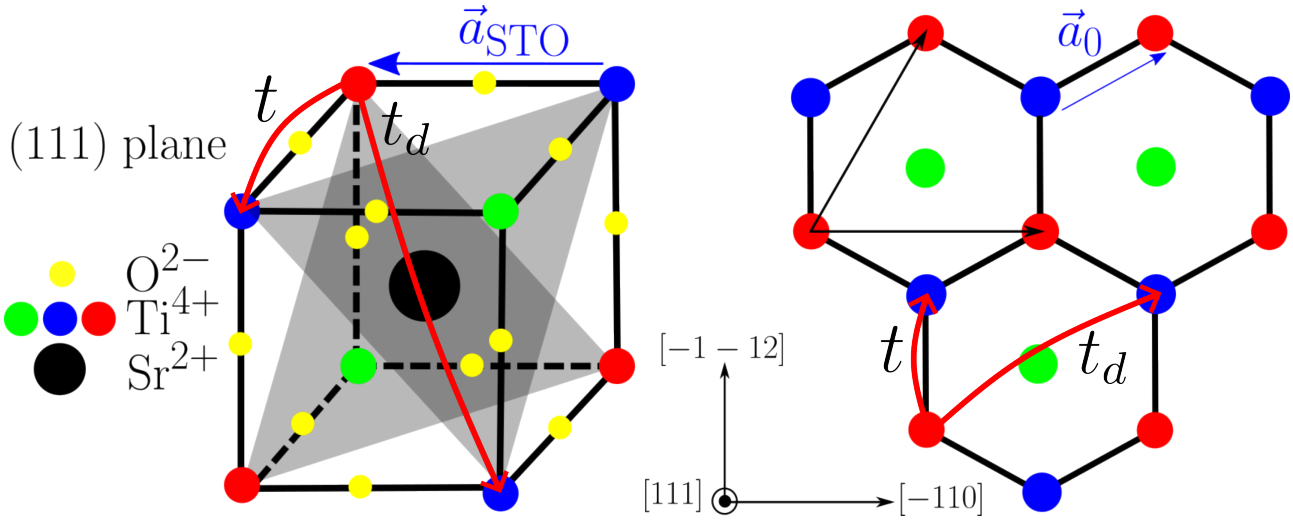

Figure 7.1: STO side, just below the (111) LAO/STO interface, adapted from [212]. Left: cubic lattice cell the corners of which are occupied by Ti^{4+} ions. The gray areas indicate planes normal to the [111] direction. Right: projection onto (111) planes. Two layers of Ti^{4+} ions (blue and red) form a honeycomb lattice, where the two triangular sublattices are displaced by the vector $\mathbf{a}_0$. Lastly, $a_{\mathrm{STO}} = 3.905$Å and $a_0 = \sqrt{2/3}a_{\mathrm{STO}}$. Two different hoppings are pictured. A nearest-neighbor hopping with strength t, and a third nearest-neighbor hopping with strength t_d. They lead to a band structure in quantitative agreement with ARPES spectra

dimensional electron gas (2DEG) is located on the STO side of the LAO/STO interface [205]. From a structural point of view, the three-dimensional (3D) $SrTiO_3$ crystal has a ABO_3 cubic perovskite structure (left panel, Fig. 7.1). In the (111) orientation, see Fig. 7.1, two consecutive (111) planes contain Ti ions for one and SrO_3 ionic groups for the other. Focusing on the Ti (111) planes, the atomic arrangement consists of layers of two-dimensional (2D) triangular lattices displaced by the vector $\mathbf{a}_0$ (see Fig. 7.1). Consequently, the Ti atoms form ABC-stacked two-dimensional 2D triangular lattices in the (111)

planes (see Fig. 7.1, left panel). From an electronic point of view, the charge carriers hop precisely between neighboring Ti atoms through direct orbital overlap or via the O sites.

While the basic building block for the description of the 2DEG would in principle contain three (ABC) layers of Ti atoms (red, blue and green in Fig. 7.1), the location of the Fermi energy for the (111) direction, as seen in Ref. [205], allows us to reduce the model to only two layers shown in Fig. 7.1 (right panel), as we have checked explicitly numerically in Appendix F.1. Indeed, for a unit trilayer stack, the TB Hamiltonian describing the kinetics of the 2DEG parallel to the (111) interface produces nine bands (not counting spin) organized in three groups (bonding, non-bonding, anti-bonding). Numerical inspection, using representative values of hopping amplitudes, shows that the energy difference between consecutive groups is on the order of several eV such that the three non-bonding bands which come from the third (green) layer are several eVs away from the Fermi energy, as discussed in Appendix F.1. Additionally, the dispersions of the occupied bonding triplet bands show very little difference with those of a bilayer model, where only the first (blue) and second (red) layers are considered (see Fig. F.1 of Appendix F.1).

We can therefore leave out the third layer and consider the system shown on the right in Fig. 7.1, *i.e.* two triangular layers (red and blue) displaced by the vector $\mathbf{a}_0$ that form a honeycomb lattice characterized by the layer/sublattice index $\{1, 2\}$. On each site, we have the three conducting t_{2g} Ti orbitals, $\{d_{yz}, d_{xz}, d_{xy}\}$, which, in the following, we denote $\{\mathsf{X}, \mathsf{Y}, \mathsf{Z}\}$, respectively.

Accounting for spin, we then have a honeycomb lattice with two spins and three orbitals per site, yielding a twelve-band system. Next, we discuss each type of hopping entering our TB model.

7.3.2 . Kinetic term

The kinetic part of the model takes into account hoppings between the different lattice sites and orbitals. This term describes carrier motions conserving the orbital character, with amplitudes t and t_d for nearest and third nearest neighbors belonging to two different layers, respectively. The general form of the kinetic term is thus diagonal in terms of the orbitals but off-diagonal in terms of the layers. Therefore, in the $\{1, 2\} \otimes \{\mathsf{X}, \mathsf{Y}, \mathsf{Z}\}$ basis the kinetic term reads

$$\begin{pmatrix} 0 & H_{\mathsf{cin}} \\ H_{\mathsf{cin}}^* & 0 \end{pmatrix} = \tau_x \otimes \mathsf{Re}(H_{\mathsf{cin}}) - \tau_y \otimes \mathsf{Im}(H_{\mathsf{cin}}), \tag{7.6}$$

with $H_{\mathsf{cin}} = t\,\mathrm{diag}(e, f, g)$ in the orbital subspace. The Pauli matrices τ_x and τ_y in Eq. (7.6) act on the layer subspace. Explicit expressions for the functions e, f and g may be found in appendix F.2.

7.3.3 . Orbital mixing term

While the kinetic term does not couple different orbitals, such couplings are generated at the interface by *orbital mixing*. In appendix F.3, we show by symmetry considerations that a natural choice is

$$\tau_x \otimes H_{\mathsf{om}} = \tau_x \otimes c_0 \begin{pmatrix} 0 & i\delta & -i\alpha \\ -i\delta & 0 & i\beta \\ i\alpha & -i\beta & 0 \end{pmatrix}, \tag{7.7}$$

where $\alpha = \sin\big(\sqrt{3}/2k_x + 3/2k_y\big)$, $\beta = \sin\big(\sqrt{3}/2k_x - 3/2k_y\big)$, $\delta = -\sin\big(\sqrt{3}k_x\big)$ and c_0 the strength of the orbital mixing. Here, we measure the wave vectors in units of the inverse a_0^{-1} of the distance between nearest-neighbor sites in the (111) plane (see Fig. 7.1), and τ_x is again a Pauli matrix acting

on the layer degree of freedom. Note that with inversion symmetry, these terms are prohibited. But in reality, interfaces between $LaAlO_3$ and $SrTiO_3$ always have corrugation [215, 216], such that inversion symmetry is broken and orbitals that would have been orthogonal are not, resulting in non-zero overlap and allowed interorbital hoppings. It will give rise to an orbital Rashba effect.

7.3.4 . Trigonal crystal field

Note that the (111) interface has a different point group symmetry than the orbitals whose symmetry is governed by the (cubic) bulk symmetry of LAO and STO. Therefore the t_{2g} orbitals are not orthogonal to each other in the honeycomb lattice, resulting in a *trigonal crystal field*, where the couplings have the same value because of the hexagonal symmetry. It lifts the degeneracy between the $e_{\pm g}$ orbitals and the a_{1g} orbital within the conducting t_{2g} orbitals of Ti. This trigonal crystal field, of strength d, thus couples the different orbitals in the same layers so that it may be written as

$$H_d = -d\tau_0 \otimes \begin{pmatrix} 0 & 1 & 1 \\ 1 & 0 & 1 \\ 1 & 1 & 0 \end{pmatrix}, \tag{7.8}$$

where τ_0 is the identity matrix indicating that the trigonal crystal field is diagonal in the layer index.

7.3.5 . Confinement energy

Finally, we need to take into account a confinement term that reflects the different onsite potentials for the two sublattices, which reside in different layers. It is equivalent to the Semenoff mass in graphene, breaking the $\mathcal{C}_6$ symmetry down to $\mathcal{C}_3$. We have $-V\Lambda_0$ for layer 1 and $V\Lambda_0$ for layer 2, so that this term may be written as $\tau_z \otimes (-V\Lambda_0)$, in terms of the 3×3 identity matrix noted Λ_0. While this term may be important for other properties of the LAO/STO interface, we will see that it does not affect the geometrical properties studied here, and we will later omit it when reducing the TB model to a low-energy model.

7.3.6 . Spinless model

With these four terms, the six-band TB model is written in the basis $\{1,2\} \otimes \{\mathsf{X},\mathsf{Y},\mathsf{Z}\}$, as

$$H_6 = \begin{pmatrix} -VI_3 + H_d & H_{\mathsf{cin}} + H_{\mathsf{om}} \\ H_{\mathsf{cin}}^* + H_{\mathsf{om}} & VI_3 + H_d \end{pmatrix}. \tag{7.9}$$

A more convenient basis is the *trigonal basis* in which the trigonal crystal field term is diagonal. The latter is detailed in appendix F.4. Hereafter, we discuss the band structure described by H_6 in the trigonal basis. We now add spin to our problem.

7.3.7 . Spin-Orbit Coupling

The spin-orbit coupling (SOC) term is identical for the two layers, and thus naturally diagonal in the layer subspace. In the $\{\uparrow,\downarrow\} \otimes \{\mathsf{X},\mathsf{Y},\mathsf{Z}\}$ basis, it reads [217]

$$H_{\mathsf{SOC}} = -\lambda\sigma_x \otimes \Lambda_7 + \lambda\sigma_y \otimes \Lambda_5 - \lambda\sigma_z \otimes \Lambda_2, \tag{7.10}$$

where the Λ-matrices denote the Gell-Mann matrices, explicited in appendix F.5. The energy scale λ is given by $\lambda \simeq 8$meV [211].

7.3.8 . Spinful model

The spinless Hamiltonian H_6 is identical for each spin, the corresponding term in the $\{\uparrow,\downarrow\} \otimes \{1,2\} \otimes \{\mathsf{X},\mathsf{Y},\mathsf{Z}\}$ basis, will be $\sigma_0 \otimes H_6$. We thus finally obtain our twelve-band TB model, as

$$\begin{aligned} H_{12} = \sigma_0 \otimes H_6 - \lambda\sigma_x \otimes \tau_0 \otimes \Lambda_7 + \lambda\sigma_y \otimes \tau_0 \otimes \Lambda_5 \\ - \lambda\sigma_z \otimes \tau_0 \otimes \Lambda_2, \end{aligned} \tag{7.11}$$

where the last three terms correspond to $\tau_0 \otimes H_{\mathsf{SOC}}$.

7.4 . Low-energy model

We now aim to derive a low-energy expression from the TB model. We first discuss the problem without spin, and derive a low-energy three-band model, valid for each spin orientation. We then add the spin degree of freedom and find that the low-energy limit leads to a two-band model. To do so, we only apply momentum-independent unitary transformations, that leave the quantum geometry invariant.

7.4.1 . Spinless low-energy model

Numerical diagonalization shows that the low-filling regime occurs near the Γ point. Moreover, in the vicinity of the latter, there are two groups of three bands separated by several eV. This is because the gap between the two groups at the Γ point is $2(2t + t_d) \sim 6.5$eV, and the kinetic energy is clearly the largest energy scale. Therefore, for low fillings, it appears possible to reduce the above six-band expression to two effective three-band models, one for each group. To make a similar structure appear explicitly in H_6, we apply the following unitary transformation

$$U = U_l \otimes \Lambda_0 = \frac{1}{\sqrt{2}} \begin{pmatrix} -1 & 1 \\ 1 & 1 \end{pmatrix} \otimes \Lambda_0, \tag{7.12}$$

which maximally entangles the two layers, in a symmetric $|s_l\rangle$ and an anti-symmetric combination $|a_l\rangle$. The six-band Hamiltonian is then transformed to

$$U^\dagger H_6 U = \begin{pmatrix} H_d - H_{\mathsf{om}} - \mathsf{Re}(H_{\mathsf{cin}}) & -VI_3 + i\mathsf{Im}(H_{\mathsf{cin}}) \\ -VI_3 - i\mathsf{Im}(H_{\mathsf{cin}}) & H_d + H_{\mathsf{om}} + \mathsf{Re}(H_{\mathsf{cin}}) \end{pmatrix}. \tag{7.13}$$

Numerical comparison of the band dispersions of the diagonal blocks in Eq. (7.13) and that of the full spinless TB Hamiltonian in Eq. (7.9) confirms that the former accurately reproduce the two groups. Thus, we may focus on the lower diagonal block, which corresponds to the symmetric entanglement of the two layers, and take it as a low-energy three-band model that reads

$$H_3 = H_d + H_{\mathsf{om}} + \mathsf{Re}(H_{\mathsf{cin}}). \tag{7.14}$$

A discussion of the validity of this approximation, done in appendix F.6, shows that with a precision of a few meV, this *three-band approximation* is valid over an area centered at Γ and covering approximately ten percent of the Brillouin zone (BZ). To be consistent with this approximation, we need to expand H_3 to quadratic order in k.

7.4.1.1 Quadratic three-band model

In appendix F.7, we show that to quadratic order, we have

$$H_3 = -(2t+t_d)\Big(1-\frac{1}{4}k^2\Big)\Lambda_0 + \begin{pmatrix} d-t_{\text{eff}}(k_x^2-k_y^2) & -2t_{\text{eff}}k_xk_y & ick_x \\ -2t_{\text{eff}}k_xk_y & d+t_{\text{eff}}(k_x^2-k_y^2) & ick_y \\ -ick_x & -ick_y & -2d \end{pmatrix}, \tag{7.15}$$

with $t_{\text{eff}} = (t-t_d)/8$ and $c = 3c_0/\sqrt{2}$. Note that H_3 is expressed in the trigonal basis (see appendix F.4). The trigonal crystal field lifts the threefold degeneracy at the Γ point (between a_{1g} and $e_{\pm g}$ states). The linear and quadratic terms arise from the orbital mixing and kinetic terms, respectively. Inspection of Eq. (7.15), reveals that the a_{1g} state is only coupled to the $e_{\pm g}$ states through the orbital mixing contribution, which generates its quantum geometry.

H_3 can then be exactly diagonalized, and we find the following eigenvalues for the last term:

$$\epsilon_1 = d + t_{\text{eff}}k^2, \quad \epsilon_2 = d + \left(\frac{c^2}{3d} - t_{\text{eff}}\right)k^2, \tag{7.16}$$

and

$$\epsilon_3 = -2d - \frac{c^2}{3d}k^2, \tag{7.17}$$

to quadratic order in the wave-vector components. The values taken hereafter are those corresponding to Refs. [205, 211, 212, 213, 214], i.e. $t = 1.6$ eV, $t_d = 70$ meV, $V = 100$ meV, $d = 3$ meV. Additionally, we estimate $c_0 = 40$ meV. We thus find an isotropic electron-like band structure.

We point out that these results may apply to other (111) oxide interfaces. In Section 7.5, we discuss the relevance of our results to the experimental context, illustrated with the case of the LAO/STO (111) interface. The lowest energy band (ϵ_3) is substantially flatter than the other two. Indeed, its band mass can be computed to be

$$m_B = \frac{\hbar^2}{2a_0^2}\left(\frac{2t+t_d}{4} - \frac{c^2}{3d}\right)^{-1} \simeq 21m_0, \tag{7.18}$$

with $m_0 \simeq 9.1\times10^{-31}$ kg the rest mass of an electron. This band presents a peak in its quantum metric at the value given by $g_{3,\mu\mu}(\Gamma) = c_0^2/9d \simeq 90a_0^2$.

Note that going beyond the low-energy model, which is obtained using a quadratic order expansion in k, we find that the interorbital contributions to cubic order, give rise to an orbital Rashba effect which moves the minimum away from the Γ point and therefore the actual band mass differs from Eq. (7.18). We then plot this band structure and contrast it with the one we get from the TB form of the kinetic and orbital mixing terms in Fig. 7.2. The band structure of the full TB model in the full Brillouin Zone (BZ) is shown in Appendix F.8. We indeed get the aforementioned precision of a few meVs. Note that the offset of 2 meV between the TB and low-energy bands as seen in Fig. 7.2, is due to the fact that V does not enter the low-energy expression of the Hamiltonian. Such a global shift does not have a physical relevance on the quantum geometry and superfluid weight as it can be compensated by a redefinition of the chemical potential with respect to the Γ point value of the lowest band. We then get a lower band that is substantially flatter than the other ones and that is close in energy to a level crossing at the Γ point.

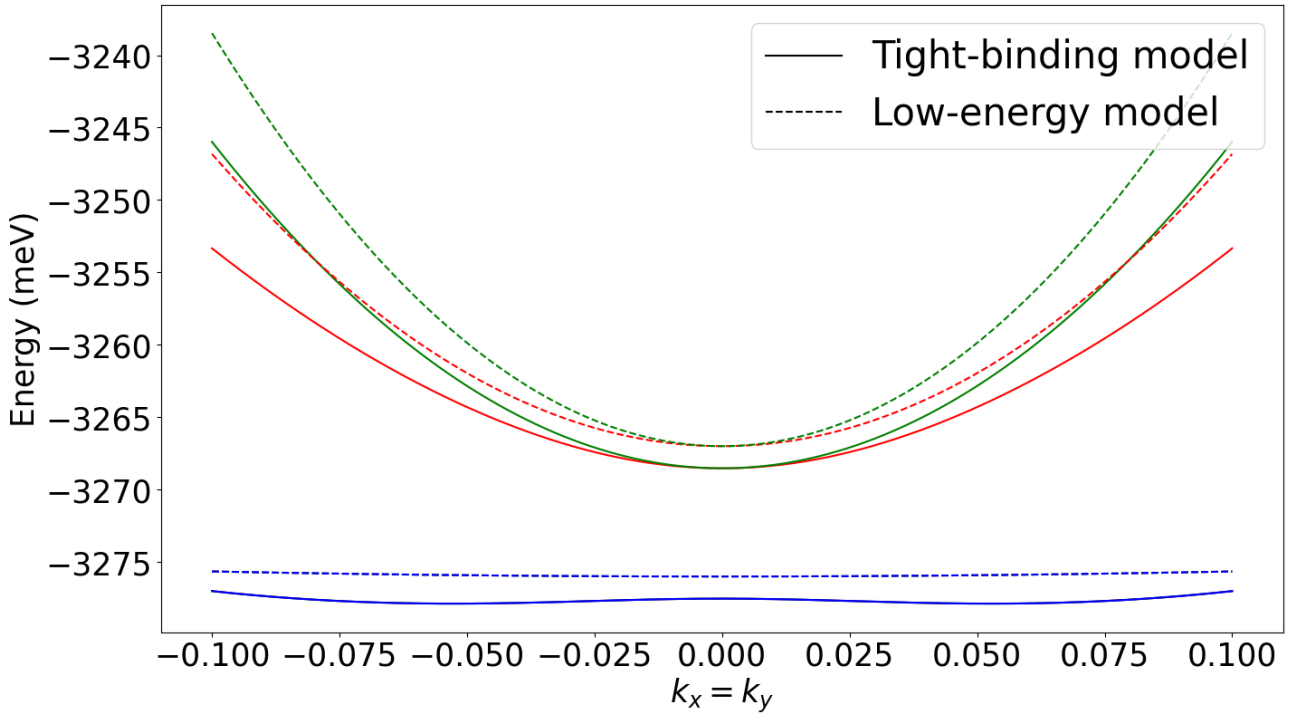

Figure 7.2: Energy dispersions near Γ, in the $k_x = k_y$ direction. Each color corresponds to one of the three bands, blue is the lowest band, red is the second lowest and green the third lowest band. Dashed lines correspond to the dispersions coming from the low-energy model, Eq. (7.15). Solid lines come from the full Tight-binding Hamiltonian, Eq. (7.9).

7.4.2 . Spinful low-energy model

In the spinless case, without spin-orbit coupling, the quantum geometry is largely generated by the orbital mixing term. However if we add the spin-orbit coupling and the spin degree of freedom, we may have a stronger quantum geometry because of changes in band degeneracies around the Γ point. To resolve the issue, we now derive a low-energy model starting from the spinful Hamiltonian H_{12}.

7.4.2.1 Derivation of the low-energy model

We start by applying, once again, the unitary matrix U given in Eq. (7.12) , and we use the matrix P, explicited in Appendix F.4, to express the orbital part in the trigonal basis. The SOC term is left unchanged by U, while the $\sigma_0 \otimes H_6$ term gets us two copies of Eq. (7.13). We then make the same approximation, and by switching the layer and spin degrees of freedom, we get a Hamiltonian which is the counterpart of the bonding and anti-bonding groups of the spinless case, only now with one copy for each spin as well as the accompanying SOC. We then restrict H_{12} to the bonding subspace, i.e. the symmetric combination of the two layers $|s_l\rangle$, and then get a six-band Hamiltonian $\tilde{H}_6$, written as

$$\tilde{H}_6 = \sigma_0 \otimes H_3 + H_{\text{SOC}}, \tag{7.19}$$

where H_{SOC} is expressed in the trigonal basis, and H_3 is given by Eq. (7.15). Further manipulation detailed in Appendix F.9, using the experimentally relevant and simplifying approximation $\lambda = 3d$, yields the two-band Hamiltonian $H_2 = h_0(\mathbf{k})\sigma_0 + \mathbf{h}(\mathbf{k}) \cdot \sigma$, with

$$h_0(\mathbf{k}) = -2t - t_d + \big(1 - 3\sqrt{3}\big)d + \frac{2t + t_d}{4}k^2, \tag{7.20}$$

and

$$\mathbf{h}(\mathbf{k}) = \frac{c_0}{2}\Big(- 2k_x, k_x + \sqrt{3}k_y, k_x - \sqrt{3}k_y\Big). \tag{7.21}$$

Note that the spin-orbit coupling mixes all three bonding spinless bands, producing three Kramers pairs of energy branches separated by an energy gap at the Γ point. The low-energy model focuses on the lowest Kramers pairs.

7.4.2.2 Dispersions

The dispersions are given by

$$\epsilon_{\pm} = -2t - t_d + \big(1 - 3\sqrt{3}\big)d \pm \sqrt{\frac{3}{2}}c_0 k + \frac{2t + t_d}{4}k^2. \tag{7.22}$$

As in the spinless case, we compare the dispersions of the latter with those of the full TB model H_{12} in Fig.7.3.

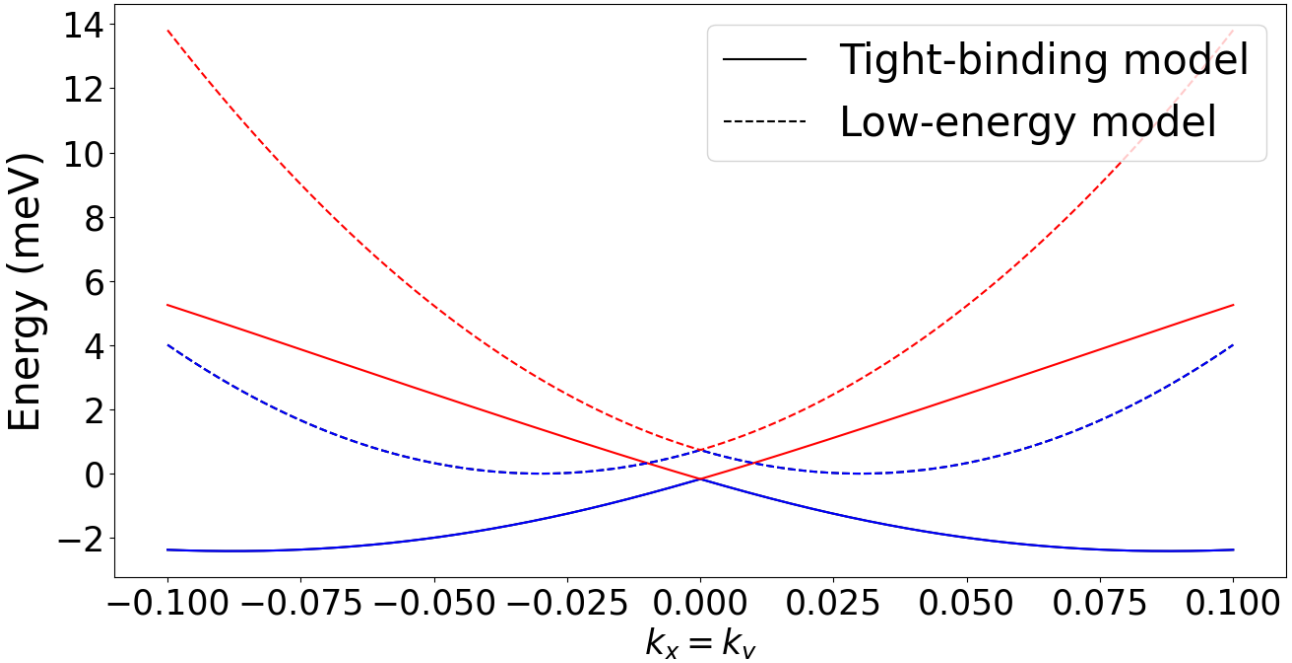

Figure 7.3: Energy dispersions of the low-energy two-band model H_2 overlaid with the two lowest band of the full TB model H_{12}, near Γ and in the $k_x = k_y$ direction. The energy is defined with respect to the crossing point of the solid lines.

7.4.2.3 Quantum/band geometry

Quantum metric The quantum metric is the same for the two bands, being equal to that of a massless Dirac fermion [207]

$$g_{\mu\nu} = \frac{k^2\delta_{\mu\nu} - k_\mu k_\nu}{4k^4}. \tag{7.23}$$

This result can be directly obtained as the $\Delta \to 0$, i.e. $\lambda_c \to +\infty$, limit of Eq. (2.115),

$$g_{\mu\nu} = \frac{\lambda_c^2}{4}\frac{\left(1+\lambda_c^2k^2\right)\delta_{\mu\nu} - k_\mu k_\nu}{\left(1+\lambda_c^2k^2\right)^2} \simeq \frac{\lambda_c^2}{4}\frac{\lambda_c^2k^2\delta_{\mu\nu} - \lambda_c^2k_\mu k_\nu}{\lambda_c^4k^4} = \frac{k^2\delta_{\mu\nu} - k_\mu k_\nu}{4k^4}. \tag{7.24}$$

Berry curvature As for the Berry curvature, the upper and lower parts of the Dirac cone yield opposite $\delta(k)$ contributions at the contact point. Note that in the full model, there are two sources of Berry curvature. One is, as we just mentioned, the spin-orbit coupling, which results in the mentioned Dirac cone. The other is the mixing of the lowest band with the others which drives a Berry curvature the order of unity in a_0^2, as mentioned in Sec. 7.5.3.

7.4.3 . Superfluid weight in the low-energy model

Initially, the theory of the geometric superfluid weight was developed for flat bands where the conventional contribution vanishes and the geometric contribution then dominates. While we do not have flat bands, the Dirac cone structure of our low-energy model gives a strong quantum metric near the Γ point. It thus seems relevant to investigate whether the normal-state quantum metric produces a sizeable effect on the superconducting state through this geometric superfluid weight. In the following two sections, we discuss the two contributions in the context of our low-energy model. We begin with a qualitative discussion aimed at explaining generic scenarios for the Berezinskii-Kosterlitz-Thouless (BKT) temperature versus the gate voltage V_g. For the superconducting state, we assume a conventional s-wave pairing, which can accommodate the disordered nature of oxide interfaces. As for the value of the s-wave gap, it has been measured to be $\Delta = 40\mu$eV at optimal doping for the (001) LAO/STO interface [203], and a similar value for the (111) interface was reported in Ref. [202].

7.4.3.1 BKT Temperature

In addition to the superfluid weight (which has the dimension of an energy in 2D), we consider the associated Berezinskii-Kosterlitz-Thouless (BKT) temperature, using the (isotropic) Nelson-Kosterlitz criterion [207],

$$T_{\text{BKT}} = \frac{\pi}{8k_B}D(T_{\text{BKT}}), \tag{7.25}$$

where $D(T)$ is the superfluid weight at temperature T. Note that we make use of the isotropic criterion because in the studied system the superfluid weight turns out to obey $D_{\mu\nu} = D\delta_{\mu\nu}$, both in the low-energy and tight-binding models. The BKT temperature T_{BKT} is the temperature above which vortex-antivortex pairs start to unbind and thus destroy superconductivity. It is generically smaller than the critical temperature calculated in the framework of a mean-field approach. For T_{BKT} not too close to T_c the mean-field critical temperature, we may approximate $D(T_{\text{BKT}})$ by $D(T=0)$. This defines a "mean-field" BKT temperature which is larger than the actual one and may thus give an upper

bound estimate,

$$T_{\text{BKT}} = \frac{\pi}{8k_B} D(T=0). \tag{7.26}$$

7.4.3.2 Conventional contribution

The conventional contribution to the superfluid weight, at $T = 0$, is given by [207, 208]

$$D_{\mu\nu,\text{conv}} = \int_{\mathscr{S}_{\text{occ}}(\mu)} \mathcal{D}_2\mathbf{k} \frac{\Delta^2}{E^3} (\partial_\mu \epsilon)(\partial_\nu \epsilon), \tag{7.27}$$

where $\mathscr{S}_{\text{occ}}(\mu)$ denotes the set of occupied states in the BZ at the chemical potential μ, and $E = \sqrt{\epsilon^2 + \Delta^2}$. $\mathcal{D}_2\mathbf{k}$ is the integration measure for the hexagonal BZ. For isotropic linearly dispersing bands, Eq. (7.27) gives $D_{\mu\nu,\text{conv}} = \delta_{\mu\nu} D_{\text{conv}}$ with $D_{\text{conv}} \propto \sqrt{\Delta^2 + \mu^2}$ [207], where Δ is the s-wave superconducting gap. In appendix F.10, we show that a similar result holds for a general isotropic quadratic band. Consequently, the conventional superfluid weight is essentially proportional to the chemical potential μ for $\mu \gtrsim \Delta$.

7.4.3.3 Geometric contribution

General expression The geometric contribution at $T = 0$ for a two-band Hamiltonian of the form $h_0\sigma_0 + \mathbf{h} \cdot \boldsymbol{\sigma}$, is given by [207]

$$D^{\pm}_{\text{geom},\mu\nu} = \pm \int_{\mathscr{S}_{\text{occ}}(\mu)} \mathcal{D}_2\mathbf{k} \frac{4\Delta^2}{E_\pm} \frac{h}{\mu - h_0} g_{\mu\nu}, \tag{7.28}$$

and more generally the geometric contribution is linked to the quantum metric in the so-called isolated limit [207], noting that Eq. (7.28) does not rely on it. Furthermore, note the additional factor of two with respect to the expression given in Ref. [207]. This is because the definition of the metric in Ref. [207] is twice the usual one [27, 92].

Qualitative dependence on the chemical potential Because of the Dirac cone at the Γ point, the quantum metric of the two lowest bands in our model will exhibit a strong peak. Even in the spinless case, the lowest band is accompanied by a strong peak at the Γ point. We therefore consider the case where the bands exhibit a peaked quantum metric around where the zero of the chemical potential μ is defined, hereafter called the zero-filling point.

The $1/E(\mathbf{k})$ factor in Eq. (7.28) enhances the contribution at the Fermi contour, making it dominant. Focusing on this contribution, we can propose a scenario explaining the emergence of a dome in the geometric superfluid weight when the metric has a peak at the zero-filling point. We sketch this scenario in Fig. 7.4, where the variation of the geometric superfluid weight is profiled as a function of the chemical potential.

At low μ, the band starts to be filled around Γ. The Fermi contour is thus at the top of the peak, but it is also narrow, such that D_{geom} is low. However, as the filling increases, the Fermi contour gets wider while still being high and thus D_{geom} becomes larger. This is the low-μ regime, shown in Fig. 7.4a. Upon an increase of the chemical potential μ, the latter reaches a value where the trade-off

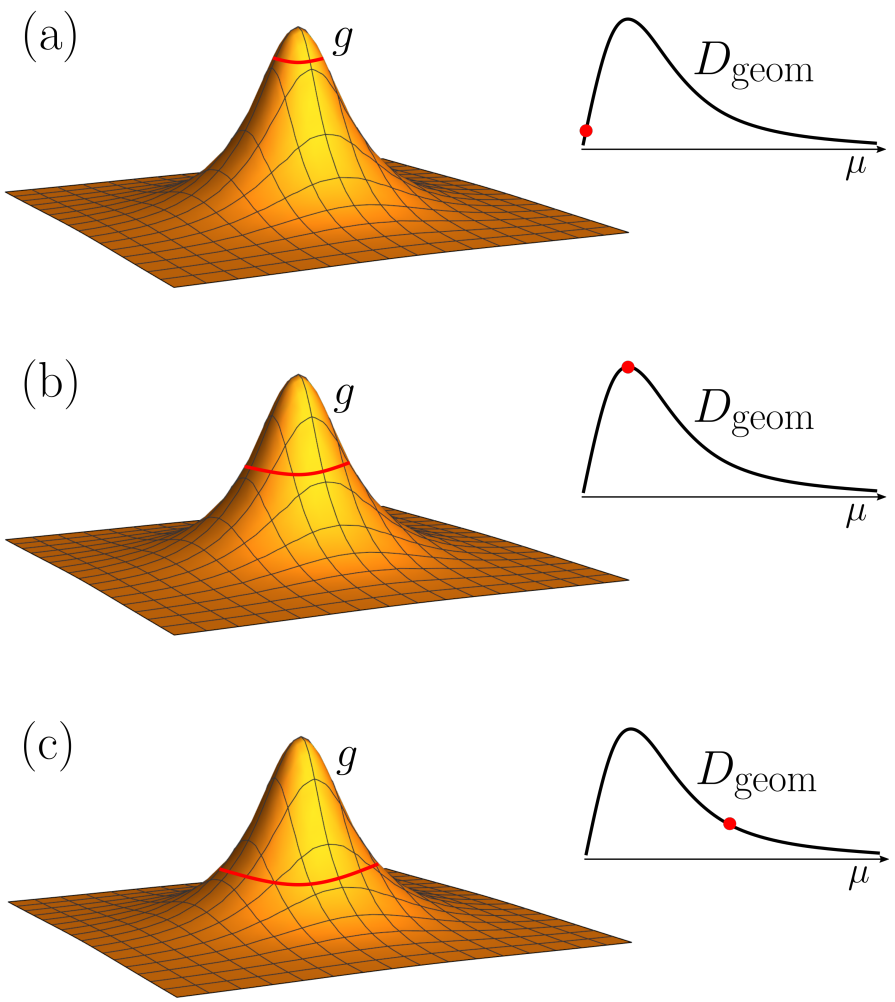

Figure 7.4: Emergence of a dome in the geometric superfluid weight from the Fermi contour contribution (in red) in Eq. (7.28) and its corresponding location in the dome (red dot). (a) Low-μ regime. (b) Intermediate-μ regime. (c) High-μ regime

.

between the height and the extent of the Fermi contour is optimal, and D_{geom} reaches its maximal value. This is the intermediate-μ regime in Fig. 7.4b. Beyond the latter, the Fermi contour still gets wider but not enough to compensate the smaller values of $g_{\mu\nu}$, resulting in a decrease of D_{geom}. This is the high-μ regime in Fig. 7.4c.

7.4.3.4 Qualitative μ-dependence of the BKT temperature

Following the above discussion, we sketch the qualitative evolution of the BKT temperature given by Eq. (7.26) as shown in Fig. 7.5, as a function of the chemical potential.

In order to showcase the role of the geometric part, Fig. 7.5 is a plot of the conventional and geometric contributions in a situation when both quantities are of the same order. We show below that

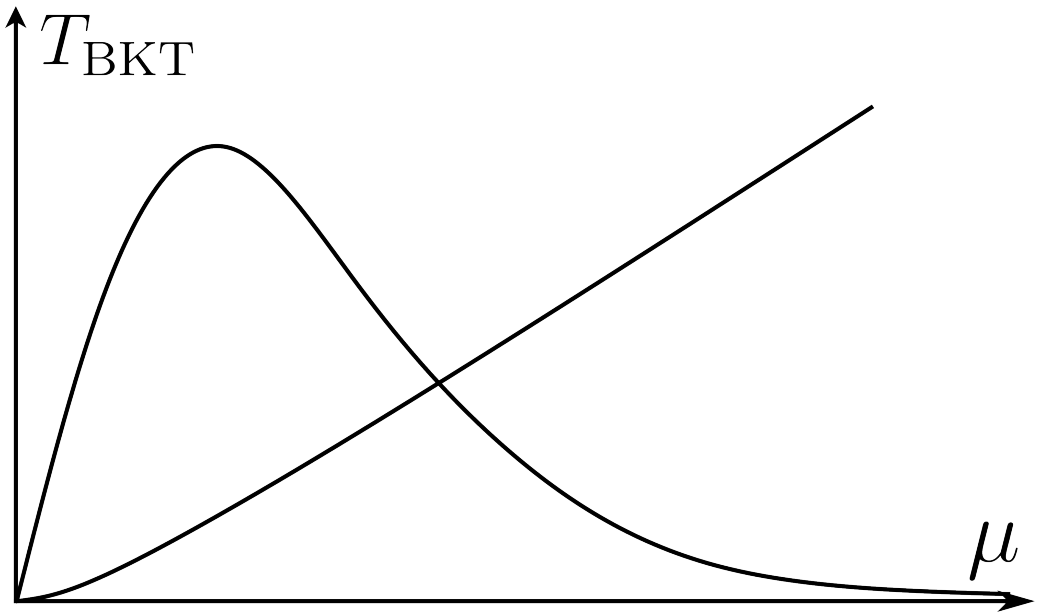

Figure 7.5: Qualitative dependence of the geometric contribution, with a dome behavior, and the conventional contribution, with a linear behavior, to the BKT temperature of Eq. (7.26).

this is the relevant case for the low-energy and full TB model. As one notices, the superfluid weight, and thus the BKT temperature, is dominated by the geometric contribution at low chemical potential and by the conventional contribution at high chemical potential. The conventional contribution grows linearly with the chemical potential while the geometric contribution exhibits a dome.

7.5 . Relating the results to experimental data

7.5.1 . Thermal and disorder effects

Experimental studies of the superconducting transition in (001) and (111) oriented LAO/STO interfaces indicate that the BKT scenario is indeed relevant [202, 218, 219, 220]. The superfluid weight is proportional to the superfluid carrier density n_s. Temperature effects could be included through the temperature dependence of the SC gap and the Fermi factor [221], however disorder effects would also need to be properly included, a task beyond the scope of the present work. Microwave measurements of the London penetration depth by Lesne *et al.* [220] show that the value of n_s at T_{BKT} is one order of magnitude smaller than it is at "zero temperature". These experiments contain, and indicate the relevance of, both disorder and thermal effects. Therefore, one may phenomenologically take these factors into account by applying such a renormalisation to the superfluid density and thus to the superfluid weight. While we do not provide a full-fledged theory of the origin of this reduction of the superfluid density, we take it as an experimental fact, and hereafter we qualitatively renormalize, and thus reduce, both the conventional and geometric contributions to the superfluid weight by a factor 10.

7.5.2 . Superfluid weight from the low-energy model

We now numerically compute both contributions of the superfluid weight for the low-energy model as a function of μ, using Eq. (7.28). The result, plotted in Fig. 7.6, is indeed consistent with the analysis made in Sec.7.4.3. Note that the chemical potential is defined with respect to the Dirac point of the low-energy model, which is slightly above the bottom of the band.

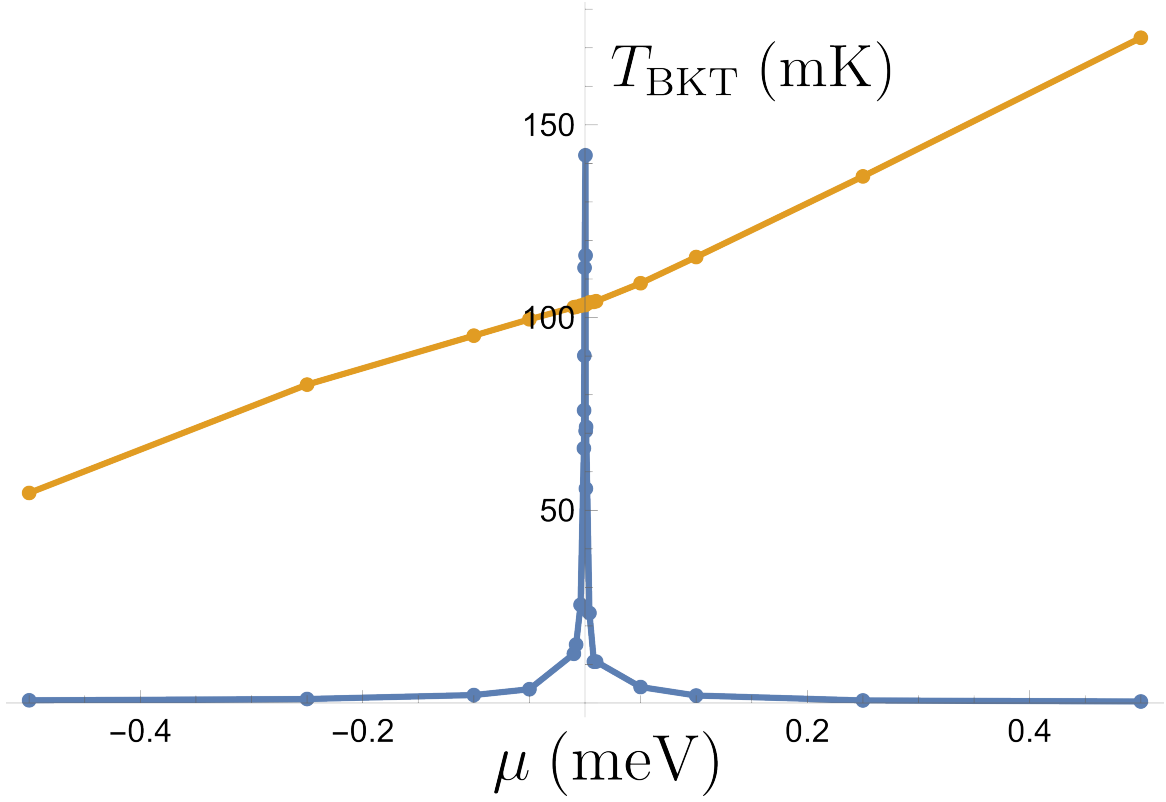

Figure 7.6: Conventional (orange) and geometric (blue) contributions to the superfluid weight from the low-energy model of Eqs. (7.20,7.21) using Eq. (7.28). The chemical potential μ is defined with respect to the Dirac point of the low-energy model. T_{BKT} is defined in Eq. (7.26).

As anticipated, the conventional contribution is essentially linear in the chemical potential μ. Note that it is non-zero below the Dirac point because the minimum of the lower band is located away from the Γ point, as seen in Fig. 7.3. Notice the small dip seen near $\mu = 0$ in Fig. 7.6, which might be due to a reduction of the density of states, because of the Dirac point.

The evolution of the geometric contribution is consistent with the scenario depicted in Sec.7.4.3 and Fig. 7.4. Because of the Dirac point, the quantum metric exhibits a strong (in fact divergent) peak at Γ, i.e. $\mu = 0$ in Fig. 7.6. For $\mu < 0$, the Fermi contour is at the bottom of the metric's peak, so the geometric contribution is low. But then as μ gets closer to zero, the Fermi contour moves to a higher position on the metric's peak. The metric diverges at the degeneracy point so that the geometric contribution diverges at $\mu = 0$. For $\mu > 0$, the Fermi contour gradually moves to the bottom of the peak, and the geometric contribution goes back to zero. All this happens on a scale of 1meV around the Dirac point, as seen in Fig. 7.6. We note that the variation of the geometric contribution is so steep

around $\mu = 0$ that one would need to get to very low values of μ in order to reach the regime where the geometric contribution dominates.

7.5.3 . Superfluid weight from the tight-binding model

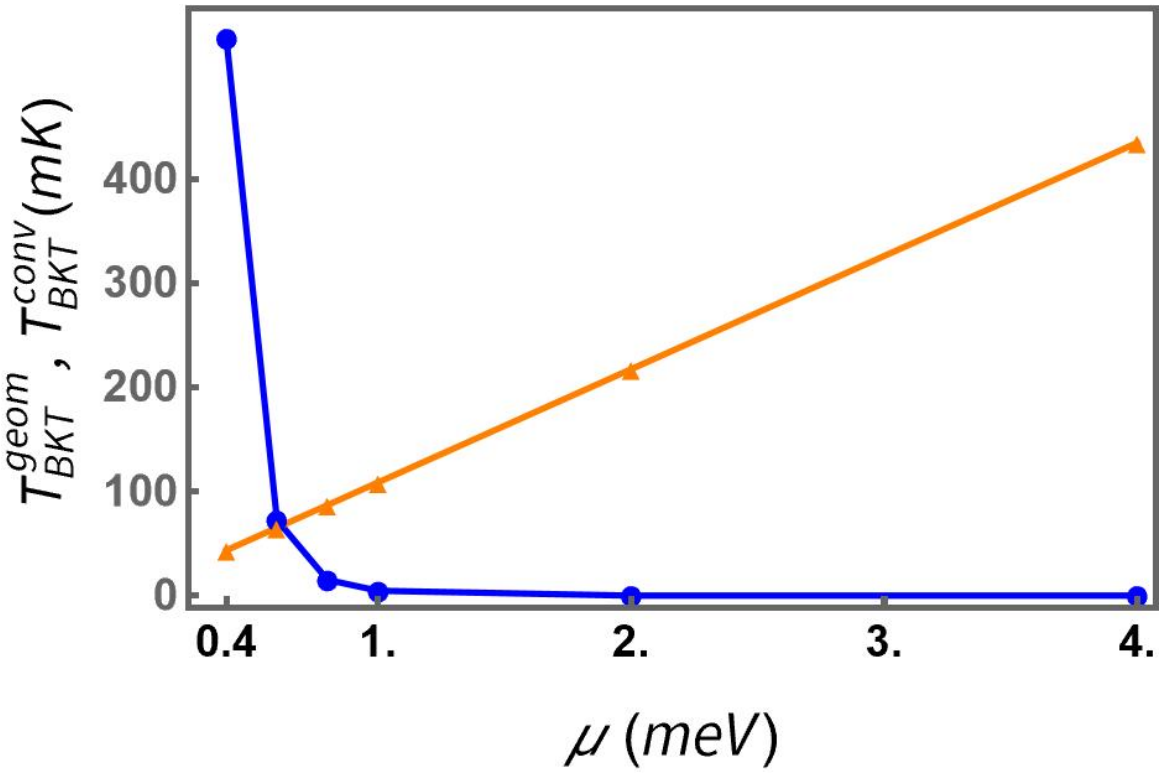

Figure 7.7: Conventional (orange) and geometric (blue) contributions to the superfluid weight from the spinful TB model. The chemical potential μ is defined with respect to the Dirac point of the spinful TB model.

As a test of the accuracy of the low-energy model, we can also compute the superfluid weight from the spinful TB model, as shown in Fig. 7.7. The chemical potential μ is defined with respect to the Dirac point of the spinful TB model. Note that although one would *a priori* have to use the multi-band formulas given in Ref. [207], we chose to use the two-band formula given in Eq. (7.28) in the following way. We took the band dispersions of the full TB model and considered their sum and differences, whose halves give an effective h_0 and h, respectively. We then plug in those along with the quantum metric of the lowest band, coming again from the full TB model, in the two-band formula. We see that our qualitative arguments of section 7.4.3 hold here as well. The geometric contribution shows a divergent behaviour in the $\mu \ll 1$meV regime, and precipitously drops to zero when we increase μ. The conventional contribution is linear in the chemical potential. One difference between Fig. 7.7 and the superfluid weight of the low-energy model is that the two contributions become equal for a larger value of μ. This may be due to the fact that bands in both the anti-bonding group, despite being 7eV higher in energy, and the other bonding bands have a non-negligible overlap with the two

bands of interest. Note that this is also the case for the Berry curvature, where this overlap between the lowest and the highest bands generates a Berry curvature of order a_0^2.

7.5.4 . Gate voltage dependence: Two-dome scenario

We have discussed the qualitative dependence of the BKT temperature [Eq. (7.26)] on the chemical potential. However, the experimentally observed superconducting dome [198, 210, 222, 223, 224] is measured when one tunes the gate voltage V_g or the conductivity of the interface. There are strong indications [210, 211] suggesting that the (Hall) carrier density (or the chemical potential) has a non-monotonic dependence on V_g or on the conductivity. Therefore, there is no simple correspondence between the superconducting domes that result from changing μ and the phase diagram that one obtains upon changing V_g. Based on the dependence of the Hall number on V_g, and that of μ on the carrier density, we propose that the variation of μ with V_g is as depicted in Fig. 7.8a. We emphasize that we discuss a qualitative scenario, based on available experimental data. The quantitative dependence of the chemical potential on the gate voltage is of the foremost importance, in order to get quantitative agreement with experiments.

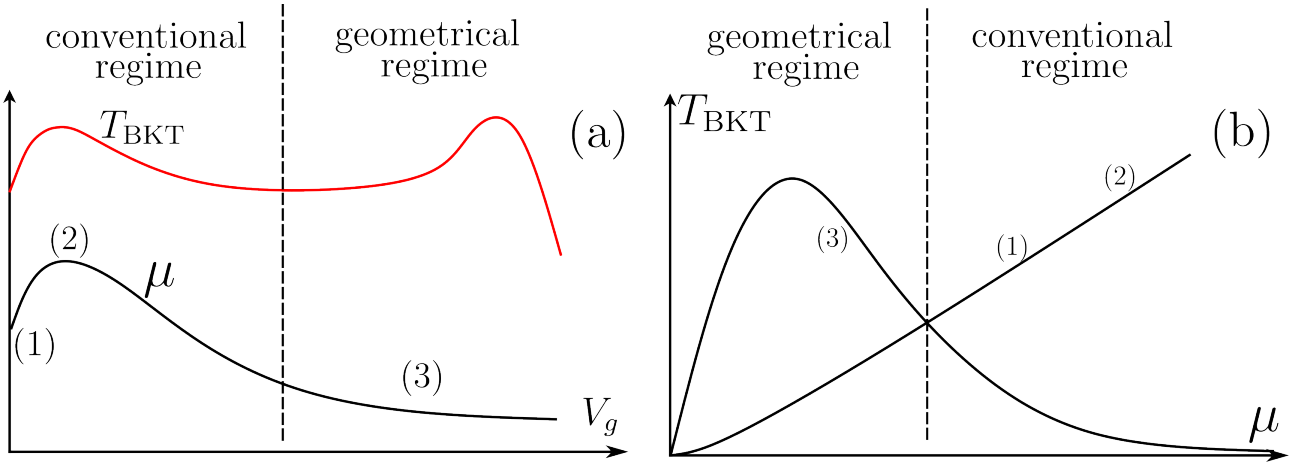

Figure 7.8: (a) Proposed dependence of the chemical potential on the gate voltage, with the resulting BKT temperature in red. (b) Correspondence between the qualitative μ and V_g dependencies of the geometric and conventional contributions. In both (a) and (b) the areas where the geometrical and conventional contributions dominate are outlined. The vertical dashed line in (a) and (b) marks the boundary between the two regimes.

The scenario depicted in Fig. 7.8 may be understood as follows. The initial value of the chemical potential (at $V_g = 0$) is at a point where the conventional contribution dominates, indicated by (1). At first, increasing the gate voltage also increases the chemical potential so that the BKT temperature also increases. This is the *underdoped regime* from (1) to (2). It is followed by the *optimal doping* region near (2), starting around the top of the dome. Further increase of the gate voltage leads to a *decrease* of the chemical potential, due to the non-monotonic relation between V_g and μ, and therefore to lower values of the BKT temperature, in the *overdoped regime*, from (2) to (3). Once again,let us stress that our qualitative plot of the evolution of μ with V_g is a rendition of the experimental curve. There could be a saturation of the chemical potential, which would result in a saturation of the superfluid weight.

The resulting qualitative gate-voltage dependence of the BKT temperature (Eq. (7.26)) is then sketched in Fig. 7.9.

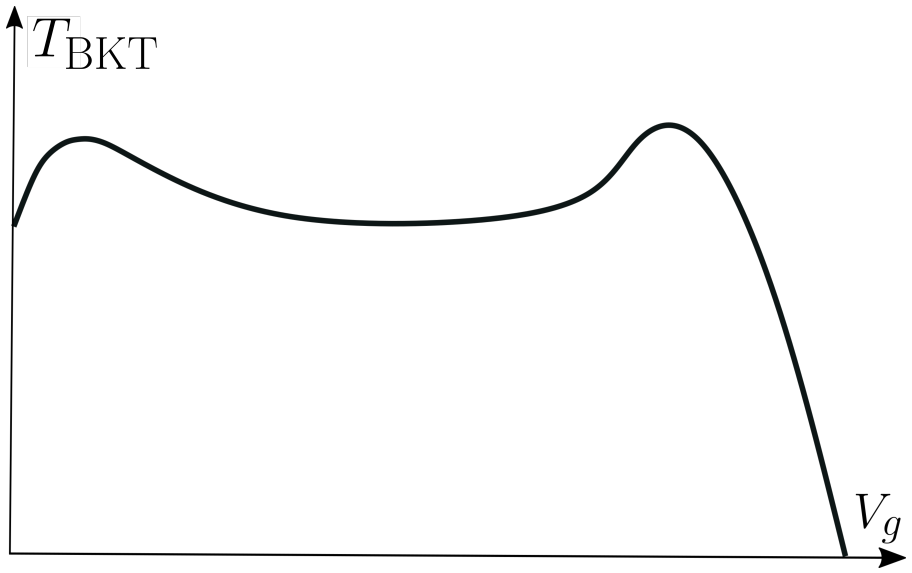

Figure 7.9: Schematic view of the proposed qualitative evolution of the BKT temperature as a function of the gate voltage.

We can draw further conclusions from this scenario. The experimentally observed dome happens in a regime when the conventional contribution dominates. But if we follow the experimental evidence indicating that μ decreases as V_g increases, we could reach the low-μ regime at higher V_g and reveal the dome due to the geometric contribution. In other words, the measured domes would be caused by the non-monotonic variation of the chemical potential with respect to the gate voltage such that there should be a *secondary superconducting dome*, coming from the geometric contribution, for higher values of the gate voltage. The evolution of the critical temperature (or superfluid density, BKT temperature) would be similar to that sketched in Fig. 7.9, as long as only the lowest energy band contributes to the superfluid condensate.

According to our picture, the two superconducting domes that one expects upon increasing the gate voltage have thus different origins. The first one corresponds to the regime when the conventional superfluid weight dominates and the second one to the regime when the geometric weight dominates.

7.6 . Conclusion

This chapter underscores the impact of the normal state quantum geometry on the superconducting state of the (111) $LaAlO_3/SrTiO_3$ interface, and possibly other (111) oxide interfaces. Building upon a tight-binding modeling of the interface, we developed a two-band low-energy model around the Γ point. This low-energy model reveals an isotropic Dirac cone at the Γ point, driven by the orbital mixing. From the low-energy model, we then drew a qualitative scenario for the chemical potential

(μ) dependence of the conventional and geometric contributions to the superfluid weight. The conventional contribution is suggested to be linear in μ, because of the dispersion's isotropy. We also argued that the strong peak in the quantum metric coming from the Dirac cone results in a dome-shaped behavior of the geometric contribution as a function of μ.

Finally, we probed the relevance of our scenario to experiments in the case of the LAO/STO interface. We first effectively took into account thermal and disorder effects by renormalizing the superfluid weight. Then, we numerically computed the superfluid weight from the two-band low-energy model and the spinful TB model. In both cases, we find the right order of magnitude for the superfluid weight (and the associated BKT temperature). The most significant difference between the two models is the value of μ below which the geometric contribution becomes dominant. In the low-energy model, the geometric contribution exhibits a very narrow peak around $\mu = 0$ and therefore the regime where it dominates would seem hard to observe, in practice. In the spinful TB model, bands from the anti-bonding group, despite being $6-7$ eVs higher up, and other bonding bands, contribute significantly to the quantum metric of the lowest Kramers' partners, thereby making the geometric contribution less steep and increasing the value of chemical potential below which the geometric contribution dominates. We then argue that, despite its simplicity, our low-energy model captures the evolution of the superfluid weight reasonably well.

Experiments tune the 2DEG with a gate voltage V_g, so that we aimed to qualitatively describe the behaviour of the superfluid weight as a function of said V_g. Hall transport experiments [210, 211] find a non-monotonic dependence of the Hall carrier density on V_g. Assuming that the Hall carrier density is monotonic in the chemical potential, this means that the chemical potential is non-monotonic in V_g. Taking this as an experimental fact, we then inferred a qualitative dependence of the superfluid weight (and thus BKT temperature) on the gate voltage. The experimentally observed dome is suggested to come from the conventional contribution and the non-monotonic dependence of μ on V_g. Extrapolating further, we also suggest the saturation of the dome mentioned earlier and the appearance of a *second superconducting dome*, due purely to the geometric contribution to the superfluid weight.

Given the ubiquituousness of quantum geometry, this *hidden influence* on the superconducting state might be apparent in other classes of materials. Finally, this positive effect of the normal-state quantum metric on superconductivity contrasts with Chapter 6, where we saw a negative impact of the normal-state Berry curvature on superconductivity. This suggests a *normal state curvature-metric competition* towards superconductivity.

8 - Normal state quantum geometry and superconductivity through non-locality

8.1 . Introduction

From the preceding Chapters 6 and 7, we may infer lingering open questions on the relation between the quantum geometry of the normal state and the superconducting phase. We note that other effects than those studied in this manuscript, such as non-linear transport, have been discovered, see Refs. [118, 162, 225, 226, 227]. We have found in Chapter 6 that the normal state Berry curvature weakens the superconducting phase by weakening the attractive interaction. In contrast, the normal state quantum metric enhances the superconducting phase by carrying an alternative source of supercurrent, one that persists even in flat-band systems [29, 168, 169, 207, 209]. We have found in Chapter 7 that in a class of materials it even drives a superconducting dome, a hallmark of superconductivity. These two facts suggest an ambivalent effect of the normal state quantum geometry on superconductivity, through a curvature-metric competition. Another open question is the general form of the renormalization of the pairing interaction derived in Chapter 6. Indeed, while the massive Dirac fermions model we considered applies to a wide range of materials, it is by no means general. Finally, the matter of the physical interpretation of both effects is arguably still an open question. Indeed, while the geometric superfluid weight and its related topological bound have been, in flat-band systems, linked with the spread of Wannier functions [29, 169], its physical meaning remains relatively obscure. We may thus explicitely formulate several open questions. *How is the pairing interaction renormalized by the normal state quantum geometry, in a general model ? How can we physically understand this renormalization ? What is the physical origin of the geometric superfluid weight ? Why is the quantum metric involved, and how is it that the contribution persists in flat-band systems, where charge carriers should be immobile ? Is there really a normal state curvature-metric competition towards the superconducting phase ?*

Our objective in this work is to shed light on these questions, and we do so based on Chapter 2. First, we briefly restate the results obtained in the second viewpoint developed in Section 2.4.2. The quantum geometric tensor was proved to be the covariance matrix of a dressed position operator $\hat{R}_\mu$ in the Bloch state $|\psi_n(\boldsymbol{k})\rangle$. The operator $\hat{R}_\mu$ approximatively reduces to the actual position operator $\hat{r}_\mu$ in the limit of a low-energy model, a regime often considered, as is the case in Chapters 6 and 7. The band quantum geometry then appears as a consequence, and quantifier, of the quantum fluctuations of the Bloch fermion's position, i.e. its non-locality.[1] When imagined over time, these quantum fluctuations may be thought of as the *zero-point motions* of the Bloch fermion. Using the uncertainty relation, we have then shown that the (diagonal) quantum metric quantifies the *typical* zero-point motion in a given direction, while the Berry curvature draws an area of *minimal* zero-point motion. It is interesting to note that somewhat similar relationships were put forward in Refs. [25, 228, 229, 230]. However, an important difference is that the relations in these works appear through integrations

[1]The non-locality itself being induced by virtual interband transitions, as argued in the third viewpoint, in Section 2.4.3

over the momentum or the energy. Our relations have the advantage of being inherently local in momentum space, and more straightforward in terms of manipulation and physical interpretation.

Once the interpretation of quantum geometry in terms of non-locality is re-established, we tackle the interpretation of the superfluid weight. The conventional and geometric superfluid weights then naturally appear as originating from two independent movements of the Bloch fermions. The conventional superfluid weight, through the group velocity $\boldsymbol{v}_n = 1/\hbar\partial_{\boldsymbol{k}}\epsilon_n$, corresponds to an overall motion of the Bloch wavepackets composing the Cooper pairs, as pictured in Fig.8.1. The geometric superfluid weight appears as originating from the zero-point motions of the Bloch fermion, as pictured in Fig.8.2. This observation explains why it is the quantum metric that appears, as it is the typical zero-point motions of the Bloch fermions that matter. The topological bound can also be explained along those lines, as the Berry curvature ensures a minimum of zero-point motion, and thus of supertransport. Finally, we can also simply explain why the geometric superfluid weight persists in flat-band systems. Indeed, a flat-band system means a constant energy dispersion, i.e. no group velocity. The zero-point motions are completely independent of the latter, and can thus persist when it is absent. We may also point out that it thus seems natural that the geometric contribution is most often subdominant compared to the conventional contribution, since zero-point motions are typically weaker than overall movements of the wavepacket.

Subsequently, we handle the interpretation and generalization of the emergent Darwin term studied in Chapter 6. To do so we make use of the phenomenological derivation of the Darwin term for vacuum electrons in relativistic quantum mechanics [54]. Proceeding similarly, we formulate a general one-body problem in an external potential and derive an effective Hamiltonian containing an emergent Darwin term due to the quantum metric, as $g^n_{\mu\nu}\partial_\mu\partial_\nu V$. The interpretation of this term is then in direct analogy with the case of electrons in relativistic quantum mechanics [54]. As erratic and virtual interband transitions occur, the Bloch fermion is not purely localizable, resulting in quantum fluctuations of its position. Since these fluctuations are linked to the quantum metric, the external potential felt by the Bloch fermion is smeared due to the latter, through an emergent Darwin term. The emergent Darwin term has therefore the exact same origin as the geometric superfluid weight, the non-locality of the Bloch fermions composing the Cooper pairs. Consequently, the curvature-metric competition we anticipated is in fact not occuring, as both effects come from the quantum metric. Both effects are thus two sides of the same coin. Building on the one-body problem, we study a two-body problem in order to generalize the results obtained in Chapter 6, and obtain a general form of the effective pairing interaction, which is indeed smeared by the emergent Darwin term. Finally, we exemplify our results and get a revised deformation of the pairing strength for two-dimensional massive Dirac fermions.

The Chapter is organized as follows. In Section 8.2, we summarize the interpretation of band quantum geometry in terms of non-locality, as obtained in Sec.2.4.2. In Section 8.3, we discuss the resulting interpretation of the conventional and geometric superfluid weights, and rederive the topological bound on the geometric contribution. In Section 8.4, we phenomenologically derive the general form of the emergent Darwin term in a one-body problem and obtain a general form for the effective pairing interaction, following the approach of the Cooper problem. Finally, we exemplify our results on two-dimensional massive Dirac fermions.

8.2 . Band quantum geometry and non-locality

In the second viewpoint of Chapter 2, in Section 2.4.2, we have shown that the quantum geometric tensor $Q^n_{\mu\nu}$ can be expressed as the covariance matrix within the Bloch state $|\psi_n\rangle$ of a dressed position operator $\hat{R}_\mu$. More precisely, we have

$$Q^n_{\mu\nu} = \langle\psi_n|\,\hat{R}_\mu\hat{R}_\nu\,|\psi_n\rangle - \langle\psi_n|\,\hat{R}_\mu\,|\psi_n\rangle\,\langle\psi_n|\,\hat{R}_\nu\,|\psi_n\rangle = \mathrm{Cov}_{|\psi_n\rangle}\left(\hat{R}_\mu, \hat{R}_\nu\right), \tag{8.1}$$

where we make the $\boldsymbol{k}$ dependences implicit, and the Hermitian operator $\hat{R}_\mu$ is expressed as

$$\hat{R}_\mu = \int_0^1 e^{-is\boldsymbol{k}\cdot\hat{\boldsymbol{r}}}\hat{r}_\mu e^{is\boldsymbol{k}\cdot\hat{\boldsymbol{r}}}\mathrm{d}s = \sum_{n=0}^{\infty}\frac{i^n}{(n+1)!}\,\mathrm{ad}^n_{\boldsymbol{k}\cdot\hat{\boldsymbol{r}}}\,\hat{r}_\mu. \tag{8.2}$$

We emphasize that the covariance matrix is taken in the actual Bloch state $|\psi_n\rangle$, and not its cell-periodic counterpart $|u_n\rangle$. In the low-energy regime where $k \ll 1$, we may approximate $\hat{R}_\mu$ by the leading term, which gives

$$k \ll 1 \;\;\Rightarrow\;\; \hat{R}_\mu \simeq \hat{r}_\mu \;\;\Rightarrow\;\; Q^n_{\mu\nu} \simeq \mathrm{Cov}_{|\psi_n\rangle}(\hat{r}_\mu, \hat{r}_\nu). \tag{8.3}$$

Consequently, in the low-energy regime we may identify $\hat{R}_\mu$ as the position operator $\hat{r}_\mu$. The quantum geometric tensor then quantifies the quantum fluctuations of the position operator within the Bloch state $|\psi_n\rangle$, and that of the Bloch fermion, since $|\psi_n\rangle$ physically represents the latter. We assume such a regime in the remainder of the chapter.

The Berry curvature and diagonal quantum metric then respectively appear as the averaged commutator of the position operator's comments and as the squared standard deviation of the position operator in the associated direction $\sigma^2_n(\hat{r}_\mu)$,

$$\mathcal{B}^n_{\mu\nu} = i\,\langle\psi_n|\left[\hat{r}_\mu, \hat{r}_\nu\right]|\psi_n\rangle\,, \;\; g^n_{\mu\mu} = \langle\psi_n|\,\hat{r}^2_\mu\,|\psi_n\rangle - \langle\psi_n|\,\hat{r}_\mu\,|\psi_n\rangle^2\,. \tag{8.4}$$

The diagonal quantum metric thus quantifies the non-locality of the Bloch fermion in a given direction. Applying the Robertson-Schrödinger uncertainty relation yields

$$\sigma_n(\hat{r}_\mu)\sigma_n(\hat{r}_\nu) \geq \frac{1}{2}\left|\langle\left[\hat{r}_\mu, \hat{r}_\nu\right]\rangle_{\psi_n}\right| \;\;\Leftrightarrow\;\; \sqrt{g^n_{\mu\mu}g^n_{\nu\nu}} \geq \frac{1}{2}|\mathcal{B}^n_{\mu\nu}|. \tag{8.5}$$

Since the square root $\sqrt{g^n_{\mu\mu}}$ gives the typical length of delocalization in the direction μ, the product $\sqrt{g^n_{\mu\mu}g^n_{\nu\nu}}$ gives the typical area of delocalization. As such the uncertainty principle implies that the Berry curvature puts a lower bound on this area, thereby forming a *minimal area of delocalization*.

8.3 . Interpretation of the superfluid weight

From the London equation $\boldsymbol{j}_s = D\boldsymbol{A}$, we see that the superfluid weight of a given band $D^n_{\mu\nu}$ describes how supertransport, transport of Cooper pairs, arises. Naturally, transport corresponds to a movement of charge carriers. Here, we use Section 8.2 to interpret the two contributions of the superfluid weight as arising from two different kinds of motion of the Bloch states forming the Cooper pairs. For simplicity we write the superfluid weight at zero temperature, but our arguments also hold for non-zero temperature.

8.3.1 . Conventional contribution

The conventional contribution to the superfluid weight of the n-th band is given by [207]

$$D^n_{\text{conv},\mu\nu} = \sum_{\boldsymbol{k}} \frac{\Delta^2}{(\epsilon_n^2 + \Delta^2)^{3/2}} \partial_\mu \epsilon_n \partial_\nu \epsilon_n, \tag{8.6}$$

with Δ the superconducting gap. The group velocity of the Bloch state may be defined as $1/\hbar\partial_{\boldsymbol{k}}\epsilon_n$. Eq. (8.6) then hints that the conventional superfluid weight comes from the group velocity of the Bloch wavepacket [29], i.e. an overall/center-of-mass movement, as visualized in Fig. 8.1.

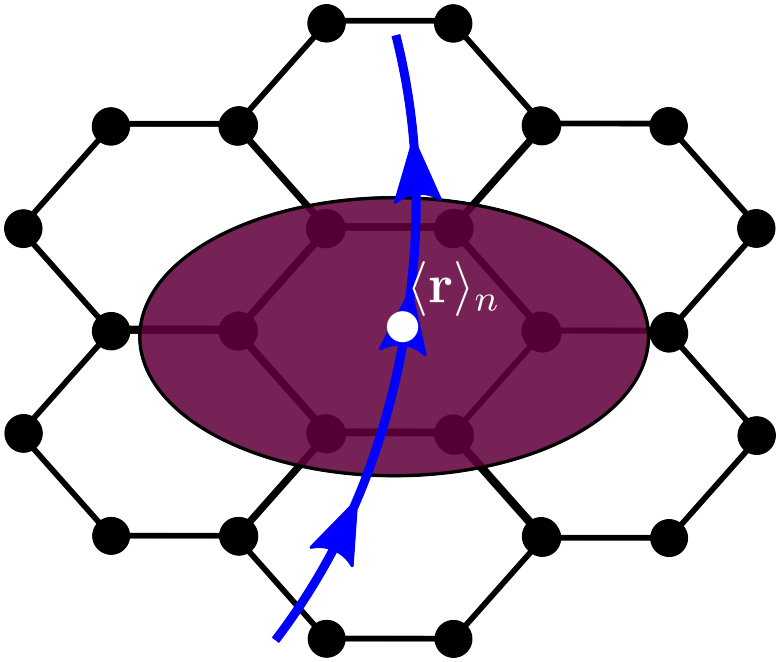

Figure 8.1: The conventional contribution is associated with an center-of-mass movement of the Bloch wavepacket, i.e. a movement of its center position. Illustration on a two-dimensional plane.

8.3.2 . Geometric contribution

In the so-called isolated band limit, where the n-th band is sufficiently separated in energy from the others, the geometrical contribution to the superfluid weight reads [207]

$$D^n_{\text{geom},\mu\nu} = \sum_{\boldsymbol{k}} \frac{4\Delta^2}{\sqrt{\epsilon_n^2 + \Delta^2}} g^n_{\mu\nu}. \tag{8.7}$$

The metric being the source of zero-point motion, it then stands to reason to state that the geometric superfluid weight describes the supertransport originating from the zero-point motion of the Bloch states forming the Cooper pairs, as pictured in Fig.8.2. We can therefore identify geometrical supertransport as uncertainty-driven supertransport. On one hand, this observation also explains why the geometric contribution persists even in flat-band systems, where the center position stays immobile

but zero-point motion can still occur. Consequently, the charge carriers are not strictly immobile in the case of a flat band. On the other hand, the observation also explains why it is the normal state quantum metric that gives rise to the geometric superfluid weight, as we expect the typical zero-point motion to appear instead of the minimal ones.

The role of the Berry curvature and Chern number as a topological lower bound [29, 207] may be rederived from the trace inequality in Eq. (2.43). Indeed, on a two-dimensional plane we have

$$\mathrm{Tr}\, D^n_{\mathrm{conv}} = D^n_{\mathrm{geom},\mu\mu} + D^n_{\mathrm{geom},\nu\nu} = \sum_{\boldsymbol{k}} \frac{4\Delta^2}{\sqrt{\Delta^2+\epsilon_n^2}}\, \mathrm{Tr}\, g^n \geq \sum_{\boldsymbol{k}} \frac{4\Delta^2}{\sqrt{\Delta^2+\epsilon_n^2}} |\mathcal{B}^n_{\mu\nu}|, \tag{8.8}$$

which, in an isotropic system where $D^n_{\mathrm{geom},\mu\nu} = D^n_{\mathrm{geom}}\delta_{\mu\nu}$, we have

$$D^n_{\mathrm{geom}} \geq \sum_{\boldsymbol{k}} \frac{2\Delta^2}{\sqrt{\Delta^2+\epsilon_n^2}} |\mathcal{B}^n_{\mu\nu}|. \tag{8.9}$$

which is the lower bound established in Refs. [29, 207], up to a factor of two due to the different definition of the QGT in Refs. [29, 207]. This lower bound can directly be understood as a translation of the fact that since the Berry curvature ensures a miminum amount of nonlocality, i.e. zero-point motion, there is a minimal amount of (geometrical) supertransport.

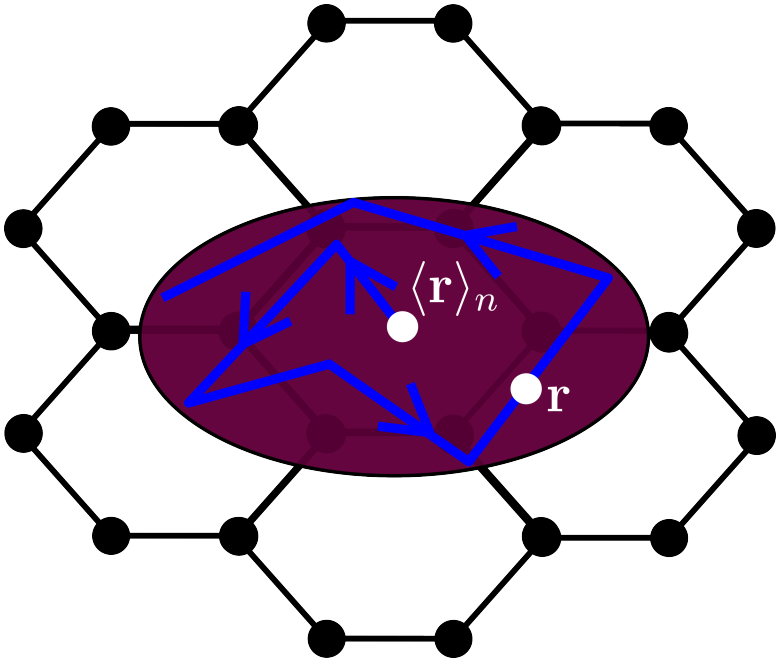

Figure 8.2: The geometric contribution describes supertransport coming from the quantum metric, which in turn comes from the quantum fluctuations of the position of the Bloch wavepacket. These quantum fluctuations can be pictured as zero-point motions, a "jittering" of the true position while the position center stays still.

8.4 . Emergent Darwin term

Based on Section 8.2, we now aim to generalize the results obtained in Chapter 6 on the renormalization of the pairing interaction through an emergent Darwin term. To this end, we aim to formulate the general form of the emergent Darwin term, its resulting interpretation and see its effects on the pairing interaction.

8.4.1 . One-body problem

We begin by investigating a one body problem following Ref. [54], where the Darwin term of elementary electrons was phenomenologically derived from its inherent non-locality in relativistic quantum mechanics.

8.4.1.1 General derivation

We follow the phenomenological discussion of Ref. [54] and consider a Bloch state under a potential $V(\boldsymbol{r})$,

$$\epsilon_n \left|\psi_n\right\rangle \left\langle\psi_n\right| + V(\boldsymbol{r}). \tag{8.10}$$

Projecting onto the Bloch state, we find

$$H_1 = \epsilon_n + \left\langle\psi_n\right| V(\boldsymbol{r}) \left|\psi_n\right\rangle . \tag{8.11}$$

We now write $\boldsymbol{r} = \langle\boldsymbol{r}\rangle_n + \boldsymbol{\delta r}$ and expand V to second order around $\langle\boldsymbol{r}\rangle_n = \left\langle\psi_n\right| \boldsymbol{r} \left|\psi_n\right\rangle$. The first order term vanishes, and we are therefore left with the following,

$$H_1 = \epsilon_n + V(\langle\boldsymbol{r}\rangle_n) + \frac{\left\langle\psi_n\right| \delta r_\mu \delta r_\nu \left|\psi_n\right\rangle}{2} \partial_\mu \partial_\nu V(\langle\boldsymbol{r}\rangle_n), \tag{8.12}$$

with $\partial_\mu = \partial_{r_\mu}$. Note that we make use of Einstein's summation convention. We recognize the covariance matrix of the position operator in the second order Taylor coefficient, which implies

$$H_1 = \epsilon_n + V(\langle\boldsymbol{r}\rangle_n) + \frac{1}{2} Q^n_{\mu\nu} \partial_\mu \partial_\nu V(\langle\boldsymbol{r}\rangle_n). \tag{8.13}$$

Furthermore, assuming the potential V to be of class $\mathcal{C}^2$ around $\langle\boldsymbol{r}\rangle_n$, we can use the symmetry of the partial derivatives under permutations to get

$$\begin{aligned} H_1 &= \epsilon_n + \frac{1}{2} g^n_{\mu\mu} \partial^2_\mu V(\langle\boldsymbol{r}\rangle_n) + \sum_{\mu<\nu} \frac{Q^n_{\mu\nu} + Q^n_{\nu\mu}}{2} \partial_\mu \partial_\nu V(\langle\boldsymbol{r}\rangle_n) \\ &= \epsilon_n + \frac{1}{2} g^n_{\mu\mu} \partial^2_\mu V(\langle\boldsymbol{r}\rangle_n) + \sum_{\mu<\nu} g^n_{\mu\nu} \partial_\mu \partial_\nu V(\langle\boldsymbol{r}\rangle_n). \end{aligned} \tag{8.14}$$

The effective one-body Hamiltonian is then obtained by replacing $\langle\boldsymbol{r}\rangle_n$ with $\boldsymbol{r}$. Note that the Darwin term obtained in Eq. (8.14) is reminiscent of terms appearing in Refs. [175, 231].

8.4.1.2 2D massive Dirac fermions

We go back to two-dimensional massive Dirac fermions in order to compare Eq. (8.14) with the results of Chapter 6. Again, the low-energy Hamiltonian is given by

$$H = \boldsymbol{h} \cdot \boldsymbol{\sigma}, \quad \boldsymbol{h} = |\Delta|\big(\lambda\!\!\!^{-}_c k_x, \lambda\!\!\!^{-}_c k_y, \operatorname{sgn}\Delta\big), \tag{8.15}$$

with Δ the band gap and $\lambda\!\!\!^{-}_c = \hbar v/|\Delta|$ the reduced Compton length. In this low-energy model, we remind the reader that the quantum metric is given by

$$g^n_{\mu\nu} = \frac{\lambda\!\!\!^{-2}_c}{4} \frac{(1+\lambda\!\!\!^{-2}_c k^2)\delta_{\mu\nu} - \lambda\!\!\!^{-2}_c k_\mu k_\nu}{(1+\lambda\!\!\!^{-2}_c k^2)^2}. \tag{8.16}$$

In Chapter 6, the prefactor of the Darwin term found was the Berry curvature at $k = 0$. The quantum metric at $k = 0$ becomes $g^n_{\mu\nu} = \lambda\!\!\!^{-2}_c/4\delta_{\mu\nu}$, so that Eq. (8.14) reads

$$H_1 = \epsilon + V(\boldsymbol{r}) + \frac{\lambda\!\!\!^{-2}_c}{4}\Delta V(\boldsymbol{r}), \tag{8.17}$$

which only differs from the result of Chapter 6 by a factor of two. This difference may come from the phenomenological character of the derivation, also present in the case of vacuum electrons [54]. The similarity between the Darwin term derived in Chapter 6 and the generalized one likely stems from the fact that, as we have shown in Section 2.6, that the quantum geometry of massive Dirac fermions near the origin is optimal, i.e. it saturates the trace and determinant inequalities.

8.4.1.3 Interpretation

We can interpret the emergence of the Darwin term by following the case of the elementary electron [54]. In relativistic quantum mechanics, quantum fluctuations induce erratic creation and annihilation of virtual electron-positron pairs. Between two such events, the pair *typically* travels a distance known as the Compton wavelength. As these virtual processes have no physical bearing, one cannot localize an electron on a length smaller than the Compton wavelength. We can thereby picture a blurred surface around the average position of the electron, in which the actual position quantum fluctuates. It is this non-locality coming from these virtual electron-positron transitions that cause the appearance of the Darwin term. We can make a similar argument for Bloch fermions. Because of erratic interband transitions, the Bloch fermion also harbors an area of *typical* quantum fluctuations of the position. As shown in Section 8.2, the length is given by the quantum metric (specifically its square root). The Bloch fermion therefore exhibits an analogue of relativistic quantum mechanics due to its quasi-ness. When the band structure is that of a massive Dirac fermion, the analogy with the vacuum electron becomes direct, the interband transitions are the positron-electron annihilations and creations, and the square root of the quantum metric becomes the Compton wavelength. These quantum fluctuations, resulting in a non-locality of the Bloch wavepacket, therefore result in an *emergent Darwin term*, as described by Eq. (8.14).

Since the emergent Darwin term expressed in Chapter 6 involved the modulus of the Berry curvature, and would therefore correspond to *minimal* quantum fluctuations, and not typical ones. The

effect of the Darwin term on the superconducting phase may thus be greater than described in Chapter 6, thereby raising the need to revisit the two-body problem.Note that while we discuss the case where the potential V is the pairing interaction, the results discussed so far, including the emergent Darwin term, also apply to any potential. This emergent Darwin term may therefore have important effects on other correlated phases, such as charge density waves, or affect other types of potentials.

8.4.2 . Two-body problem

We now tackle a two-body problem. Having superconductivity in mind, without spin-orbit coupling, we consider an intraband two-body problem involving the Bloch states $|\psi_{n\uparrow}(\boldsymbol{k})\rangle$ and $|\psi_{n\downarrow}(-\boldsymbol{k})\rangle$ under a central potential $V(\boldsymbol{r}_1 - \boldsymbol{r}_2)$. We first find an effective two-body Hamiltonian and then tackle the Cooper problem, following Chapter 6 and Ref. [7].

8.4.2.1 Effective Hamiltonian

The two-body Hamiltonian then reads

$$\epsilon_{n\uparrow}(\boldsymbol{k})\mathcal{P}_{n\uparrow}(\boldsymbol{k}) + \epsilon_{n\downarrow}(-\boldsymbol{k})\mathcal{P}_{n\downarrow}(-\boldsymbol{k}) + V(\boldsymbol{r}_1 - \boldsymbol{r}_2), \tag{8.18}$$

with $\mathcal{P}_{n\sigma}(\boldsymbol{k}) = |\psi_{n\sigma}(\boldsymbol{k})\rangle \langle\psi_{n\sigma}(\boldsymbol{k})|$. Assuming time-reversal symmetry, we have $\mathcal{P}_{n\downarrow}(-\boldsymbol{k}) = \mathcal{P}_{n\uparrow}(\boldsymbol{k}) = \mathcal{P}_n(\boldsymbol{k})$ and $\epsilon_{n\downarrow}(-\boldsymbol{k}) = \epsilon_{n\uparrow}(\boldsymbol{k}) = \epsilon_n(\boldsymbol{k})$. As in the one-body problem, we can then project Eq. (8.18) to find

$$H_2 = 2\epsilon_n(\boldsymbol{k}) + \langle\psi_n(\boldsymbol{k})| V(\boldsymbol{r}_1 - \boldsymbol{r}_2) |\psi_n(\boldsymbol{k})\rangle . \tag{8.19}$$

In appendix G.1, we show that expanding the potential to second order in $\boldsymbol{\rho} = \boldsymbol{r}_1 - \boldsymbol{r}_2$, and assuming the quantum fluctuations of the two Bloch states to be uncorrelated, we find the effective Hamiltonian to be

$$H_2 = 2\epsilon_n(\boldsymbol{k}) + V(\boldsymbol{\rho}) + Q^n_{\mu\nu}(\boldsymbol{k})\partial_{\rho_\mu}\partial_{\rho_\nu}V(\boldsymbol{\rho}), \tag{8.20}$$

with $Q^n_{\mu\nu}(\boldsymbol{k}) = Q^{n\uparrow}_{\mu\nu}(\boldsymbol{k}) = Q^{n\downarrow}_{\mu\nu}(-\boldsymbol{k})$ the spinless QGT. Again, using the symmetry of the derivatives under permutations, and making the $\boldsymbol{k}$-dependences implicit, we find

$$H_2 = 2\epsilon_n + V(\boldsymbol{\rho}) + g^n_{\mu\mu}\partial^2_{\rho_\mu}V(\boldsymbol{\rho}) + 2\sum_{\mu<\nu} g^n_{\mu\nu}\partial_{\rho_\mu}\partial_{\rho_\nu}V(\boldsymbol{\rho}). \tag{8.21}$$

8.4.2.2 Cooper problem: example of 2D massive Dirac fermions

We can now tackle the Cooper problem, again following Chapter 6 and Ref. [7]. For simplicity, and in order to compare with Chapter 6, we will restrict our discussion to two-dimensional massive Dirac fermions. The pair wavefunction $\Psi(\boldsymbol{\rho})$, with energy E, and the pairing potential are Fourier-decomposed as follows,

$$\Psi(\boldsymbol{\rho}) = \sum_{\boldsymbol{k}} g_{\boldsymbol{k}} e^{i\boldsymbol{k}\cdot\boldsymbol{\rho}}, \quad V(\boldsymbol{\rho}) = \sum_{\boldsymbol{k},\boldsymbol{k}'} V_{\boldsymbol{k}\boldsymbol{k}'} e^{i(\boldsymbol{k}-\boldsymbol{k}')\cdot\boldsymbol{\rho}}. \tag{8.22}$$

The eigenvalue equation with the effective Hamiltonian in Eq. (8.20) then yields

$$\big(E - 2\epsilon_n\big) g_{\boldsymbol{k}} = \sum_{\boldsymbol{k}'} V^{\text{eff}}_{\boldsymbol{k}\boldsymbol{k}'} g_{\boldsymbol{k}'}, \tag{8.23}$$

with the effective interaction

$$V^{\text{eff}}_{\boldsymbol{k}\boldsymbol{k}'} = \left[1 - g^n_{\mu\mu}(\boldsymbol{k})(k_\mu - k'_\mu)^2 - 2\sum_{\mu<\nu} g^n_{\mu\nu}(\boldsymbol{k})(k_\mu - k'_\mu)(k_\nu - k'_\nu)\right] V_{\boldsymbol{k}\boldsymbol{k}'}. \tag{8.24}$$

Therefore, as in Chapter 6 and as pictured in Fig.8.3, the pairing of non-local Bloch wavepackets with strength V is, from the point of view of BCS theory, mappable to a pairing of *local* wavepackets with an effective pairing strength that is generically *lower* than V. Note that, unlike the case of vacuum electrons where V is the Coulomb repulsion and only the s-state is affected by the Darwin term, the emergent Darwin term may also affect other states because V is not necessarily the Coulomb repulsion. Moving on, we then find the self-consistency equation

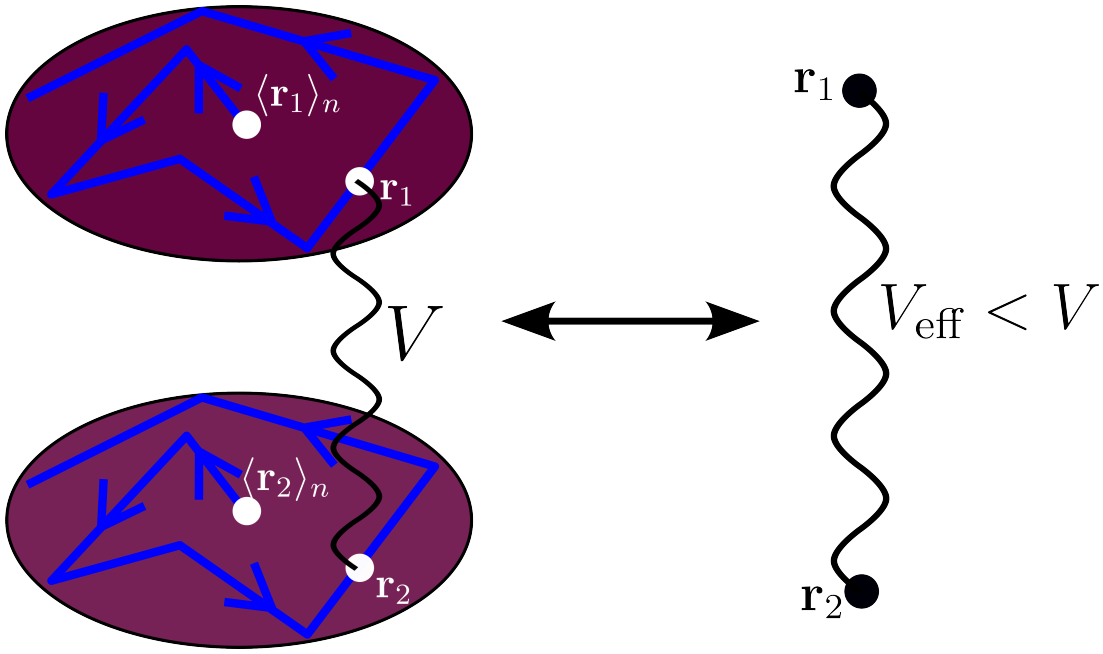

Figure 8.3: The pairing of non-local Bloch wavepackets (i.e. with quantum geometry) with strength V can be mapped to the pairing of local wavepackets where the effective pairing strength is weaker than V.

$$\sum_{\boldsymbol{k}} \frac{\langle V^{\text{eff}}_{\boldsymbol{k}\boldsymbol{k}'} \rangle}{E - 2\epsilon_n(\boldsymbol{k})} = 1, \tag{8.25}$$

with

$$\langle \mathcal{O} \rangle = \frac{\sum_{\boldsymbol{k}'} \mathcal{O} g_{\boldsymbol{k}'}}{\sum_{\boldsymbol{k}'} g_{\boldsymbol{k}'}}. \tag{8.26}$$

Using standard BCS theory, we now specify $V_{\boldsymbol{k}\boldsymbol{k}'} = -V \mathbb{1}_{\mathscr{D}}(\boldsymbol{k}) \mathbb{1}_{\mathscr{D}}(\boldsymbol{k}')$ with

$$\mathscr{D} = \left\{ \boldsymbol{k} \in \text{BZ} \;\middle|\; \epsilon_F \leq \epsilon_n(\boldsymbol{k}) \leq \epsilon_F + \hbar\omega_D \right\}, \tag{8.27}$$

and $\mathbb{1}_{\mathscr{D}}$ the indicator function of $\mathscr{D}$. Therefore the interaction concerns all $\boldsymbol{k}$ in the Brillouin Zone such that the band energy is between the Fermi level ϵ_F and the latter plus the Debye energy $\hbar\omega_D$. As in Chapter 6, all the linear terms in $\boldsymbol{k}'$ vanish in $\langle V^{\text{eff}}_{\boldsymbol{k}\boldsymbol{k}'}\rangle$. In appendix G.2, we show that further symplifying $\langle V^{\text{eff}}_{\boldsymbol{k}\boldsymbol{k}'}\rangle$ yields

$$\langle V^{\text{eff}}_{\boldsymbol{k}\boldsymbol{k}'}\rangle \simeq -V\left[1-\frac{\lambda\!\!\!^{-2}_c k_F^2(4+\lambda\!\!\!^{-2}_c k_F^2)}{8(1+\lambda\!\!\!^{-2}_c k_F^2)^2}\right]. \tag{8.28}$$

We emphasize that the phenomenological character of the derivation is such that the renormalization in Eq. (8.28) may differ from the exact one by a numerical prefactor, as is the case for electrons in the vacuum with Coulomb repulsion [54]. The qualitative behaviour of Eq. (8.28) is roughly similar to the one found in Chapter 6. In the $\lambda\!\!\!^{-}_c k_F \ll 1$ regime, we have

$$\frac{\langle V^{\text{eff}}_{\boldsymbol{k}\boldsymbol{k}'}\rangle}{-V} \underset{\lambda\!\!\!^{-}_c k_F\ll 1}{\sim} 1-\frac{\lambda\!\!\!^{-2}_c k_F^2}{2}, \tag{8.29}$$

which is exactly the same behavior observed in Ref. [1]. Then, the maximal renormalization occurs at $\lambda\!\!\!^{-}_c k_F=\sqrt{2}$ where $\langle V^{\text{eff}}_{\boldsymbol{k}\boldsymbol{k}'}$ is 19% lower than V, again almost exactly as in Chapter 6. The peculiarity comes at the regime of large $\lambda\!\!\!^{-}_c k_F$, indeed there we have

$$\frac{\langle V^{\text{eff}}_{\boldsymbol{k}\boldsymbol{k}'}\rangle}{-V} \underset{\lambda\!\!\!^{-}_c k_F\to+\infty}{\longrightarrow} \frac{7}{8}\neq 1. \tag{8.30}$$

I.e. the effective pairing interaction does not go back to its original value when $\lambda\!\!\!^{-}_c k_F$ becomes large, as it does in Chapter 6. Instead it shows a stagnation of the renormalization where the effective interaction is $\sim 13\%$ lower than the original interaction. Such behavior seems rather puzzling as well as counterintuitive, and might be an artefact of earlier approximations, as this limit may go beyond the validity of our derivation.

8.5 . Conclusion

In conclusion this work puts forward the importance of the link between quantum geometry and non-locality in understanding the effect of the normal state quantum geometry on electronic correlations, and particularly on superconductivity. Using the latter, we were able to answer the open questions we formulated at the beginning of this chapter. We first saw, contrary to what we anticipated from Chapters 6 and 7, there is no normal state curvature-metric competition towards superconductivity. Both effects turn out to be two sides of the same coin, that is the non-locality of the Bloch fermion through the normal state quantum metric. On one hand, the geometric superfluid weight, through the quantum metric, is a consequence of the zero-point motion of the Bloch fermion. This observation explains why the contribution persists even in flat-band systems since the zero-point motion are completely independent of the overall motion of the wavepackets. It is therefore not exactly true to state that the charge carriers are immobile or inert in flat band systems. It also explains why it is the quantum metric that appears, and why the geometric superfluid weight is bounded from below by the Berry curvature, as the latter protects a minimum amount of zero-point motion. On the other hand, we have also generally derived, albeit phenomenologically, the general form of the emergent Darwin term and the subsequent renormalization of the pairing interaction first derived in Chapter

6. The general form of the latter is actually driven by the normal state quantum metric, and is remarkably also driven by the non-locality of the Bloch fermion. The revised results for massive Dirac fermions turn out to be closely similar to the results of Chapter 6, probably owing to the fact that the non-locality of the massive Dirac fermions at the origin is minimal.

Our study suffers some limitations. The phenomenological character of the derivation of the Darwin term implies that experimental predictions should not be taken to be quantitative, as the derivation might be off by a numerical prefactor (as it is for elementary electrons [54]). A more exact derivation of the emergent Darwin term is thus needed for further research and quantitative predictions. Finally, the peculiar behaviour of the effective interaction found in Eq. (8.28) calls for further attention regarding the assumptions needed in the practical calculation of said effective interaction.

Given the intense attention recently given on superfluid weight in the hope of getting higher superconducting critical temperatures [36, 169] and in theoretical calculations on specific materials as done in Chapter 7, the effect of the Darwin term described in this paper should be taken into account and the interplay between the two effects is a direction for future research. Furthermore, it would be interesting to explore if the interpretation of quantum geometry in terms of non-locality offers a physical interpretation of other effects of the normal state quantum geometry on superconductivity that were discovered [118, 162, 225, 226, 227].

Conclusion and perspectives

We now conclude the second part of the manuscript, and outline some perspectives.

8.6 . Conclusion

In the introduction of the second part of the manuscript, we argued that in the standard paradigm of BCS theory, a caveat was that the quasiness of the Bloch fermions, the charge carriers of the normal state, was not taken into account. The matter of the difference between Bloch fermion pairing and electron pairing thus came forward. Moreover, as quantum geometry is a consequence of the quasiness of the Bloch fermions, this posed the question of the effect of the normal state quantum geometry on the superconducting state.

In Chapter 6, further motivated by preceding works on excitons, we aimed at studying the effect of the normal state Berry curvature on the superconducting state of two-dimensional massive Dirac fermions. Utilizing a perturbation projection, we formulated an effective single-band model containing two corrective terms. First a spin-orbit coupling term reminiscent of the role of the Berry curvature as a helicity axis of the wavepacket, and secondly a Darwin term. By investigating the Cooper problem and BCS theory, we found that the Darwin term weakens the attractive interaction forming the Cooper pairs. In doing so, the normal state Berry curvature thus appeared to weaken to superconducting phase.

In Chapter 7, we studied the impact of the normal state quantum metric on the superconducting state in (111)-oriented oxide interfaces, through the geometric superfluid weight. The geometric superfluid weight is a contribution to the London equation, which stems purely from the geometry of the band structure of the normal state, which reduces to the quantum metric in the isolated band limit. The normal state quantum metric thus appears as a source of supercurrent, and consequently seems to have a positive influence on the superconducting state. By employing a tight-binding modeling of the interface, and the derivation of low-energy models, we could qualitatively discuss, and quantitatively compute both contributions to the superfluid weight. Based on experimental data relating the chemical potential to the gate voltage, we then argued that the interface displays two domes as a function of the latter. The first dome is due to the conventional contribution, while the second is purely due to the geometric contribution. We have thus found that the normal state quantum metric can drive a superconducting dome, and is therefore indeed a positive influence on the superconducting state.

From Chapters 6 and 7, we then inferred some open questions. One was the physical interpretation of the effects of the normal state quantum geometry on superconductivity, how can we interpret the geometric superfluid weight and the weakening of the pairing interaction ? Another was the observation from Chapters 6 and 7 that the Berry curvature and the quantum metric seem to have opposite effects on the superconducting state, thereby hinting at a competition between the two. The aim of Chapter 8 was to resolve these matters, using the interpretation of quantum geometry in terms of the non-locality of the Bloch fermion, as developed in Chapter 2. Using this interpretation, we argued

that the geometric superfluid weight originates from the zero-point motion of the Bloch fermions forming the Cooper pairs, which thereby explains why it persists in flat-band systems, as well as why it is bounded from below by the Berry curvature. Based on a phenomenological derivation of the Darwin term [54], we formulated the general form of the emergent Darwin term, where it remarkably appears in terms of the quantum metric, and not the Berry curvature as found in Chapter 6. We then re-examined the Cooper problem and BCS theory to find the general form of the weakening of the pairing interaction. The latter can then also be interpreted as the consequence of the non-locality of the Bloch fermion. We can then conclude that there is no normal state curvature-metric competition towards superconductivity, as both effects we discussed originate from the non-locality of the Bloch fermion, through the normal state quantum metric.

On a final note, we can conclude that the quantum geometry of the normal state has an ambivalent effect towards the superconducting phase. Indeed, on one hand the non-locality of the Bloch fermions implies that the Cooper pairs exhibit zero-point motions, which can be seen as a type of supercurrent. This effect can be sizable, as we argued in Chapter 7 that it drives a superconducting dome. On the other hand, the same non-locality of the Bloch fermions implies that an emergent Darwin term appears in their Hamiltonian descriptions, which will then smear any potential it is subjected to, for example the pairing potential.

8.7 . Perspectives

We now outline some directions in which the work done in the second part of the manuscript can serve as an inspiration.

Effect of non-interacting quantum geometry on interacting phases While we studied the example of superconductivity, the problem of the influence of the non-interacting quantum geometry on the interacting state is a general matter for interacting phases. Studying such effects for various interacting phases, such as Mott insulators, spin-density waves, quantum spin liquids, etc... is an interesting direction of future research.

Quantum geometry of Cooper pairs and quasiparticles The interplay of the normal state quantum geometry and superconductivity falls into a larger problem, the subtlety of formulating the geometry of quasiparticles. Consider the example of Cooper pairs. Through mean-field theory, i.e. the Bogoliubov-de Gennes Hamiltonian

$$\mathcal{H}_{\text{BdG}}(\boldsymbol{k}) = \begin{pmatrix} H_0(\boldsymbol{k}) & \hat{\Delta}(\boldsymbol{k}) \\ \hat{\Delta}(\boldsymbol{k})^\dagger & -H_0^*(-\boldsymbol{k}) \end{pmatrix}, \tag{8.31}$$

one can bring the notion of quantum geometry on Cooper pairs themselves, and it is this quantum geometry that gives rise to (intrinsic) topological superconductivity [163]. We see in Eq. (8.31) that two contributions arise. One is that of the constituents of the Cooper pair, coming from the normal state H_0. Indeed, being composite quasiparticles, the components of the Cooper pair themselves have their own quantum geometry, which we called the normal state quantum geometry. Additionally, the interaction "gluing" the components, through $\hat{\Delta}$, might also carry its, although non-Hermitian,

quantum geometry. Studying the quantum geometry of the BdG Hamiltonian through that of its components, as done recently in Ref. [162], might shed light on the full complexity of the notion of topological superconductivity, and may even allow to consider and engineer routes towards intrinsic topological superconductivity.

Part III

Band quantum geometry and topology with Green functions

Introduction

In the third and last part of the manuscript, we explore interplays between the single-particle Green's function and quantum geometry as well as topology. Chapter 9 is focused on non-interacting systems, where we show that the value of topological invariants (namely, the $\mathbb{Z}_2$ invariants) can be extracted from the analytic properties of the Green's function. Based on Ref. [232], where it was discovered that the zeros of the diagonal components of the Green's function, represented in the orbital basis, signal the topological character of a band structure through crossings between diagonal zeros. We show in Chapter 9, within two-band models, that these crossings between diagonal zeros separate TRIMs with opposite diagonal zeros. By counting the TRIMs on either side, one can then directly extract the values of the $\mathbb{Z}_2$ topological invariants. We further conjecture a generalization of this relation to N-band systems. This work may open the possibility to measure the $\mathbb{Z}_2$ topological invariants from spectroscopic experiments such as ARPES, in a visual way.

Contrary to the second part of the manuscript where we focused on the effects of the non-interacting quantum geometry on electronic correlations, we explore in Chapter 10 the effects of electronic correlations on the non-interacting quantum geometry. Specifically, we use the Green's function to define a dynamic quantum geometric tensor, the dQGT, and a generalised quantum geometric tensor, dubbed the gQGT. We find that the dQGT has a similar form as that of the classical Fisher information where the Green's function appears as the probability distribution, suggesting a persisting link to information geometry. We also find that singularities in the Green's function result in singularities of the gQGT, and that the self-energy may drive correlation-driven quantum geometry. Finally, we study the paradigmatic example of a Lorentzian broadening of the spectral functions. We find that both the quantum geometry and the resulting Chern number are weakened by the broadening. We then interpret this finding in several ways, e.g. from the link between quantum geometry and non-locality or as a consequence of the blurring of the band gap.

The work presented in this part of the manuscript has not yet been the subject of scientific publications, and thus represent incomplete results.

9 - $\mathbb{Z}_2$ topological invariant from the Green function's diagonal zeros

9.1 . Introduction

Green's functions are essential tools in condensed matter physics, forming the foundation for many approaches used to address interactions. In the field of topological materials, it has been used to formulate topological invariants for interacting materials [233, 234, 235, 236, 237], of which a notable example is the Ishikawa-Matsuyama invariant [238, 239, 240].[1] Another interplay of Green's functions with topological materials in correlated systems is through the divergences of the self-energy. Indeed when the self-energy displays divergences the Green's function becomes singular, leading to a breakdown of Luttinger's theorem and an alteration of interacting topological invariants [233, 242, 243, 244, 245, 246].

However, Green's functions are not solely useful for topological materials in correlated systems. It was discovered in Ref. [232] that in non-interacting systems the analytic properties of the Green's function G, i.e. the relation between its zeros and poles, can be used to detect whether a band structure is topological or not. Specifically the zeros of the diagonal elements G_{jj}, when plotted in the Brillouin zone, display crossings within the band gap and fully traverse the latter, which signifies a band inversion. We emphasize the difference between these *diagonal zeros* with the *singular zeros* mentioned earlier, as the latter are also the zeros of the diagonal elements of the Green's function *when the latter is represented in the band basis*. The Green's function can therefore also prove useful in non-interacting topological materials.

Building on Ref. [232], we might wonder if it is possible to extract more information about the topology of a band structure from the Green's function. Beyond knowing whether a band structure is topological or not, can we also extract the value of a topological invariant from the diagonal zeros of the Green's function ? This question is of special interest since the analytic properties of the Green's function can be determined by first-principle calculations and measured by ARPES measurements. Topological invariants could then be directly measured. In this chapter we address this issue in the example of $\mathbb{Z}_2$ topological invariants. We start by reviewing the formalism developed in Ref. [232], revising the notations and taking special care on interpreting the different relations that arise between the Bloch state and the analytic properties of the Green's function. The zeros ζ_{nj} thus appear as marginal band dispersions, the eigenvalues of the Bloch Hamiltonian H when neglecting the orbital basis state $|\phi_j\rangle$. The poles are the actual band dispersions ϵ_n, as usual. The eigenvector-eigenvalue relation rediscovered in Ref. [247] then remarkably shows that the modulus $|u_n^{(j)}|$ can be expressed in terms of the poles and the diagonal zeros of the Green's function. The points where a diagonal zero and a pole coincide then induce zeros in the components of the Bloch state, as well as phase singularities. Both of which we have argued in Chapter 3 to be the origin of topology in a band structure. By reformulating the $\mathbb{Z}_2$ invariants as the number modulo 2 of TRIMs with the same parity eigenvalue, we conjecture a relationship between the diagonal zeros and the $\mathbb{Z}_2$ invariant. Specifically, we conjecture

[1] Note that other interacting invariants exists, e.g. the many-body Chern number [238, 241].

that the surface in the BZ defined by the crossings of the diagonal zeros separates TRIMs with opposite parity eigenvalues. One can then count the number of TRIMs on either side and directly infer the values of the $\mathbb{Z}_2$ topological invariants. We then prove this proposition within two-band models, where we explicit the relationship between band inversions, the diagonal zeros and parity eigenvalues. We exemplify our result in a paradigmatic toy model of $\mathbb{Z}_2$ topological insulators, physically relevant for materials such as Bi_2Se_3. There we consider the model in a trivial phase, a weak topological phase, and a strong topological phase. Each time the surface of crossings of diagonal zeros, dubbed the *zeros surface*, yields the correct values for the $\mathbb{Z}_2$ invariants. Finally, we propose a conjecture extending our result beyond two-band systems.

The chapter is organized as follows. In Section 9.2, we review the formalism developed in Ref. [232], and reformulate the $\mathbb{Z}_2$ topological invariants using the Fu-Kane-Mele formula. In Section 9.3, we formulate and provide a proof of the relation between the zeros of the diagonal components of the Green's function, thereby showing that the $\mathbb{Z}_2$ invariants can be determined from the knowledge of the Green's function. In Section 9.4 we study the example of the Wilson-Dirac model, a paradigmatic toy model of $\mathbb{Z}_2$ band topology, and show that the diagonal zeros can indeed be used to determine the value of the topological invariants. Finally, in Section 9.5 we propose a conjecture extending our result to a general N band system.

9.2 . Diagonal zeros: formalism

In this section we review the formalism of the diagonal zeros presented in Ref. [232], with revised notations. Finally, we aim to go further and formulate how the diagonal zeros may give access to the value of the $\mathbb{Z}_2$ topological invariants.

9.2.1 . Notations

Recall that $\mathcal{M}_N(\mathbb{C})$ is the set of N by N complex matrices. For a hermitian matrix $A \in \mathcal{M}_N(\mathbb{C})$, we consider the convention in which its eigenvalues are arranged in ascending order, namely $\lambda_1(A) \leq \lambda_2(A) \leq \cdots \leq \lambda_N(A)$. $[A]_{ij} \in \mathcal{M}_{N-1}(\mathbb{C})$ denotes the matrix $A \in \mathcal{M}_N(\mathbb{C})$ without its i-th row and j-th column. The eigenvalues of the Hamiltonian H and $[H]_{ij}$ are denoted as ϵ_n and $\zeta_{n,ij}$, respectively. Finally, for lightness of notation, we will use ζ_{nj} instead of $\zeta_{n,jj}$. We consider a spinless Bloch Hamiltonian H represented in an orbital basis $(|\phi_1\rangle, \ldots, |\phi_N\rangle)$.[2] In this basis, the Bloch state of the n-th band $|u_n\rangle$ reads

$$|u_n(\boldsymbol{k})\rangle = \sum_{j=1}^{N} u_n^{(j)}(\boldsymbol{k}) \, |\phi_j\rangle \, , \tag{9.1}$$

with $u_n^{(j)}(\boldsymbol{k}) = \langle u_n(\boldsymbol{k}) | \phi_j \rangle \in \mathbb{C}$.

9.2.2 . Formalism

The formalism developed in Ref. [232] can be summarized in three main relations. The first one is the zero-pole representation of the Green's function, which expresses the latter as a rational function

[2] As in Ref. [36], we refer to any collection of internal degrees of freedom (spin, orbital, sublattice,..) as an orbital.

with ζ_{nj} appearing as its zeros and ϵ_n as its poles. The second relation is the eigenvector-eigenvalue relation, which expresses the modulus of the components of the Bloch state in terms of the ϵ_n and ζ_{nj}. The final and third relation is the Cauchy interlacing inequality, stating that ζ_{nj} always lies between ϵ_n and ϵ_{n+1}.

9.2.2.1 Zero-pole representation of G

As derived in Chapter 5, the Green's function of a quadratic Hamiltonian H in frequency space is given by the Hamiltonian's resolvent $G = \big(\hbar\omega\mathbb{1} - H\big)^{-1}$. Using the relation $A\,\mathrm{adj}(A) = \det(A)\mathbb{1}$ with $\mathrm{adj}(A)_{ij} = (-1)^{i+j}\det[A]_{ji}$ the adjugate matrix of A, one gets

$$G_{ij} = (-1)^{i+j}\frac{\det\big([\hbar\omega\mathbb{1} - H]_{ji}\big)}{\det\big(\hbar\omega\mathbb{1} - H\big)}, \tag{9.2}$$

assuming $\hbar\omega \neq \epsilon_n$.

Zero-pole representation For a diagonal component, the latter then simplifies to

$$G_{jj} = \frac{\det\big(\hbar\omega\mathbb{1} - [H]_{jj}\big)}{\det\big(\hbar\omega\mathbb{1} - H\big)} = \frac{\prod_{n=1}^{N-1}\big(\hbar\omega - \zeta_{nj}\big)}{\prod_{n=1}^{N}\big(\hbar\omega - \epsilon_n\big)}. \tag{9.3}$$

We will call Eq. (9.3) the *zero-pole representation* of G. ζ_{nj} then appears as the n-th zero of the j-th diagonal component of G. As such, we refer to them as *diagonal zeros* of G. We emphasize the difference between the diagonal zeros, those of G_{jj} with G written in the orbital basis, and the *singular zeros* of G, those of $\det G$ that appear only in correlated systems due to divergences of the self-energy [233, 242, 243, 244, 245, 246]. It is interesting to note that points where a zero ζ_{nj} and a pole ϵ_m coincide result in pole-skipping points [248, 249, 250], a notion related to the concept of unparticles [251, 252].

Interpretation ζ_{nj}, as the eigenenergy of $[H]_{jj}$, can be interpreted as a *marginal band dispersion*. Indeed $[H]_{jj}$ being the Hamiltonian without the degree of freedom $|\phi_j\rangle$, the ζ_{nj} are what the band dispersion ϵ_n would be *without* the degree of freedom $|\phi_j\rangle$, analogously to marginal probability distributions. Thus, it is consistent to identify these points as the zeros of G_{jj} with respect to $\hbar\omega$. The function G_{jj}, being the Fourier transform of the $|\phi_j\rangle$–$|\phi_j\rangle$ response function, has zeros at the energies where the orbital $|\phi_j\rangle$ has no influence.

9.2.2.2 Eigenvector-eigenvalue relation

Another central relation is the *eigenvector-eigenvalue relation* [232, 247], which in band theory notation states

$$\prod_{m=1}^{N-1}\big(\epsilon_n - \zeta_{mj}\big) = \big|u_n^{(j)}\big|^2 \prod_{\substack{m=1\\m\neq n}}^{N}\big(\epsilon_n - \epsilon_m\big), \tag{9.4}$$

with $u_n^{(j)} = \langle \phi_j | u_n \rangle$. Eq. (9.4) implies in particular that the j-th component of the n-th Bloch state is zero when one diagonal zero of G_{jj} coincides with the n-th pole (or dispersion) ϵ_n, assuming no band crossing. We refer to this scenario as a *zero-pole touching*. A generalized version of the eigenvector-eigenvalue relation can be used to extract the relative phase between $u_n^{(i)}$ and $u_n^{(j)}$,

$$\exp\left[i(\phi_n^{(i)} - \phi_n^{(j)})\right] = \frac{(-1)^{i+j} \det\left[\epsilon_n \mathbb{1} - H\right]_{ji}}{\sqrt{\prod_{m=1}^{N-1} (\epsilon_n - \zeta_{mi})(\epsilon_n - \zeta_{mj})}}. \tag{9.5}$$

The presence of differences between zeros and poles in the denominator directly connect zero-pole touchings to phase singularities in the Bloch states' components, and therefore to their winding numbers, which add up to the Chern number [35, 106, 107, 109, 110]. Proofs for Eqs. (9.4,9.5) are given in appendix H.1.

The fact the zeros of the Bloch states components are equivalent with zero-pole touchings can be further explained from the interpretation of the diagonal zeros. Indeed, the Bloch state is a superposition of the orbitals,

$$|u_n(\boldsymbol{k})\rangle = \sum_{j=1}^{N} u_n^{(j)}(\boldsymbol{k}) \, |\phi_j\rangle \, . \tag{9.6}$$

Furthermore, we interpreted ζ_{nj} as a marginal band dispersion, when the orbital $|\phi_j\rangle$ is disregarded. It then stands to reason to think that a point $\boldsymbol{k}$ such that $\zeta_{nj}(\boldsymbol{k})$ is equal to $\epsilon_n(\boldsymbol{k})$ is a point where the orbital $|\phi_j\rangle$ does not contribute to the Bloch state $|u_n(\boldsymbol{k})\rangle$. I.e, at such points we have $u_n^{(j)}(\boldsymbol{k}) = 0$.

9.2.2.3 Cauchy interlacing inequality

The last fundamental relation is the Cauchy interlacing inequality [232, 247, 253], stating that the zeros of G_{jj} interlace its poles, i.e.

$$\epsilon_n \leq \zeta_{nj} \leq \epsilon_{n+1}, \tag{9.7}$$

restricting the possible zero-pole touchings. Indeed, applying this to the eigenvector-eigenvalue relation yields

$$u_n^{(j)} = 0 \quad \Rightarrow \quad \zeta_{n-1,j} = \epsilon_n \;\text{ or }\; \zeta_{nj} = \epsilon_n. \tag{9.8}$$

The Cauchy interlacing inequality is proven in appendix H.2, based on Ref. [232].

9.2.3 . Diagonal zeros and $\mathbb{Z}_2$ topological invariants

By exploring the non-trivial classes of the tenfold way [96, 97, 254, 255], Ref. [232] discovered that upon a band inversion, the zero-pole crossings rearrange themselves such that two diagonal zeros ζ_{ni} and ζ_{nj} cross in the gap between two inverted zero-pole touchings. These *zero-zero crossings*, by their presence then signal band inversions. If this band inversion is non-trivial, then the zero-zero crossings are a signal of the topological character of the band structure.

One can then wonder if it is possible to go further and extract the value of topological invariants from the diagonal zeros of the Green's function. We now formulate a proposition to do so in $\mathbb{Z}_2$ topological systems. Specifically, we focus on time-reversal invariant and inversion symmetric

three-dimensional topological insulators. However, our reasoning can readily be adapted to systems in other dimensions. As explained in Chapter 3, in this case we have four $\mathbb{Z}_2$ topological invariants $(\nu_0;\nu_1\nu_2\nu_3)$ given by the Fu-Kane-Mele formula [125, 126]

$$(-1)^{\nu_j} = \prod_{\Gamma\in\mathsf{T}_j} \xi(\Gamma) = \prod_{\Gamma\in\mathsf{T}_j}\prod_{n=1}^{N_{\text{occ}}} \xi_n(\Gamma), \tag{9.9}$$

where $\xi_n(\Gamma)$ is the parity eigenvalue of the n-th band at the time-reversal invariant momenta (TRIM) Γ and T_j is the subset of TRIMs in the Brillouin zone (BZ) introduced in Chapter 3. Additionally, $\xi(\Gamma)$ is the parity eigenvalue of the TRIM Γ and N_{occ} is the number of occupied bands.

It is then readily shown from Eq. (9.9) that

$$\nu_j \equiv |\mathcal{P}_{j,\pm}| \ \ [2], \tag{9.10}$$

with $\mathcal{P}_{j,\pm} \subset \mathsf{T}_j$ the set of TRIM in T_j with parity ±1, and $|\mathcal{P}_{j,\pm}|$ its cardinality. The invariants ν_j can then be obtained by counting the number of TRIM in T_j within the same parity sector, i.e. having the same parity. This is where we can draw a link with the results of Ref. [232]. First, as explained in Chapter. 3, the FKM formula applies in the transverse gauge [126] where the Berry connection is identically zero everywhere *but* at the TRIMs where a Kramers' degeneracy is protected by time-reversal symmetry. Therefore the zero-pole touchings can, and do, only occur at the TRIMs.

Following Ref. [232], a non-trivial band inversion results in a rearrangement of these zero-pole touchings, thereby necessarily yielding a zero-zero crossing. If any pair of TRIMs are inverted, they should therefore be separated by a zero-zero crossing. Furthermore, if the inversion is non-trivial then the two TRIM points will be of opposite parity. There lies our proposition. There is a surface of zero-zero crossings in the BZ, dubbed the *zeros surface*, separating the two parity sectors $\mathcal{P}_{j,\pm}$. Then, by counting the TRIM points on each side, one can infer the $\mathbb{Z}_2$ topological invariants by Eq. (9.10).

9.3 . Two-band models: Paradigmatic (s,p)-band inversion

We now prove our proposition in the case of two-band models. We start by providing a clear formulation, which we then aim to prove. We consider $N_{\text{occ}} = 1$.

9.3.1 . Proposition

Our goal here is to provide a formulation of how one can extract the $\mathbb{Z}_2$ topological invariants from the diagonal zeros. We consider a Hamiltonian H written in the orbital basis $(|\phi_1\rangle, |\phi_2\rangle)$ with orbital parities (ξ_1,ξ_2) respectively. The two Bloch states $|u_1\rangle$ and $|u_2\rangle$ have, at a TRIM Γ, band parities $\xi_1(\Gamma)$ and $\xi_2(\Gamma)$, respectively. As we argued in Section 9.2.3, the key point of the argument is to prove that TRIMs with opposite parity are separated by zero-zero crossings. Pursuing this line of thought, let $\Gamma_1,\Gamma_2 \in \mathsf{T}_j$ be two TRIM points in T_j. Their parities are then given by $\xi(\Gamma_{1,2}) = \xi_1(\Gamma_{1,2})$. For the diagonal zeros ζ_{11} and ζ_{12}, we define the zeros surface as follows,

$$\mathscr{S}_0 = \Big\{ \boldsymbol{k} \in \mathsf{BZ} \ \Big|\ \zeta_{11}(\boldsymbol{k}) = \zeta_{12}(\boldsymbol{k}) \Big\}. \tag{9.11}$$

Our proposition is then written as

$$\xi(\Gamma_1) \neq \xi(\Gamma_2) \iff \mathscr{S}_0 \text{ separates } \Gamma_1 \text{ and } \Gamma_2. \tag{9.12}$$

We emphasize the importance of the *non-triviality of the zeros surface*. Indeed, we call $\mathscr{S}_0$ non-trivial iff the two orbitals $|\phi_1\rangle$ and $|\phi_2\rangle$ are of opposite parity. Otherwise, $\mathscr{S}_0$ is called trivial. This non-trivial character is a consequence of that of band inversions, which are referred to as *non-trivial* (*trivial*) iff the inversion is made between two orbitals of *opposite* (*equal*) parity.

An interesting point is the physical interpretation of such zero-zero crossings. In Section 9.2.2 we have interpreted the diagonal zeros as marginal band dispersions, corresponding to the disregard of one orbital. Here ζ_{11}, the lowest zero of G_{11}, is associated to the dismissal of $|\phi_1\rangle$ while ζ_{12} comes from the omission of $|\phi_2\rangle$. The point $\boldsymbol{k} \in$ BZ where $\zeta_{11}(\boldsymbol{k}) = \zeta_{12}(\boldsymbol{k})$ thereby appears as a point where removing one orbital is equivalent to removing another.

9.3.2 . Diagonal zeros and band inversions

By clarifying the link between the diagonal zeros and band inversions, we now prove Eq. (9.12) for two-band models. In the basis $(|\phi_1\rangle, |\phi_2\rangle)$, we write $H = \boldsymbol{h}(\boldsymbol{k}) \cdot \boldsymbol{\sigma}$. We will prove Eq. (9.12) through the notion of *band inversion*. A band inversion, in two-band models, is characterized by a reversal of characters of the two bands between two points in the Brillouin zone, here Γ_1 and Γ_2. Consider for example a s-p model, where each Bloch state, by Eq. (9.1), is a superposition of the s and p states. At Γ_1 the first band would be purely s while the second is purely p. However at Γ_2, an inverted band structure would have the first band purely p while the second is purely s.

9.3.2.1 Situation at Γ_1 and Γ_2

Coming back to the general case, we then assume such a band structure, as pictured in Fig.9.1.

At Γ_1, the first (second) band is purely of character $|\phi_1\rangle$ ($|\phi_2\rangle$). I.e. $u_1^{(2)}(\Gamma_1) = 0$ and $u_2^{(1)}(\Gamma_2) = 0$, respectively. By the eigenvector-eigenvalue relation in Eq. (9.4), we then have $\zeta_{12}(\Gamma_1) = \epsilon_1(\Gamma_1)$ and $\zeta_{11}(\Gamma_1) = \epsilon_2(\Gamma_1)$. As a case in point, consider the first band. Since it is purely $|\phi_1\rangle$ at Γ_1, the character $|\phi_2\rangle$ does not contribute *at all* to the Bloch state $|u_1(\Gamma_1)\rangle$. The corresponding band dispersion $\epsilon_1(\Gamma_1)$ will then be the same whether $|\phi_2\rangle$ is disregarded or not, i.e. $\zeta_{12}(\Gamma_1) = \epsilon_1(\Gamma_1)$. Furthermore, using $\xi_n(\Gamma) = \langle u_n(\Gamma)| P |u_n(\Gamma)\rangle$ with P the parity operator, one can show that

$$\xi_n(\Gamma) = \sum_{j=1}^{N} \xi_j \left|u_n^{(j)}(\Gamma)\right|^2. \tag{9.13}$$

From this we directly have $\xi_1(\Gamma_1) = \xi_1$ and $\xi_2(\Gamma_1) = \xi_2$ as pictured in Fig.9.1. Again it is physically coherent that since the first (second) band is purely $|\phi_1\rangle$ ($|\phi_2\rangle$), its band parity is the orbital parity of $|\phi_1\rangle$ ($|\phi_2\rangle$).

At Γ_2 the situation is reversed. The first and second bands are purely of character $|\phi_2\rangle$ and $|\phi_1\rangle$, respectively. I.e. $u_1^{(1)}(\Gamma_2) = 0$ and $u_2^{(2)}(\Gamma_2) = 0$. Again by Eq. (9.4) this means $\zeta_{11}(\Gamma_2) = \epsilon_1(\Gamma_2)$ and $\zeta_{12}(\Gamma_2) = \epsilon_2(\Gamma_2)$. Additionally, Eq. (9.13) gives $\xi_1(\Gamma_2)) = \xi_2$ and $\xi_2(\Gamma_2) = \xi_1$. The situation is thus as shown in Fig.9.1.

9.3.2.2 Equivalence between band inversions and zero-zero crossings

Band inversion $\Rightarrow$ Zero-zero crossing. Because of the band inversion, the diagonal zeros "follow the opposite character" and thus fully cross the gap between Γ_1 and Γ_2. Being continuous functions, they must therefore cross, at least once, between the two points. The band inversion therefore implies a zero-zero crossing between Γ_1 and Γ_2, which establishes the separation of the two by the zeros surface $\mathscr{S}_0$.

Band inversion $\Leftarrow$ Zero-zero crossing. Conversely, assume that $\mathscr{S}_0$ separates Γ_1 and Γ_2. The possibility of *accidental* zero-zero crossings that does not result from a full traversal of the gap, as seen in Fig.9.1, was shown in Ref. [232]. However, it was also argued that these crossings can be removed by deforming the Hamiltonian without closing the band gap, i.e. staying in the same topological phase [232]. Furthermore, even without removing them, these accidental crossings are distinguishable from the ones associated with band inversions by probing the position of the diagonal zeros at Γ_1 and Γ_2 [232]. These accidental zero crossings are therefore a possibility that we neglect in the following. Without loss of generality, the diagonal zeros therefore behave as in Fig.9.1. At Γ_1 we have $\zeta_{12}(\Gamma_1) = \epsilon_1(\Gamma_1)$ and $\zeta_{11}(\Gamma_1) = \epsilon_2(\Gamma_2)$. Applying the eigenvector-eigenvalue then gives $u_1^{(2)}(\Gamma_1) = 0$ and $u_2^{(1)}(\Gamma_1) = 0$. Similarly, at Γ_2 we find $u_1^{(1)}(\Gamma_2) = 0$ and $u_1^{(2)}(\Gamma_1) = 0$. The band inversion between Γ_1 and Γ_2 is thus established.

9.3.3 . Orbital and band parities

We have now shown the equivalence between the band inversion at two TRIM points and the fact that they are separated by the zeros surface $\mathscr{S}_0$. The next step is to link this with the parities of Γ_1 and Γ_2. Because $N_{\text{occ}} = 1$, we have $\xi(\Gamma) = \xi_1(\Gamma)$. So $\xi(\Gamma_1)\xi(\Gamma_2) = \xi_1(\Gamma_1)\xi_1(\Gamma_2)$. From Fig.9.1, we see that $\xi_1(\Gamma_1) = \xi_1$ and $\xi_1(\Gamma_2) = \xi_2$. We then have

$$\xi(\Gamma_1)\xi(\Gamma_2) = \xi_1\xi_2. \tag{9.14}$$

It is here that the importance of the non-triviality of the band inversion comes in. Eq. (9.14) shows that $\xi(\Gamma_1) \neq \xi(\Gamma_2)$ is equivalent to $\xi_1 \neq \xi_2$. I.e. that the band inversion is non-trivial because it happens between two characters (orbitals) of opposite parity. Therefore, if we assume that $\xi_1 \neq \xi_1$, as in a s-p model for example, Eq. (9.12) is verified for two-band models.

9.3.4 . Diagonal zeros and parity sectors

As we have anticipated in Section 9.2.3, the equivalence between band inversions and zero-zero crossings implies that the parity sectors are delimitated by the zeros surface $\mathscr{S}_0$. Indeed, as Fig.9.1 shows, a path between Γ_1 and Γ_2 will necessarily pass through a zero-zero crossing. Since the reasoning holds for any path between the two points (or its BZ equivalents) the two points are thus fully separated by the zeros surface $\mathscr{S}_0$.

9.4 . Example: Wilson-Dirac model

In this section we exemplify the results proven in Section 9.3 using the Wilson-Dirac model, a direct generalization of the low-energy model of Bi_2Se_3 [256, 257] and a standard model for $\mathbb{Z}_2$ topological

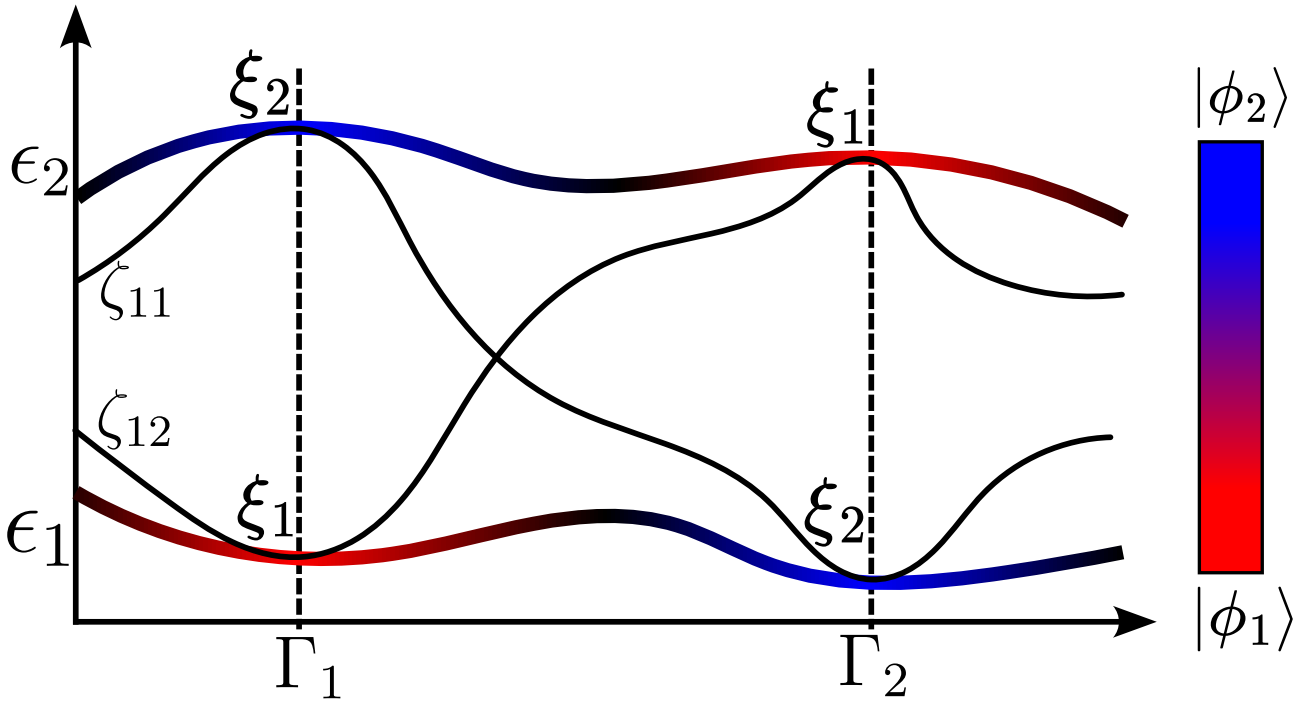

Figure 9.1: Graphical representation of a band inversion in a two-band system. A band inversion is characterized by an inversion of characters of two bands between two points of the Brillouin Zone. At Γ_1, the first (second) band is purely of character $|\phi_1\rangle$ ($|\phi_2\rangle$). The first (second) band will then have parity ξ_1 (ξ_2). By Eq. (9.4), we then have $\zeta_{12}(\Gamma_1) = \epsilon_1(\Gamma_1)$ and $\zeta_{11}(\Gamma_1) = \epsilon_2(\Gamma_1)$. Since Γ_2 is inverted with respect to Γ_1, the situation is reversed. At Γ_2, the first (second) band is purely of character $|\phi_2\rangle$ (ϕ_1). Thus the first (second) band has parity ξ_1 (ξ_2) at Γ_2. By Eq. (9.4), we have $\zeta_{11}(\Gamma_2) = \epsilon_1(\Gamma_2)$ and $\zeta_{12}(\Gamma_2) = \epsilon_2(\Gamma_2)$. The band inversion is thus accompanied by a reverse traverse of the gap from the two diagonal zeros, as shown in Ref. [232]. The two must then cross on any path between Γ_1 and Γ_2. The zeros surface $\mathscr{S}_0$ thus separates band inverted TRIM points, and consequently delimitates the two parity sectors in the case where $\xi_2 = -\xi_1$.

insulators [256]. We start by briefly setting and studying the model. We then explicit its topological phase diagram, and finally we compute the topological invariants from the zeros surface according to Eq. (9.12).

9.4.1 . Model

9.4.1.1 Hamiltonian

The Hamiltonian is given by [256, 257]

$$H = (m - b_\mu \cos k_\mu)\beta + t_\mu \sin k_\mu \alpha_\mu, \tag{9.15}$$

with $\beta = \tau_z \otimes \sigma_0$ and $\alpha_\mu = \tau_x \otimes \sigma_\mu$ and where we make use of the Einstein summation convention over $\mu \in \{x, y, z\}$. The Pauli matrices τ_μ and σ_μ act on the orbital and spin degrees of freedom, respectively.

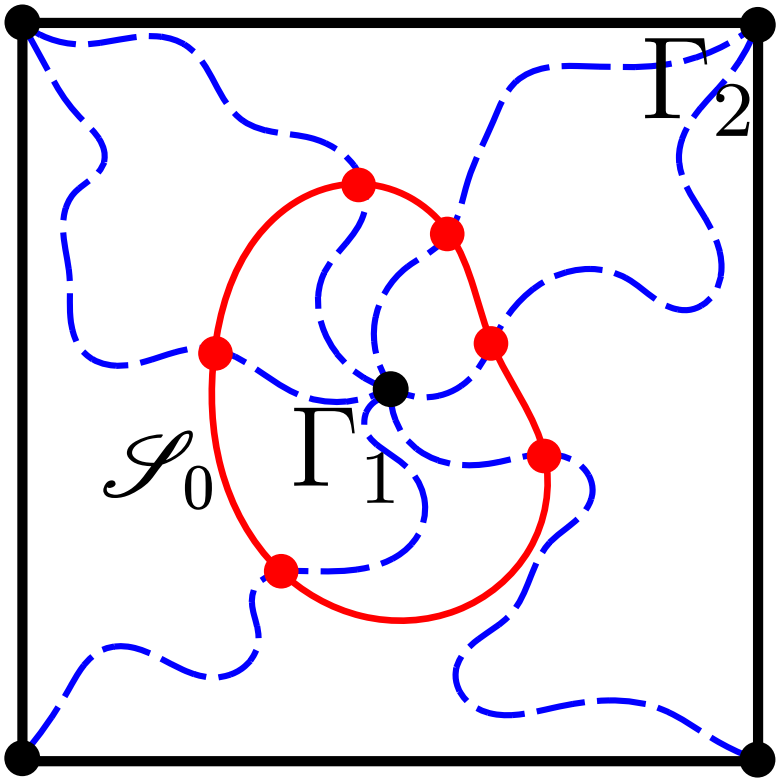

Figure 9.2: Separation of two non-trivially inverted points Γ_1 and Γ_2 by the zeros surface $\mathscr{S}_0$. For illustration, a two-dimensional of the cubic BZ is shown. Any path (dashed blue lines) between Γ_1 and Γ_2 (or its BZ equivalents), will cross the zeros surface $\mathscr{S}_0$ (in red). The TRIM points belonging to different parity sectors are then fully separated by $\mathscr{S}_0$.

9.4.1.2 Band dispersions and diagonal zeros

The four band dispersions are doubly degenerate:

$$\epsilon_{1,2} = -\epsilon_{3,4} = -\sqrt{(m - b_\mu \cos k_\mu)^2 + t_\mu^2 \sin^2 k_\mu}. \tag{9.16}$$

As for the diagonal zeros, since the model has four bands with the spin degree of freedom, we have $4 \times 3 = 12$ diagonal zeros. However, since $\epsilon_1 = \epsilon_2$ and $\epsilon_3 = \epsilon_4$, the Cauchy interlacing inequality in Eq. (9.7) implies that $\zeta_{1j} = \epsilon_2$ and $\zeta_{3j} = \epsilon_4$ for $j \in [\![1, 4]\!]$. Finally, for the ζ_{2j}, we find

$$\zeta_{21} = \zeta_{22} = b_\mu \cos k_\mu - m = -\zeta_{23} = -\zeta_{24}. \tag{9.17}$$

9.4.1.3 Green's function

The zero-pole representation of the Green's function G reads

$$G_{jj} = \frac{(\hbar\omega - \zeta_{1j})(\hbar\omega - \zeta_{2j})(\hbar\omega - \zeta_{3j})}{(\hbar\omega - \epsilon_1)(\hbar\omega - \epsilon_2)(\hbar\omega - \epsilon_3)(\hbar\omega - \epsilon_4)} \tag{9.18a}$$

$$= \frac{\hbar\omega - \zeta_{2j}}{(\hbar\omega - \epsilon_2)(\hbar\omega - \epsilon_4)}. \tag{9.18b}$$

Thus, the only spectroscopically observable diagonal zeros and band dispersions are the ζ_{2j} and the $\epsilon_{2,4}$. This reduces our problem to a spinless one.

9.4.1.4 zeros surface

As stated in Eq. (9.11), the zeros surface $\mathscr{S}_0$ is defined by the crossing of two diagonal zeros. Eq. (9.18b) shows that only the four diagonal zeros ζ_{2j} are spectroscopically relevant. Only two of them are not identically degenerate, we will therefore focus on them. The zero-zero crossings thus happen when $\zeta_{22} = \zeta_{24}$, i.e.

$$b_x \cos k_x + b_y \cos k_y + b_z \cos k_z - m = 0. \tag{9.19}$$

As in Refs. [256, 257], we now set $b_x = b_y = b_\parallel$ which we assume to be non-zero. Eq. (9.19) can then be rewritten as

$$\cos k_x + \cos k_y + \frac{b_z}{b_\parallel} \cos k_z = \frac{m}{b_\parallel}. \tag{9.20}$$

The zeros surface $\mathscr{S}_0$ is thereby the set of $\boldsymbol{k} \in$ BZ obeying Eq. (9.20).

9.4.2 . Topological phase diagram

The topological phase diagram, as a function of $b_z/b_\parallel$ and $m/b_\parallel$, was established in Ref. [256] to be as pictured in Fig.9.3.

9.4.3 . $\mathbb{Z}_2$ invariants from $\mathscr{S}_0$

Let us now rederive the $\mathbb{Z}_2$ topological invariants using the zeros surface. Specifically, we will do so in three examples. First, the trivial $(0;000)$ phase. We will then treat the weak topological insulator (WTI) $(0;111)$ phase and finally the strong topological insulator (STI) $(1;000)$ phase. The results also hold for the other phases.

9.4.3.1 Trivial phase $(0;000)$

For the trivial phase, specifically the one on the left of Fig.9.3, the zeros surface with corresponding $(m/b_{parallel}, b_z/b_\parallel)$ parameters is depicted within the BZ in Fig.9.4. Using Eqs. (9.12,9.10), we now recompute the four $\mathbb{Z}_2$ invariants.

Strong invariant ν_0. For the strong invariant ν_0, all eight TRIM points of the BZ are considered. As we can see in Fig.9.4, $\mathscr{S}_0$ separates the four upper TRIM points with the four lower ones. From Eq. (9.10), we then have $\nu_0 \equiv 4 \ [2] \equiv 0 \ [2]$, i.e. the ν_0 is trivial.

Weak invariants (ν_1, ν_2, ν_3). For the weak invariant ν_1, we consider the TRIM points in T_1, i.e. the projection of the eighth cube in the x direction. We then see in Fig.9.4 that the four TRIM points are split in two groups of two. So each parity sector has two TRIM points, which by Eq. (9.10) means that ν_1 is trivial. For the weak invariant ν_2, the situation is the same as for ν_1 but on the y-projection of the one eighth of the BZ. So ν_2 is also trivial. Lastly, for the weak invariant ν_3, we look at the top four TRIM points on the eighth cube. The zeros surface is not present in this plane, therefore each parity sector has an even number of TRIM points, either four or zero. By Eq. (9.10) we then obtain that ν_3 is trivial.

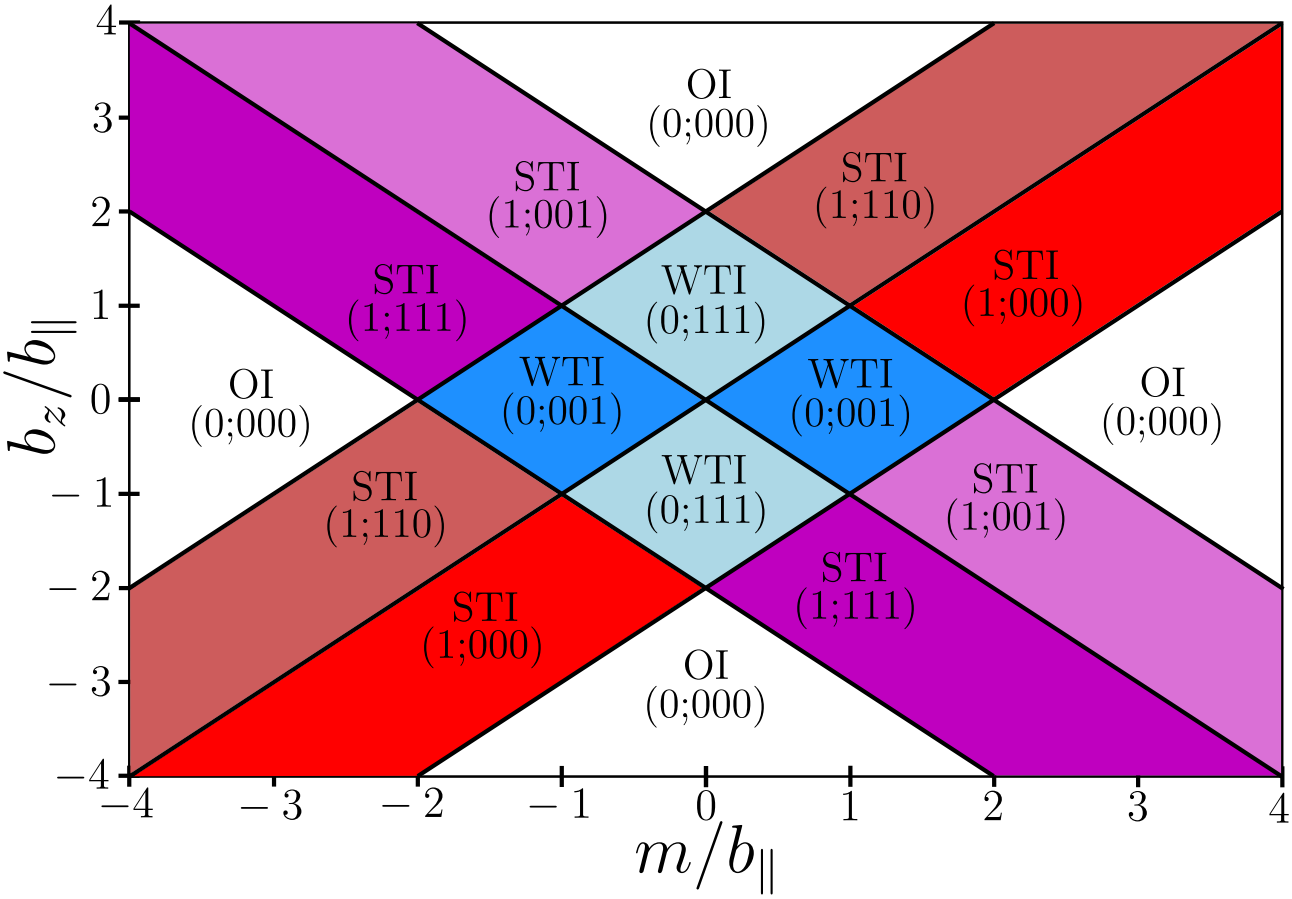

Figure 9.3: Topological phase diagram of the Wilson-Dirac model, taken from Ref. [257].

Summary. We have thus found purely from the zeros surface that the phase pictured in Fig.9.4 is a trivial $(0;000)$ phase.

9.4.3.2 Weak topological phase $(0;111)$

We now focus on the upper WTI $(0;111)$ phase shown in Fig.9.3. The zeros surface in the BZ, with corresponding $(m/b_\parallel, b_z/b_\parallel)$ parameters, is shown in Fig.9.5.

Strong invariant ν_0. For the strong invariant ν_0, we see that in the eighth cube we have three X points as well as the Γ point enclosed by $\mathscr{S}_0$. So an even number of TRIMs are in each parity sector, which implies that ν_0 is trivial.

Weak invariants (ν_1, ν_2, ν_3). For the weak invariants (ν_1, ν_2, ν_3) we care about the projection of the eighth cube along the (x, y, z) direction, respectively. We then see in Fig.9.5 that in each case, the X point is separated from the other three TRIM points. By Eqs. (9.12,9.10), the three weak invariants (ν_1, ν_2, ν_3) are then non-trivial.

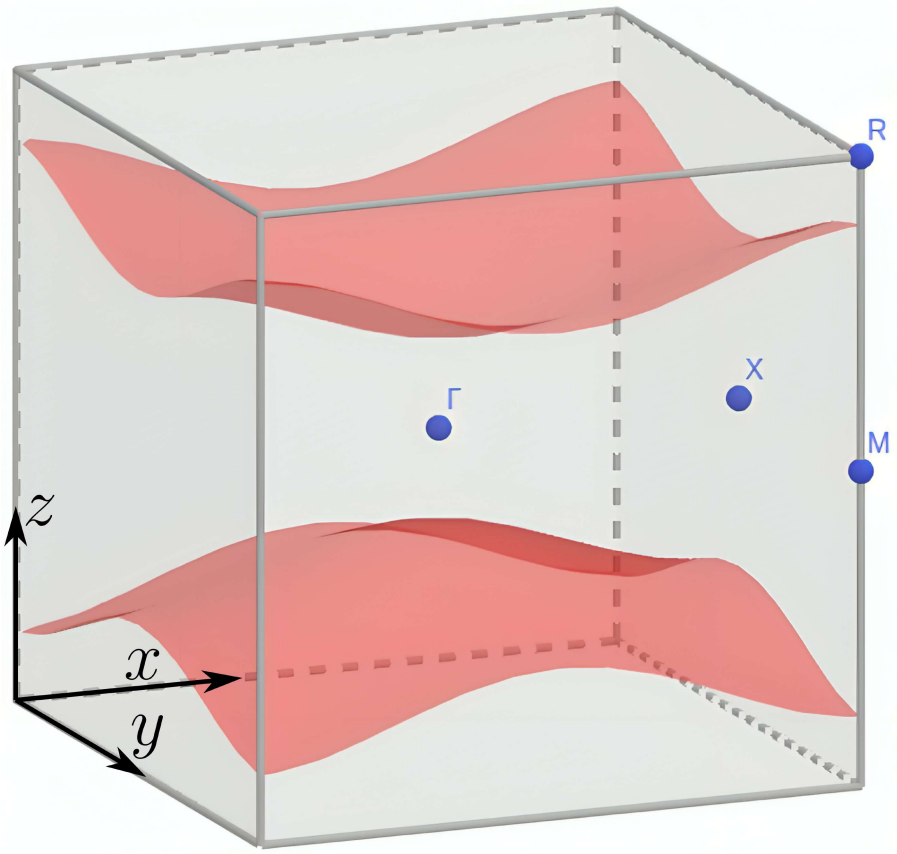

Figure 9.4: zeros surface $\mathscr{S}_0$ in red in the cubic BZ for the trivial phase $(0;000)$. Specifically the OI (ordinary insulator) phase on the left of Fig.9.3.

Summary. From the zeros surface plotted in Fig.9.5, we then get infer that the phase is WTI $(0;111)$.

9.4.3.3 Strong topological phase $(1;000)$

Finally, consider the strong $(1;000)$ topological phase shown in the upper part of Fig.9.3. The corresponding zeros surface is shown in Fig.9.6.

Strong invariant ν_0. First, for ν_0 we see in Fig.9.6 that the Γ is the only TRIM enclosed by the zeros surface $\mathscr{S}_0$, which implies that ν_0 is non-trivial.

Weak invariants (ν_1,ν_2,ν_3). As before the weak invariants (ν_1,ν_2,ν_3) are associated with the projection of the eighth cube in the (x,y,z) direction, respectively. We see that in each case, the zeros surface does not separate any TRIM from another. By Eqs. (9.12,9.10), we then infer that all three weak invariants are trivial.

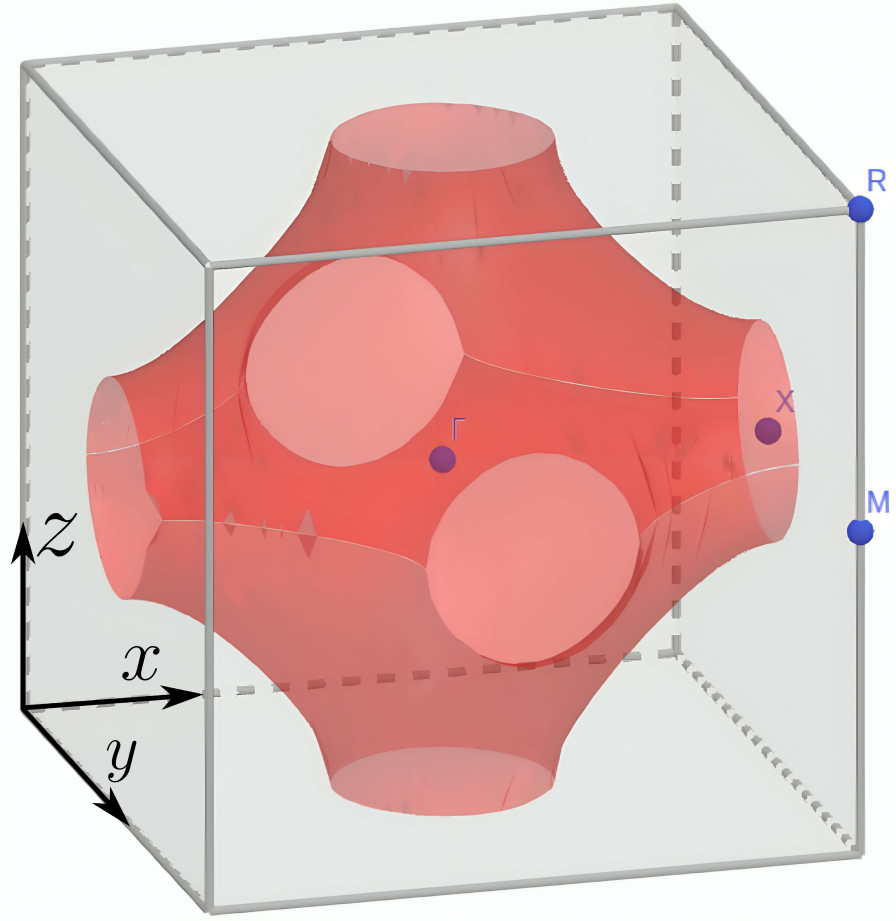

Figure 9.5: zeros surface $\mathscr{S}_0$ in red in the cubic BZ for the upper WTI phase $(0;111)$ shown in Fig.9.3.

Summary. From the zeros surface displayed in Fig.9.6 we then obtain that the phase is a STI $(1;000)$.

9.5 . Beyond two-band systems: Conjecture

In Section 9.3, we have proven the link between diagonal zeros and $\mathbb{Z}_2$ topological invariants within two-band models. In this section we go beyond and formulate a conjecture for a general N band system. Consider a N band Bloch Hamiltonian represented in the orbital basis $(|\phi_1\rangle, \ldots, |\phi_N\rangle)$.

9.5.1 . zeros surfaces

We first need to generalize the notion of zeros surface. A N-band system will harbor $(N-1)N$ diagonal zeros ζ_{nj}. Focusing on crossings of the type $\zeta_{ni} = \zeta_{nj}$, we generalize Eq. (9.11) as

$$\mathscr{S}^n_{0,ij} = \Big\{ \boldsymbol{k} \in \mathrm{BZ} \;\Big|\; \zeta_{ni}(\boldsymbol{k}) = \zeta_{nj}(\boldsymbol{k}) \Big\}. \tag{9.21}$$

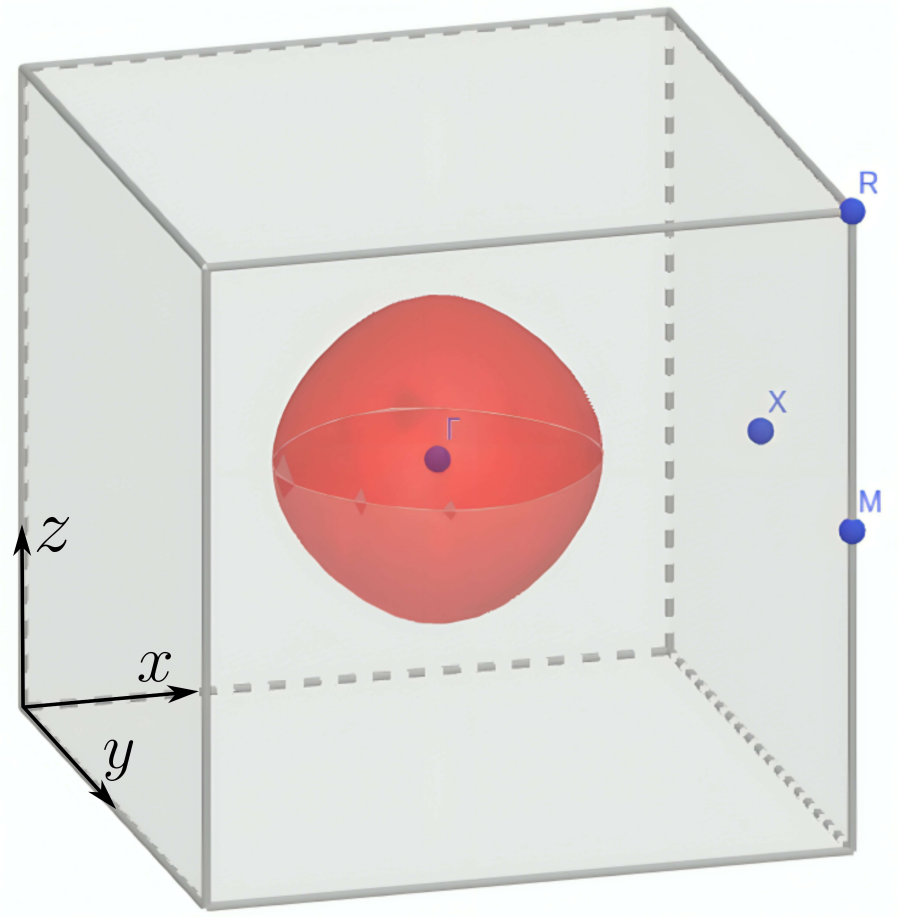

Figure 9.6: zeros surface $\mathscr{S}_0$ in red in the cubic BZ for the right STI phase $(1;000)$ shown in Fig.9.3.

As in the two-band case, $\mathscr{S}^n_{0,ij}$ is *non-trivial* iff $|\phi_i\rangle$ and $|\phi_j\rangle$ are of opposite parity. Otherwise, it is called trivial.

Note that since $1 \leq n \leq N-1$ and $1 \leq i,j \leq N$, a N-band system will therefore harbor $N(N-1)^2/2$ zeros surfaces. Note that we focus only on pairs (i,j) such that $j > i$, because $\mathscr{S}^n_{0,ji} = \mathscr{S}^n_{0,ji}$ and $\mathscr{S}_{0,jj}$ is always trivial.

9.5.2 . General Proposition

Eq. (9.12) states the parity sectors are delimitated by the zeros surface. However, as we have seen in Eq. (9.21), a N-band system has more than one zeros surface. The matter at hand is then to know which ones are relevant for discriminating TRIM points with opposite parity.

First, we can speculate that only the diagonal zeros where the chemical potential is matter. This amounts to focusing on the zeros surfaces for which $n = N_{\text{occ}}$.

Furthermore, it is apparent that Γ_1 and Γ_2 are of opposite parity iff an odd number of non-trivial band inversions happen at these points. Motivated by this, we then propose the following general-

ization of Eq. (9.12),

$$\xi(\Gamma_1) \neq \xi(\Gamma_2) \;\Leftrightarrow\; \text{an odd number of non-trivial } \mathscr{S}_{0,ij}^{N_{\text{occ}}} \text{ separate } \Gamma_1 \text{ and } \Gamma_2. \tag{9.22}$$

9.6 . Conclusion

In this Chapter, based on Ref. [232] we studied the possibility of extracting the values of $\mathbb{Z}_2$ topological invariants from the analytic properties of the non-interacting Green's function. We started by reviewing the formalism presented in Ref. [232]. When represented in the orbital basis, the diagonal elements G_{jj} features the band dispersions ϵ_n as its poles and the marginal band dispersions ζ_{nj} as its zeros. The latter are referred as such owing to the fact that they are the eigenvalues of $[H]_{jj}$, obtained by removing the j-th orbital basis state $|\phi_j\rangle$ from the Bloch Hamiltonian H. The eigenvector-eigenvalue relation then relates the band dispersions and the diagonal zeros to the components of the Bloch states, with the latter's zeros coming from touching points between the zeros and poles of G_{jj}. Since we argued in Chapter 3 that the zeros of the Bloch state components are the origin of non-trivial topology, we can already at this stage anticipate the link between band topology and zeros and poles of the Green's function. Additionally, the Cauchy interlacing inequality state that the n-th zero of the j-th diagonal component of the Green's function lies between its n-th and $n+1$-th pole.

We then used the Fu-Kane-Mele formula for the $\mathbb{Z}_2$ topological invariants to show that the latter are equal to the number of TRIMs with the same parity eigenvalue. We can then determine the invariants by counting the number of TRIMs with the same parity eigenvalue. Following this observation we conjectured that, in two-band models, defining the surface in the Brillouin zone where the diagonal zeros cross, the *zeros surface*, allows to separate TRIMs with opposite parity eigenvalues. By explicating the relation between band inversions, parity eigenvalues and the diagonal zeros we provided a proof of our conjecture. In two-band models, we can then indeed determine the $\mathbb{Z}_2$ topological invariants from the Green's function associated to the Bloch Hamiltonian. We then exemplified our result in a paradigmatic toy model for $\mathbb{Z}_2$ topology, where we considered three different topological phases, a trivial one, as well as a weak and strong phases. In each case, the zeros surface yields the correct values for the topological invariants. Finally, we formulated a conjecture for extracting the $\mathbb{Z}_2$ invariants from the diagonal zeros in a general N-band system.

The results of this chapter could be of practical significance for the field of topological materials. Indeed the Green's function is directly tied to spectroscopic observables such as the spectral function, and is also an important quantity in numerical simulations of band structures. An interesting future direction of research would thus be to explore whether one could directly measure topological invariants from spectroscopic measurements such as ARPES, and easily compute it from numerical methods. Additionally, research is needed to prove, or disprove, the conjecture we formulated for general N-band systems. Lastly, it would be very interesting to see if other topological invariants could be determined from the diagonal zeros. For example, we have proven in Chapter 3 that the Chern number is the sum of the winding numbers of the transition functions. Can we determine their values from the analytic properties of the Green's function ? For example, by using the eigenvector-eigenvalue relation to get the order of the Bloch state components' zeros ?

10 - A Green's function generalization of the quantum geometric tensor

10.1 . Introduction

In Part II, we studied an example of how a correlated phase can be influenced by the quantum geometry of the underlying non-interacting state. One could then wonder, is the interplay reciprocal ? In other words, what about the effects of the electronic correlations on the quantum geometry of the non-interacting state ? When electronic correlations are turned on, the Hamiltonian describing the material is not periodic under Bravais translations anymore, and the Bloch theorem is thus no longer valid. Consequently, band theory as a whole is expected to breakdown in correlated systems, and with it the associated geometry and topology. Contrarily to this intuition, it has been argued numerous times that correlations can in fact induce topology. For example, correlation-induced topological phases were argued to occur in twisted bilayer graphene [258, 259], as well as in topological Mott and Kondo insulators [260, 261].[1] In addition, as we mentioned in Chapter 9 several topological invariants were formulated in terms of Green's functions [233, 234, 235, 236, 237, 238, 239, 240]. In contrast, fewer works have focused on how the underlying quantum geometry is affected by electronic correlations [263, 264].

In this Chapter we aim to investigate how quantum geometry is affected when correlations are present, by formulating a generalization of the quantum geometric tensor (QGT) using the Green's function. We begin by revisiting the derivation of the Hamiltonian formulation of the QGT, presented in Chapter 10. This way the non-interacting Green's function G_0 appears naturally, and the quantum geometric tensor can be expressed in terms of the latter. By replacing the G_0 with the interacting Green's function G, we define a frequency dependent tensor that we dub the *dynamical QGT (dQGT)*. The latter then also takes the form of a covariance matrix, this time of the operators $\partial_\mu \ln G$. The final step is to convolute the dQGT with the spectral function, yielding the *generalized QGT (gQGT)*. The dQGT and gQGT obey some of the properties of the QGT, as they are Hermitian and positive semidefinite. We then discuss general properties that we notice about the two tensors. First, the expression of the dQGT is reminiscent of that of the classical Fisher information discussed in Chapter 2. Then, we then notice that the singular zeros of the Green's function discussed earlier [233, 242, 243, 244, 245, 246] also appear as singularities of the dQGT, and thus of the gQGT. Finally, expanding the dQGT in terms of the self-energy suggests that the latter can generate its own quantum geometry, hinting at the possibility of correlation driven quantum geometry. We then proceed by considering a paradigmatic example of self-energy, that giving rise to the Lorentzian broadening of the spectral function, often interpreted as giving a lifetime to the Bloch fermion. As the Mott transition shows, interactions can tend to localize particles. As we argued in Chapter 2 that the quantum geometry quantifies the non-locality of the Bloch fermion, we can then anticipate that the interaction-induced spectral broadening will weaken the quantum geometry. This is indeed what we find when explicitly calculating the dQGT and gQGT. After discussing the latter, we then use the imaginary part of the gQGT

[1] Note that the same was argued for disorder, with topological Anderson insulators [262]

to define a generalized Berry curvature, and the ensuing generalized Chern number. The simplicity of the self-energy then allows to analytically compute the generalized Chern number. By considering the example of massive Dirac fermions, we show that the spectral broadening breaks the quantization of the generalized Chern number, and the ratio of the broadening with the band gap fixes the value of the latter. As the broadening is strengthened and the Bloch fermion becomes increasingly incoherent, the generalized Chern number goes from its original quantized value to zero.

The Chapter is organized as follows. In Section 10.2 we derive the dQGT and the gQGT, and discuss some basic properties. In Section 10.3, we further discuss some observations on the generalized tensors. Finally in Section 10.4, we compute the gQGT and a generalized Chern number in the example of a Lorenztian spectral broadening of the Bloch fermion.

10.2 . Generalization of the Quantum Geometric Tensor

In this section, we formulate the QGT of the Bloch Hamiltonian H in terms of its associated non-interacting Green's function G_0.

10.2.1 . Dynamical Quantum Geometric Tensor

Following the derivation of the Hamiltonian formulation of the QGT, we start by the eigenvalue problem $H\left|u_n\right\rangle = \epsilon_n \left|u_n\right\rangle$. Differentiating with respect to $\partial_\mu = \partial_{k_\mu}$ gives

$$\partial_\mu (H-\epsilon_n)\left|u_n\right\rangle + (H-\epsilon_n)\left|\partial_\mu u_n\right\rangle = 0. \tag{10.1}$$

Projecting on the bra $\langle u_m|$ with $m \neq n$, we have

$$\left\langle u_m\right| \partial_\mu (H-\epsilon_n)\left|u_n\right\rangle + (\epsilon_m - \epsilon_n)\left\langle u_m|\partial_\mu u_n\right\rangle = 0. \tag{10.2}$$

Assuming $\epsilon_n \neq \epsilon_m$ we then get

$$\begin{aligned}
\langle u_m|\partial_\mu u_n\rangle &= -\frac{1}{\epsilon_m-\epsilon_n}\left\langle u_m\right| \partial_\mu (H-\epsilon_n)\left|u_n\right\rangle = -\left\langle u_m\right| (H-\epsilon_n)^{-1}\partial_\mu (H-\epsilon_n)\left|u_n\right\rangle && \text{(10.3a)}\\
&= -\left\langle u_m\right| G_0(\epsilon_n)\partial_\mu G_0^{-1}(\epsilon_n)\left|u_n\right\rangle = \left\langle u_m\right| \partial_\mu \ln G_0(\epsilon_n)\left|u_n\right\rangle, && \text{(10.3b)}
\end{aligned}$$

where the introduction of $G(\epsilon_n)$ is well-defined because $m \neq n$. Furthermore, $\ln G(\epsilon_n)$ stays well-defined unless G is singular [265].

The quantum geometric tensor then becomes

$$\begin{aligned}
Q^n_{\mu\nu} &= \sum_{m\neq n} \langle \partial_\mu u_n|u_m\rangle \langle u_m|\partial_\nu u_n\rangle = \sum_{m\neq n} \left\langle u_m\right| \partial_\mu \ln G_0(\epsilon_n)\left|u_n\right\rangle^* \left\langle u_m\right| \partial_\nu \ln G_0(\epsilon_n)\left|u_m\right\rangle && \text{(10.4a)}\\
&= \left\langle u_n\right| \partial_\mu \ln G_0^\dagger(\epsilon_n)\big(\mathbb{1} - \left|u_n\right\rangle\left\langle u_n\right|\big)\partial_\nu \ln G_0(\epsilon_n)\left|u_n\right\rangle && \text{(10.4b)}\\
&= \mathrm{Tr}\left[\mathcal{P}_n \partial_\mu \ln G_0^\dagger(\epsilon_n)\big(\mathbb{1}-\mathcal{P}_n\big)\partial_\nu \ln G_0(\epsilon_n)\right], && \text{(10.4c)}
\end{aligned}$$

with $\mathcal{P}_n = \left|u_n\right\rangle\left\langle u_n\right|$. Replacing G_0 by its interacting counterpart G, we now define the *dynamic QGT (dQGT)* by

$$\mathcal{Q}^n_{\mu\nu}(\epsilon) = \mathrm{Tr}\left[\mathcal{P}_n \partial_\mu \ln G^\dagger(\epsilon)\big(\mathbb{1}-\mathcal{P}_n\big)\partial_\nu \ln G(\epsilon)\right] = \mathrm{Cov}_n\left(\partial_\mu \ln G(\epsilon)^\dagger, \partial_\nu \ln G(\epsilon)\right), \tag{10.5}$$

such that $\mathcal{Q}^n_{\mu\nu}(\epsilon_n) = Q^n_{\mu\nu}$ for non-interacting systems, with $\mathrm{Cov}_n = \mathrm{Cov}_{|u_n\rangle}$ and where $\epsilon = \hbar\omega$ with respect to our previous notation in Chapter 5.

It can be seen that the dQGT is a Hermitian matrix. It is also positive semidefinite, as a covariance matrix.

10.2.2 . Generalised Quantum Geometric Tensor

Introducing the density of states $\rho_n(\epsilon) = \delta(\epsilon - \epsilon_n)$, for non-interacting systems we have

$$Q^n_{\mu\nu} = \mathcal{Q}^n_{\mu\nu}(\epsilon_n) = \int_{-\infty}^{+\infty} \mathcal{Q}^n_{\mu\nu}(\epsilon)\rho_n(\epsilon)\mathrm{d}\epsilon. \tag{10.6}$$

We argued in Chapter 5 that the generalisation of the density of states beyond non-interacting systems is given by the spectral function $\mathcal{A}_n$. Consequently, we finally get

$$Q^n_{\mu\nu} = \int_{-\infty}^{+\infty} \mathcal{Q}^n_{\mu\nu}(\epsilon)\mathcal{A}_n(\epsilon)\mathrm{d}\epsilon. \tag{10.7}$$

From this expression, we then again replace G_0 by G and define the *generalised QGT (gQGT)*,

$$\mathfrak{Q}^n_{\mu\nu} = \int_{-\infty}^{+\infty} \mathcal{Q}^n_{\mu\nu}(\epsilon)\mathcal{A}_n(\epsilon)\mathrm{d}\epsilon. \tag{10.8}$$

The gQGT $\mathfrak{Q}^n_{\mu\nu}$ is a Hermitian matrix since the spectral function is real. However, it is positive semidefinite only if the spectral function is positive.

10.3 . General discussion

In this section, we further discuss some properties of the gQGT and dQGT.

10.3.1 . Classical Fisher information matrix

In Chapter 2, we have introduced the classical Fisher information matrix $\mathcal{I}_{\mu\nu}$, whose expression for parameters $\boldsymbol{\theta}$ is

$$\mathcal{I}_{\mu\nu}(\boldsymbol{\theta}) = \mathbb{E}\Big[\partial_\mu \ln f(\boldsymbol{\theta})\partial_\nu \ln f(\boldsymbol{\theta})\Big]. \tag{10.9}$$

We notice a similarity with the dQGT which also appears as an average,[2] with $\mathbb{E}[\cdot] = \mathrm{Tr}[\mathcal{P}_n\cdot]$, of the second moment of the logarithm of the Green's function. In this analogy, the Green's function appears as the probability distribution. This similarity suggests that the gQGT also has links to information geometry.

10.3.2 . Singular zeros of the Green's function

As we noticed in its derivation, the dQGT is not well-defined when the logarithm of G is. As a function of a matrix, the logarithm of the Green's function is well-defined so long as it does not have zero eigenvalues [265]. These eigenvalues are the singular zeros we mentioned in Chapter 9, and may be viewed as Luttinger surfaces [243, 266]. An example of situation in which they arise is Mott insulators [266].

[2] Save for the factor $\mathbb{1} - \mathcal{P}_n$ in the trace

10.3.3 . Correlation-driven quantum geometry

Expanding the derivative of $\ln G$ in terms of the Hamiltonian H and the self-energy Σ, we find

$$\mathcal{Q}^n_{\mu\nu} = \sum_{m\neq n} \langle u_n| \partial_\mu H G^\dagger |u_m\rangle \langle u_m| G\partial_\nu H |u_n\rangle + \sum_{m\neq n} \langle u_n| \partial_\mu \Sigma^\dagger G^\dagger |u_m\rangle \langle u_m| G\partial_\nu H |u_n\rangle$$
$$+ \sum_{m\neq n} \langle u_n| \partial_\mu H G^\dagger |u_m\rangle \langle u_m| G\partial_\nu \Sigma |u_n\rangle + \sum_{m\neq n} \langle u_n| \partial_\mu \Sigma^\dagger G^\dagger |u_m\rangle \langle u_m| G\partial_\nu \Sigma |u_n\rangle . \tag{10.10}$$

Using Eq. (10.10), we can interpret the different contributions in the dQGT. The first can be seen as the effect of the interactions on the non-interacting quantum geometry. In contrast, the fourth term is purely driven by the self-energy, hinting the existence of *correlation-driven quantum geometry*! The remaining two-terms then appear as cross terms, which could by themselves also drive a quantum geometry. From the point of view of topological Mott and Kondo insulators [260, 261], which are correlation-driven topological phases, it is interesting to speculate on whether our generalised quantum geometric tensor could be the underlying driver of such phases.

10.4 . Lorentzian spectral broadening

A common consequence of effects beyond the free-fermion limit, e.g. temperature, scattering, or interactions, is a broadening of the spectral function, initially a Dirac delta at $\epsilon = \epsilon_n$, to a Lorentzian peak centered at ϵ_n. This may be thought of as having a Bloch fermion with a finite lifetime, and coherence. Such effect may be modeled by the self-energy defined by

$$\Sigma |u_n\rangle = -i\Gamma_n |u_n\rangle , \tag{10.11}$$

with $\Gamma_n \in \mathbb{R}$.

10.4.1 . Non-interacting model

For simplicity, we consider the model of massive Dirac fermions as the non-interacting model,

$$H = |\Delta| \begin{pmatrix} \operatorname{sgn}\Delta & \lambda\!\!\!^{-}_c(k_x - ik_y) \\ \lambda\!\!\!^{-}_c(k_x + ik_y) & -\operatorname{sgn}\Delta \end{pmatrix} . \tag{10.12}$$

Again, the band dispersions are given by $\epsilon_n = n|\Delta|\sqrt{1+\lambda\!\!\!^{-2}_c k^2}$, and the Berry curvature reads

$$\mathcal{B}_n = -\frac{n\operatorname{sgn}\Delta}{2} \frac{\lambda\!\!\!^{-2}_c}{(1+\lambda\!\!\!^{-2}_c k^2)^{3/2}} . \tag{10.13}$$

10.4.2 . Green's function and spectral function

The interacting Green's function is given by

$$G |u_n\rangle = \frac{1}{\epsilon - \epsilon_n + i\Gamma_n} |u_n\rangle , \tag{10.14}$$

and the spectral function reads

$$\mathcal{A}_n = \frac{1}{\pi} \frac{\Gamma_n}{(\epsilon-\epsilon_n)^2 + \Gamma_n^2} , \tag{10.15}$$

and is indeed a Lorentzian peak centered at $\epsilon = \epsilon_n$, and of half-width Γ_n.

10.4.3 . dQGT

The dQGT can readily be derived to be

$$\mathcal{Q}^n_{\mu\nu} = \sum_{m\neq n} \frac{\langle u_n|\,\partial_\mu H\,|u_m\rangle\,\langle u_m|\,\partial_\nu H\,|u_n\rangle}{(\epsilon-\epsilon_m)^2+\Gamma_m^2}. \tag{10.16}$$

We notice that for the dQGT, the finite coherence of other bands has the effect to weaken their respective terms. This observation is coherent with the necessity of the band structure to exhibit multiple bands to harbor quantum geometry. Indeed, if other bands become less coherent then the band structure is "less" multiband because of interactions, and therefore has a weaker quantum geometry. Furthermore, in Chapter 2 we have linked the quantum geometry to the non-locality of the Bloch fermions. However from the insight of the Mott transition we may expect electronic correlations to localize the Bloch fermions, and thereby weakening their quantum geometry.

10.4.4 . gQGT

The gQGT can generally be expressed as

$$\mathfrak{Q}^n_{\mu\nu} = \sum_{m\neq n} I_{mn}\,\langle u_n|\,\partial_\mu H\,|u_m\rangle\,\langle u_m|\,\partial_\nu H\,|u_n\rangle\,, \tag{10.17}$$

where I_{mn} reads

$$I_{mn} = \frac{1}{\pi}\int_{-\infty}^{+\infty} \frac{\Gamma_n}{\left[(\epsilon-\epsilon_m)^2+\Gamma_m^2\right]\left[(\epsilon-\epsilon_n)^2+\Gamma_n^2\right]}\mathrm{d}\epsilon. \tag{10.18}$$

Computing I_{mn} from the residue theorem then yields

$$\mathfrak{Q}^n_{\mu\nu} = \sum_{m\neq n} \frac{\Gamma_n+\Gamma_m}{\Gamma_m}\frac{(\epsilon_n-\epsilon_m)^2}{(\epsilon_n-\epsilon_m)^2+(\Gamma_n+\Gamma_m)^2}\frac{\langle u_n|\partial_\mu H|u_m\rangle\langle u_m|\partial_\nu H|u_n\rangle}{(\epsilon_n-\epsilon_m)^2}. \tag{10.19}$$

We then indeed see that the quantum geometry, according to our generalisation, is weakened by the finite coherence of the band interest *as well as that of the others*. Finally, note that one has to be careful about how to get back to the non-interacting limit. Indeed, we have

$$\lim_{\Gamma_m\to 0^+}\lim_{\Gamma_n\to 0^+}\mathfrak{Q}^n_{\mu\nu} = Q^n_{\mu\nu},\quad \lim_{\Gamma_n\to 0^+}\lim_{\Gamma_m\to 0^+}\mathfrak{Q}^n_{\mu\nu} = +\infty. \tag{10.20}$$

10.4.5 . generalized Chern number

Finally let us consider the imaginary of the gQGT as a generalised Berry curvature, associated to a generalised Chern number

$$\mathfrak{C}_n = \frac{1}{2\pi}\int_{\mathsf{BZ}} -2\,\mathrm{Im}\,\mathfrak{Q}^n_{\mu\nu}\mathrm{d}\boldsymbol{k}. \tag{10.21}$$

The calculation can be analytically done for massive Dirac fermions, and yields

$$\frac{\mathfrak{C}_+}{C_0} = \frac{2\Delta}{\Gamma_-}\arctan\left(\frac{\Gamma_++\Gamma_-}{2\Delta}\right), \tag{10.22}$$

with $C_0 = -n\,\mathrm{sgn}\,\Delta/2$ the non-interacting Chern number, and $\Gamma_\pm$ the halfwidths of the bands $\epsilon_\pm$, respectively. If the opposite band ϵ_- is made fully incoherent then the band structure virtually has

one band, which gives a zero Chern number. Additionally, we see that the halfwidths are compared in energy to the band gap. If the lifetime of the Bloch fermion is much bigger than the one associated with the band gap, then the Chern number stays virtually unchanged. However, when the widths of the spectral function become comparable to the band gap, then the quantization of the Chern number is truly broken, its value progressively going to zero.

10.5 . Conclusion

In this Chapter, we have aimed to investigate the effect of electronic correlations on quantum geometry. Our approach was to reformulate the quantum geometric tensor in terms of the non-interacting Green's function, thereby yielding a generalisation of the QGT upon replacing the non-interacting Green's function by its interacting counterpart. Doing so led to the gQGT defined as

$$\mathfrak{Q}^n_{\mu\nu} = \int_{-\infty}^{+\infty} \mathcal{Q}^n_{\mu\nu}(\epsilon)\mathcal{A}_n(\epsilon)\mathrm{d}\epsilon, \tag{10.23}$$

with $\mathcal{A}_n$ the spectral function of the n-th band. The tensor $\mathcal{Q}^n_{\mu\nu}(\epsilon)$ may be interpreted as a "QGT density", and is dubbed the dQGT. It is defined as

$$\mathcal{Q}^n_{\mu\nu}(\epsilon) = \mathrm{Tr}\left[\mathcal{P}_n\partial_\mu \ln G(\epsilon)^\dagger\big(\mathbb{1}-\mathcal{P}_n\big)\partial_\nu \ln G(\epsilon)\right], \tag{10.24}$$

which has the form of a covariance matrix with respect to the cell-periodic Bloch state $|u_n\rangle$. Consequently, the dQGT is a Hermitian and positive semidefinite matrix. The gQGT is also Hermitian, but is only positive semidefinite if the spectral function is positive.

We then further discussed several observations on the dQGT and gQGT. First the dQGT interestingly has a similar form as the classical Fisher information matrix, where the Green's function appears as the probability distribution. This observation suggests that the dQGT, and thus the gQGT, also has relations with information geometry. Second, the apparition of the matrix logarithm of the Green's function implies that the dQGT, and thus the gQGT, has singularities at points where the Green's function is singular. The same singularities have also been shown to occur in Green's function-based topological invariants. Finally, expanding the dQGT reveals the fact that the self-energy can also drive a quantum geometry. This observation hints at the possibility of correlation-driven quantum geometry.

Finally, we studied a paradigmatic example of self-energy, which gives rise to a spectral broadening of the bands' spectral functions. We have generally derived the forms of the dQGT and gQGT, and both show that the finite coherence of other bands negatively impacts the quantum geometry. This observation can be interpreted in two ways. First, quantum geometry is a result of the multiband character of a band structure. However, the bands that undergo a spectral broadening are blurred and thus progressively disappear from the band structure, leaving the band structure less multiband. Second, we have argued in Chapter 2 that quantum geometry quantifies the non-locality of the Bloch fermion. And it is expected that a certain degree of electronic interactions tends to localize the latter. It then makes sense to anticipate that the spectral broadening weakens quantum geometry. We finished by defining a generalised Chern number from the imaginary part of the gQGT, and computed it in the example of massive Dirac fermions. As expected from our observations on the gQGT,

the Chern number is weakened by the spectral broadening. It is also coherent with the fact that the spectral broadening of the bands also blurs the band gap between the two, thereby weakening the topological phase.

We can outline several perspectives of our work. First, there are several other self-energies to be investigated. For example, Fermi liquids exhibit a self-energy whose imaginary part is proportional to $(\hbar\omega)^2$ [267]. Another example is the self-energy of a Mott insulator, which exhibits singular zeros [245]. Another perspective, which could be investigated using the self-energy of a Mott insulator, is to further investigate the effect of the singular zeros of the gQGT. An open question is the relation between the gQGT and the Hall conductance. Is the Hall conductance in interacting systems proportional to the gQGT ? Is there a relation between the gQGT and Green's function-based topological invariants ? Another perspective would be to systemically revisit Fermi's liquid theory by carefully keeping the multiband character of a Bloch Hamiltonian in mind. The Hatsugai-Kohmoto interaction [268] has recently garnered significant attention for interacting topological materials due to its solvability [244, 269, 270, 271]. It would be interesting to see how such an interaction affects the gQGT. Finally, while we have considered the example of electronic interactions, there are other possible effects beyond the free-fermion limit that could affect quantum geometry. Two examples of such effects are temperature, disorder, and the cases of open and non-equilibrium systems.

Conclusion

In this thesis we explored interplays between the quantum geometry of bands and electronic interactions. One motivation is to bring closer two pillars of modern condensed matter physics that have mostly evolved separately. The manuscript is organised into three parts.

In the first part of the manuscript, we started in Chapter 1 by presenting and interpreting Bloch's theorem, the bedrock of band theory. The Bloch theorem states that the eigenstates describing a perfect crystal with a single electron is a combination of a plane-wave factor $\exp(i\boldsymbol{k}\cdot\hat{\boldsymbol{r}})$ and a periodic state $|u_n(\boldsymbol{k})\rangle$. We argued that the plane-wave factor is a consequence of the kinetic term in the Hamiltonian while the periodic state is a consequence of the Coulomb interaction between the electron and the lattice of atomic nuclei. The material then harbors emergent quasiparticles that we refer to as Bloch fermions. While the term "quasiparticle" usually refers to states emerging from the electron-electron Coulomb interaction, it is also relevant to use it for states emerging from the electron-nuclei Coulomb interaction. We referred to its quasiparticle character as its *quasiness*. This is evidenced by our discussion on quantum geometry in Chapter 2. We presented a series of derivations and viewpoints on this notion, to present a relatively thorough overview of the topic. We saw when deriving it that it directly comes from the periodic Bloch state, and can thus already be seen as a consequence of the quasiness of the Bloch fermion. We first derived a direct link between quantum geometry and the non-locality of the Bloch fermion. This non-locality arises as quantum fluctuations of its position, which can be thought of as zero-point motions when imagined over time. The quantum geometry quantifies these zero-point motions. Specifically, the quantum metric gives an idea of the typical length over which the zero-point motions occur while the Berry curvature bounds from below the typical area of zero-point motion. The Berry curvature thereby quantifies the minimal area of zero-point motion, offering an interpretation of why it appears as a lower bound on several physical observables. In the third viewpoint, we argued that the non-locality of the Bloch fermion stems from virtual interband transitions, in full analogy with relativistic electrons that undergo virtual electron-positron transitions. This also explains why quantum geometry is non-trivial only in multiband (or equivalently, multiorbital) systems. When the Bloch Hamiltonian is represented in a finite basis, say the electronic degrees of freedom within a unit lattice, the Bloch fermion is an entangled state of the latter. In the fourth and fifth viewpoints, we saw that the Berry curvature appears both as a dual to the magnetic field and as a helicity axis of the wavepacket of the Bloch fermion. In Chapter 3, we summarized some aspects of topological band theory. We argued that the Chern number is the result of topological defects in the entanglement pattern of the Bloch fermion, that each contributes to the Chern number through their winding number. In the case of time-reversal and inversion symmetric systems, these singularities can be gauged out except at the TRIMs which allows to express the $\mathbb{Z}_2$ invariants purely in terms of properties of the band structure at these points. In Chapters 4 and 5 we presented some aspects of superconductivity and Green functions that we use later in the manuscript.

In the second part of the manuscript, we investigate some effects of the normal state quantum geometry on superconductivity. Such effects are examples of how the quantum geometric of a non-interacting state can influence interactions happening on top of it. In Chapter 6, motivated by preceding works on excitons, we studied how the Berry curvature of the normal state affects the superconducting state, in the example of massive Dirac fermions. We have seen that an emergent Darwin term weakens the pairing interaction, and thus the superconducting critical temperature and gap. We

might then conclude that the Berry curvature of the normal state is antagonistic to superconductivity. In Chapter 7, we computed the geometric superfluid weight in the case of (111) oriented oxide interfaces. The geometric superfluid weight is a contribution to the London equation that purely comes from the geometry of the band structure, particularly through the quantum metric. Based on a tight-binding modeling of the interface, derivation of low-energy models, and available experimental data, we argued that the interface should exhibit a two-dome scenario in terms of the gate voltage. The first dome is due to the conventional superfluid weight, while the second is due to the geometric contribution. The two domes are separated by a plateau. From this work and others on the geometric superfluid weight, we may conclude that the normal state quantum metric has a positive influence on superconductivity. Chapters 6 and 7 thus hint at a competition between the normal state Berry curvature and quantum metric towards superconductivity. The aim of Chapter 8 was then to clarify the matter and offer physical interpretations of both effects. We did so based on the viewpoints done in the first part of the manuscript. The geometric superfluid weight then appeared as the consequence of the zero-point motions of the Bloch fermions, which explains most of its properties. The Darwin term can also be interpreted as coming from the non-locality of the Bloch fermion, and we used the analogy with relativistic electrons to phenomenologically derive a general expression for the emergent Darwin term. The latter is then fully expressed in terms of the quantum metric, and not the Berry curvature as we have seen in Chapter 6. We trace this back to the minimality of the quantum fluctuations of massive Dirac fermions, which implies that the revised results differ only slightly in the case of this model. From Chapter 8 we can then conclude that there is no curvature-metric competition towards superconductivity, as both effects come from the metric and are two sides of the same coin, that of the non-locality of the Bloch fermion. Finally, we may reflect on the ambivalent effect of the normal state quantum geometry on superconductivity. On one hand, the non-locality of the Bloch fermion weakens the pairing interaction, and thus the superconducting phase. On the other hand, the same non-locality offers another source of supercurrent, that is insensitive on the dispersion of the Bloch fermion.

In the third part of the manuscript, we have explored some interplays between quantum geometry, topology and Green's functions. In Chapter 9, we explored how the Green's function relates to $\mathbb{Z}_2$ topology in non-interacting systems. Specifically, the zeros of the diagonal components of the Green's function, represented in the orbital basis, were discovered to be related to the topological character of a band structure. One could then determine if a system was topological or not by looking at their behavior throughout the Brillouin zone. Based on these findings, we showed that within two-band models we can go further and extract the value of $\mathbb{Z}_2$ topological invariants from the diagonal zeros of the Green's functions. The latter are deeply related to the entanglement pattern of the Bloch fermions, which explains why they are a signal of band inversions and can thus detect the topological character of a band. We end the chapter by proposing a conjecture extending this result beyond two-band models. In Chapter 10 we explored some effects of electronic correlations on the non-interacting quantum geometry, by generalising the QGT using the Green's function. In doing so, we defined two extensions of the quantum geometric tensor. One is the dynamic QGT (dQGT), which takes a similar form as the classical Fisher information, suggesting a persisting link to information geometry. The other is the generalised QGT (gQGT), which is the convolution of the dQGT with the spectral function. We found that the self-energy may drive a quantum geometry by itself, even if the non-interacting

band structure is not geometric. This hints at the possibility of correlation-driven quantum geometry, which may itself drive correlation-driven topological phases, such as the Mott or Kondo topological insulators. We explicitly investigated the case of a Lorentzian broadening of the bands. We found that the quantum geometry and the ensuing generalised Chern number get weakened as the bands are made fully incoherent, a fact that we can interpret in several ways. We may thus anticipate the conclusion that electronic correlations also have an ambivalent effect on the non-interacting quantum geometry. On one hand, the addition of the self-energy may drive quantum geometry, and thus topology. On the other hand, the non-Hermitian effects of the self-energy seem to generically weaken them.

The present work opens several questions and directions of research, of which we may list a few. First, the second part of the manuscript studied how the quantum geometry of the components of the Cooper pairs affects their properties. This subject is part of a larger matter, the geometry of the Cooper pairs themselves which gives rise to topological superconductivity. The geometry of the Cooper pairs should reflect their composite character, and one may thus be able to express their geometries in terms of that of its constituents and some cross-terms coming from the interaction between the components. Even larger is the question of the geometry of quasiparticles. Various strongly interacting theories may be described by elementary excitations, i.e. quasiparticles, using various mean-field techniques. Some quasiparticles are fractionalized while others are composite, some are bosonic while others are fermionic. The question of formulating their quantum geometry and relating to that of electrons is an open question. Further work is also needed to establish whether the diagonal zeros can indeed be used to measure topological invariants via spectroscopic measurements. Finally, further research is warranted on the effects of electronic correlations, and other effects such as temperature or disorder, on quantum geometry. Of particular interest is the possibility of driving quantum geometry and topology via the self-energy.

Bibliography

[1] F. Simon, M. Gabay, M. O. Goerbig, and L. Pagot, "Role of the berry curvature on bcs-type superconductivity in two-dimensional materials," *Physical Review B*, vol. 106, Dec. 2022.

[2] F. Simon, M. O. Goerbig, and M. Gabay, "Normal state quantum geometry and superconducting domes in (111) oxide interfaces," *Phys. Rev. B*, vol. 110, p. 104512, Sep 2024.

[3] S. J. Blundell, *Superconductivity: A Very Short Introduction*. Oxford University Press, May 2009.

[4] H. Rogalla and P. H. Kes, eds., *100 Years of Superconductivity*. Taylor & Francis, dec 2011.

[5] P. F. Dahl, *Superconductivity*. New York, NY: American Institute of Physics, 1992 ed., feb 1992.

[6] L. N. Cooper and D. Feldman, *BCS: 50 Years*. WORLD SCIENTIFIC, Nov. 2010.

[7] M. Tinkham, *Introduction to Superconductivity*. Dover Publications, 2nd ed., 2004.

[8] P. K. Misra, "Basic properties of crystals," in *Physics of Condensed Matter*, pp. 1–35, Elsevier, 2012.

[9] M. Born and R. Oppenheimer, "Zur quantentheorie der molekeln," *Annalen der Physik*, vol. 389, p. 457–484, Jan. 1927.

[10] G. P. Srivastava, *The Physics of Phonons*. CRC Press, Aug. 2022.

[11] M.-O. Goerbig, *Introduction to Quantum Mesoscopic Transport and Topological Matter*. Lecture notes at École Polytechnique, Palaiseau, Engineering school. France. hal-04248649, 2023.

[12] C. Kittel and P. McEuen, *Introduction to Solid State Physics*". John Wiley & Sons, 2018.

[13] N. W. Ashcroft and N. Mermin, *Solid State Physics*. Florence, KY: Brooks/Cole, jan 1976.

[14] H. Brown and etc., *Crystallographic groups of four-dimensional space*. Monographs on Crystallography, Nashville, TN: John Wiley & Sons, oct 1978.

[15] C. Texier, "Waves in disordered media and localisation phenomena," 2013-2021.

[16] J. Cayssol and J. N. Fuchs, "Topological and geometrical aspects of band theory," *Journal of Physics: Materials*, vol. 4, p. 034007, apr 2021.

[17] S. H. Simon, *The Oxford Solid State Basics*. London, England: Oxford University Press, jun 2013.

[18] N. A. o. S. Office of the Home Secretary, *Biographical Memoirs: v. 64*. Washington, D.C., DC: National Academies Press, jan 1994.

[19] M. O. Goerbig, "Electronic properties of graphene in a strong magnetic field," *Reviews of Modern Physics*, vol. 83, p. 1193–1243, Nov. 2011.

[20] A. Clerk, "Introduction to quantum non-reciprocal interactions: from non-hermitian hamiltonians to quantum master equations and quantum feedforward schemes," *SciPost Physics Lecture Notes*, Mar. 2022.

[21] Z. Gong, Y. Ashida, K. Kawabata, K. Takasan, S. Higashikawa, and M. Ueda, "Topological phases of non-hermitian systems," *Phys. Rev. X*, vol. 8, p. 031079, Sep 2018.

[22] E. J. Bergholtz, J. C. Budich, and F. K. Kunst, "Exceptional topology of non-hermitian systems," *Rev. Mod. Phys.*, vol. 93, p. 015005, Feb 2021.

[23] N. Okuma and M. Sato, "Non-hermitian topological phenomena: A review," *Annual Review of Condensed Matter Physics*, vol. 14, p. 83–107, Mar. 2023.

[24] C. Bena and G. Montambaux, "Remarks on the tight-binding model of graphene," *New Journal of Physics*, vol. 11, p. 095003, Sept. 2009.

[25] J. P. Provost and G. Vallee, "Riemannian structure on manifolds of quantum states," *Commun. Math. Phys.*, vol. 76, pp. 289–301, sep 1980.

[26] A. Graf, *Aspects of multiband systems : Quantum geometry, flat bands, and multifold fermions*. Theses, Université Paris-Saclay, Dec. 2022.

[27] M. V. Berry, "The Quantum Phase, Five Years After," in *Geometric Phases in Physics*, World Scientific, 1989.

[28] R. Roy, "Band geometry of fractional topological insulators," *Phys. Rev. B*, vol. 90, p. 165139, Oct 2014.

[29] S. Peotta and P. Törmä, "Superfluidity in topologically nontrivial flat bands," *Nature Communications*, vol. 6, p. 8944, Nov 2015.

[30] J. M. Lee, *Introduction to Riemannian Manifolds*. Springer International Publishing, 2018.

[31] M. Claassen, C. H. Lee, R. Thomale, X.-L. Qi, and T. P. Devereaux, "Position-momentum duality and fractional quantum hall effect in chern insulators," *Phys. Rev. Lett.*, vol. 114, p. 236802, Jun 2015.

[32] B. Andrews, M. Raja, N. Mishra, M. P. Zaletel, and R. Roy, "Stability of fractional chern insulators with a non-landau level continuum limit," *Phys. Rev. B*, vol. 109, p. 245111, Jun 2024.

[33] V. K. SHODA, "Einige sätze über matrizen," *Japanese journal of mathematics:transactions and abstracts*, vol. 13, no. 0, p. 361–365, 1936.

[34] A. A. Albert and B. Muckenhoupt, "On matrices of trace zeros.," *Michigan Mathematical Journal*, vol. 4, Jan. 1957.

[35] B. A. Bernevig, *Topological Insulators and Topological Superconductors*. Princeton University Press, Dec. 2013.

[36] P. Törmä, "Essay: Where can quantum geometry lead us?," *Phys. Rev. Lett.*, vol. 131, p. 240001, Dec 2023.

[37] A. Grothendieck, *Récoltes et semailles: Coffret en 2 volumes : Tomes 1 et 2. Réflexions et témoignage d'un passé de mathématicien*. Éditions Gallimard, jan 2022.

[38] J. S. Sidhu and P. Kok, "Geometric perspective on quantum parameter estimation," *AVS Quantum Science*, vol. 2, Feb. 2020.

[39] J. Lambert and E. S. Sørensen, "From classical to quantum information geometry: a guide for physicists," *New Journal of Physics*, vol. 25, p. 081201, Aug. 2023.

[40] J. Liu, H. Yuan, X.-M. Lu, and X. Wang, "Quantum fisher information matrix and multiparameter estimation," *Journal of Physics A: Mathematical and Theoretical*, vol. 53, p. 023001, Dec. 2019.

[41] S.-I. Amari and H. Nagaoka, *Methods of information geometry*. Translations of mathematical monographs, Providence, RI: American Mathematical Society, apr 2007.

[42] A. Fujiwara, "Hommage to chentsov's theorem," *Information Geometry*, vol. 7, p. 79–98, Nov. 2022.

[43] S. L. Braunstein and C. M. Caves, "Statistical distance and the geometry of quantum states," *Phys. Rev. Lett.*, vol. 72, pp. 3439–3443, May 1994.

[44] S. Pang and T. A. Brun, "Quantum metrology for a general hamiltonian parameter," *Physical Review A*, vol. 90, Aug. 2014.

[45] J. S. Sidhu, Y. Ouyang, E. T. Campbell, and P. Kok, "Tight bounds on the simultaneous estimation of incompatible parameters," *Phys. Rev. X*, vol. 11, p. 011028, Feb 2021.

[46] S. Ragy, M. Jarzyna, and R. Demkowicz-Dobrzański, "Compatibility in multiparameter quantum metrology," *Physical Review A*, vol. 94, Nov. 2016.

[47] W. Guo, W. Zhong, X.-X. Jing, L.-B. Fu, and X. Wang, "Berry curvature as a lower bound for multiparameter estimation," *Physical Review A*, vol. 93, Apr. 2016.

[48] A. Carollo, B. Spagnolo, A. A. Dubkov, and D. Valenti, "On quantumness in multi-parameter quantum estimation," *Journal of Statistical Mechanics: Theory and Experiment*, vol. 2019, p. 094010, Sept. 2019.

[49] H. Xing and L. Fu, "Measure of the density of quantum states in information geometry and quantum multiparameter estimation," *Physical Review A*, vol. 102, Dec. 2020.

[50] X.-M. Lu and X. Wang, "Incorporating heisenberg's uncertainty principle into quantum multiparameter estimation," *Physical Review Letters*, vol. 126, Mar. 2021.

[51] B. Xia, J. Huang, H. Li, H. Wang, and G. Zeng, "Toward incompatible quantum limits on multiparameter estimation," *Nature Communications*, vol. 14, Feb. 2023.

[52] W. Rossmann, *Lie Groups: An Introduction through Linear Groups*. Oxford Graduate Texts in Mathematics, London, England: Oxford University Press, jun 2006.

[53] L. Campos Venuti and P. Zanardi, "Quantum critical scaling of the geometric tensors," *Phys. Rev. Lett.*, vol. 99, p. 095701, Aug 2007.

[54] V. Zelevinsky, *Quantum physics*, vol. 1. Weinheim, Germany: Wiley-VCH Verlag, Nov. 2010.

[55] B. M. V., "Quantal phase factors accompanying adiabatic changes," *Proceedings of the Royal Society of London. A. Mathematical and Physical Sciences*, vol. 392, p. 45–57, Mar. 1984.

[56] D. Vanderbilt, *Berry Phases in Electronic Structure Theory: Electric Polarization, Orbital Magnetization and Topological Insulators*. Cambridge University Press, Oct. 2018.

[57] M. El-Batanouny, *Advanced Quantum Condensed Matter Physics: One-Body, Many-Body, and Topological Perspectives*. Cambridge University Press, Mar. 2020.

[58] P. Gosselin, F. Ménas, A. Bérard, and H. Mohrbach, "Semiclassical dynamics of electrons in magnetic bloch bands: A hamiltonian approach," *Europhysics Letters (EPL)*, vol. 76, no. 4, pp. 651–656, 2006.

[59] J. Zhou, W.-Y. Shan, W. Yao, and D. Xiao, "Berry phase modification to the energy spectrum of excitons," *Phys. Rev. Lett.*, vol. 115, p. 166803, Oct 2015.

[60] M. C. Chang and Q. Niu, "Berry curvature, orbital moment, and effective quantum theory of electrons in electromagnetic fields," *Journal of Physics: Condensed Matter*, vol. 20, p. 193202, 2008.

[61] P. Gosselin, H. Boumrar, and H. Mohrbach, "Semiclassical quantization of electrons in magnetic fields: The generalized peierls substitution," *EPL (Europhysics Letters)*, vol. 84, p. 50002, Nov 2008.

[62] M. Trushin, M. O. Goerbig, and W. Belzig, "Model prediction of self-rotating excitons in two-dimensional transition-metal dichalcogenides," *Phys. Rev. Lett.*, vol. 120, p. 187401, May 2018.

[63] A. Hichri, S. Jaziri, and M. O. Goerbig, "Charged excitons in two-dimensional transition metal dichalcogenides: Semiclassical calculation of berry curvature effects," *Physical Review B*, vol. 100, Sep 2019.

[64] D. Xiao, M.-C. Chang, and Q. Niu, "Berry phase effects on electronic properties," *Rev. Mod. Phys.*, vol. 82, pp. 1959–2007, Jul 2010.

[65] X. Liu, F. Lunić, D. Song, Z. Dai, S. Xia, L. Tang, J. Xu, Z. Chen, and H. Buljan, "Wavepacket self-rotation and helical zitterbewegung in symmetry-broken honeycomb lattices," *Laser amp; Photonics Reviews*, vol. 15, may 2021.

[66] R. Matsumoto and S. Murakami, "Theoretical prediction of a rotating magnon wave packet in ferromagnets," *Phys. Rev. Lett.*, vol. 106, p. 197202, May 2011.

[67] C.-P. Chuu, M.-C. Chang, and Q. Niu, "Semiclassical dynamics and transport of the dirac spin," *Solid State Communications*, vol. 150, p. 533–537, Mar. 2010.

[68] J. C. W. Song and G. Vignale, "Low-dissipation edge currents without edge states," *Phys. Rev. B*, vol. 99, p. 235405, Jun 2019.

[69] R. Burgos Atencia, A. Agarwal, and D. Culcer, "Orbital angular momentum of bloch electrons: equilibrium formulation, magneto-electric phenomena, and the orbital hall effect," *Advances in Physics: X*, vol. 9, July 2024.

[70] L. Zhang, "Berry curvature and various thermal hall effects," *New Journal of Physics*, vol. 18, p. 103039, Oct. 2016.

[71] R. Karplus and J. M. Luttinger, "Hall effect in ferromagnetics," *Phys. Rev.*, vol. 95, pp. 1154–1160, Sep 1954.

[72] C.-X. Liu, S.-C. Zhang, and X.-L. Qi, "The quantum anomalous hall effect: Theory and experiment," *Annual Review of Condensed Matter Physics*, vol. 7, p. 301–321, Mar. 2016.

[73] C.-Z. Chang, C.-X. Liu, and A. H. MacDonald, "Colloquium: Quantum anomalous hall effect," *Rev. Mod. Phys.*, vol. 95, p. 011002, Jan 2023.

[74] M. Papaj and L. Fu, "Magnus hall effect," *Phys. Rev. Lett.*, vol. 123, p. 216802, Nov 2019.

[75] nLab authors, "Vector bundle." https://ncatlab.org/nlab/show/vector+bundle. Retrieved on the 30/08/2024.

[76] M. Fruchart and D. Carpentier, "An introduction to topological insulators," *Comptes Rendus. Physique*, vol. 14, p. 779–815, Oct. 2013.

[77] B. Simon, "Holonomy, the quantum adiabatic theorem, and berry's phase," *Physical Review Letters*, vol. 51, p. 2167–2170, Dec. 1983.

[78] J. E. Avron, R. Seiler, and B. Simon, "Homotopy and quantization in condensed matter physics," *Physical Review Letters*, vol. 51, p. 51–53, July 1983.

[79] T. Ozawa and B. Mera, "Relations between topology and the quantum metric for chern insulators," *Physical Review B*, vol. 104, July 2021.

[80] B. Mera and T. Ozawa, "Kähler geometry and chern insulators: Relations between topology and the quantum metric," *Physical Review B*, vol. 104, July 2021.

[81] B. Mera and T. Ozawa, "Engineering geometrically flat chern bands with fubini-study kähler structure," *Physical Review B*, vol. 104, Sept. 2021.

[82] nLab authors, "Valence bundle." https://ncatlab.org/nlab/show/valence+bundle. Retrieved on the 30/08/2024.

[83] nLab authors, "Line bundle." https://ncatlab.org/nlab/show/line+bundle. Retrieved on the 03/09/2024.

[84] J. Baez and J. P. Muniain, *Gauge Fields, Knots and Gravity*. WORLD SCIENTIFIC, Oct. 1994.

[85] T. Frankel, *The Geometry of Physics: An Introduction*. Cambridge University Press, Nov. 2011.

[86] T. W. B. Kibble, "Geometrization of quantum mechanics," *Communications in Mathematical Physics*, vol. 65, p. 189–201, June 1979.

[87] nLab authors, "Geometrical formulation of quantum mechanics." https://ncatlab.org/nlab/show/geometrical+formulation+of+quantum+mechanics. Retrieved on the 30/08/2024.

[88] L. P. Hughston, "Geometry of stochastic state vector reduction," *Proc. Math. Phys. Eng. Sci.*, vol. 452, pp. 953–979, apr 1996.

[89] A. Ashtekar and T. A. Schilling, *Geometrical Formulation of Quantum Mechanics*, p. 23–65. Springer New York, 1999.

[90] D. C. Brody and L. P. Hughston, "Geometric quantum mechanics," *Journal of Geometry and Physics*, vol. 38, p. 19–53, Apr. 2001.

[91] H. Heydari, "Geometric formulation of quantum mechanics," 2015.

[92] A. Graf and F. Piéchon, "Berry curvature and quantum metric in n-band systems: An eigenprojector approach," *Phys. Rev. B*, vol. 104, p. 085114, Aug 2021.

[93] J. M. Lee, *Introduction to Smooth Manifolds*. Springer New York, 2012.

[94] J. Milnor and J. D. Stasheff, *Characteristic classes. (AM-76), volume 76*. Annals of Mathematics Studies, Princeton, NJ: Princeton University Press, aug 1974.

[95] A. Hatcher, *Algebraic Topology*. Cambridge, England: Cambridge University Press, dec 2001.

[96] A. Kitaev, V. Lebedev, and M. Feigel'man, "Periodic table for topological insulators and superconductors," in *AIP Conference Proceedings*, AIP, 2009.

[97] C.-K. Chiu, J. C. Teo, A. P. Schnyder, and S. Ryu, "Classification of topological quantum matter with symmetries," *Reviews of Modern Physics*, vol. 88, Aug. 2016.

[98] A. Altland and M. R. Zirnbauer, "Nonstandard symmetry classes in mesoscopic normal-superconducting hybrid structures," *Phys. Rev. B*, vol. 55, pp. 1142–1161, Jan 1997.

[99] D.-L. Deng, S.-T. Wang, C. Shen, and L.-M. Duan, "Hopf insulators and their topologically protected surface states," *Phys. Rev. B*, vol. 88, p. 201105, Nov 2013.

[100] J. Ahn, S. Park, D. Kim, Y. Kim, and B.-J. Yang, "Stiefel–whitney classes and topological phases in band theory," *Chinese Physics B*, vol. 28, p. 117101, Nov. 2019.

[101] M. Ezawa, "Topological euler insulators and their electric circuit realization," *Phys. Rev. B*, vol. 103, p. 205303, May 2021.

[102] J. K. Asbóth, L. Oroszlány, and A. Pályi, *A Short Course on Topological Insulators*. Springer International Publishing, 2016.

[103] nLab authors, "Atiyah-singer index theorem." https://ncatlab.org/nlab/show/Atiyah-Singer+index+theorem. Retrieved on the 04/09/2024.

[104] E. Prodan and H. Schulz-Baldes, *Bulk and Boundary Invariants for Complex Topological Insulators: From K-Theory to Physics*. Springer International Publishing, 2016.

[105] S.-Q. Shen, *Topological Insulators: Dirac Equation in Condensed Matter*. Springer Singapore, 2017.

[106] Y. Hatsugai, "Chern number and edge states in the integer quantum hall effect," *Phys. Rev. Lett.*, vol. 71, pp. 3697–3700, Nov 1993.

[107] Y. Hatsugai, "Topological aspects of the quantum hall effect," *Journal of Physics: Condensed Matter*, vol. 9, p. 2507–2549, Mar. 1997.

[108] M. Kohmoto, "Topological invariant and the quantization of the hall conductance," *Annals of Physics*, vol. 160, p. 343–354, Apr. 1985.

[109] T. M. Gunawardana, A. M. Turner, and R. Barnett, "Optimally localized single-band wannier functions for two-dimensional chern insulators," *Phys. Rev. Res.*, vol. 6, p. 023046, Apr 2024.

[110] A. Fünfhaus, T. Kopp, and E. Lettl, "Winding vectors of topological defects: multiband chern numbers," *Journal of Physics A: Mathematical and Theoretical*, vol. 55, p. 405202, Sept. 2022.

[111] nLab authors, "Fiber bundle." https://ncatlab.org/nlab/show/fiber+bundle. Retrieved on the 04/09/2024.

[112] K. v. Klitzing, G. Dorda, and M. Pepper, "New method for high-accuracy determination of the fine-structure constant based on quantized hall resistance," *Phys. Rev. Lett.*, vol. 45, pp. 494–497, Aug 1980.

[113] K. von Klitzing, "The quantized hall effect," *Reviews of Modern Physics*, vol. 58, p. 519–531, July 1986.

[114] D. J. Thouless, M. Kohmoto, M. P. Nightingale, and M. den Nijs, "Quantized hall conductance in a two-dimensional periodic potential," *Phys. Rev. Lett.*, vol. 49, pp. 405–408, Aug 1982.

[115] M. O. Goerbig, "Quantum hall effects," 2009.

[116] F. D. M. Haldane, "Model for a quantum hall effect without landau levels: Condensed-matter realization of the "parity anomaly"," *Phys. Rev. Lett.*, vol. 61, pp. 2015–2018, Oct 1988.

[117] J. E. Moore, "The birth of topological insulators," *Nature*, vol. 464, p. 194–198, Mar. 2010.

[118] J. Yu, C. J. Ciccarino, R. Bianco, I. Errea, P. Narang, and B. A. Bernevig, "Non-trivial quantum geometry and the strength of electron–phonon coupling," *Nature Physics*, May 2024.

[119] Y. Onishi and L. Fu, "Fundamental bound on topological gap," *Phys. Rev. X*, vol. 14, p. 011052, Mar 2024.

[120] Y. Onishi and L. Fu, "Topological bound on structure factor," 2024.

[121] M. Z. Hasan and C. L. Kane, "Colloquium: Topological insulators," *Rev. Mod. Phys.*, vol. 82, pp. 3045–3067, nov 2010.

[122] C. L. Kane and E. J. Mele, "Quantum spin hall effect in graphene," *Phys. Rev. Lett.*, vol. 95, p. 226801, nov 2005.

[123] C. L. Kane and E. J. Mele, "Z_2 topological order and the quantum spin hall effect," *Phys. Rev. Lett.*, vol. 95, p. 146802, Sep 2005.

[124] L. Fu and C. L. Kane, "Time reversal polarization and a<mml:math xmlns:mml="http://www.w3.org/1998/math/mathml" display="inline"><mml:msub><mml:mi>z</mml:mi><
spin pump," *Physical Review B*, vol. 74, Nov. 2006.

[125] L. Fu, C. L. Kane, and E. J. Mele, "Topological insulators in three dimensions," *Phys. Rev. Lett.*, vol. 98, p. 106803, Mar 2007.

[126] L. Fu and C. L. Kane, "Topological insulators with inversion symmetry," *Phys. Rev. B*, vol. 76, p. 045302, Jul 2007.

[127] C. Kane, "Interview of charles kane by david zierler." Niels Bohr Library & Archives, American Institute of Physics, May 13 2021.

[128] Y. Yao, F. Ye, X.-L. Qi, S.-C. Zhang, and Z. Fang, "Spin-orbit gap of graphene: First-principles calculations," *Phys. Rev. B*, vol. 75, p. 041401, Jan 2007.

[129] J. Sichau, M. Prada, T. Anlauf, T. J. Lyon, B. Bosnjak, L. Tiemann, and R. H. Blick, "Resonance microwave measurements of an intrinsic spin-orbit coupling gap in graphene: A possible indication of a topological state," *Phys. Rev. Lett.*, vol. 122, p. 046403, Feb 2019.

[130] J. Bardeen, L. N. Cooper, and J. R. Schrieffer, "Theory of Superconductivity," *Physical Review*, vol. 108, pp. 1175–1204, Dec. 1957.

[131] L. N. Cooper, "Bound electron pairs in a degenerate fermi gas," *Physical Review*, vol. 104, nov 1956.

[132] F. Papanelopoulou, "Louis paul cailletet: The liquefaction of oxygen and the emergence of low-temperature research," *Notes and Records of the Royal Society*, vol. 67, p. 355–373, Oct. 2013.

[133] H. Kamerlingh Onnes, "The liquefaction of helium," *KNAW, Proceedings*, vol. 11, pp. 168–185, 1909.

[134] M. Cardona, "Albert einstein as the father of solid state physics," 2005.

[135] T. Sauer, "Einstein and the early theory of superconductivity, 1919–1922," *Archive for History of Exact Sciences*, vol. 61, p. 159–211, Feb. 2007.

[136] D. Goodstein and J. R. Goodstein, "Richard feynman and the history of superconductivity," *Physics in Perspective*, vol. 2, pp. 30–47, 2000.

[137] W. Meissner and R. Ochsenfeld, "Ein neuer effekt bei eintritt der supraleitfhigkeit," *Die Naturwissenschaften*, vol. 21, p. 787–788, Nov. 1933.

[138] F. London and H. London, "The electromagnetic equations of the supraconductor," *Proc. R. Soc. Lond.*, vol. 149, pp. 71–88, mar 1935.

[139] V. L. Ginzburg and L. D. Landau, "On the theory of superconductivity," *Zhurnal Eksperimental'noi i Teoreticheskoi Fiziki*, vol. 20, pp. 1064–1082, 1950.

[140] E. Maxwell, "Isotope effect in the superconductivity of mercury," *Phys. Rev.*, vol. 78, pp. 477–477, May 1950.

[141] C. A. Reynolds, B. Serin, W. H. Wright, and L. B. Nesbitt, "Superconductivity of isotopes of mercury," *Phys. Rev.*, vol. 78, pp. 487–487, May 1950.

[142] H. Fröhlich, "Theory of the superconducting state. i. the ground state at the absolute zero of temperature," *Phys. Rev.*, vol. 79, pp. 845–856, Sep 1950.

[143] M. R. Schafroth, "Superconductivity of a charged boson gas," *Phys. Rev.*, vol. 96, pp. 1149–1149, Nov 1954.

[144] M. R. Schafroth, "Theory of superconductivity," *Phys. Rev.*, vol. 96, pp. 1442–1442, Dec 1954.

[145] J. Bardeen and D. Pines, "Electron-phonon interaction in metals," *Phys. Rev.*, vol. 99, pp. 1140–1150, Aug 1955.

[146] P. Fulde and R. A. Ferrell, "Superconductivity in a strong spin-exchange field," *Physical Review*, vol. 135, p. A550–A563, Aug. 1964.

[147] A. I. Larkin and Y. N. Ovchinnikov, "Inhomogeneous state of superconductors," *Sov. Phys. JETP*, vol. 20, p. 762, 1965.

[148] D. F. Agterberg, J. S. Davis, S. D. Edkins, E. Fradkin, D. J. Van Harlingen, S. A. Kivelson, P. A. Lee, L. Radzihovsky, J. M. Tranquada, and Y. Wang, "The physics of pair-density waves: Cuprate superconductors and beyond," *Annual Review of Condensed Matter Physics*, vol. 11, p. 231–270, Mar. 2020.

[149] N. N. Bogoljubov, "On a new method in the theory of superconductivity," *Il Nuovo Cimento*, vol. 7, p. 794–805, Mar. 1958.

[150] A. A. Abrikosov, L. P. Gorkov, and I. Dzyaloshinskii, *Methods of quantum field theory in statistical physics*. Dover Books on Physics, Mineola, NY: Dover Publications, oct 1975.

[151] A. L. Fetter and W. J. D., *Quantum theory of many-particle systems*. Dover Books on Physics, Mineola, NY: Dover Publications, may 2003.

[152] H. Bruus and K. Flensburg, *Many-body quantum theory in condensed matter physics*. Oxford Graduate Texts, London, England: Oxford University Press, sep 2004.

[153] A. Altland and B. D. Simons, *Condensed Matter Field Theory*. Cambridge University Press, Mar. 2010.

[154] E. Fradkin, *Field Theories of Condensed Matter Physics*. Cambridge University Press, Feb. 2013.

[155] R. Courant and D. Hilbert, *Methods of mathematical physics*. Wiley Classics Library, Nashville, TN: John Wiley & Sons, apr 1989.

[156] W. A. Strauss, *Partial Differential Equations*. Chichester, England: John Wiley & Sons, 2 ed., dec 2007.

[157] I. Stakgold and M. J. Holst, *Green's functions and boundary value problems*. Pure and Applied Mathematics: A Wiley Series of Texts, Monographs and Tracts, Hoboken, NJ: Wiley-Blackwell, 3 ed., jan 2011.

[158] L. C. Evans, *Partial differential equations*. Providence, RI: American Mathematical Society, mar 2022.

[159] V. S. Vladimirov, *Equations of mathematical physics*. New York, NY": Marcel Dekker, 1971.

[160] J. Nagamatsu, N. Nakagawa, T. Muranaka, Y. Zenitani, and J. Akimitsu, "Superconductivity at 39k in magnesium diboride," *Nature*, vol. 410, p. 63–64, Mar. 2001.

[161] S. L. Bud'ko and P. C. Canfield, "Superconductivity of magnesium diboride," *Physica C: Superconductivity and its Applications*, vol. 514, p. 142–151, July 2015.

[162] A. Daido, T. Kitamura, and Y. Yanase, "Quantum geometry encoded to pair potentials," *Phys. Rev. B*, vol. 110, p. 094505, Sep 2024.

[163] M. Sato and Y. Ando, "Topological superconductors: a review," *Reports on Progress in Physics*, vol. 80, p. 076501, may 2017.

[164] A. Bansil, H. Lin, and T. Das, "Colloquium: Topological band theory," *Rev. Mod. Phys.*, vol. 88, p. 021004, Jun 2016.

[165] M. G. Vergniory, B. J. Wieder, L. Elcoro, S. S. P. Parkin, C. Felser, B. A. Bernevig, and N. Regnault, "All topological bands of all stoichiometric materials," 2021.

[166] X.-L. Qi and S.-C. Zhang, "Topological insulators and superconductors," *Rev. Mod. Phys.*, vol. 83, pp. 1057–1110, Oct 2011.

[167] N. P. Armitage, E. J. Mele, and A. Vishwanath, "Weyl and dirac semimetals in three-dimensional solids," *Rev. Mod. Phys.*, vol. 90, p. 015001, Jan 2018.

[168] E. Rossi, "Quantum metric and correlated states in two-dimensional systems," *Current Opinion in Solid State and Materials Science*, vol. 25, p. 100952, Oct. 2021.

[169] P. Törmä, S. Peotta, and B. A. Bernevig, "Superconductivity, superfluidity and quantum geometry in twisted multilayer systems," *Nature Reviews Physics*, vol. 4, pp. 528–542, June 2022.

[170] H. Tian, X. Gao, Y. Zhang, S. Che, T. Xu, P. Cheung, K. Watanabe, T. Taniguchi, M. Randeria, F. Zhang, C. N. Lau, and M. W. Bockrath, "Evidence for Dirac flat band superconductivity enabled by quantum geometry," *Nature*, vol. 614, pp. 440–444, Feb. 2023.

[171] S. Manzeli, D. Ovchinnikov, D. Pasquier, O. V. Yazyev, and A. Kis, "2d transition metal dichalcogenides," *Nature Reviews Materials*, vol. 2, p. 17033, Jun 2017.

[172] J. N. Fuchs, F. Piéchon, M. O. Goerbig, and G. Montambaux, "Topological berry phase and semiclassical quantization of cyclotron orbits for two dimensional electrons in coupled band models," *The European Physical Journal B*, vol. 77, pp. 351–362, Oct 2010.

[173] K. He, N. Kumar, L. Zhao, Z. Wang, K. F. Mak, H. Zhao, and J. Shan, "Tightly bound excitons in monolayer wse_2," *Phys. Rev. Lett.*, vol. 113, p. 026803, Jul 2014.

[174] A. Chernikov, T. C. Berkelbach, H. M. Hill, A. Rigosi, Y. Li, O. B. Aslan, D. R. Reichman, M. S. Hybertsen, and T. F. Heinz, "Exciton binding energy and nonhydrogenic rydberg series in monolayer ws_2," *Phys. Rev. Lett.*, vol. 113, p. 076802, Aug 2014.

[175] A. Srivastava and A. m. c. Imamoğlu, "Signatures of bloch-band geometry on excitons: Nonhydrogenic spectra in transition-metal dichalcogenides," *Phys. Rev. Lett.*, vol. 115, p. 166802, Oct 2015.

[176] D. Xiao, G.-B. Liu, W. Feng, X. Xu, and W. Yao, "Coupled spin and valley physics in monolayers of mos_2 and other group-vi dichalcogenides," *Phys. Rev. Lett.*, vol. 108, p. 196802, May 2012.

[177] M. O. Goerbig, G. Montambaux, and F. Piéchon, "Measure of diracness in two-dimensional semiconductors," *EPL (Europhysics Letters)*, vol. 105, p. 57005, mar 2014.

[178] M. Trushin, M. O. Goerbig, and W. Belzig, "Optical absorption by dirac excitons in single-layer transition-metal dichalcogenides," *Phys. Rev. B*, vol. 94, p. 041301, Jul 2016.

[179] L. L. Foldy and S. A. Wouthuysen, "On the dirac theory of spin 1/2 particles and its non-relativistic limit," *Phys. Rev.*, vol. 78, pp. 29–36, Apr 1950.

[180] A. Kormányos, G. Burkard, M. Gmitra, J. Fabian, V. Zólyomi, N. D. Drummond, and V. Fal'ko, "k·p theory for two-dimensional transition metal dichalcogenide semiconductors," *2D Materials*, vol. 2, p. 022001, Apr. 2015.

[181] A. V. Kolobov and J. Tominaga, *Two-Dimensional Transition-Metal Dichalcogenides*. Springer International Publishing, 2016.

[182] E. I. Blount, "Extension of the foldy-wouthuysen transformation," *Phys. Rev.*, vol. 128, pp. 2454–2458, Dec 1962.

[183] G. Sundaram and Q. Niu, "Wave-packet dynamics in slowly perturbed crystals: Gradient corrections and berry-phase effects," *Phys. Rev. B*, vol. 59, pp. 14915–14925, Jun 1999.

[184] A. Castellanos-Gomez, "Black phosphorus: Narrow gap, wide applications," *The Journal of Physical Chemistry Letters*, vol. 6, no. 21, pp. 4280–4291, 2015. PMID: 26600394.

[185] C. Li and Z. Wang, "9 - computational modelling and ab initio calculations in max phases – i," in *Advances in Science and Technology of Mn+1AXn Phases* (I. Low, ed.), pp. 197–222, Woodhead Publishing, 2012.

[186] V. P. Mineev and K. V. Samokhin, *Introduction to unconventional superconductivity*. Gordon and Breach Science Publishers, 1999.

[187] M. Sigrist and K. Ueda, "Phenomenological theory of unconventional superconductivity," *Rev. Mod. Phys.*, vol. 63, pp. 239–311, Apr 1991.

[188] M. Sigrist, "Introduction to unconventional superconductivity," *AIP Conference Proceedings*, 2005.

[189] D. Möckli, "Unconventional singlet-triplet superconductivity," *Journal of Physics: Conference Series*, vol. 2164, p. 012009, mar 2022.

[190] S. Khim, J. F. Landaeta, J. Banda, N. Bannor, M. Brando, P. M. R. Brydon, D. Hafner, R. Küchler, R. Cardoso-Gil, U. Stockert, A. P. Mackenzie, D. F. Agterberg, C. Geibel, and E. Hassinger, "Field-induced transition within the superconducting state of cerh₂as₂," *Science*, vol. 373, no. 6558, pp. 1012–1016, 2021.

[191] Y. Cao, V. Fatemi, S. Fang, K. Watanabe, T. Taniguchi, E. Kaxiras, and P. Jarillo-Herrero, "Unconventional superconductivity in magic-angle graphene superlattices," *Nature*, vol. 556, pp. 43–50, Apr 2018.

[192] E. Lake, A. S. Patri, and T. Senthil, "Pairing symmetry of twisted bilayer graphene: A phenomenological synthesis," *Phys. Rev. B*, vol. 106, p. 104506, Sep 2022.

[193] P. A. Frigeri, D. F. Agterberg, I. Milat, and M. Sigrist, "Phenomenological theory of the s-wave state in superconductors without an inversion center," *The European Physical Journal B - Condensed Matter and Complex Systems*, vol. 54, pp. 435–448, Dec 2006.

[194] P. Zubko, S. Gariglio, M. Gabay, P. Ghosez, and J.-M. Triscone, "Interface physics in complex oxide heterostructures," *Annual Review of Condensed Matter Physics*, vol. 2, p. 141–165, Mar. 2011.

[195] J. F. Schooley, W. R. Hosler, and M. L. Cohen, "Superconductivity in semiconducting srti<mml:math xmlns:mml="http://www.w3.org/1998/math/mathml" display="inline"><mml:mrow><mml:msub><mml:mrow><mml:mi mathvariant="normal">o</mml:mi></mml:mrow><mml:mrow><mml:mn>3</mml:mn></mml:mrow></mml:msub>
Physical Review Letters, vol. 12, p. 474–475, Apr. 1964.

[196] C. S. Koonce, M. L. Cohen, J. F. Schooley, W. R. Hosler, and E. R. Pfeiffer, "Superconducting transition temperatures of semiconducting srti<mml:math xmlns:mml="http://www.w3.org/1998/math/mathml" display="inline"><mml:mrow><mml:msub><mml:mrow><mml:mi mathvariant="normal">o</mml:mi></mml:mrow><mml:mrow><mml:mn>3</mml:mn></mml:mrow></mml:msub>
Physical Review, vol. 163, p. 380–390, Nov. 1967.

[197] A. Ohtomo and H. Y. Hwang, "A high-mobility electron gas at the laalo3/srtio3 heterointerface," *Nature*, vol. 427, p. 423–426, Jan. 2004.

[198] S. Gariglio, M. Gabay, and J.-M. Triscone, "Research update: Conductivity and beyond at the LaAlOsub3/sub/SrTiOsub3/sub interface," *APL Materials*, vol. 4, p. 060701, June 2016.

[199] H. Y. Hwang, Y. Iwasa, M. Kawasaki, B. Keimer, N. Nagaosa, and Y. Tokura, "Emergent phenomena at oxide interfaces," *Nature Materials*, vol. 11, p. 103–113, Jan. 2012.

[200] N. Reyren, S. Thiel, A. D. Caviglia, L. F. Kourkoutis, G. Hammerl, C. Richter, C. W. Schneider, T. Kopp, A.-S. Ruetschi, D. Jaccard, M. Gabay, D. A. Muller, J.-M. Triscone, and J. Mannhart, "Superconducting interfaces between insulating oxides," *Science*, vol. 317, p. 1196–1199, Aug. 2007.

[201] S. Gariglio, N. Reyren, A. D. Caviglia, and J.-M. Triscone, "Superconductivity at the laalo3/srtio3interface," *Journal of Physics: Condensed Matter*, vol. 21, p. 164213, Mar. 2009.

[202] I. Groen, "Electronic and superconducting properties of the two-dimensional electron system at the $LaAlO_3/SrTiO_3$ (111) interface." https://repository.tudelft.nl, 2016. Delft University of Technology, Kavli Institute of Nanoscience.

[203] C. Richter, H. Boschker, W. Dietsche, E. Fillis-Tsirakis, R. Jany, F. Loder, L. F. Kourkoutis, D. A. Muller, J. R. Kirtley, C. W. Schneider, and J. Mannhart, "Interface superconductor with gap behaviour like a high-temperature superconductor," *Nature*, vol. 502, pp. 528–531, Oct. 2013.

[204] D. Doennig, W. E. Pickett, and R. Pentcheva, "Massive symmetry breaking in $\mathrm{laalo_3/srtio_3}(111)$ quantum wells: A three-orbital strongly correlated generalization of graphene," *Phys. Rev. Lett.*, vol. 111, p. 126804, Sep 2013.

[205] K. Song, S. Ryu, H. Lee, T. R. Paudel, C. T. Koch, B. Park, J. K. Lee, S.-Y. Choi, Y.-M. Kim, J. C. Kim, H. Y. Jeong, M. S. Rzchowski, E. Y. Tsymbal, C.-B. Eom, and S. H. Oh, "Direct imaging of the electron liquid at oxide interfaces," *Nature Nanotechnology*, vol. 13, pp. 198–203, Feb. 2018.

[206] F. London, "On the problem of the molecular theory of superconductivity," *Physical Review*, vol. 74, p. 562–573, Sept. 1948.

[207] L. Liang, T. I. Vanhala, S. Peotta, T. Siro, A. Harju, and P. Törmä, "Band geometry, Berry curvature, and superfluid weight," *Physical Review B*, vol. 95, p. 024515, Jan. 2017.

[208] B. S. Chandrasekhar and D. Einzel, "The superconducting penetration depth from the semiclassical model," *Annalen der Physik*, vol. 505, no. 6, pp. 535–546, 1993.

[209] M. Iskin, "Exposing the quantum geometry of spin-orbit-coupled fermi superfluids," *Phys. Rev. A*, vol. 97, p. 063625, Jun 2018.

[210] A. M. R. V. L. Monteiro, M. Vivek, D. J. Groenendijk, P. Bruneel, I. Leermakers, U. Zeitler, M. Gabay, and A. D. Caviglia, "Band inversion driven by electronic correlations at the (111) ${\mathrm{LaAlO}}_{3}/{\mathrm{SrTiO}}_{3}$ interface," *Physical Review B*, vol. 99, p. 201102, May 2019.

[211] U. Khanna, P. K. Rout, M. Mograbi, G. Tuvia, I. Leermakers, U. Zeitler, Y. Dagan, and M. Goldstein, "Symmetry and correlation effects on band structure explain the anomalous transport properties of (111) $\mathrm{laalo}_3/\mathrm{srtio}_3$," *Phys. Rev. Lett.*, vol. 123, p. 036805, Jul 2019.

[212] T. Rödel, C. Bareille, F. Fortuna, C. Baumier, F. Bertran, P. Le Fèvre, M. Gabay, O. Hijano Cubelos, M. Rozenberg, T. Maroutian, P. Lecoeur, and A. Santander-Syro, "Orientational Tuning of the Fermi Sea of Confined Electrons at the ${\mathrm{SrTiO}}_{3}$ (110) and (111) Surfaces," *Physical Review Applied*, vol. 1, p. 051002, June 2014.

[213] G. M. De Luca, R. Di Capua, E. Di Gennaro, A. Sambri, F. M. Granozio, G. Ghiringhelli, D. Betto, C. Piamonteze, N. B. Brookes, and M. Salluzzo, "Symmetry breaking at the (111) interfaces of ${\mathrm{SrTiO}}_{3}$ hosting a two-dimensional electron system," *Physical Review B*, vol. 98, p. 115143, Sept. 2018.

[214] M. Vivek, M. O. Goerbig, and M. Gabay, "Topological states at the (001) surface of mml:math xmlns:mml="http://www.w3.org/1998/math/MathML"mml:msubmml:miSrTiO/mml:mimml:mn3/mml:mn/r *Physical Review B*, vol. 95, Apr. 2017.

[215] G. Khalsa, B. Lee, and A. H. MacDonald, "Theory of ${t}_{2g}$ electron-gas Rashba interactions," *Physical Review B*, vol. 88, p. 041302, July 2013.

[216] Z. Zhong, A. Tóth, and K. Held, "Theory of spin-orbit coupling at LaAlO${}_{3}$/SrTiO${}_{3}$ interfaces and SrTiO${}_{3}$ surfaces," *Physical Review B*, vol. 87, p. 161102, Apr. 2013.

[217] G. Khalsa and A. H. MacDonald, "Theory of the srtio_3 surface state two-dimensional electron gas," *Phys. Rev. B*, vol. 86, p. 125121, Sep 2012.

[218] A. M. R. V. L. Monteiro, D. J. Groenendijk, I. Groen, J. de Bruijckere, R. Gaudenzi, H. S. J. van der Zant, and A. D. Caviglia, "Two-dimensional superconductivity at the

(111)$\mathrm{LaAlO}{}_{3}/\mathrm{SrTiO}{}_{3}$ interface," *Physical Review B*, vol. 96, p. 020504, July 2017.

[219] N. Manca, D. Bothner, A. M. R. V. L. Monteiro, D. Davidovikj, Y. G. Sağlam, M. Jenkins, M. Gabay, G. A. Steele, and A. D. Caviglia, "Bimodal phase diagram of the superfluid density in $\mathrm{laalo}_3/\mathrm{SrTio}_3$ revealed by an interfacial waveguide resonator," *Phys. Rev. Lett.*, vol. 122, p. 036801, Jan 2019.

[220] E. Lesne, Y. Gozde Saglam, M. Kounalakis, M. Gabay, G. Steele, and A. D. Caviglia, "Microwave spectroscopy of two-dimensional superconductivity at laalo_3/srtio_3(111) interfaces," in *APS March Meeting 2021*, vol. 66, 2021.

[221] M. Tinkham, *Introduction to Superconductivity*. New York, NY: McGraw-Hill, 2 ed., Nov. 1995.

[222] P. K. Rout, E. Maniv, and Y. Dagan, "Link between the superconducting dome and spin-orbit interaction in the (111) $\mathrm{laalo}_3/\mathrm{SrTio}_3$ interface," *Phys. Rev. Lett.*, vol. 119, p. 237002, Dec 2017.

[223] J. A. Bert, K. C. Nowack, B. Kalisky, H. Noad, J. R. Kirtley, C. Bell, H. K. Sato, M. Hosoda, Y. Hikita, H. Y. Hwang, and K. A. Moler, "Gate-tuned superfluid density at the superconducting LaAlO${}_{3}$/SrTiO${}_{3}$ interface," *Physical Review B*, vol. 86, p. 060503, Aug. 2012.

[224] S. Gariglio, M. Gabay, J. Mannhart, and J.-M. Triscone, "Interface superconductivity," *Physica C: Superconductivity and its Applications*, vol. 514, pp. 189–198, July 2015.

[225] T. Kitamura, A. Daido, and Y. Yanase, "Quantum geometric effect on fulde-ferrell-larkin-ovchinnikov superconductivity," *Phys. Rev. B*, vol. 106, p. 184507, Nov 2022.

[226] T. Kitamura, S. Kanasugi, M. Chazono, and Y. Yanase, "Quantum geometry induced anapole superconductivity," *Phys. Rev. B*, vol. 107, p. 214513, Jun 2023.

[227] T. Kitamura, A. Daido, and Y. Yanase, "Spin-triplet superconductivity from quantum-geometry-induced ferromagnetic fluctuation," *Phys. Rev. Lett.*, vol. 132, p. 036001, Jan 2024.

[228] M. F. Lapa and T. L. Hughes, "Semiclassical wave packet dynamics in nonuniform electric fields," *Phys. Rev. B*, vol. 99, p. 121111, Mar 2019.

[229] N. Marzari and D. Vanderbilt, "Maximally localized generalized wannier functions for composite energy bands," *Phys. Rev. B*, vol. 56, pp. 12847–12865, Nov 1997.

[230] I. Komissarov, T. Holder, and R. Queiroz, "The quantum geometric origin of capacitance in insulators," *Nature Communications*, vol. 15, May 2024.

[231] P. Gosselin and H. Mohrbach, "Appearance of gauge fields and forces beyond the adiabatic approximation," *Journal of Physics A: Mathematical and Theoretical*, vol. 43, p. 354025, Aug. 2010.

[232] T. Misawa and Y. Yamaji, "Zeros of green functions in topological insulators," *Physical Review Research*, vol. 4, June 2022.

[233] G. E. Volovik, *The Universe in a Helium Droplet*. Oxford University PressOxford, Feb. 2009.

[234] Z. Wang, X.-L. Qi, and S.-C. Zhang, "Equivalent topological invariants of topological insulators," *New Journal of Physics*, vol. 12, p. 065007, June 2010.

[235] V. Gurarie, "Single-particle green's functions and interacting topological insulators," *Phys. Rev. B*, vol. 83, p. 085426, Feb 2011.

[236] L. Wang, H. Jiang, X. Dai, and X. C. Xie, "Pole expansion of self-energy and interaction effect for topological insulators," *Phys. Rev. B*, vol. 85, p. 235135, Jun 2012.

[237] Z. Wang and S.-C. Zhang, "Simplified topological invariants for interacting insulators," *Phys. Rev. X*, vol. 2, p. 031008, Aug 2012.

[238] Q. Niu, D. J. Thouless, and Y.-S. Wu, "Quantized hall conductance as a topological invariant," *Phys. Rev. B*, vol. 31, pp. 3372–3377, Mar 1985.

[239] K. Ishikawa and T. Matsuyama, "Magnetic field induced multi-component QED3 and quantum hall effect," *Zeitschrift fr Physik C Particles and Fields*, vol. 33, pp. 41–45, Mar. 1986.

[240] T. Matsuyama, "Quantization of conductivity induced by topological structure of energy-momentum space in generalized QED3," *Progress of Theoretical Physics*, vol. 77, pp. 711–730, Mar. 1987.

[241] K. Kudo, H. Watanabe, T. Kariyado, and Y. Hatsugai, "Many-body chern number without integration," *Physical Review Letters*, vol. 122, Apr. 2019.

[242] K. Seki and S. Yunoki, "Topological interpretation of the luttinger theorem," *Phys. Rev. B*, vol. 96, p. 085124, Aug 2017.

[243] J. Skolimowski and M. Fabrizio, "Luttinger's theorem in the presence of luttinger surfaces," *Phys. Rev. B*, vol. 106, p. 045109, Jul 2022.

[244] J. Zhao, P. Mai, B. Bradlyn, and P. Phillips, "Failure of topological invariants in strongly correlated matter," *Phys. Rev. Lett.*, vol. 131, p. 106601, Sep 2023.

[245] N. Wagner, L. Crippa, A. Amaricci, P. Hansmann, M. Klett, E. J. König, T. Schäfer, D. D. Sante, J. Cano, A. J. Millis, A. Georges, and G. Sangiovanni, "Mott insulators with boundary zeros," *Nature Communications*, vol. 14, Nov. 2023.

[246] A. Blason and M. Fabrizio, "Unified role of green's function poles and zeros in correlated topological insulators," *Phys. Rev. B*, vol. 108, p. 125115, Sep 2023.

[247] P. B. Denton, S. J. Parke, T. Tao, and X. Zhang, "Eigenvectors from eigenvalues: A survey of a basic identity in linear algebra," *Bulletin of the American Mathematical Society*, vol. 59, p. 31–58, Feb. 2021.

[248] X. Wu, "Higher curvature corrections to pole-skipping," *Journal of High Energy Physics*, vol. 2019, Dec. 2019.

[249] N. Čeplak, K. Ramdial, and D. Vegh, "Fermionic pole-skipping in holography," *Journal of High Energy Physics*, vol. 2020, July 2020.

[250] Y. j. Ahn, V. Jahnke, H.-S. Jeong, K.-S. Lee, M. Nishida, and K.-Y. Kim, "Classifying pole-skipping points," *Journal of High Energy Physics*, vol. 2021, Mar. 2021.

[251] H. Georgi, "Unparticle physics," *Physical Review Letters*, vol. 98, May 2007.

[252] J. P. F. LeBlanc and A. G. Grushin, "Unparticle mediated superconductivity," *New Journal of Physics*, vol. 17, p. 033039, Mar. 2015.

[253] S. Fisk, "A very short proof of cauchy's interlace theorem for eigenvalues of hermitian matrices," 2005.

[254] A. P. Schnyder, S. Ryu, A. Furusaki, and A. W. W. Ludwig, "Classification of topological insulators and superconductors in three spatial dimensions," *Phys. Rev. B*, vol. 78, p. 195125, Nov 2008.

[255] S. Ryu, A. P. Schnyder, A. Furusaki, and A. W. W. Ludwig, "Topological insulators and superconductors: tenfold way and dimensional hierarchy," *New Journal of Physics*, vol. 12, p. 065010, June 2010.

[256] Y. Yoshimura, W. Onishi, K. Kobayashi, T. Ohtsuki, and K.-I. Imura, "Comparative study of weyl semimetal and topological/chern insulators: Thin-film point of view," *Phys. Rev. B*, vol. 94, p. 235414, Dec 2016.

[257] C. Morice, T. Kopp, and A. P. Kampf, "Nonunique connection between bulk topological invariants and surface physics," *Phys. Rev. B*, vol. 100, p. 235427, Dec 2019.

[258] Y. Choi, H. Kim, Y. Peng, A. Thomson, C. Lewandowski, R. Polski, Y. Zhang, H. S. Arora, K. Watanabe, T. Taniguchi, J. Alicea, and S. Nadj-Perge, "Correlation-driven topological phases in magic-angle twisted bilayer graphene," *Nature*, vol. 589, p. 536–541, Jan. 2021.

[259] Y. Da Liao, J. Kang, C. N. Breiø, X. Y. Xu, H.-Q. Wu, B. M. Andersen, R. M. Fernandes, and Z. Y. Meng, "Correlation-induced insulating topological phases at charge neutrality in twisted bilayer graphene," *Phys. Rev. X*, vol. 11, p. 011014, Jan 2021.

[260] S. Raghu, X.-L. Qi, C. Honerkamp, and S.-C. Zhang, "Topological mott insulators," *Phys. Rev. Lett.*, vol. 100, p. 156401, Apr 2008.

[261] M. Dzero, J. Xia, V. Galitski, and P. Coleman, "Topological kondo insulators," *Annual Review of Condensed Matter Physics*, vol. 7, no. 1, pp. 249–280, 2016.

[262] J. Li, R.-L. Chu, J. K. Jain, and S.-Q. Shen, "Topological anderson insulator," *Phys. Rev. Lett.*, vol. 102, p. 136806, Apr 2009.

[263] W. Chen and G. von Gersdorff, "Measurement of interaction-dressed berry curvature and quantum metric in solids by optical absorption," *SciPost Physics Core*, vol. 5, Aug. 2022.

[264] T. Kashihara, Y. Michishita, and R. Peters, "Quantum metric on the brillouin zone in correlated electron systems and its relation to topology for chern insulators," *Phys. Rev. B*, vol. 107, p. 125116, Mar 2023.

[265] N. J. Higham, *Functions of matrices: Theory and computation*. Society for Industrial and Applied Mathematics, 2008.

[266] M. Fabrizio, "Emergent quasiparticles at luttinger surfaces," *Nature Communications*, vol. 13, Mar. 2022.

[267] A. V. Chubukov and D. L. Maslov, "First-matsubara-frequency rule in a fermi liquid. i. fermionic self-energy," *Physical Review B*, vol. 86, Oct. 2012.

[268] Y. Hatsugai and M. Kohmoto, "Exactly solvable model of correlated lattice electrons in any dimensions," *Journal of the Physical Society of Japan*, vol. 61, p. 2056–2069, June 1992.

[269] C. Setty, F. Xie, S. Sur, L. Chen, M. G. Vergniory, and Q. Si, "Electronic properties, correlated topology, and green's function zeros," *Phys. Rev. Res.*, vol. 6, p. 033235, Sep 2024.

[270] S. Sinha and B. Bradlyn, "Computing the $\mathbb{Z}_2$ invariant in two-dimensional strongly-correlated systems," 2024.

[271] D. Guerci, G. Sangiovanni, A. J. Millis, and M. Fabrizio, "Electrical transport in the hatsugai-kohmoto model," 2024.

[272] P. M. Chaikin and T. C. Lubensky, *Principles of Condensed Matter Physics*. Cambridge University Press, June 1995.

[273] M. Abramowitz and I. A. Stegun, *Handbook of Mathematical Functions with Formulas, Graphs, and Mathematical Tables*. New York City: Dover, ninth dover printing, tenth gpo printing ed., 1964.

[274] D. Xiao, W. Zhu, Y. Ran, N. Nagaosa, and S. Okamoto, "Interface engineering of quantum Hall effects in digital transition metal oxide heterostructures," *Nature Communications*, vol. 2, p. 596, Dec. 2011.

[275] Y. Nakatsukasa, "Off-diagonal perturbation, first-order approximation and quadratic residual bounds for matrix eigenvalue problems," in *Eigenvalue Problems: Algorithms, Software and Applications in Petascale Computing* (T. Sakurai, S.-L. Zhang, T. Imamura, Y. Yamamoto, Y. Kuramashi, and T. Hoshi, eds.), Lecture Notes in Computational Science and Engineering, (Cham), pp. 233–249, Springer International Publishing, 2017.

Appendices

A - Appendices of Chapter 1

A.1 . Proof of Property 1.2.1

Let us restate Property 1.2.1.

Property (Properties of $\mathcal{T}_{\boldsymbol{m}}$)**.** *Let $\boldsymbol{n}, \boldsymbol{m} \in \mathbb{Z}^d$. The Bravais translation operators then obey the following properties.*

1. *Additivity: $\mathcal{T}_{\boldsymbol{n}}\mathcal{T}_{\boldsymbol{m}} = \mathcal{T}_{\boldsymbol{n}+\boldsymbol{m}}$.*
2. *Inverse operator: $\mathcal{T}_{\boldsymbol{m}}^{-1} = \mathcal{T}_{-\boldsymbol{m}}$.*
3. *Unitarity: $\mathcal{T}_{\boldsymbol{m}}^{\dagger} = \mathcal{T}_{\boldsymbol{m}}^{-1} = \mathcal{T}_{-\boldsymbol{m}}$.*
4. *Commutation with position operator: For any function f, $\mathcal{T}_{\boldsymbol{m}} f(\hat{\boldsymbol{r}}) = f\big(\hat{\boldsymbol{r}} - \boldsymbol{R}_{\boldsymbol{m}}\big)\mathcal{T}_{\boldsymbol{m}}$.*

Proof. 1. The equality is readily shown as follows,

$$\mathcal{T}_{\boldsymbol{n}}\mathcal{T}_{\boldsymbol{m}} |\boldsymbol{r}\rangle = \mathcal{T}_{\boldsymbol{n}} |\boldsymbol{r} + \boldsymbol{R}_{\boldsymbol{m}}\rangle = |\boldsymbol{r} + \boldsymbol{R}_{\boldsymbol{m}} + \boldsymbol{R}_{\boldsymbol{n}}\rangle = |\boldsymbol{r} + \boldsymbol{R}_{\boldsymbol{n}+\boldsymbol{m}}\rangle = \mathcal{T}_{\boldsymbol{n}+\boldsymbol{m}} |\boldsymbol{r}\rangle . \tag{A.1}$$

2. From the additive property we have that

$$\mathcal{T}_{\boldsymbol{m}}\mathcal{T}_{-\boldsymbol{m}} = \mathcal{T}_{-\boldsymbol{m}}\mathcal{T}_{\boldsymbol{m}} = \mathcal{T}_{\boldsymbol{m}-\boldsymbol{m}} = \mathcal{T}_{\boldsymbol{0}} = \mathbb{1}. \tag{A.2}$$

3. $\mathcal{T}_{\boldsymbol{m}}$ is unitary iff it preserves the Hermitian product $\langle \boldsymbol{r}_1 | \boldsymbol{r}_2 \rangle = \delta^d(\boldsymbol{r}_1 - \boldsymbol{r}_2)$.

$$\langle \mathcal{T}_{\boldsymbol{m}}\boldsymbol{r}_1 | \mathcal{T}_{\boldsymbol{m}}\boldsymbol{r}_2 \rangle = |\mathcal{T}_{\boldsymbol{m}}\boldsymbol{r}_1\rangle^{\dagger} |\mathcal{T}_{\boldsymbol{m}}\boldsymbol{r}_2\rangle = |\boldsymbol{r}_1 + \boldsymbol{R}_{\boldsymbol{m}}\rangle^{\dagger} |\boldsymbol{r}_2 + \boldsymbol{R}_{\boldsymbol{m}}\rangle = \langle \boldsymbol{r}_1 + \boldsymbol{R}_{\boldsymbol{m}} | \boldsymbol{r}_2 + \boldsymbol{R}_{\boldsymbol{m}}\rangle \tag{A.3a}$$

$$= \delta^d\big[\boldsymbol{r}_1 + \boldsymbol{R}_{\boldsymbol{m}} - (\boldsymbol{r}_2 - \boldsymbol{R}_{\boldsymbol{m}})\big] = \delta^d(\boldsymbol{r}_1 - \boldsymbol{r}_2) = \langle \boldsymbol{r}_1 | \boldsymbol{r}_2 \rangle . \tag{A.3b}$$

The Bravais translation operator is thus unitary and we have $\mathcal{T}_{\boldsymbol{m}}^{\dagger} = \mathcal{T}_{\boldsymbol{m}}^{-1} = \mathcal{T}_{-\boldsymbol{m}}$. From this relation we can know how the Bravais translation operator acts on bras,

$$\langle \boldsymbol{r}| \mathcal{T}_{\boldsymbol{m}} = \big(\mathcal{T}_{\boldsymbol{m}}^{\dagger} |\boldsymbol{r}\rangle\big)^{\dagger} = \big(\mathcal{T}_{-\boldsymbol{m}} |\boldsymbol{r}\rangle\big)^{\dagger} = |\boldsymbol{r} - \boldsymbol{R}_{\boldsymbol{m}}\rangle^{\dagger} = \langle \boldsymbol{r} - \boldsymbol{R}_{\boldsymbol{m}}| . \tag{A.3c}$$

4. The transfer theorem allows to represent $f(\hat{\boldsymbol{r}})$ as

$$f(\hat{\boldsymbol{r}}) = \int d\boldsymbol{r} f(\boldsymbol{r}) |\boldsymbol{r}\rangle \langle \boldsymbol{r}| . \tag{A.4}$$

Using the latter, we write

$$\mathcal{T}_{\boldsymbol{m}} f(\hat{\boldsymbol{r}}) = \int d\boldsymbol{r} f(\boldsymbol{r}) \mathcal{T}_{\boldsymbol{m}} |\boldsymbol{r}\rangle \langle \boldsymbol{r}| = \int d\boldsymbol{r} f(\boldsymbol{r}) |\boldsymbol{r} + \boldsymbol{R}_{\boldsymbol{m}}\rangle \langle \boldsymbol{r}| \tag{A.5a}$$

$$= \int d\boldsymbol{r}' f\big(\boldsymbol{r}' - \boldsymbol{R}_{\boldsymbol{m}}\big) |\boldsymbol{r}'\rangle \big\langle \boldsymbol{r}' - \boldsymbol{R}_{\boldsymbol{m}}\big| \tag{A.5b}$$

with $\boldsymbol{r}' = \boldsymbol{r} + \boldsymbol{R}_{\boldsymbol{m}}$. Using $\langle \boldsymbol{r}| \mathcal{T}_{\boldsymbol{m}} = \langle \boldsymbol{r} - \boldsymbol{R}_{\boldsymbol{m}}|$, we then have

$$\mathcal{T}_{\boldsymbol{m}} f(\hat{\boldsymbol{r}}) = \int d\boldsymbol{r} f\big(\boldsymbol{r} - \boldsymbol{R}_{\boldsymbol{m}}\big) |\boldsymbol{r}\rangle \langle \boldsymbol{r}| \mathcal{T}_{\boldsymbol{m}} = f\big(\hat{\boldsymbol{r}} - \boldsymbol{R}_{\boldsymbol{m}}\big)\mathcal{T}_{\boldsymbol{m}} \tag{A.6}$$

□

A.2 . Reciprocal primitive lattice vectors

A.2.1 . Proof of existence

Let $i \in [\![1, d]\!]$. The reciprocal primitive lattice vectors $\boldsymbol{b}_i \in \mathbb{R}^d$ are then defined by

$$\forall j \in [\![1, d]\!], \;\; \boldsymbol{b}_i \cdot \boldsymbol{a}_j = 2\pi\delta_{ij}. \tag{A.7}$$

Decomposing both vectors in the directions $\boldsymbol{e}_\mu$, we then have

$$\forall j \in [\![1, d]\!], \;\; \sum_{\mu=1}^{d} b_{i,\mu} a_{j,\mu} = 2\pi\delta_{ij} \tag{A.8}$$

This is a d by d linear system of equations. Defining the matrix $A = (a_{j\mu})_{j,\mu\in[\![1,d]\!]} \in \mathcal{M}_d(\mathbb{R})$, we have

$$A\boldsymbol{b}_i = 2\pi\boldsymbol{e}_i, \tag{A.9}$$

with $\boldsymbol{e}_i$ the unitary vector with only i-th component being non-zero. $\boldsymbol{b}_i$ then exists iff $\det A \neq 0$. Now since the vectors $\boldsymbol{a}_j$ are linearly independent, $\det A \neq 0$ and consequently we have proved the existence of the vectors $\boldsymbol{b}_i$. Moreover, since all the d vectors $\boldsymbol{a}_j$ are linearly independent, $\boldsymbol{A}$ is a matrix of rank d. This ensures the unicity of the solutions $\boldsymbol{b}_i$. Therefore, while the choice of real space parametrization $\boldsymbol{a}_j$ is not unique, the resulting reciprocal space parametrization is.

A.2.2 . General expressions in two and three dimensions

A.2.2.1 Two-dimensional case

In the two-dimensional case, the reciprocal primitive lattice vectors are defined by

$$b_{1x}a_{1x} + b_{1y}a_{1y} = 2\pi, \;\; b_{1x}a_{2x} + b_{1y}a_{2y} = 0 \tag{A.10a}$$

$$b_{2x}a_{1x} + b_{2y}a_{1y} = 0, \;\; b_{2x}a_{2x} + b_{2y}a_{2y} = 2\pi. \tag{A.10b}$$

We can solve Eq. (A.10) by a usual Gauss elimination. Consider $\boldsymbol{b}_1$. Isolating b_{1y} in the second equation gives

$$b_{1y} = -\frac{a_{2x}}{a_{2y}} b_{1x}. \tag{A.11}$$

Injecting this in the first equation then gives

$$b_{1x}a_{1x} - \frac{a_{2x}a_{1y}}{a_{2y}} b_{1x} = 2\pi \Leftrightarrow \frac{a_{1x}a_{2y} - a_{1y}a_{2x}}{a_{2y}} b_{1x} = 2\pi. \tag{A.12}$$

Recognizing $a_{1x}a_{2y} - a_{1y}a_{2x} = (\boldsymbol{a}_1 \times \boldsymbol{a}_2)_z$, we thus have

$$b_{1x} = \frac{2\pi a_{2y}}{(\boldsymbol{a}_1 \times \boldsymbol{a}_2)_z} \Rightarrow b_{1y} = -\frac{2\pi a_{2x}}{(\boldsymbol{a}_1 \times \boldsymbol{a}_2)_z}. \tag{A.13}$$

$\boldsymbol{b}_2$ is found in the same way, and we can concisely write the result as

$$\boldsymbol{b}_1 = \frac{2\pi}{(\boldsymbol{a}_1 \times \boldsymbol{a}_2)_z} \begin{pmatrix} a_{2y} \\ -a_{2x} \end{pmatrix}, \;\; \boldsymbol{b}_2 = \frac{2\pi}{(\boldsymbol{a}_1 \times \boldsymbol{a}_2)_z} \begin{pmatrix} -a_{1y} \\ a_{1x} \end{pmatrix}. \tag{A.14}$$

A.2.2.2 Three-dimensional case

In the three-dimensional case we have nine equations for the three vectors $\boldsymbol{b}_{1,2,3}$. In matrix notations, $\boldsymbol{b}_i$ is determined by

$$\begin{pmatrix} a_{1x} & a_{1y} & a_{1z} \\ a_{2x} & a_{2y} & a_{2z} \\ a_{3x} & a_{3y} & a_{3z} \end{pmatrix} \begin{pmatrix} b_{ix} \\ b_{iy} \\ b_{iz} \end{pmatrix} = \begin{pmatrix} 2\pi\delta_{i1} \\ 2\pi\delta_{i2} \\ 2\pi\delta_{i3} \end{pmatrix}. \tag{A.15}$$

So we need to invert the matrix. To do so we use Laplace's formula

$$A^{-1} = \frac{1}{\det A} \operatorname{adj} A, \quad (\operatorname{adj} A)_{ij} = (-1)^{i+j} \det[A]_{ji} \tag{A.16}$$

with $[A]_{ij}$ the matrix A without its i-th row and j-th column. First, we compute the determinant of the matrix,

$$\det \begin{pmatrix} a_{1x} & a_{1y} & a_{1z} \\ a_{2x} & a_{2y} & a_{2z} \\ a_{3x} & a_{3y} & a_{3z} \end{pmatrix} = a_{1x} \begin{vmatrix} a_{2y} & a_{2z} \\ a_{3y} & a_{3z} \end{vmatrix} - a_{1y} \begin{vmatrix} a_{2x} & a_{2z} \\ a_{3x} & a_{3z} \end{vmatrix} + a_{1z} \begin{vmatrix} a_{2x} & a_{2y} \\ a_{3x} & a_{3y} \end{vmatrix} \tag{A.17a}$$

$$= a_{1x}(a_{2y}a_{3z} - a_{3y}a_{2z}) + a_{1y}(a_{2z}a_{3x} - a_{2x}a_{3z}) + a_{1z}(a_{2x}a_{3y} - a_{2y}a_{3x}) \tag{A.17b}$$

$$= \boldsymbol{a}_1 \cdot (\boldsymbol{a}_2 \times \boldsymbol{a}_3). \tag{A.17c}$$

We then have

$$\begin{pmatrix} a_{1x} & a_{1y} & a_{1z} \\ a_{2x} & a_{2y} & a_{2z} \\ a_{3x} & a_{3y} & a_{3z} \end{pmatrix}^{-1} = \frac{1}{\boldsymbol{a}_1 \cdot (\boldsymbol{a}_2 \times \boldsymbol{a}_3)} \begin{pmatrix} a_{2y}a_{3z} - a_{2z}a_{3y} & a_{1z}a_{3y} - a_{1y}a_{3z} & a_{1y}a_{2z} - a_{1z}a_{2y} \\ a_{2z}a_{3x} - a_{2x}a_{3z} & a_{1x}a_{3z} - a_{1z}a_{3x} & a_{1z}a_{2x} - a_{1x}a_{2z} \\ a_{2x}a_{3y} - a_{2y}a_{3x} & a_{1y}a_{3x} - a_{1x}a_{3y} & a_{1x}a_{2y} - a_{1y}a_{2x} \end{pmatrix} \tag{A.18a}$$

$$= \frac{1}{\boldsymbol{a}_1 \cdot (\boldsymbol{a}_2 \times \boldsymbol{a}_3)} \begin{pmatrix} (\boldsymbol{a}_2 \times \boldsymbol{a}_3)_x & (\boldsymbol{a}_3 \times \boldsymbol{a}_1)_x & (\boldsymbol{a}_1 \times \boldsymbol{a}_2)_x \\ (\boldsymbol{a}_2 \times \boldsymbol{a}_3)_y & (\boldsymbol{a}_3 \times \boldsymbol{a}_1)_y & (\boldsymbol{a}_1 \times \boldsymbol{a}_2)_y \\ (\boldsymbol{a}_2 \times \boldsymbol{a}_3)_z & (\boldsymbol{a}_3 \times \boldsymbol{a}_1)_z & (\boldsymbol{a}_1 \times \boldsymbol{a}_2)_z \end{pmatrix}. \tag{A.18b}$$

Applying this result we finally find

$$\boldsymbol{b}_1 = \frac{2\pi}{\boldsymbol{a}_1 \cdot (\boldsymbol{a}_2 \times \boldsymbol{a}_3)} \boldsymbol{a}_2 \times \boldsymbol{a}_3, \quad \boldsymbol{b}_2 = \frac{2\pi}{\boldsymbol{a}_1 \cdot (\boldsymbol{a}_2 \times \boldsymbol{a}_3)} \boldsymbol{a}_3 \times \boldsymbol{a}_1, \quad \boldsymbol{b}_3 = \frac{2\pi}{\boldsymbol{a}_1 \cdot (\boldsymbol{a}_2 \times \boldsymbol{a}_3)} \boldsymbol{a}_1 \times \boldsymbol{a}_2. \tag{A.19}$$

A.2.3 . Examples

Square lattice The square lattice is parametrized by

$$\boldsymbol{a}_1 = a\boldsymbol{e}_x, \quad \boldsymbol{a}_2 = a\boldsymbol{e}_y, \tag{A.20}$$

with $a \in \mathbb{R}_+^*$ the interatomic distance. We then have $(\boldsymbol{a}_1 \times \boldsymbol{a}_2)_z = (a^2\boldsymbol{e}_z)_z = a^2$. Applying Eq. (A.14) yields

$$\boldsymbol{b}_1 = \frac{2\pi}{a^2} \begin{pmatrix} a \\ 0 \end{pmatrix} = \frac{2\pi}{a} \begin{pmatrix} 1 \\ 0 \end{pmatrix}, \quad \boldsymbol{b}_2 = \frac{2\pi}{a^2} \begin{pmatrix} 0 \\ a \end{pmatrix} = \frac{2\pi}{a} \begin{pmatrix} 0 \\ 1 \end{pmatrix}. \tag{A.21}$$

Face Centered Cubic (FCC) lattice The face centered cubic (FCC) lattice is parametrized as [272]

$$\boldsymbol{a}_1 = \frac{a}{2}(1,1,0), \quad \boldsymbol{a}_2 = \frac{a}{2}(0,1,1), \quad \boldsymbol{a}_3 = \frac{a}{2}(1,0,1), \tag{A.22}$$

with again $a \in \mathbb{R}_+^*$ the interatomic distance. We first compute the volume factor to be

$$\boldsymbol{a}_1 \cdot (\boldsymbol{a}_2 \times \boldsymbol{a}_3) = \frac{a^3}{8} \begin{pmatrix} 1 \\ 1 \\ 0 \end{pmatrix} \cdot \begin{pmatrix} 1 \\ 1 \\ -1 \end{pmatrix} = \frac{a^3}{4}. \tag{A.23}$$

Applying Eq. (A.19) for $\boldsymbol{b}_1$ then gives

$$\boldsymbol{b}_1 = \frac{2\pi}{a}(1,1,-1), \quad \boldsymbol{b}_2 = \frac{2\pi}{a}(1,-1,1), \quad \boldsymbol{b}_3 = \frac{2\pi}{a}(1,1,1). \tag{A.24}$$

Honeycomb lattice One parametrization of the honeycomb lattice is [11, 24]

$$\boldsymbol{a}_1 = a\left(\frac{\sqrt{3}}{2}, \frac{3}{2}\right), \quad \boldsymbol{a}_2 = a\left(-\frac{\sqrt{3}}{2}, \frac{3}{2}\right). \tag{A.25}$$

To apply Eq. (A.14), we first compute

$$\boldsymbol{a}_1 \times \boldsymbol{a}_2 = a^2 \begin{pmatrix} \sqrt{3}/2 \\ 3/2 \\ 0 \end{pmatrix} \times \begin{pmatrix} -\sqrt{3}/2 \\ 3/2 \\ 0 \end{pmatrix} = \frac{3\sqrt{3}}{2} a^2 \boldsymbol{e}_z. \tag{A.26}$$

The reciprocal primitive lattice vectors then become

$$\boldsymbol{b}_1 = \frac{4\pi}{3\sqrt{3}a}\left(\frac{3}{2}, \frac{\sqrt{3}}{2}\right), \quad \boldsymbol{b}_2 = \frac{4\pi}{3\sqrt{3}a}\left(-\frac{3}{2}, \frac{\sqrt{3}}{2}\right). \tag{A.27}$$

A.3 . Proof of Bloch's theorem

We can find an orthonormal basis of eigenvectors of both $\hat{H}$ and $\mathcal{T}_{\boldsymbol{m}}$. Let $|\psi\rangle$ be such an eigenvector. For $\epsilon \in \operatorname{Sp} \hat{H}$ and $c_{\boldsymbol{m}} \in \operatorname{Sp} \mathcal{T}_{\boldsymbol{m}}$, we then have $\hat{H}|\psi\rangle = \epsilon |\psi\rangle$ and $\mathcal{T}_{\boldsymbol{m}} |\psi\rangle = c_{\boldsymbol{m}} |\psi\rangle$. Using the closure relation of the kets $|\boldsymbol{r}\rangle$ we have

$$|\psi\rangle = \left(\int d\boldsymbol{r} \, |\boldsymbol{r}\rangle \langle \boldsymbol{r}| \right) |\psi\rangle = \int d\boldsymbol{r} \, \langle \boldsymbol{r}|\psi\rangle \, |\boldsymbol{r}\rangle = \int d\boldsymbol{r} \psi(\boldsymbol{r}) \, |\boldsymbol{r}\rangle \, . \tag{A.28}$$

Applying the Bravais translation opeator in two parallel ways then gives

$$\mathcal{T}_{\boldsymbol{m}} |\psi\rangle = \int d\boldsymbol{r} \psi(\boldsymbol{r}) \mathcal{T}_{\boldsymbol{m}} |\boldsymbol{r}\rangle = \int d\boldsymbol{r} \psi(\boldsymbol{r}) \, |\boldsymbol{r} + \boldsymbol{R}_{\boldsymbol{m}}\rangle = \int d\boldsymbol{r} \psi\big(\boldsymbol{r} - \boldsymbol{R}_{\boldsymbol{m}}\big) \, |\boldsymbol{r}\rangle \tag{A.29a}$$

$$= c_{\boldsymbol{m}} |\psi\rangle = \int d\boldsymbol{r} c_{\boldsymbol{m}} \psi(\boldsymbol{r}) \, |\boldsymbol{r}\rangle \, . \tag{A.29b}$$

The orthonormality of the kets $|\boldsymbol{r}\rangle$ then gives

$$\psi\big(\boldsymbol{r}-\boldsymbol{R_m}\big)=c_{\boldsymbol{m}}\psi(\boldsymbol{r}). \tag{A.30}$$

The next step is to determine the eigenvalues of the Bravais translation operator. The additivity formula yields

$$\mathcal{T}_{\boldsymbol{m}}=\mathcal{T}_{\sum_{j=1}^{d}m_j\boldsymbol{a}_j}=\prod_{j=1}^{d}\mathcal{T}_{\boldsymbol{a}_j}^{m_j}\Rightarrow c_{\boldsymbol{m}}=\prod_{j=1}^{d}c_{\boldsymbol{a}_j}^{m_j}. \tag{A.31}$$

Additionally, the relation $\mathcal{T}_{\boldsymbol{a}_j}^{\dagger}=\mathcal{T}_{\boldsymbol{a}_j}^{-1}$ tells us that

$$c_{\boldsymbol{a}_j}^{*}=c_{\boldsymbol{a}_j}^{-1}\Leftrightarrow|c_{\boldsymbol{a}_j}|^2=1\Leftrightarrow\exists\theta_j\in\mathbb{R}\ \text{ s.t. }\ c_{\boldsymbol{a}_j}=e^{-2i\pi\theta_j}. \tag{A.32}$$

Putting the two together, we obtain

$$c_{\boldsymbol{m}}=\exp\left(-2i\pi\sum_{j=1}^{d}m_j\theta_j\right). \tag{A.33}$$

We can use the reciprocal lattice vectors to simplify the expression of $c_{\boldsymbol{m}}$, as follows,

$$c_{\boldsymbol{m}}=\exp\left(-2i\pi\sum_{j=1}^{d}m_j\theta_j\right)=\exp\left(-i\sum_{i,j=1}^{d}m_i\theta_j2\pi\delta_{ij}\right)=\exp\left[-i\left(\sum_{j=1}^{d}\theta_j\boldsymbol{b}_j\right)\cdot\left(\sum_{i=1}^{d}m_j\boldsymbol{a}_j\right)\right]. \tag{A.34}$$

We recognize the Bravais lattice vector $\boldsymbol{R_m}$. Introducing $\lfloor\theta_j\rfloor\in\mathbb{Z}$ the integer part of θ_j and $\{\theta_j\}\in[0,1[$ its fractional part we have $\theta_j=\lfloor\theta_j\rfloor+\{\theta_j\}$, such that

$$c_{\boldsymbol{m}}=\exp\left[-i\left(\sum_{j=1}^{d}\{\theta_j\}\boldsymbol{b}_j+\sum_{j=1}^{d}\lfloor\theta_j\rfloor\boldsymbol{b}_j\right)\cdot\boldsymbol{R_m}\right]=\exp\Big[-i\big(\boldsymbol{k}+\boldsymbol{G}_{\lfloor\boldsymbol{\theta}\rfloor}\big)\cdot\boldsymbol{R_m}\Big]=e^{-i\boldsymbol{k}\cdot\boldsymbol{R_m}}e^{-i\boldsymbol{G}_{\lfloor\boldsymbol{\theta}\rfloor}\cdot\boldsymbol{R_m}}. \tag{A.35}$$

The argument of the second term is

$$\boldsymbol{G}_{\lfloor\boldsymbol{\theta}\rfloor}\cdot\boldsymbol{R_m}=\sum_{i,j}^{d}m_i\lfloor\theta_j\rfloor\boldsymbol{a}_i\cdot\boldsymbol{b}_j=2\pi\sum_{i,j}^{d}m_j\lfloor\theta_j\rfloor\delta_{ij}=2\pi\sum_{j=1}^{d}m_j\lfloor\theta_j\rfloor\in2\pi\mathbb{Z}, \tag{A.36}$$

so that $\exp\big(-i\boldsymbol{G}_{\lfloor\boldsymbol{\theta}\rfloor}\cdot\boldsymbol{R_m}\big)=1$, and finally

$$c_{\boldsymbol{m}}=e^{-i\boldsymbol{k}\cdot\boldsymbol{R_m}},\ \ \boldsymbol{k}=\sum_{j=1}^{d}k_j\boldsymbol{b}_j\ \text{ with }\ k_j\in[0,1[. \tag{A.37}$$

The eigenstate $|\psi\rangle$ will then depend on the parameter $\boldsymbol{k}$. Introducing the latter, Eq. (A.30) then becomes

$$\psi\big(\boldsymbol{k},\boldsymbol{r}-\boldsymbol{R_m}\big)=e^{-i\boldsymbol{k}\cdot\boldsymbol{R_m}}\psi(\boldsymbol{k},\boldsymbol{r})\Leftrightarrow\psi(\boldsymbol{k},\boldsymbol{r})=e^{i\boldsymbol{k}\cdot\boldsymbol{R_m}}\psi\big(\boldsymbol{k},\boldsymbol{r}-\boldsymbol{R_m}\big). \tag{A.38}$$

Multiplying both sides by $e^{-i\boldsymbol{k}\cdot\boldsymbol{r}}$ then gives

$$e^{-i\boldsymbol{k}\cdot\boldsymbol{r}}\psi(\boldsymbol{k},\boldsymbol{r}) = e^{-i\boldsymbol{k}\cdot(\boldsymbol{r}-\boldsymbol{R_m})}\psi\big(\boldsymbol{k},\boldsymbol{r}-\boldsymbol{R_m}\big). \tag{A.39}$$

The function $\boldsymbol{r} \mapsto e^{-i\boldsymbol{k}\cdot\boldsymbol{r}}\psi(\boldsymbol{k},\boldsymbol{r})$ is a periodic function, with the periodicity of the Bravais lattice vectors. Denoting it as $u(\boldsymbol{k},\boldsymbol{r})$, we thus have

$$|\psi(\boldsymbol{k})\rangle = \int d\boldsymbol{r}\psi(\boldsymbol{k},\boldsymbol{r})\,|\boldsymbol{r}\rangle = \int d\boldsymbol{r}e^{i\boldsymbol{k}\cdot\boldsymbol{r}}u(\boldsymbol{k},\boldsymbol{r})\,|\boldsymbol{r}\rangle = \int d\boldsymbol{r}e^{i\boldsymbol{k}\cdot\boldsymbol{r}}\,\langle\boldsymbol{r}|u(\boldsymbol{k})\rangle\,|\boldsymbol{r}\rangle \tag{A.40a}$$

$$= \left(\int d\boldsymbol{r}e^{i\boldsymbol{k}\cdot\boldsymbol{r}}\,|\boldsymbol{r}\rangle\,\langle\boldsymbol{r}|\right)|u(\boldsymbol{k})\rangle = e^{i\boldsymbol{k}\cdot\hat{\boldsymbol{r}}}\left(\int d\boldsymbol{r}\,|\boldsymbol{r}\rangle\,\langle\boldsymbol{r}|\right)|u(\boldsymbol{k})\rangle = e^{i\boldsymbol{k}\cdot\hat{\boldsymbol{r}}}\,|u(\boldsymbol{k})\rangle\,. \tag{A.40b}$$

We have finally found the eigenstates of the Hamiltonian $\hat{H}$, and proved the Bloch theorem.

B - Appendices of Chapter 2

B.1 . Expressions of $\mathcal{F}_\psi$ and Φ_ψ

Modulus Making the $\boldsymbol{s}$ dependences implicit and multiplying Eq. (2.20b) with its conjugate expression yields

$$\mathcal{F}_\psi^2 = \left(1 - i\mathcal{A}_\mu^\psi \mathrm{d}s_\mu + \frac{1}{2}\langle\psi|\partial_\mu\partial_\nu\psi\rangle\,\mathrm{d}s_\mu\mathrm{d}s_\nu\right)\left(1 + i\mathcal{A}_\mu^\psi \mathrm{d}s_\mu + \frac{1}{2}\langle\partial_\mu\partial_\nu\psi|\psi\rangle\,\mathrm{d}s_\mu\mathrm{d}s_\nu\right) \tag{B.1a}$$

$$= 1 - i\mathcal{A}_\psi^\mu \mathrm{d}s_\mu + \frac{1}{2}\langle\psi|\partial_\mu\partial_\nu\psi\rangle\,\mathrm{d}s_\mu\mathrm{d}s_\nu + i\mathcal{A}_\mu^\psi \mathrm{d}s_\mu + \mathcal{A}_\mu^\psi\mathcal{A}_\nu^\psi \mathrm{d}s_\mu\mathrm{d}s_\nu + \frac{1}{2}\langle\partial_\mu\partial_\nu\psi|\psi\rangle\,\mathrm{d}s_\mu\mathrm{d}s_\nu + \mathcal{O}(\mathbf{d}\boldsymbol{s}^3) \tag{B.1b}$$

$$= 1 + \Big(\operatorname{Re}\langle\psi|\partial_\mu\partial_\nu\psi\rangle + \mathcal{A}_\mu^\psi\mathcal{A}_\nu^\psi\Big)\mathrm{d}s_\mu\mathrm{d}s_\nu + \mathcal{O}(\mathbf{d}\boldsymbol{s}^3). \tag{B.1c}$$

Using[1] $\operatorname{Re}\langle\psi|\partial_\mu\partial_\nu\psi\rangle = -\operatorname{Re}\langle\partial_\mu\psi|\partial_\nu\psi\rangle$, we can then rexpress the second order term as

$$\operatorname{Re}\langle\psi|\partial_\mu\partial_\nu\psi\rangle + \mathcal{A}_\mu^\psi\mathcal{A}_\nu^\psi = -\operatorname{Re}\langle\partial_\mu\psi|\partial_\nu\psi\rangle + \mathcal{A}_\mu^\psi\mathcal{A}_\nu^\psi = -\operatorname{Re}\big(\langle\partial_\mu\psi|\partial_\nu\psi\rangle - \mathcal{A}_\mu^\psi\mathcal{A}_\nu^\psi\big) \tag{B.2a}$$

$$= -\operatorname{Re}\big(\langle\partial_\mu\psi|\partial_\nu\psi\rangle + \langle\psi|\partial_\mu\psi\rangle\langle\psi|\partial_\nu\psi\rangle\big) \tag{B.2b}$$

$$= -\operatorname{Re}\big(\langle\partial_\mu\psi|\partial_\nu\psi\rangle - \langle\partial_\mu\psi|\psi\rangle\langle\psi|\partial_\nu\psi\rangle\big) \tag{B.2c}$$

$$= -\operatorname{Re}\langle\partial_\mu\psi|\left[\mathbb{1} - |\psi\rangle\langle\psi|\right]|\partial_\nu\psi\rangle = -g_{\mu\nu}^\psi, \tag{B.2d}$$

so to second order we finally have Eq. (2.14c)

$$\mathcal{F}_\psi^2 = |\langle\psi(\boldsymbol{s})|\psi(\boldsymbol{s}+\mathbf{d}\boldsymbol{s})\rangle|^2 = 1 - g_{\mu\nu}^\psi \mathrm{d}s_\mu\mathrm{d}s_\nu. \tag{B.3}$$

Phase Using the principal value of the complex (natural) logarithm, we write

$$\ln\langle\psi(\boldsymbol{s})|\psi(\boldsymbol{s}+\boldsymbol{d}\boldsymbol{s})\rangle = \ln\mathcal{F}_\psi(\boldsymbol{s}) + i\Phi_\psi(\boldsymbol{s}). \tag{B.4}$$

Again making the $\boldsymbol{s}$ dependences implicit, we have

$$\ln\langle\psi(\boldsymbol{s})|\psi(\boldsymbol{s}+\boldsymbol{d}\boldsymbol{s})\rangle = \ln\left(1 - i\mathcal{A}_\mu^\psi\mathrm{d}s_\mu + \frac{1}{2}\langle\psi|\partial_\mu\partial_\nu\psi\rangle\,\mathrm{d}s_\mu\mathrm{d}s_\nu\right) \tag{B.5a}$$

$$= -i\mathcal{A}_\mu^\psi\mathrm{d}s_\mu + \frac{1}{2}\langle\psi|\partial_\mu\partial_\nu\psi\rangle\,\mathrm{d}s_\mu\mathrm{d}s_\nu \tag{B.5b}$$

$$= -i\mathcal{A}_\mu^\psi\mathrm{d}s_\mu + \frac{1}{2}\Big(\langle\psi|\partial_\mu\partial_\nu\psi\rangle - \mathcal{A}_\mu^\psi\mathcal{A}_\nu^\psi\Big)\mathrm{d}s_\mu\mathrm{d}s_\nu + \mathcal{O}(\mathbf{d}\boldsymbol{s}^3). \tag{B.5c}$$

As for the modulus $\mathcal{F}_\psi$,

$$\ln\mathcal{F}_\psi = \ln\left(1 - \operatorname{Re}\langle\partial_\mu\psi|\left[\mathbb{1} - |\psi\rangle\langle\psi|\right]|\partial_\nu\psi\rangle\,\mathrm{d}s_\mu\mathrm{d}s_\nu\right) \tag{B.6a}$$

$$= -\operatorname{Re}\langle\partial_\mu\psi|\left[\mathbb{1} - |\psi\rangle\langle\psi|\right]|\partial_\nu\psi\rangle\,\mathrm{d}s_\mu\mathrm{d}s_\nu + \mathcal{O}(\mathbf{d}\boldsymbol{s}^3). \tag{B.6b}$$

[1] This is also shown by using the fact the norm of $|\psi(\boldsymbol{s})\rangle$ is a constant with respect to $\boldsymbol{s}$, and by applying the second order derivative $\partial_\mu\partial_\nu$.

Therefore, to leading order we have

$$i\Phi_\psi = \ln\langle\psi(\boldsymbol{s})|\psi(\boldsymbol{s}+\boldsymbol{ds})\rangle - \ln\mathcal{F}_\psi = -i\mathcal{A}^\psi_\mu \mathrm{d}s_\mu + \mathcal{O}\big(\mathbf{d}\boldsymbol{s}^2\big), \tag{B.7}$$

which finally gives $\Phi_\psi = -\boldsymbol{\mathcal{A}}^{\boldsymbol{\psi}} \cdot \mathbf{d}\boldsymbol{s}$ to leading order.

B.2 . Proof of some properties of the QGT

B.2.1 . U(N) gauge dependence

Let $U(\boldsymbol{k}) \in \mathrm{U}(N)$. The Bloch state is then transformed as

$$|u_n(\boldsymbol{k})\rangle \longmapsto \big|u'_n(\boldsymbol{k})\big\rangle = U(\boldsymbol{k})\,|u_n(\boldsymbol{k})\rangle\,. \tag{B.8}$$

For the QGT, we have $Q^n_{\mu\nu} \mapsto Q^{n\prime}_{\mu\nu}$ with

$$\begin{aligned}
Q^{n\prime}_{\mu\nu} &= \big\langle \partial_\mu u'_n\big|\,\big[\mathbb{1} - \big|u'_n\big\rangle\big\langle u'_n\big|\,\big]\,\big|\partial_\nu u'_n\big\rangle = \Big[\partial_\mu\big(U\,|u_n\rangle\big)\Big]^\dagger\big[\mathbb{1} - U\,|u_n\rangle\,\langle u_n|\,U^\dagger\big]\partial_\mu\big(U\,|u_n\rangle\big) && \text{(B.9a)}\\
&= \big[\,\langle u_n|\,\partial_\mu U^\dagger + \langle\partial_\mu u_n|\,U^\dagger\big]\big[UU^\dagger - U\,|u_n\rangle\,\langle u_n|\,U^\dagger\big]\big[\partial_\nu U\,|u_n\rangle + U\,|\partial_\nu u_n\rangle\,\big] && \text{(B.9b)}\\
&= \big[\,\langle u_n|\,\partial_\mu U^\dagger + \langle\partial_\mu u_n|\,U^\dagger\big]U\big[\mathbb{1} - |u_n\rangle\,\langle u_n|\,\big]U^\dagger\big[\partial_\nu U\,|u_n\rangle + U\,|\partial_\nu u_n\rangle\,\big] && \text{(B.9c)}\\
&= \Big[\,\langle\partial_\mu u_n| + \langle u_n|\,\big(\partial_\mu U^\dagger\big)U\Big]\big[\mathbb{1} - |u_n\rangle\,\langle u_n|\,\big]\big[\,|\partial_\nu u_n\rangle + U^\dagger\partial_\nu U\,|u_n\rangle\,\big] && \text{(B.9d)}\\
&= Q^n_{\mu\nu} + \langle u_n|\,\big(\partial_\mu U^\dagger\big)U\big[\mathbb{1} - |u_n\rangle\,\langle u_n|\,\big]\,|\partial_\nu u_n\rangle + \langle\partial_\mu u_n|\,\big[\mathbb{1} - |u_n\rangle\,\langle u_n|\,\big]U^\dagger\partial_\nu U\,|u_n\rangle\\
&\quad + \langle u_n|\,\big(\partial_\mu U^\dagger\big)U\big[\mathbb{1} - |u_n\rangle\,\langle u_n|\,\big]U^\dagger\partial_\nu U\,|u_n\rangle\,. && \text{(B.9e)}
\end{aligned}$$

B.3 . Formulations of the Quantum Geometric Tensor

B.3.1 . Projector formulation

$$\mathrm{Tr}\left[\mathcal{P}_n\partial_\mu\mathcal{P}_n(\mathbb{1}-\mathcal{P}_n)\partial_\nu\mathcal{P}_n\right] = \sum_{\substack{m=1\\m\neq n}}^{N}\langle u_n|\,\partial_\mu\mathcal{P}_n\,|u_m\rangle\,\langle u_m|\,\partial_\nu\mathcal{P}_n\,|u_n\rangle \tag{B.10a}$$

$$= \sum_{\substack{m=1\\m\neq n}}^{N}\langle u_n|\,\big(\,|\partial_\mu u_n\rangle\,\langle u_n| + |u_n\rangle\,\langle\partial_\mu u_n|\,\big)\,|u_m\rangle\,\langle u_m|\,\big(\,|\partial_\mu u_n\rangle\,\langle u_n| + |u_n\rangle\,\langle\partial_\mu u_n|\,\big)\,|u_n\rangle \tag{B.10b}$$

$$= \sum_{\substack{m=1\\m\neq n}}^{N}\Big[\,\langle u_n|\partial_\mu u_n\rangle\,\cancel{\langle u_n|u_m\rangle} + \langle u_n|u_n\rangle\,\langle\partial_\mu u_n|u_m\rangle\,\Big]\Big[\,\langle u_m|\partial_\mu u_n\rangle\,\langle u_n|u_n\rangle + \cancel{\langle u_m|u_n\rangle}\,\langle\partial_\nu u_n|u_m\rangle\,\Big] \tag{B.10c}$$

$$= \sum_{\substack{m=1\\m\neq n}}^{N}\langle\partial_\mu u_n|u_m\rangle\,\langle u_m|\partial_\nu u_n\rangle = Q^n_{\mu\nu}. \tag{B.10d}$$

B.3.2 . Hamiltonian formulation

Starting from the band eigenproblem,

$$H\left|u_n\right\rangle = \epsilon_n \left|u_n\right\rangle, \tag{B.11}$$

a differentiation ∂_μ gives

$$\partial_\mu H\left|u_n\right\rangle + H\left|\partial_\mu u_n\right\rangle = \partial_\mu \epsilon_n \left|u_n\right\rangle + \epsilon_n \left|\partial_\mu u_n\right\rangle. \tag{B.12}$$

Projecting on $\langle u_m|$ with $m \neq n$ then yields

$$\left\langle u_m\right| \partial_\mu H\left|u_n\right\rangle + \epsilon_m \left\langle u_m|\partial_\mu u_n\right\rangle = \epsilon_n \left\langle u_m|\partial_\mu u_n\right\rangle \tag{B.13a}$$

$$\Leftrightarrow \quad \left\langle u_m|\partial_\mu u_n\right\rangle = \frac{\left\langle u_m\right| \partial_\nu H\left|u_n\right\rangle}{\epsilon_n - \epsilon_m}. \tag{B.13b}$$

Plugging the latter in the original formulation of the QGT gives

$$Q^n_{\mu\nu} = \sum_{\substack{m=1\\m\neq n}}^{N} \left\langle u_m|\partial_\mu u_n\right\rangle^* \left\langle u_m|\partial_\nu u_n\right\rangle = \sum_{\substack{m=1\\m\neq n}}^{N} \frac{\left\langle u_n\right| \partial_\mu H\left|u_m\right\rangle \left\langle u_m\right| \partial_\nu H\left|u_n\right\rangle}{(\epsilon_n - \epsilon_m)^2}. \tag{B.14}$$

B.3.3 . Bloch vector formulation

Starting from

$$\mathcal{P}_\lambda = \frac{1}{2}\big(\sigma_0 + \boldsymbol{b}_\lambda \cdot \boldsymbol{\sigma}\big), \qquad \boldsymbol{b}_\lambda = \lambda \frac{\boldsymbol{h}}{|\boldsymbol{h}|}, \tag{B.15}$$

the projector formulation becomes

$$Q^\lambda_{\mu\nu} = \mathrm{Tr}\left[\mathcal{P}_\lambda \partial_\mu \mathcal{P}_\lambda \mathcal{P}_{-\lambda} \partial_\nu \mathcal{P}_\lambda\right] = \frac{1}{16}\,\mathrm{Tr}\left[\big(\sigma_0 + \boldsymbol{b}_\lambda\cdot\boldsymbol{\sigma}\big)\partial_\mu \boldsymbol{b}_\lambda\cdot\boldsymbol{\sigma}\big(\sigma_0 - \boldsymbol{b}_\lambda\cdot\boldsymbol{\sigma}\big)\partial_\nu \boldsymbol{b}_\lambda\cdot\boldsymbol{\sigma}\right] \tag{B.16a}$$

$$= \frac{1}{16}\,\mathrm{Tr}\Big\{\left[\partial_\mu \boldsymbol{b}_\lambda\cdot\boldsymbol{\sigma} + (\boldsymbol{b}_\lambda\cdot\boldsymbol{\sigma})(\partial_\mu \boldsymbol{b}_\lambda\cdot\boldsymbol{\sigma})\right]\left[\partial_\nu \boldsymbol{b}_\lambda\cdot\boldsymbol{\sigma} - (\boldsymbol{b}_\lambda\cdot\boldsymbol{\sigma})(\partial_\nu \boldsymbol{b}_\lambda\cdot\boldsymbol{\sigma})\right]\Big\}. \tag{B.16b}$$

Now we use the following identity,

$$(\boldsymbol{a}\cdot\boldsymbol{\sigma})(\boldsymbol{b}\cdot\boldsymbol{\sigma}) = \boldsymbol{a}\cdot\boldsymbol{b}\sigma_0 + i\boldsymbol{a}\times\boldsymbol{b}\cdot\boldsymbol{\sigma}. \tag{B.17}$$

This yields

$$Q^\lambda_{\mu\nu} = \frac{1}{16}\,\mathrm{Tr}\left[\big(\partial_\mu \boldsymbol{b}_\lambda\cdot\boldsymbol{\sigma} + \boldsymbol{b}_\lambda\cdot\partial_\mu \boldsymbol{b}_\lambda\sigma_0 + i\boldsymbol{b}_\lambda\times\partial_\mu \boldsymbol{b}_\lambda\cdot\boldsymbol{\sigma}\big)\big(\partial_\nu \boldsymbol{b}_\lambda\cdot\boldsymbol{\sigma} - \boldsymbol{b}_\lambda\cdot\partial_\nu \boldsymbol{b}_\lambda\sigma_0 - i\boldsymbol{b}_\lambda\times\partial_\nu \boldsymbol{b}_\lambda\cdot\boldsymbol{\sigma}\big)\right] \tag{B.18a}$$

$$\begin{aligned}
&= \frac{1}{16}\,\mathrm{Tr}\Big[(\partial_\mu \boldsymbol{b}_\lambda\cdot\boldsymbol{\sigma})(\partial_\mu \boldsymbol{b}_\lambda\cdot\boldsymbol{\sigma}) - (\boldsymbol{b}_\lambda\cdot\partial_\nu \boldsymbol{b}_\lambda)\partial_\mu \boldsymbol{b}_\lambda\cdot\boldsymbol{\sigma} - i(\partial_\mu \boldsymbol{b}_\lambda\cdot\boldsymbol{\sigma})(\boldsymbol{b}_\lambda\times\partial_\nu \boldsymbol{b}_\lambda\cdot\boldsymbol{\sigma})\\
&+ (\boldsymbol{b}_\lambda\cdot\partial_\mu \boldsymbol{b}_\lambda)(\partial_\nu \boldsymbol{b}_\lambda\cdot\boldsymbol{\sigma}) - (\boldsymbol{b}_\lambda\cdot\partial_\mu \boldsymbol{b}_\lambda)(\boldsymbol{b}_\lambda\cdot\partial_\nu \boldsymbol{b}_\lambda)\sigma_0 - i(\boldsymbol{b}_\lambda\cdot\partial_\mu \boldsymbol{b}_\lambda)\boldsymbol{b}_\lambda\times\partial_\nu \boldsymbol{b}_\lambda\cdot\boldsymbol{\sigma}\\
&+ i(\boldsymbol{b}_\lambda\times\partial_\mu \boldsymbol{b}_\lambda\cdot\boldsymbol{\sigma})(\partial_\nu \boldsymbol{b}_\lambda\cdot\boldsymbol{\sigma}) - i(\boldsymbol{b}_\lambda\cdot\partial_\nu \boldsymbol{b}_\lambda)\boldsymbol{b}_\lambda\times\partial_\mu \boldsymbol{b}_\lambda\cdot\boldsymbol{\sigma} + (\boldsymbol{b}_\lambda\times\partial_\mu \boldsymbol{b}_\lambda\cdot\boldsymbol{\sigma})(\boldsymbol{b}_\lambda\times\partial_\nu \boldsymbol{b}_\lambda\cdot\boldsymbol{\sigma})\Big].
\end{aligned} \tag{B.18b}$$

Since the three Pauli matrices in $\boldsymbol{\sigma}$ are of trace zero, we can reapply the identity again and drop every term that is not in σ_0, which yields

$$\begin{aligned} Q^{\lambda}_{\mu\nu} &= \frac{1}{16}\,\mathrm{Tr}\Big[\partial_\mu \boldsymbol{b}_\lambda \cdot \partial_\nu \boldsymbol{b}_\lambda \sigma_0 - i\partial_\mu \boldsymbol{b}_\lambda \cdot \boldsymbol{b}_\lambda \times \partial_\nu \boldsymbol{b}_\lambda \sigma_0 - (\boldsymbol{b}_\lambda \cdot \partial_\mu \boldsymbol{b}_\lambda)(\boldsymbol{b}_\lambda \cdot \partial_\nu \boldsymbol{b}_\lambda)\sigma_0 + i\boldsymbol{b}_\lambda \times \partial_\mu \boldsymbol{b}_\lambda \cdot \partial_\nu \boldsymbol{b}_\lambda \sigma_0 \\ &\quad + \boldsymbol{b}_\lambda \times \partial_\mu \boldsymbol{b}_\lambda \cdot \boldsymbol{b}_\lambda \times \partial_\nu \boldsymbol{b}_\lambda \sigma_0\Big] \qquad \text{(B.19a)} \\ &= \frac{1}{8}\Big(\partial_\mu \boldsymbol{b}_\lambda \cdot \partial_\nu \boldsymbol{b}_\lambda - i\partial_\mu \boldsymbol{b}_\lambda \cdot \boldsymbol{b}_\lambda \times \partial_\nu \boldsymbol{b}_\lambda - (\boldsymbol{b}_\lambda \cdot \partial_\mu \boldsymbol{b}_\lambda)(\boldsymbol{b}_\lambda \cdot \partial_\nu \boldsymbol{b}_\lambda) + i\boldsymbol{b}_\lambda \times \partial_\mu \boldsymbol{b}_\lambda \cdot \partial_\nu \boldsymbol{b}_\lambda \\ &\quad + \boldsymbol{b}_\lambda \times \partial_\mu \boldsymbol{b}_\lambda \cdot \boldsymbol{b}_\lambda \times \partial_\nu \boldsymbol{b}_\lambda\Big). \qquad \text{(B.19b)} \end{aligned}$$

Now we can use the fact that the triple product $\boldsymbol{a}\cdot\boldsymbol{b}\times\boldsymbol{c}$ is invariant under cyclic permutations to show

$$\boldsymbol{b}_\lambda \times \partial_\mu \boldsymbol{b}_\lambda \cdot \partial_\nu \boldsymbol{b}_\lambda = \partial_\nu \boldsymbol{b}_\lambda \cdot \boldsymbol{b}_\lambda \times \partial_\mu \boldsymbol{b}_\lambda = \boldsymbol{b}_\lambda \cdot \partial_\mu \boldsymbol{b}_\lambda \times \partial_\nu \boldsymbol{b}_\lambda, \tag{B.20}$$

and

$$\partial_\mu \boldsymbol{b}_\lambda \cdot \boldsymbol{b}_\lambda \times \partial_\nu \boldsymbol{b}_\lambda = \boldsymbol{b}_\lambda \cdot \partial_\nu \boldsymbol{b}_\lambda \times \partial_\mu \boldsymbol{b}_\lambda = -\boldsymbol{b}_\lambda \cdot \partial_\mu \boldsymbol{b}_\lambda \times \partial_\nu \boldsymbol{b}_\lambda. \tag{B.21}$$

Additionally, using the Binet-Cauchy identity

$$\boldsymbol{a} \times \boldsymbol{b} \cdot \boldsymbol{c} \times \boldsymbol{d} = (\boldsymbol{a} \cdot \boldsymbol{d})(\boldsymbol{b} \cdot \boldsymbol{c}) - (\boldsymbol{a} \cdot \boldsymbol{c})(\boldsymbol{b} \cdot \boldsymbol{d}), \tag{B.22}$$

we get

$$\begin{aligned} \boldsymbol{b}_\lambda \times \partial_\mu \boldsymbol{b}_\lambda \cdot \boldsymbol{b}_\lambda \times \partial_\nu \boldsymbol{b}_\lambda &= (\boldsymbol{b}_\lambda \cdot \partial_\nu \boldsymbol{b}_\lambda)(\boldsymbol{b}_\lambda \cdot \partial_\mu \boldsymbol{b}_\lambda) - (\boldsymbol{b}_\lambda \cdot \boldsymbol{b}_\lambda)(\partial_\mu \boldsymbol{b}_\lambda \cdot \partial_\nu \boldsymbol{b}_\lambda) \qquad \text{(B.23a)} \\ &= (\boldsymbol{b}_\lambda \cdot \partial_\nu \boldsymbol{b}_\lambda)(\boldsymbol{b}_\lambda \cdot \partial_\mu \boldsymbol{b}_\lambda) - \partial_\mu \boldsymbol{b}_\lambda \cdot \partial_\nu \boldsymbol{b}_\lambda, \qquad \text{(B.23b)} \end{aligned}$$

since $\boldsymbol{b}_\lambda^2 = 1$. The QGT now reads

$$\begin{aligned} Q^{\lambda}_{\mu\nu} &= \frac{1}{8}\Big[\partial_\mu \boldsymbol{b}_\lambda \cdot \partial_\nu \boldsymbol{b}_\lambda + i\boldsymbol{b}_\lambda \cdot \partial_\mu \boldsymbol{b}_\lambda \times \partial_\nu \boldsymbol{b}_\lambda - (\boldsymbol{b}_\lambda \cdot \partial_\mu \boldsymbol{b}_\lambda)(\boldsymbol{b}_\lambda \cdot \partial_\nu \boldsymbol{b}_\lambda) + i\boldsymbol{b}_\lambda \cdot \partial_\mu \boldsymbol{b}_\lambda \times \partial_\nu \boldsymbol{b}_\lambda \\ &\quad + (\boldsymbol{b}_\lambda \cdot \partial_\mu \boldsymbol{b}_\lambda)(\boldsymbol{b}_\lambda \cdot \partial_\nu \boldsymbol{b}_\lambda) - \partial_\mu \boldsymbol{b}_\lambda \cdot \partial_\nu \boldsymbol{b}_\lambda\Big] = \frac{1}{4}\partial_\mu \boldsymbol{b}_\lambda \cdot \partial_\nu \boldsymbol{b}_\lambda + \frac{i}{4}\boldsymbol{b}_\lambda \cdot \partial_\mu \boldsymbol{b}_\lambda \times \partial_\nu \boldsymbol{b}_\nu \end{aligned} \tag{B.24}$$

B.4 . Quantum geometric tensor of massive Dirac fermions

Let $\boldsymbol{\alpha} = \lambda_c \boldsymbol{k}$. Then, the Bloch vector is given by

$$\boldsymbol{b}_n = \frac{n}{\sqrt{1+\alpha^2}}\big(\xi\alpha_x, \alpha_y, \operatorname{sgn}\Delta\big), \tag{B.25}$$

such that $\partial_\mu \boldsymbol{b}_n = \lambda_c \partial_{\alpha_\mu} \boldsymbol{b}_n$. Using

$$\partial_{\alpha_\mu} \frac{\alpha_\mu}{\sqrt{1+\alpha^2}} = \frac{1+\alpha_{\overline{\mu}}^2}{(1+\alpha^2)^{3/2}}, \qquad \partial_{\alpha_\mu} \frac{\alpha_{\overline{\mu}}}{\sqrt{1+\alpha^2}} = -\frac{\alpha_x \alpha_y}{(1+\alpha^2)^{3/2}}, \tag{B.26}$$

with $\overline{\mu}$ denoting the other value of μ. We then have

$$\partial_{\alpha_\mu} \boldsymbol{b}_n = n\partial_{\alpha_\mu}\left(\frac{\xi\alpha_x}{\sqrt{1+\alpha^2}}, \frac{\alpha_y}{\sqrt{1+\alpha^2}}, \frac{\operatorname{sgn}\Delta}{\sqrt{1+\alpha^2}}\right) \tag{B.27}$$

$$= \frac{n}{(1+\alpha^2)^{3/2}}\Big(\xi(1+\alpha_y^2), -\alpha_x\alpha_y, -\operatorname{sgn}(\Delta)\alpha_x\Big)\delta_{\mu x}$$

$$+ \frac{n}{(1+\alpha^2)^{3/2}}\Big(-\xi\alpha_x\alpha_y, 1+\alpha_x^2, -\operatorname{sgn}(\Delta)\alpha_y\Big)\delta_{\mu y} \tag{B.28}$$

Since the QGT is Hermitian, there are three independent components of the quantum metric $(g^n_{xx}, g^n_{xy}, g^n_{yy})$ and one for the Berry curvature $\mathcal{B}^n_{xy}$.

Quantum metric For the quantum metric we have

$$\partial_{\alpha_x}\boldsymbol{b}_n \cdot \partial_{\alpha_x}\boldsymbol{b}_n = \frac{(1+\alpha_y^2)^2 + \alpha_x^2\alpha_y^2 + \alpha_x^2}{(1+\alpha^2)^3} = \frac{(1+\alpha_y^2)(1+\alpha_y^2+\alpha_x^2)}{(1+\alpha^2)^3} = \frac{1+\alpha_y^2}{(1+\alpha^2)^2}, \tag{B.29}$$

and similarly

$$\partial_{\alpha_y}\boldsymbol{b}_n \cdot \partial_{\alpha_y}\boldsymbol{b}_n = \frac{1+\alpha_x^2}{(1+\alpha^2)^2}. \tag{B.30}$$

Additionally,

$$\partial_{\alpha_x}\boldsymbol{b}_n \cdot \partial_{\alpha_y}\boldsymbol{b}_n = \frac{-\alpha_x\alpha_y(1+\alpha_y^2) - \alpha_x\alpha_y(1+\alpha_x^2) + \alpha_x\alpha_y}{(1+\alpha^2)^3} \tag{B.31}$$

$$= -\alpha_x\alpha_y\frac{1+\alpha_y^2+1+\alpha_x^2-1}{(1+\alpha^2)^3} = -\frac{\alpha_x\alpha_y}{(1+\alpha^2)^2}. \tag{B.32}$$

This way we obtain the quantum metric as

$$g^n_{xx} = \frac{\lambda_c^2}{4}\frac{1+\alpha_y^2}{(1+\alpha^2)^2}, \quad g^n_{yy} = \frac{\lambda_c^2}{4}\frac{1+\alpha_x^2}{(1+\alpha^2)^2}, \quad g^n_{xy} = \frac{\lambda_c^2}{4}\frac{-\alpha_x\alpha_y}{(1+\alpha^2)^2}. \tag{B.33}$$

We then see that in each case, we can rewrite the metric as

$$g^n_{\mu\nu} = \frac{\lambda_c^2}{4}\frac{(1+\alpha^2)\delta_{\mu\nu} - \alpha_\mu\alpha_\nu}{(1+\alpha^2)^2} = \frac{\lambda_c^2}{4}\frac{(1+\lambda_c^2k^2)\delta_{\mu\nu} - \lambda_c^2k_\mu k_\nu}{(1+\lambda_c^2k^2)^2}. \tag{B.34}$$

Berry curvature We start with

$$\partial_{\alpha_x}\boldsymbol{b}_n \times \partial_{\alpha_y}\boldsymbol{b}_n = \frac{1}{(1+\alpha^2)^3}\Big(\xi(1+\alpha_y^2), -\alpha_x\alpha_y, -\operatorname{sgn}(\Delta)\alpha_x\Big) \times \Big(-\xi\alpha_x\alpha_y, 1+\alpha_x^2, -\operatorname{sgn}(\Delta)\alpha_y\Big) \tag{B.35}$$

$$= \frac{1}{(1+\alpha^2)^2}\Big(\operatorname{sgn}(\Delta)\alpha_x, \xi\operatorname{sgn}(\Delta)\alpha_y, \xi\alpha_x\Big). \tag{B.36}$$

Therefore

$$\boldsymbol{b}_n \cdot \partial_{\alpha_x}\boldsymbol{b}_n \times \partial_{\alpha_y}\boldsymbol{b}_n = \frac{n}{(1+\alpha^2)^{7/2}} \begin{pmatrix} \xi\alpha_x \\ \alpha_y \\ -\operatorname{sgn}(\Delta) \end{pmatrix} \cdot \begin{pmatrix} \operatorname{sgn}(\Delta)\alpha_x \\ \xi \operatorname{sgn}(\Delta)\alpha_y \\ \xi\alpha_x \end{pmatrix} \tag{B.37}$$

$$= \frac{n\xi \operatorname{sgn}\Delta}{(1+\alpha^2)^{5/2}}\left(\alpha_x^2+\alpha_y^2+1\right) = \frac{n\xi \operatorname{sgn}(\Delta)}{(1+\alpha^2)^{3/2}}. \tag{B.38}$$

And finally we have

$$\mathcal{B}_{xy}^n = -\frac{n\xi \operatorname{sgn}(\Delta)}{2}\frac{\lambda\!\!\!^{-2}_c}{(1+\lambda\!\!\!^{-2}_c k^2)^{3/2}}. \tag{B.39}$$

C - Appendices of Chapter 4

C.1 . Approximation of Eq. (4.26)

In this appendix, we show that when $\Lambda \gg 1$ we have

$$\int_0^\Lambda \frac{\tanh(x)}{x} dx \underset{\Lambda \gg 1}{\simeq} \ln\left(\frac{4e^\gamma \Lambda}{\pi}\right), \tag{C.1}$$

with $\gamma \simeq 0.577$ the Euler-Mascheroni constant. First, we write

$$\int_0^\Lambda \frac{\tanh(x)}{x} dx = \int_0^1 \frac{\tanh(x)}{x} dx + \int_1^\Lambda \frac{\tanh(x)}{x} dx. \tag{C.2}$$

On one hand,

$$\int_1^\Lambda \frac{\tanh(x)}{x} dx = \int_1^\Lambda \frac{1}{x}\frac{1-e^{-2x}}{1+e^{2x}} dx = \int_1^\Lambda \sum_{n=0}^{+\infty} (-1)^n \frac{e^{-2nx} - e^{-(2n+2)x}}{x} dx \tag{C.3}$$

$$= \int_1^\Lambda \frac{1-e^{-2x}}{x} dx + \sum_{n=1}^{+\infty} (-1)^n \int_1^\Lambda \frac{e^{-2nx} - e^{-(2n+2)x}}{x} dx. \tag{C.4}$$

We then make the following approximation

$$\forall n \in \mathbb{N}^*, \quad \int_1^\Lambda \frac{e^{-2nx}}{x} dx \simeq \int_1^{+\infty} \frac{e^{-2nx}}{x} dx = \int_{2n}^{+\infty} \frac{e^{-x}}{x} dx = -\operatorname{Ei}(-2n), \tag{C.5}$$

with Ei the exponential integral function [273]. We then have

$$\int_1^\Lambda \frac{\tanh(x)}{x} dx \simeq \ln(\Lambda) + \operatorname{Ei}(-2) - \sum_{n=1}^{+\infty} (-1)^n \Big[\operatorname{Ei}(-2n) - \operatorname{Ei}(-2n-2)\Big] \tag{C.6}$$

On the other hand,

$$\int_0^1 \frac{\tanh(x)}{x} dx = \int_0^1 \sum_{n=0}^{+\infty} (-1)^n \frac{e^{-2nx} - e^{-(2n+2)x}}{x} dx = \sum_{n=0}^{+\infty} (-1)^n \sum_{k=1}^{+\infty} \frac{(-2n)^k - (-2n-2)^k}{k!} \int_0^1 x^{k-1} dx \tag{C.7}$$

$$= \sum_{n=0}^{+\infty} (-1)^n \left[\sum_{k=1}^{+\infty} \frac{(-2n)^k}{k \cdot k!} - \sum_{k=1}^{+\infty} \frac{(-2n-2)^k}{k \cdot k!}\right] \tag{C.8}$$

$$= -\sum_{k=1}^{+\infty} \frac{(-2)^k}{k \cdot k!} + \sum_{n=1}^{+\infty} (-1)^n \left[\sum_{k=1}^{+\infty} \frac{(-2n)^k}{k \cdot k!} - \sum_{k=1}^{+\infty} \frac{(-2n-2)^k}{k \cdot k!}\right] \tag{C.9}$$

Here we make use of the identity [273]

$$\forall x \in \mathbb{R}^*, \quad \sum_{k=1}^{+\infty} \frac{x^k}{k \cdot k!} = \operatorname{Ei}(x) - \gamma - \ln|x| \tag{C.10}$$

so that we have

$$\int_0^1 \frac{\tanh(x)}{x}dx = \gamma + \ln(2) - \mathrm{Ei}(-2) + \sum_{n=1}^{+\infty}(-1)^n\Big[\mathrm{Ei}(-2n) - \gamma - \ln(2n) - \mathrm{Ei}(-2n-2) + \gamma + \ln(2n+2)\Big] \tag{C.11}$$

$$= \gamma + \ln(2) + \sum_{n=1}^{+\infty}(-1)^n \ln\left(\frac{n+1}{n}\right) - \mathrm{Ei}(-2) + \sum_{n=1}^{+\infty}(-1)^n\Big[\mathrm{Ei}(-2n) - \mathrm{Ei}(-2n-2)\Big] \tag{C.12}$$

Putting the two together,

$$\int_0^\Lambda \frac{\tanh(x)}{x}dx \underset{\Lambda\gg 1}{\simeq} \ln(\Lambda) + \gamma + \ln(2) + \sum_{n=1}^{+\infty}(-1)^n \ln\left(\frac{n+1}{n}\right) \tag{C.13}$$

The last thing to compute is

$$\sum_{n=1}^{+\infty}(-1)^n \ln\left(\frac{n+1}{n}\right) = \ln\left[\prod_{n=1}^{+\infty}\left(\frac{n+1}{n}\right)^{(-1)^n}\right] \tag{C.14}$$

One can show that

$$\forall N \in \mathbb{N}^*, \quad \prod_{n=1}^{2N}\left(\frac{n+1}{n}\right)^{(-1)^n} = \prod_{n=1}^{N}\frac{2n-1}{2n}\cdot\frac{2n+1}{2n} \tag{C.15}$$

thus (by convergence of the product),

$$\prod_{n=1}^{+\infty}\left(\frac{n+1}{n}\right)^{(-1)^n} = \prod_{n=1}^{+\infty}\frac{2n-1}{2n}\cdot\frac{2n+1}{2n} = \prod_{n=1}^{+\infty}\frac{4n^2-1}{4n^2} \tag{C.16}$$

the latter is known as the Wallis product

$$\prod_{n=1}^{+\infty}\frac{4n^2}{4n^2-1} = \frac{\pi}{2} \tag{C.17}$$

So we finally have

$$\int_0^\Lambda \frac{\tanh(x)}{x}dx \underset{\Lambda\gg 1}{\simeq} \ln(\Lambda) + \gamma + \ln(2) + \ln\left(\frac{2}{\pi}\right) = \ln\left(\frac{4e^\gamma\Lambda}{\pi}\right) \tag{C.18}$$

D - Appendices of Chapter 5

D.1 . Proof that Eq. (5.6) defines a Green's function

Let us start from Eq. (5.6),

$$G_{\alpha\beta}(t,t',\boldsymbol{k}) = -\frac{i}{\hbar}\Theta(t-t')\langle\{c_{\boldsymbol{k}\alpha}(t), c^\dagger_{\boldsymbol{k}\beta}(t')\}\rangle. \tag{D.1}$$

In the following, we make the $\boldsymbol{k}$ dependences implicit. We begin by applying the operator $i\hbar\partial_t$,

$$i\hbar\partial_t G_{\alpha\beta}(t,t') = i\hbar\partial_t\Big[-\frac{i}{\hbar}\Theta(t-t')\langle\{c_\alpha(t), c^\dagger_\beta(t')\}\rangle\Big] \tag{D.2a}$$

$$= \delta(t-t')\langle\{c_\alpha(t), c^\dagger_\beta(t')\}\rangle + \Theta(t-t')\langle\{\partial_t c_\alpha(t), c^\dagger_\beta(t')\}\rangle. \tag{D.2b}$$

The derivative $\partial_t c_\alpha(t)$ may be derived using the definition of $c_\alpha(t)$,

$$c_\alpha(t) = e^{iHt/\hbar}c_\alpha e^{-iHt/\hbar}, \tag{D.3}$$

which yields

$$\partial_t c_\alpha(t) = \frac{i}{\hbar}e^{iHt/\hbar}[H, c_\alpha]e^{-iHt/\hbar}. \tag{D.4}$$

The commutator $[H, c_\alpha]$ can then be derived using Eq. (5.5),

$$[H, c_\alpha] = \sum_{\beta,\gamma=1}^{N} h_{\beta\gamma}[c^\dagger_\beta c_\gamma, c_\alpha] = \sum_{\beta,\gamma=1}^{N} h_{\beta\gamma}\big(c^\dagger_\beta[c_\gamma, c_\alpha] + [c^\dagger_\beta, c_\alpha]c_\gamma\big) \tag{D.5a}$$

$$= \sum_{\beta,\gamma=1}^{N} h_{\beta\gamma}\big(-2c^\dagger_\beta c_\alpha c_\gamma + \delta_{\alpha\beta}c_\gamma - 2c_\alpha c^\dagger_\beta c_\alpha\big) = \sum_{\beta,\gamma=1}^{N} h_{\beta\gamma}\big(\delta_{\alpha\beta}c_\gamma - 2\{c^\dagger_\beta, c_\alpha\}c_\gamma\big) \tag{D.5b}$$

$$= \sum_{\beta,\gamma=1}^{N} h_{\beta\gamma}\big(\delta_{\alpha\beta}c_\gamma - 2\delta_{\alpha\beta}c_\gamma\big) = -\sum_{\gamma=1}^{N} h_{\alpha\gamma}c_\gamma. \tag{D.5c}$$

We thus have

$$\partial_t c_\alpha(t) = -\frac{i}{\hbar}\sum_{\gamma=1}^{N} h_{\alpha\gamma}c_\gamma(t). \tag{D.6}$$

This way we get

$$\Theta(t-t')\langle\{\partial_t c_\alpha(t), c^\dagger_\beta(t')\}\rangle = -\frac{i}{\hbar}\Theta(t-t')\sum_{\gamma=1}^{N}\langle\{c_\gamma(t), c^\dagger_\beta(t')\} = \sum_{\gamma=1}^{N} h_{\alpha\gamma}G_{\gamma\beta}(t,t') \tag{D.7a}$$

$$= \Big[HG(t,t')\Big]_{\alpha\beta}. \tag{D.7b}$$

The remaining term to handle contains the equal-time commutator $\{c_\alpha(t), c_\beta^\dagger(t)\}$ because of the Dirac delta $\delta(t-t')$, which can be handled as follows,

$$\{c_\alpha(t), c_\beta^\dagger(t)\} = e^{iHt/\hbar}c_\alpha e^{-iHt/\hbar}e^{iHt/\hbar}c_\beta^\dagger e^{-iHt/\hbar} + e^{iHt/\hbar}c_\beta^\dagger e^{-iHt/\hbar}e^{iHt/\hbar}c_\alpha e^{-iHt/\hbar} \tag{D.8a}$$

$$= e^{iHt/\hbar}\{c_\alpha, c_\beta^\dagger\}e^{-iHt/\hbar} = e^{iHt/\hbar}\delta_{\alpha\beta}e^{-iHt/\hbar} = \delta_{\alpha\beta}. \tag{D.8b}$$

Finally, we get

$$i\hbar\partial_t G_{\alpha\beta}(t,t') = \delta(t-t')\delta_{\alpha\beta} + \big[HG(t,t')\big]_{\alpha\beta} \quad \Leftrightarrow \quad \big[i\hbar\partial_t - H\big]G(t,t') = \delta(t-t')\mathbb{1}. \tag{D.9a}$$

D.2 . Fourier transform of the single-particle Green's function

Let us compute

$$G(\omega) = \int_{-\infty}^{+\infty} G(t)e^{i\omega t}\mathrm{d}t, \tag{D.10}$$

where again we make the $\boldsymbol{k}$ dependences implicit. The single-particle Hamiltonian H is defined as

$$H = \sum_{\alpha,\beta=1}^{N} h_{\alpha\beta}c_\alpha^\dagger c_\beta, \tag{D.11}$$

where the coefficients $h_{\alpha\beta}$ define a Hermitian matrix $h \in \mathcal{M}_N(\mathbb{C})$. Since h is Hermitian, we can find a unitary matrix U such that $h = U^\dagger \Lambda U$, with $\Lambda = \mathrm{diag}(\epsilon_1, \dots, \epsilon_N)$. We can express the coefficient $h_{\alpha\beta}$ as

$$h_{\alpha\beta} = \big[U^\dagger \Lambda U\big]_{\alpha\beta} = \sum_{n,m=1}^{N} \big[U^\dagger\big]_{\alpha n}\Lambda_{nm}U_{m\beta} = \sum_{n=1}^{N} \epsilon_n \big[U^\dagger\big]_{\alpha n}U_{n\beta}, \tag{D.12}$$

such that

$$H = \sum_{\alpha,\beta=1}^{N}\sum_{n=1}^{N} \epsilon_n \big[U^\dagger\big]_{\alpha n}U_{n\beta}c_\alpha^\dagger c_\beta = \sum_{n=1}^{N}\epsilon_n\left[\sum_{\alpha=1}^{N}\big[U^\dagger\big]_{\alpha n}c_\alpha^\dagger\right]\left[\sum_{\beta=1}^{N}U_{n\beta}c_\beta\right] = \sum_{n=1}^{N}\epsilon_n\gamma_n^\dagger\gamma_n, \tag{D.13}$$

with

$$\gamma_n = \sum_{\alpha=1}^{N}U_{n\alpha}c_\alpha, \quad \gamma_n^\dagger = \sum_{\alpha=1}^{N}\big[U^\dagger\big]_{\alpha n}c_\alpha^\dagger. \tag{D.14}$$

We can invert the transformation, so that

$$c_\alpha = \sum_{n=1}^{N}\big[U^\dagger\big]_{\alpha n}\gamma_n, \quad c_\alpha^\dagger = \sum_{n=1}^{N}U_{n\alpha}\gamma_n^\dagger \tag{D.15}$$

The Green function's coefficients can thus be re-expressed as

$$G_{\alpha\beta}(t) = -\frac{i}{\hbar}\Theta(t)\langle\{c_\alpha(t), c_\beta^\dagger\}\rangle = -\frac{i}{\hbar}\Theta(t)\sum_{n,m=1}^{N}\big[U^\dagger\big]_{\alpha n}U_{m\beta}\langle\{\gamma_n(t), \gamma_m\}\rangle. \tag{D.16}$$

We can compute $\gamma_n(t)$ by considering its time derivative

$$\partial_t \gamma_n(t) = \frac{i}{\hbar} e^{iHt/\hbar} \big[H, \gamma_n\big] e^{-iHt/\hbar}, \tag{D.17}$$

and the commutator

$$\big[H, \gamma_n\big] = \sum_{m=1}^{N} \epsilon_m \big[\gamma_m^\dagger \gamma_m, \gamma_n\big] = \sum_{m=1}^{N} \epsilon_m \Big(\gamma_m^\dagger \big[\gamma_m, \gamma_n\big] + \big[\gamma_m^\dagger, \gamma_n\big]\gamma_m\Big) \tag{D.18a}$$

$$= \sum_{m=1}^{N} \epsilon_m \Big(-2\gamma_m^\dagger \gamma_n \gamma_m + \delta_{mn}\gamma_m - 2\gamma_n \gamma_m^\dagger \gamma_m\Big) = \sum_{m=1}^{N} \epsilon_m \Big(\delta_{mn}\gamma_m - 2\big\{\gamma_m^\dagger, \gamma_n\big\}\gamma_m\Big) = -\epsilon_n \gamma_n. \tag{D.18b}$$

This yields

$$\partial_t \gamma_n(t) = \frac{i}{\hbar} e^{iHt/\hbar}(-\epsilon_n \gamma_n) e^{-iHt/\hbar} = -\frac{i}{\hbar}\epsilon_n \gamma_n(t) \quad \Rightarrow \quad \gamma_n(t) = e^{-i\epsilon_n t/\hbar}\gamma_n, \tag{D.19}$$

which in turn gives

$$\langle\big\{\gamma_n(t), \gamma_m^\dagger\big\}\rangle = e^{-i\epsilon_n t/\hbar}\langle\big\{\gamma_n, \gamma_m^\dagger\big\}\rangle = e^{-i\epsilon_n t/\hbar}\delta_{nm}. \tag{D.20}$$

The Green's function thus becomes

$$G_{\alpha\beta}(t) = -\frac{i}{\hbar}\Theta(t) \sum_{n,m=1}^{N} \big[U^\dagger\big]_{\alpha n} U_{m\beta} \langle\big\{\gamma_n(t), \gamma_m\big\}\rangle = -\frac{i}{\hbar}\Theta(t) \sum_{n=1}^{N} \big[U^\dagger\big]_{\alpha n} U_{n\beta} e^{-i\epsilon_n t/\hbar}. \tag{D.21}$$

Coming back to its Fourier transform,

$$G_{\alpha\beta}(\omega) = -\frac{i}{\hbar} \sum_{n=1}^{N} \big[U^\dagger\big]_{\alpha n} U_{n\beta} \int_{-\infty}^{+\infty} \Theta(t) e^{-i\epsilon_n t/\hbar} e^{i\omega t} \mathrm{d}t. \tag{D.22}$$

We see that the integral is not convergent. We thus introduce a regulator $\eta \to 0^+$, such that

$$G_{\alpha\beta}(\omega) = -\frac{i}{\hbar} \lim_{\eta\to 0^+} \sum_{n=1}^{N} \big[U^\dagger\big]_{\alpha n} U_{n\beta} \int_{-\infty}^{+\infty} \Theta(t) \exp\left(i\frac{(\hbar\omega - \epsilon_n)t}{\hbar}\right) \exp\Big(-\frac{\eta}{\hbar}t\Big)\mathrm{d}t \tag{D.23a}$$

$$= -\frac{i}{\hbar} \lim_{\eta\to 0^+} \sum_{n=1}^{N} \big[U^\dagger\big]_{\alpha n} U_{n\beta} \int_{0}^{+\infty} \exp\left(\frac{-\eta + i(\hbar\omega - \epsilon_n)}{\hbar}t\right)\mathrm{d}t \tag{D.23b}$$

$$= -\frac{i}{\hbar} \lim_{\eta\to 0^+} \sum_{n=1}^{N} \big[U^\dagger\big]_{\alpha n} U_{n\beta} \left[\frac{\hbar}{i(\hbar\omega - \epsilon_n) - \eta} \exp\left(\frac{-\eta + i(\hbar\omega - \epsilon_n)}{\hbar}t\right)\right]_0^{+\infty} \tag{D.23c}$$

$$= \frac{i}{\hbar} \lim_{\eta\to 0^+} \sum_{n=1}^{N} \big[U^\dagger\big]_{\alpha n} U_{n\beta} \frac{\hbar}{i(\hbar\omega - \epsilon_n) - \eta} = \lim_{\eta\to 0^+} \sum_{n=1}^{N} \big[U^\dagger\big]_{\alpha n} U_{n\beta} \frac{1}{\hbar\omega - \epsilon_n + i\eta} \tag{D.23d}$$

$$= \lim_{\eta\to 0^+} \sum_{n=1}^{N} \big[U^\dagger\big]_{\alpha n} \left[\mathrm{diag}\left(\frac{1}{\hbar\omega - \epsilon_n + i\eta}\right)\right]_{nn} U_{n\beta} \tag{D.23e}$$

$$= \lim_{\eta\to 0^+} \left[U^\dagger \,\mathrm{diag}\left(\frac{1}{\hbar\omega - \epsilon_n + i\eta}\right) U\right]_{\alpha\beta} = \left[\lim_{\eta\to 0^+} \frac{1}{\hbar\omega\mathbb{1} - H + i\eta\mathbb{1}}\right]_{\alpha\beta}. \tag{D.23f}$$

E - Appendices of Chapter 6

E.1 . Gap equation for non-unitary pairings

We take the gap equation

$$\Delta_{\boldsymbol{k}}^{\sigma_1\sigma_2} = -\sum_{\sigma_3\sigma_4}\sum_{\boldsymbol{k'}} V_{\text{eff},\boldsymbol{k}\boldsymbol{k'}}^{\substack{\sigma_2\sigma_1\\ \sigma_3\sigma_4}} \mathscr{I}_\beta^{\sigma_3\sigma_4}(\boldsymbol{k'}). \tag{E.1}$$

and pick a non-unitary triplet pairing. In that case, the kernel is given by [187]

$$\hat{\mathscr{I}}_\beta(\boldsymbol{k}) = i\boldsymbol{\alpha}_\beta(\boldsymbol{k})\cdot\boldsymbol{\sigma}\sigma_y \tag{E.2}$$

with

$$\begin{aligned}\boldsymbol{\alpha}_\beta(\boldsymbol{k}) = &\frac{1}{2E_{\boldsymbol{k},+}}\left(\boldsymbol{d}(\boldsymbol{k}) + \frac{1}{|\boldsymbol{q}(\boldsymbol{k})|}\boldsymbol{d}(\boldsymbol{k})\times\boldsymbol{q}(\boldsymbol{k})\right)\tanh\left(\frac{\beta}{2}E_{\boldsymbol{k},+}\right)\\ &+\frac{1}{2E_{\boldsymbol{k},-}}\left(\boldsymbol{d}(\boldsymbol{k}) - \frac{1}{|\boldsymbol{q}(\boldsymbol{k})|}\boldsymbol{d}(\boldsymbol{k})\times\boldsymbol{q}(\boldsymbol{k})\right)\tanh\left(\frac{\beta}{2}E_{\boldsymbol{k},-}\right).\end{aligned} \tag{E.3}$$

Moreover, $\boldsymbol{q} = i\boldsymbol{d}\times\boldsymbol{d}^*$ and $E_{\boldsymbol{k},\pm} = \sqrt{\xi_{\boldsymbol{k}}^2 + |\boldsymbol{d}(\boldsymbol{k})|^2 \pm |\boldsymbol{q}(\boldsymbol{k})|}$. Since $\boldsymbol{d}$ is an odd function of $\boldsymbol{k}$ and $E_{\boldsymbol{k},\pm}$ an even one, $\boldsymbol{\alpha}_\beta$ is an odd function of $\boldsymbol{k}$ and therefore the kernel $\hat{\mathscr{I}}$ as well. Another thing to notice is that expliciting the matrix form of the kernel yields

$$\hat{\mathscr{I}}_\beta(\boldsymbol{k}) = \begin{pmatrix} -\alpha_{\beta,x}(\boldsymbol{k}) + i\alpha_{\beta,y}(\boldsymbol{k}) & \alpha_{\beta,z}(\boldsymbol{k}) \\ \alpha_{\beta,z}(\boldsymbol{k}) & \alpha_{\beta,x}(\boldsymbol{k}) + i\alpha_{\beta,y}(\boldsymbol{k})\end{pmatrix} \tag{E.4}$$

which is obviously a symmetric matrix. Putting the two together, we have

$$\mathscr{I}_\beta^{\sigma_3\sigma_4}(-\boldsymbol{k}) = -\mathscr{I}_\beta^{\sigma_3\sigma_4}(\boldsymbol{k}) = \mathscr{I}_\beta^{\sigma_4\sigma_3}(\boldsymbol{k}) \tag{E.5}$$

which is what we used to show that the Berry dipole term does not change the gap or the critical temperature. So the latter also extends to non-unitary triplet pairings.

F - Appendices of Chapter 7

F.1 . Bilayer model

Here, we explain in more detail the choice shown in Fig. 7.1 to only include two layers of Ti atoms in the TB model. As said in the main text, one should *a priori* consider three layers, so a nine band TB model (without spin). In Fig. F.1 we show a comparison of the band dispersions obtained from the bilayer TB model (on the left) and a similarly obtained nine band trilayer TB model.

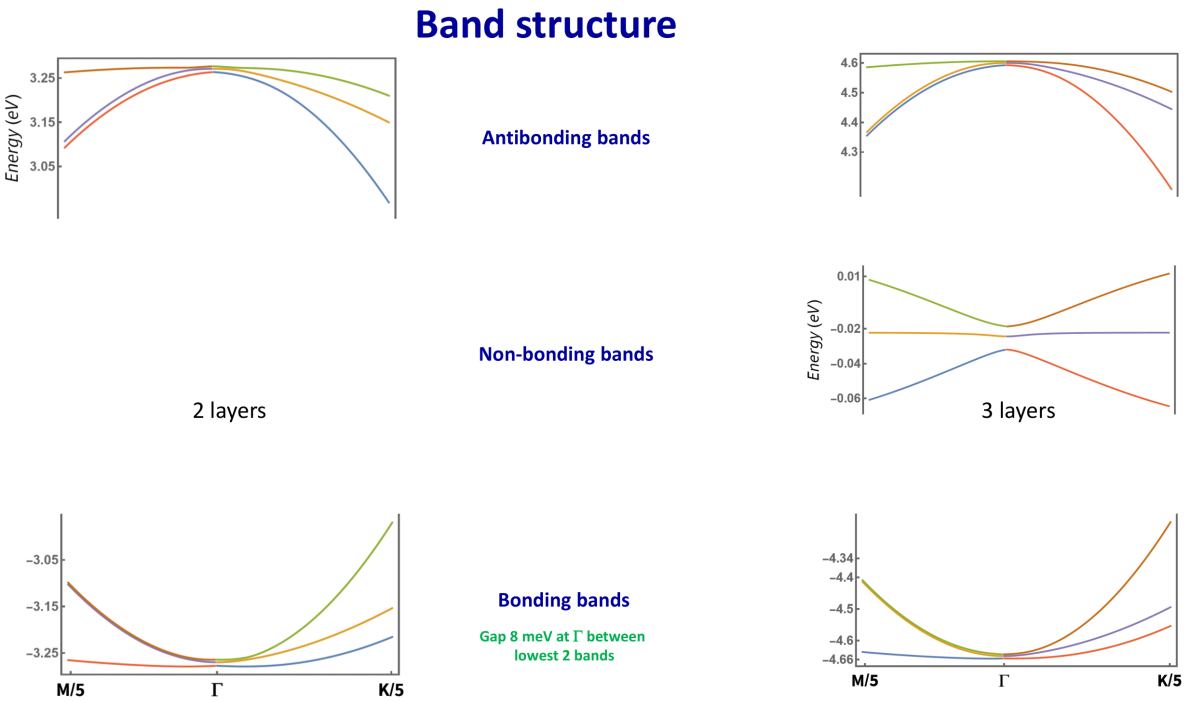

Figure F.1: Comparison between the bilayer (left) and trilayer (right) TB models.

First, we see that the bonding and anti-bonding triplets are not visibly modified by the addition of the third layer. Furthermore, the three additional bands are approximately at zero energy, and therefore several eVs away from the band we are concerned about, in the bonding triplet. Second, also the eigenstates of the bonding triplet should not be modified by the additional bands because, again, of their energy difference. Finally, from Eq. (F.1), we also see that following the same argument, the quantum geometric tensor [27] should not be modified by the additional bands.

$$Q^n_{\mu\nu} = \sum_{m\neq n} \frac{\langle u_n|\,\partial_\mu H\,|u_m\rangle\,\langle u_m|\,\partial_\nu H\,|u_n\rangle}{(E_n - E_m)^2}. \tag{F.1}$$

In conclusion, we can reasonably discard the third layer and consider a bilayer model of Ti atoms, as shown in Fig. 7.1.

F.2 . Expression of the kinetic terms

Hoppings are between two neighboring layers, with amplitude t for π-hoppings and t_d for δ-hoppings between blue and red sites (Fig. 1). The origin of the basis lattice vectors is chosen at the center of an hexagon. e, f and g have the following expressions [212, 274],

$$e = -\Big\{ \exp(ik_y) + \exp\Big[i\Big(\frac{\sqrt{3}}{2}k_x - \frac{1}{2}k_y\Big)\Big]\Big\} - r\exp\Big[-i\Big(\frac{\sqrt{3}}{2}k_x + \frac{1}{2}k_y\Big)\Big] \tag{F.2a}$$

$$f = -\Big\{ \exp(ik_y) + \exp\Big[-i\Big(\frac{\sqrt{3}}{2}k_x + \frac{1}{2}k_y\Big)\Big]\Big\} - r\exp\Big[i\Big(\frac{\sqrt{3}}{2}k_x - \frac{1}{2}k_y\Big)\Big] \tag{F.2b}$$

$$g = -\exp\Big(-\frac{i}{2}k_y\Big) \times 2\cos\Big(\frac{\sqrt{3}}{2}k_x\Big) - r\exp(ik_y) \tag{F.2c}$$

, with $r = t_d/t$. As example, we schematize the case of the d_{xy} orbitals corresponding to the hopping term g in Fig. F.2, and we derive g. First, consider the hopping pictured on the right of Fig. F.2, going

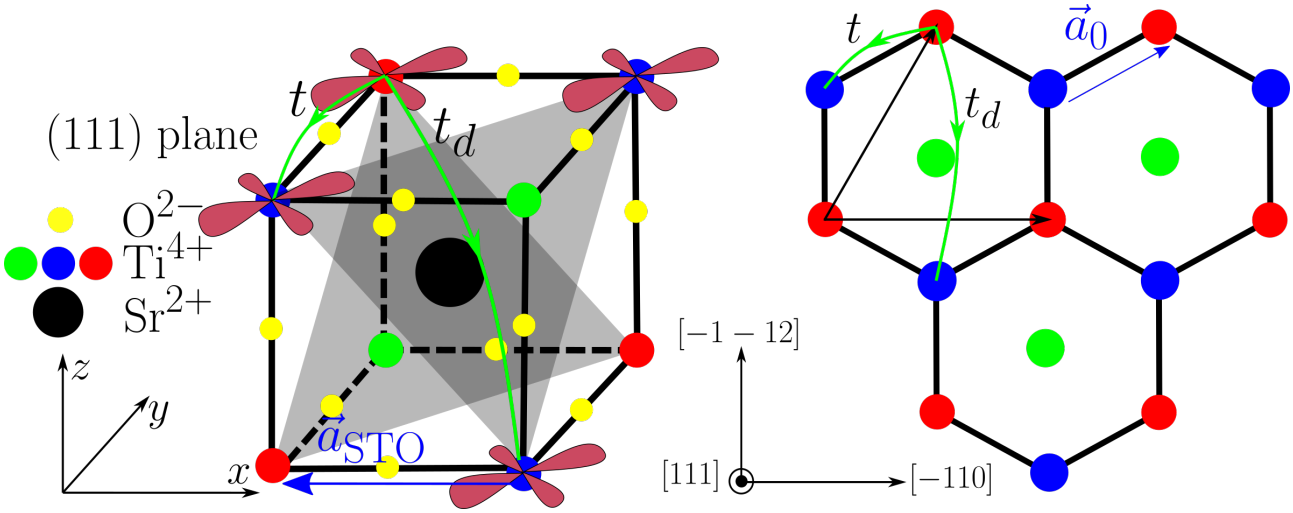

Figure F.2: Diagram of the inter-layer and intra-orbital hoppings for the d_{xy} orbitals. On the left, the 3D cubic lattice and the d_{xy} orbitals of the Ti atoms. Hopping paths and corresponding amplitudes are shown as green color lines. On the right, the associated projection in the (111) orientation.

from the top red atom to the neighbouring left blue atom, with an amplitude of t. As seen in Fig. F.2, the associated overlap in the cubic lattice is a π-overlap through the intermediate O site. The amplitude of this hopping is $t = 1.6$eV. The associated phase is $\exp(-i\mathbf{k}\cdot\mathbf{a}_2)$ with $\mathbf{a}_1 = (-\sqrt{3}/2, 3/2)$, by equivalence with the red atom in the same motif. The similar hopping to the right also has amplitude t and is associated to the phase $\exp(-i\mathbf{k}\cdot\mathbf{a}_1)$ with $\mathbf{a}_1 = (\sqrt{3}/2, 3/2)$. The other hopping from the top red atom to the lower blue atom is, as seen on the left of Fig. F.2, the result of the direct overlap of the d orbitals of the two atoms. It is therefore a δ-hopping, associated with an energy amplitude $t_d = 70$meV. As for its phase, it does not come with a phase shift, as the two atoms are part of the same motif. This way, and shifting every term by $\exp(ik_y)$ so that the origin is at the central green atom, the interlayer $d_{xy} - d_{xy}$ hopping term is given by

$$
\begin{aligned}
g &= -te^{-i/2(-\sqrt{3}k_x+k_y)} - te^{-i/2(\sqrt{3}k_x+k_y)} - t_d e^{ik_y} \\
&= -2te^{-ik_y/2}\cos\left(\frac{\sqrt{3}}{2}k_x\right) - t_d e^{ik_y}.
\end{aligned} \tag{F.3}
$$

F.3 . Derivation of the orbital mixing term

In the orbital basis, H_{om} can be written as $A \otimes B$ with A and B acting in the layer and orbital subspaces respectively. The orbital mixing term consists of the interlayer and interorbital couplings so the diagonal elements of A and B must vanish. The honeycomb lattice structure seen in Fig. 7.1 has the $\mathcal{C}_{3v}$ symmetry. In order to respect the latter, we assume that all the couplings have the same magnitude in energy and that those between layer 1 to layer 2 are the same as those from layer 2 to layer 1. Therefore we can write

$$
A \otimes B = c_0 \begin{pmatrix} 0 & a \\ a & 0 \end{pmatrix} \otimes \begin{pmatrix} 0 & b_1 & b_2 \\ b_3 & 0 & b_4 \\ b_5 & b_6 & 0 \end{pmatrix}, \tag{F.4}
$$

where the coefficients are complex, and of modulus 1 in order to have the same magnitude c_0 in energy. They are further constrained by the fact that the term must be Hermitian. Using $(A \otimes B)^\dagger = A^\dagger \otimes B^\dagger$, this means that we must have $a^* = a$, $b_3 = b_1^*$, $b_5 = b_2^*$ and $b_6 = b_3^*$. We choose $a = 1$, such that

$$
A \otimes B = c_0 \tau_x \otimes \begin{pmatrix} 0 & b_1 & b_2 \\ b_1^* & 0 & b_3 \\ b_2^* & b_3^* & 0 \end{pmatrix}. \tag{F.5}
$$

We then introduce (ϕ_i, ψ_i) such that $b_i(\mathbf{k}) = \cos(\phi_i(\mathbf{k})) + i\sin(\psi_i(\mathbf{k}))$. We look for ϕ_i and ψ_i that are linear combinations of k_x and k_y, which is natural for TB models. These hoppings are also anti-symmetric under an inversion operation $\mathbf{r} \longmapsto -\mathbf{r}$ [215], which adds the constraint $b_i(-\mathbf{k}) = -b_i(\mathbf{k})$ since in $\exp(i\mathbf{k}\cdot\mathbf{r})$ doing $\mathbf{r} \longmapsto -\mathbf{r}$ is equivalent to $\mathbf{k} \longmapsto -\mathbf{k}$. Hence, $\cos(\phi_i(\mathbf{k})) = 0$. Writing the allowed hoppings between the red and blue sites explicitly (Fig. 7.1) with the above requirements then gives $b_i(\mathbf{k}) = i\sin(\psi_i(\mathbf{k})) = i\sin(\alpha_i k_x + \beta_i k_y)$, with $\psi_i(\mathbf{k}) = \alpha_i k_x + \beta_i k_y$. Next, the orbital mixing term needs to obey the $\mathcal{C}_{3v}$ symmetry, i.e. a $2\pi/3$ rotation with an axis perpendicular to the (111) plane and a mirror symmetry parallel to the $(\overline{1}12)$ orientation. The $2\pi/3$ rotation transforms $\mathbf{r} = (x, y, z)$ into $\mathbf{r}' = (z, x, y)$ in the original cubic unit cell. Therefore the orbitals are transformed as $(d_{yz}, d_{xz}, d_{xy}) \longmapsto (d_{xy}, d_{yz}, d_{xz})$. In order to obey this $\mathcal{C}_3$ symmetry, we must therefore have $b_1(\mathbf{k}') = b_3(\mathbf{k})$, $b_2(\mathbf{k}') = b_1^*(\mathbf{k})$ and $b_3(\mathbf{k}') = b_2^*(\mathbf{k})$ with $\mathbf{k}' = (-1/2k_x - \sqrt{3}/2k_y, \sqrt{3}/2k_x - 1/2k_y)$. The mirror operation maps $\mathbf{r} = (x, y, z)$ to $\mathbf{r}' = (y, x, z)$ and $\mathbf{k} = (k_x, k_y)$ to $\mathbf{k}' = (-k_x, k_y)$, so that the orbitals transform as $(d_{yz}, d_{xz}, d_{xy}) \longmapsto (d_{xz}, d_{yz}, d_{xy})$. In order to obey this symmetry, we must have $b_1(\mathbf{k}') = b_1^*(\mathbf{k})$, $b_2(\mathbf{k}') = b_3(\mathbf{k})$ and $b_3(\mathbf{k}') = b_2(\mathbf{k})$. These constraints on the b_is put constraints on the coefficients (α_i, β_i) by taking the low-k limit and identifying the k_x and k_y components (this is allowed since the constraints must be valid for all $\mathbf{k}$). The resulting system of equations puts five independent constraints such that $\beta_1 = 0$, $(\alpha_2, \beta_2) = (1/2\alpha_1, \sqrt{3}/2\alpha_1)$ and $(\alpha_3, \beta_3) = (-1/2\alpha_1, \sqrt{3}/2\alpha_1)$. We then recover Eq. (7.7) with $\alpha_1 = -\sqrt{3}$.

F.4 . Trigonal basis

Let U be the following unitary transformation in the $\{1,2\} \otimes \{\mathsf{X},\mathsf{Y},\mathsf{Z}\}$ basis

$$U = \tau_0 \otimes P, \quad P = \begin{pmatrix} -\frac{1}{\sqrt{2}} & -\frac{1}{\sqrt{6}} & \frac{1}{\sqrt{3}} \\ \frac{1}{\sqrt{2}} & -\frac{1}{\sqrt{6}} & \frac{1}{\sqrt{3}} \\ 0 & \frac{2}{\sqrt{6}} & \frac{1}{\sqrt{3}} \end{pmatrix}. \tag{F.6}$$

In this basis, the trigonal crystal field becomes diagonal,

$$P^\dagger d H_d P = \begin{pmatrix} d & 0 & 0 \\ 0 & d & 0 \\ 0 & 0 & -2d \end{pmatrix}. \tag{F.7}$$

The first two-fold degenerate eigenvalues represent the e_{+g} and e_{-g} orbitals while the third one represents the a_{1g} orbital. They are separated by an energy gap of $3d \simeq 10$ meV. The kinetic term is transformed as

$$H_{\mathsf{cin}} = t \begin{pmatrix} \frac{e+f}{2} & \frac{e-f}{2\sqrt{3}} & -\frac{e-f}{\sqrt{6}} \\ \frac{e-f}{2\sqrt{3}} & \frac{e+f+4g}{6} & -\frac{e+f-2g}{3\sqrt{2}} \\ -\frac{e-f}{\sqrt{6}} & -\frac{e+f-2g}{3\sqrt{2}} & \frac{e+f+g}{3} \end{pmatrix}, \tag{F.8}$$

while the orbital mixing term becomes

$$H_{\mathsf{om}} = c_0 \begin{pmatrix} 0 & iD & -iA \\ -iD & 0 & iB \\ iA & -iB & 0 \end{pmatrix}, \tag{F.9}$$

with

$$\begin{cases} A = -\frac{1}{\sqrt{6}}(\alpha + \beta - 2\delta) \\ B = \frac{1}{\sqrt{2}}(\alpha - \beta) \\ D = \frac{1}{\sqrt{3}}(\alpha + \beta + \delta). \end{cases} \tag{F.10}$$

F.5 . Gell-Mann matrices

$$\Lambda_1 = \begin{pmatrix} 0 & 1 & 0 \\ 1 & 0 & 0 \\ 0 & 0 & 0 \end{pmatrix}, \ \Lambda_2 = \begin{pmatrix} 0 & -i & 0 \\ i & 0 & 0 \\ 0 & 0 & 0 \end{pmatrix}, \ \Lambda_3 = \begin{pmatrix} 1 & 0 & 0 \\ 0 & -1 & 0 \\ 0 & 0 & 0 \end{pmatrix}, \ \Lambda_4 = \begin{pmatrix} 0 & 0 & 1 \\ 0 & 0 & 0 \\ 1 & 0 & 0 \end{pmatrix}$$
$$\Lambda_5 = \begin{pmatrix} 0 & 0 & -i \\ 0 & 0 & 0 \\ i & 0 & 0 \end{pmatrix}, \ \Lambda_6 = \begin{pmatrix} 0 & 0 & 0 \\ 0 & 0 & 1 \\ 0 & 1 & 0 \end{pmatrix}, \ \Lambda_7 = \begin{pmatrix} 0 & 0 & 0 \\ 0 & 0 & -i \\ 0 & i & 0 \end{pmatrix}, \ \Lambda_8 = \frac{1}{\sqrt{3}} \begin{pmatrix} 1 & 0 & 0 \\ 0 & 1 & 0 \\ 0 & 0 & -2 \end{pmatrix}. \tag{F.11}$$

F.6 . Validity of the quadratic three-band approximation

We now discuss the validity of the three-band approximation. Doing so amounts to neglecting the off-diagonal blocks in Eq. (7.13) which contain the confinement energy and the imaginary part of the kinetic term. From Ref. [275], the effect of such off-diagonal terms is in $\mathcal{O}\left(\frac{||E||^2}{\text{gap}}\right)$, where E is the off-diagonal perturbation. The numerically observed gap (with our choice of parameters) is around $6-7$ eV. The biggest contribution of the two terms is at zeroth and first order in k, i.e. in terms of scalar quantities, we have $E \sim V \pm itk$ to linear order. Therefore the intrinsic error of the three-band approximation is roughly given by

$$\frac{V^2+t^2k^2}{6.5\text{eV}} \simeq (1.5+400k^2)\text{meV}. \tag{F.12}$$

This means that if we want a precision on the order of 1 meV, we find that the approximation holds until $k \sim 0.1$, so about a tenth of the BZ. This is indeed what we find when we compare the band structure with and without the off-diagonal blocks. More precisely, the confinement energy globally shifts every band by 1 to 2 meV while the imaginary part of the kinetic term breaks the isotropy of the band structure obtained within the low-energy model and gives rise to the $\mathcal{C}_3$ symmetric structure of ellipses seen in experimental studies (see Ref. [212] for example). So the validity of the low-energy model is restrained to the first tenth of the BZ around the Γ point. Knowing this, what is the natural order of expansion we can do to the low-energy model ? The relevant terms will be the ones above or around our precision of a few meVs. For the orbital mixing term, the first two corrections are linear and cubic in k. We then have $c_0k \sim 4$ meV and $c_0k^3 \sim 0.04$ meV for $k \sim 0.1$, so we only take the linear term. As for the kinetic term, the first two corrections are of order tk^2 and tk^4. This gives $tk^2 \sim 10$ meV and $tk^4 \sim 0.1$ meV, we therefore only keep the quadratic term. In conclusion, we can thus expand our three-band model to quadratic order while being coherent with the three-band approximation.

F.7 . Quadratic expansion of H_3

Here, we derive the quadratic expansion of H_3 in Eq. (7.15). We remind the reader that the matrices are written in the trigonal basis. For the orbital mixing term, we have

$$H_{\text{om}} = \begin{pmatrix} 0 & 0 & ick_x \\ 0 & 0 & ick_y \\ -ick_x & -ick_y & 0 \end{pmatrix} + \mathcal{O}(k^3), \tag{F.13}$$

with $c = (3/\sqrt{2})c_0$. For the kinetic term, we have

$$\text{Re}(H_{\text{cin}}) = -t(2+r)\left(1-\frac{1}{4}k^2\right)\Lambda_0 + t\begin{pmatrix} -\frac{1}{8}(1-r)(k_x^2-k_y^2) & -\frac{1}{4}(1-r)k_xk_y & \frac{1}{2\sqrt{2}}(1-r)k_xk_y \\ -\frac{1}{4}(1-r)k_xk_y & \frac{1}{8}(1-r)(k_x^2-k_y^2) & \frac{1}{4\sqrt{2}}(1-r)(k_x^2-k_y^2) \\ \frac{1}{2\sqrt{2}}(1-r)k_xk_y & \frac{1}{4\sqrt{2}}(1-r)(k_x^2-k_y^2) & 0 \end{pmatrix} + \mathcal{O}(k^4), \tag{F.14}$$

where we separated the traceful and traceless parts using

$$\begin{pmatrix} a & 0 & 0 \\ 0 & b & 0 \\ 0 & 0 & c \end{pmatrix} = \frac{a+b+c}{3}\Lambda_0 + \frac{a-b}{2}\Lambda_3 + \frac{a+b-2c}{2\sqrt{3}}\Lambda_8, \tag{F.15}$$

in terms of the Gell-Mann matrices. Now, if we define $t_{\text{eff}} = (t - t_d)/8$, we indeed find Eq. (7.15), neglecting the quadratic terms whenever there already exists a linear term.

F.8 . Band structure of the spinless TB model

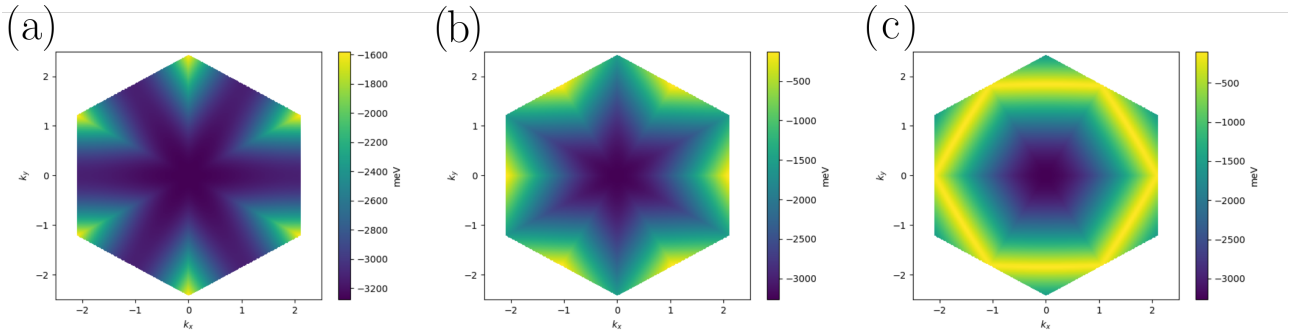

Figure F.3: Lower triplet of the TB model in Eq. (7.9). **(a)** Lowest band in the full BZ. **(b)** Second lowest band in the full BZ. **(c)** Third lowest band in the full BZ.

An important issue for our discussion here, from the electronic point of view, is the absence of other electron or hole pockets in the first BZ that would provide other and possibly different metallic and superconducting properties of the system. We therefore plot the dispersion of the lowest three bands in the entire BZ (see Fig. F.3), where we clearly see that the band minima are situated at the Γ point and that there are no other pockets in the BZ for our range of chemical potential. Note that Fig.F.3 was obtained using the spinless TB Hamiltonian, but the result also holds for the spinful TB Hamiltonian, there is no electron pocket other than the one we consider at the Γ point.

F.9 . Derivation of the spinful two-band low-energy model

We begin things at Eq. (7.19),

$$\tilde{H}_6 = \sigma_0 \otimes H_3 + H_{\text{SOC}}, \tag{F.16}$$

where we also apply $U_s = (\sigma_0 - i\sigma_y)/\sqrt{2}$ on the spin part, so that H_{SOC} reads

$$H_{\text{SOC}} = i\lambda\sigma_x \otimes \begin{pmatrix} 0 & -\frac{1}{\sqrt{3}} & \frac{2}{\sqrt{6}} \\ \frac{1}{\sqrt{3}} & 0 & 0 \\ -\frac{2}{\sqrt{6}} & 0 & 0 \end{pmatrix} + i\lambda\sigma_y \otimes \begin{pmatrix} 0 & \frac{1}{\sqrt{3}} & \frac{1}{\sqrt{6}} \\ -\frac{1}{\sqrt{3}} & 0 & \frac{1}{\sqrt{2}} \\ -\frac{1}{\sqrt{6}} & -\frac{1}{\sqrt{2}} & 0 \end{pmatrix} - i\lambda\sigma_z \otimes \begin{pmatrix} 0 & \frac{1}{\sqrt{3}} & \frac{1}{\sqrt{6}} \\ -\frac{1}{\sqrt{3}} & 0 & -\frac{1}{\sqrt{2}} \\ -\frac{1}{\sqrt{6}} & \frac{1}{\sqrt{2}} & 0 \end{pmatrix}. \tag{F.17}$$

We then use that fact that close to the Γ point, the exact eigenbasis should not be far from the one exactly at the Γ point. Consequently, we exactly diagonalize $\tilde{H}_6(\Gamma)$, for the particular case $\lambda = 3d$. This choice is in line with the experimentally determined values of the parameters and happens to greatly simplify the resulting expressions. We thus determine the eigenstates of the two lowest energies, which we denote as $|u_1\rangle$ and $|u_2\rangle$. We then define a two-band Hamiltonian H_2 in the latter's basis, i.e.

$$H_2 = \sum_{i,j=1}^{2} \langle u_i|\tilde{H}_6|u_j\rangle |u_i\rangle\langle u_j| \tag{F.18}$$

This way we get to Eqs. (7.20,7.21).

F.10 . Calculation of D_{conv} for a general quadratic and isotropic band dispersion.

Let us consider a general isotropic and quadratic band $\epsilon = \epsilon_0 + \alpha k^2$. Then, we can readily show that $D_{xx}^{\text{conv}} = D_{yy}^{\text{conv}} = D_{\text{conv}}$ and $D_{xy}^{\text{conv}} = 0$. We also see that $\mathscr{S}_{\text{occ}}(\mu) = B\big(0; \sqrt{\mu/\alpha}\big)$. We then have

$$D_{\text{conv}} = \frac{1}{2}\int_{\mathscr{S}_{\text{occ}}(\mu)} \frac{\Delta^2}{\left[\Delta^2 + (\alpha k^2 - \mu)^2\right]^{3/2}} 4\alpha^2 k^2 \mathcal{D}_2 \mathbf{k} \tag{F.19a}$$

$$\propto \frac{2\alpha^2}{(2\pi)^2}\int_0^{2\pi}\int_0^{\sqrt{\mu/\alpha}} \frac{\Delta^2}{\left[\Delta^2 + (\alpha k^2 - \mu)^2\right]^{3/2}} k^3 dk d\theta \tag{F.19b}$$

$$= \frac{2\alpha^2}{2\pi}\int_0^{\sqrt{\mu/\alpha}} \frac{\Delta^2}{\left[\Delta^2 + (\alpha k^2 - \mu)^2\right]^{3/2}} k^3 dk \tag{F.19c}$$

$$= \frac{\alpha^2}{\pi}\frac{1}{2\alpha^2}\int_0^{\mu} \frac{\Delta^2}{\left[\Delta^2 + (\epsilon - \mu)^2\right]^{3/2}} \epsilon d\epsilon = \frac{1}{2\pi}\Big(\sqrt{\Delta^2 + \mu^2} - \Delta\Big). \tag{F.19d}$$

G - Appendices of Chapter 8

G.1 . Expansion of the potential in Eq. (8.18)

Let $\boldsymbol{\rho} = \boldsymbol{r}_1 - \boldsymbol{r}_2$ such that $\langle \boldsymbol{\rho} \rangle_n = \langle \boldsymbol{r}_1 \rangle_n - \langle \boldsymbol{r}_2 \rangle_n$. Then, expanding the projected potential to second order yields

$$\langle V(\langle \boldsymbol{\rho} \rangle_n + \boldsymbol{\delta\rho}) \rangle_n = V(\langle \boldsymbol{\rho} \rangle_n + \langle \delta\rho_\mu \rangle_n \partial_{\rho_\mu} V(\langle \boldsymbol{\rho} \rangle_n) + \frac{1}{2} \langle \delta\rho_\mu \delta\rho_\nu \rangle_n \partial_{\rho_\mu} \partial_{\rho_\nu} V(\langle \boldsymbol{\rho} \rangle_n). \tag{G.1}$$

By linearity of $\langle \cdot \rangle_n$, the first order term vanishes. As for the second order term, defining $\delta_{1\mu} = \delta r_{1,\mu}$ and $\delta_{2\mu} = \delta r_{2,\mu}$, we can rewrite $\langle \delta\rho_\mu \delta\rho_\nu \rangle_n$ as

$$\langle \delta\rho_\mu \delta\rho_\nu \rangle_n = \langle (\delta_{1\mu} - \delta_{2\mu})(\delta_{1\nu} - \delta_{2\nu}) \rangle_n = \langle \delta_{1\mu}\delta_{1\nu} \rangle_n + \langle \delta_{2\mu}\delta_{2\nu} \rangle_n - \langle \delta_{1\mu}\delta_{2\nu} \rangle_n - \langle \delta_{2\mu}\delta_{1\nu} \rangle_n. \tag{G.2}$$

Assuming the quantum fluctuations of the two Bloch wavepackets to be uncorrelated, we then have $\langle \delta_{1\mu}\delta_{2\nu} \rangle_n = \langle \delta_{2\mu}\delta_{1\nu} \rangle_n = 0$, so that

$$\langle \delta\rho_\mu \delta\rho_\nu \rangle_n = \langle \delta_{1\mu}\delta_{1\nu} \rangle_n + \langle \delta_{2\mu}\delta_{2\nu} \rangle_n = Q^n_{\mu\nu} + Q^n_{\mu\nu} = 2Q^n_{\mu\nu}, \tag{G.3}$$

with $Q^n_{\mu\nu}(\boldsymbol{k}) = Q^{n\uparrow}_{\mu\nu}(\boldsymbol{k}) = Q^{n\downarrow}_{\mu\nu}(-\boldsymbol{k})$. Replacing $\langle \boldsymbol{\rho} \rangle_n$ by $\boldsymbol{\rho}$, we then find Eq. (8.20)

G.2 . Simplification of the averaged effective interaction for 2D massive Dirac fermions

As the linear terms in $\boldsymbol{k'}$ vanish, $\langle V^{\text{eff}}_{\boldsymbol{kk'}} \rangle$ becomes

$$\langle V^{\text{eff}}_{\boldsymbol{kk'}} \rangle = \left[1 - g^n_{\mu\mu}(\boldsymbol{k}) k_\mu^2 - 2 \sum_{\mu<\nu} g^n_{\mu\nu}(\boldsymbol{k}) k_\mu k_\nu \right] \langle V_{\boldsymbol{kk'}} \rangle - g^n_{\mu\mu}(\boldsymbol{k}) \langle k'^2_\mu V_{\boldsymbol{kk'}} \rangle - 2 \sum_{\mu<\nu} g^n_{\mu\nu}(\boldsymbol{k}) \langle k'_\mu k'_\nu V_{\boldsymbol{kk'}} \rangle. \tag{G.4}$$

Restricting the discussion to two-dimensional massive Dirac fermions, we have

$$g^n_{\mu\mu}(\boldsymbol{k}) k_\mu^2 + 2 \sum_{\mu<\nu} g^n_{\mu\nu}(\boldsymbol{k}) k_\mu k_\nu = \frac{\lambda_c^2}{4(1+\lambda_c^2 k^2)^2} \left[(1+\lambda_c^2 k_y^2) k_x^2 + (1+\lambda_c^2 k_x^2) k_y^2 - 2\lambda_c^2 k_x^2 k_y^2 \right] = \frac{\lambda_c^2 k^2}{4(1+\lambda_c^2 k^2)^2}. \tag{G.5}$$

As for the other terms, we find

$$g^n_{\mu\mu}(\boldsymbol{k}) k'^2_\mu + 2 \sum_{\mu<\nu} g^n_{\mu\nu}(\boldsymbol{k}) k'_\mu k'_\nu = \frac{\lambda_c^2}{4(1+\lambda_c^2 k^2)^2} \left[(1+\lambda_c^2 k_y^2) k'^2_x + (1+\lambda_c^2 k_x^2) k'^2_y - 2\lambda_c^2 k_x k_y k'_x k'_y \right] \tag{G.6}$$

$$= \frac{\lambda_c^2}{4(1+\lambda_c^2 k^2)^2} \left[k'^2 + \lambda_c^2 (k_x k'_y - k'_x k_y)^2 \right]. \tag{G.7}$$

$$g^n_{\mu\mu}(\boldsymbol{k}) k'^2_\mu + 2 \sum_{\mu<\nu} g^n_{\mu\nu}(\boldsymbol{k}) k'_\mu k'_\nu = \frac{\lambda_c^2 k_F^2}{4(1+\lambda_c^2 k_F^2)^2} \left[1 + \lambda_c^2 k_F^2 \sin^2(\theta - \phi) \right] \tag{G.8}$$

Using the specified interaction, and parametrizing $\boldsymbol{k}' = k_F(\cos\phi, \sin\phi)$ and $\boldsymbol{k} = k_F(\cos\theta, \sin\theta)$, then yields

$$\langle V^{\text{eff}}_{\boldsymbol{k}\boldsymbol{k}'}\rangle = -\left[1 - \frac{\lambda_c^2 k^2}{4(1+\lambda_c^2 k^2)^2}\right]V + \frac{\lambda_c^2}{4(1+\lambda_c^2 k^2)^2}\langle\left[1 + \lambda_c^2 k^2 \sin^2(\theta-\phi)\right]k'^2\rangle V. \tag{G.9}$$

Now, similarly to Chapter 6, we restrict the formation of Cooper pairs to the Fermi surface, such that $g_{\boldsymbol{k}} = \delta(k - k_F)$, which is spherically symmetric if s-wave pairing is assumed. For coherence, we then also take $k \simeq k_F$, which thereby yields

$$\langle V^{\text{eff}}_{\boldsymbol{k}\boldsymbol{k}'}\rangle \simeq -\left[1 - \frac{\lambda_c^2 k_F^2}{4(1+\lambda_c^2 k_F^2)^2} - \frac{\lambda_c^2 k_F^2(1+\lambda_c^2 k_F^2/2)}{4(1+\lambda_c^2 k_F^2)^2}\right]V \tag{G.10}$$

$$= -\left[1 - \frac{\lambda_c^2 k_F^2(4+\lambda_c^2 k_F^2)}{8(1+\lambda_c^2 k_F^2)^2}\right]V. \tag{G.11}$$

H - Appendices of Chapter 9

H.1 . Proof of the eigenvector eigenvalue relation

There are many proofs of Eq (9.4), we will use the adjugate proof [247]. First, let $A = \epsilon_{n_0}\mathbb{1} - H$ for some n_0, and $\lambda_n(A), \mu_n(A)$ be the respective eigenvalues of A and $\mathrm{adj}(A)$. The two matrices are linked by the Laplace relation,

$$A\,\mathrm{adj}(A) = \det(A)\mathbb{1}. \tag{H.1}$$

Assuming $\epsilon_n \neq \epsilon_{n_0}$, A is invertible and therefore $\mathrm{adj}(A) = \det(A)A^{-1}$, yielding

$$\mu_n(A) = \frac{\det(A)}{\lambda_n(A)} = \prod_{\substack{m=1\\m\neq n}}^{N} \lambda_m(A). \tag{H.2}$$

Moreover, $\mathrm{adj}(A)$ is diagonalizable in the same basis as A, namely the vectors $|u_n\rangle$,

$$\mathrm{adj}(A) = \sum_{n=1}^{N} \prod_{\substack{m=1\\m\neq n}}^{N} \lambda_m(A)\,|u_n\rangle\langle u_n|\,. \tag{H.3}$$

Now since $A = \epsilon_{n_0}\mathbb{1} - H$, we have $\lambda_m(A) = \epsilon_{n_0} - \epsilon_m$ and

$$\mu_n(A) = \prod_{\substack{m=1\\m\neq n}}^{N} \left(\epsilon_{n_0} - \epsilon_m\right) = 0 \;\text{ if }\; n_0 \neq n, \tag{H.4}$$

since otherwise there will be a term in the product for which $m = n_0$. We thus find

$$\mathrm{adj}\left(\epsilon_{n_0}\mathbb{1} - H\right) = \prod_{\substack{m=1\\m\neq n_0}}^{N} \left(\epsilon_{n_0} - \epsilon_m\right)|u_{n_0}\rangle\langle u_{n_0}|\,. \tag{H.5}$$

Let us rename n_0 as n for simplicity. Taking the (i,j) element of the last equation then gives two equalities. First,

$$\begin{aligned}\langle\phi_i|\,\mathrm{adj}\left(\epsilon_n\mathbb{1} - H\right)|\phi_j\rangle &= \prod_{\substack{m=1\\m\neq n}}^{N}\left(\epsilon_n - \epsilon_m\right)\langle\phi_i|u_n\rangle\langle u_n|\phi_j\rangle \\ &= u_n^{(i)}\left(u_n^{(j)}\right)^* \prod_{\substack{m=1\\m\neq n}}^{N}\left(\epsilon_n - \epsilon_m\right),\end{aligned} \tag{H.6}$$

and second, by the definition of the adjugate matrix,

$$\langle\phi_i|\,\mathrm{adj}\left(\epsilon_n\mathbb{1} - H\right)|\phi_j\rangle = (-1)^{i+j}\det\left[\epsilon_n\mathbb{1} - H\right]_{ji}. \tag{H.7}$$

Putting the two equalities together then yields the generalized eigenvector-eigenvalue relation

$$(-1)^{i+j}\det\left[\epsilon_n\mathbb{1}-H\right]_{ji}=u_n^{(i)}\left(u_n^{(j)}\right)^*\prod_{\substack{m=1\\m\neq n}}^{N}\left(\epsilon_n-\epsilon_m\right). \tag{H.8}$$

Restricting the latter to the $i=j$ case and noticing that $\left[\epsilon_n\mathbb{1}-H\right]_{jj}=\epsilon_n\mathbb{1}-[H]_{jj}$, we then get Eq. (9.4),

$$\prod_{m=1}^{N-1}\left(\epsilon_n-\zeta_{mj}\right)=\left|u_n^{(j)}\right|^2\prod_{\substack{m=1\\m\neq n}}^{N}\left(\epsilon_n-\epsilon_m\right). \tag{H.9}$$

Applying the latter to the product $u_n^{(i)}u_n^{(j)}$, we get

$$\left|u_n^{(i)}\right|^2\left|u_n^{(j)}\right|^2=\frac{\prod_{m=1}^{N-1}\left(\epsilon_n-\zeta_{mi}\right)\left(\epsilon_n-\zeta_{mj}\right)}{\prod_{\substack{m=1\\m\neq n}}^{N}\left(\epsilon_n-\epsilon_m\right)^2}. \tag{H.10}$$

Plugging that in the generalized eigenvector-eigenvalue relation then gives the relative phase,

$$e^{i(\phi_n^{(i)}-\phi_n^{(j)})}=\frac{(-1)^{i+j}\det\left[\epsilon_n\mathbb{1}-H\right]_{ji}}{\sqrt{\prod_{m=1}^{N-1}\left(\epsilon_n-\zeta_{mi}\right)\left(\epsilon_n-\zeta_{mj}\right)}}. \tag{H.11}$$

H.2 . Proof of the Cauchy interlacing inequality

We will use a Green's function based proof, as seen in Refs. [232, 242]. The j-th diagonal component of G can be expressed as follows

$$G_{jj}=\sum_{n=1}^{N}\frac{\left|u_n^{(j)}\right|^2}{\hbar\omega-\epsilon_n}=\frac{P_j(\hbar\omega)}{\prod_{n=1}^{N}\left(\hbar\omega-\epsilon_n\right)}, \tag{H.12}$$

with

$$P_j(X)=\sum_{n=1}^{N}\left|u_n^{(j)}\right|^2\prod_{\substack{m=1\\m\neq n}}^{N}\left(X-\epsilon_m\right). \tag{H.13}$$

Let us consider a specific $n_0\in[\![1,N]\!]$. The goal is to show that P_j changes sign between ϵ_{n_0} and ϵ_{n_0+1}, which will imply the existence of a zero since P_j is continuous, as a polynomial. Let's assume that $u_{n_0}^{(j)}$

and $u^{(j)}_{n_0+1}$ are not zero. First, we compute the sign of $P_j(\epsilon_{n_0})$,

$$\begin{aligned} P_j(\epsilon_{n_0}) &= \sum_{n=1}^{N} \left|u_n^{(j)}\right|^2 \prod_{\substack{m=1 \\ m\neq n}}^{N} \left(\epsilon_{n_0} - \epsilon_m\right) \\ &= \left|u_{n_0}^{(j)}\right|^2 \prod_{\substack{m=1 \\ m\neq n_0}}^{N} \left(\epsilon_{n_0} - \epsilon_m\right). \end{aligned} \tag{H.14}$$

Therefore,

$$\operatorname{sgn} P_j(\epsilon_{n_0}) = \prod_{\substack{m=1 \\ m\neq n_0}}^{N} \operatorname{sgn}\left(\epsilon_{n_0} - \epsilon_m\right). \tag{H.15}$$

But by our ordering convention of the eigenvalues,

$$\operatorname{sgn}\left(\epsilon_{n_0} - \epsilon_m\right) = \begin{cases} +1 \text{ if } m \in [\![1, n_0 - 1]\!] \\ -1 \text{ if } m \in [\![n_0 + 1, N]\!] \end{cases}, \tag{H.16}$$

which implies

$$\begin{aligned} \operatorname{sgn} P_j(\epsilon_{n_0}) &= \prod_{\substack{m=1 \\ m\neq n_0}}^{N} \operatorname{sgn}\left(\epsilon_{n_0} - \epsilon_m\right) \\ &= 1^{n_0-1-1+1}(-1)^{N-(n_0+1)+1} = (-1)^{N-n_0}. \end{aligned} \tag{H.17}$$

Similarly, for $P_j(\epsilon_{n_0+1})$, we have

$$\operatorname{sgn} P_j(\epsilon_{n_0+1}) = \prod_{\substack{m=1 \\ m\neq n_0+1}}^{N} \operatorname{sgn}\left(\epsilon_{n_0+1} - \epsilon_m\right), \tag{H.18}$$

and

$$\operatorname{sgn}\left(\epsilon_{n_0+1} - \epsilon_m\right) = \begin{cases} +1 \text{ if } m \in [\![1, n_0]\!] \\ -1 \text{ if } m \in [\![n_0 + 2, N]\!] \end{cases}, \tag{H.19}$$

so

$$\begin{aligned} \operatorname{sgn} P_j(\epsilon_{n_0+1}) &= \prod_{\substack{m=1 \\ m\neq n_0+1}}^{N} \operatorname{sgn}\left(\epsilon_{n_0+1} - \epsilon_m\right) \\ &= 1^{n_0-1+1}(-1)^{N-(n_0+2)+1} \\ &= (-1)^{N-n_0-1} = -\operatorname{sgn} P_j(\epsilon_{n_0}). \end{aligned} \tag{H.20}$$

Therefore P_j changes sign at least once between ϵ_{n_0} and ϵ_{n_0+1}, meaning P_j has at least one zero in that interval. Now the question is, how many zeros are there in $]\epsilon_{n_0}, \epsilon_{n_0+1}[$? We have shown that between two consecutive ϵ there is *at least* one zero of P_j. Since there are n different ϵ, P_j has at

least $n-1$ roots. But P_j is a polynome with degree $n-1$, therefore there must be *at most* one zero of P_j between ϵ_{n_0} and ϵ_{n_0+1}. We can then conclude, and state that the $n-1$ roots of P_j interlace the $\epsilon_1, \cdots, \epsilon_N$. And because of the zero-pole representation of G_{jj}, these roots are given by the $\zeta_{1j}, \cdots, \zeta_{Nj}$. We thus have proven the Cauchy interlacing inequality,

$$\forall n \in [\![1, N-1]\!], \quad \epsilon_n \leq \zeta_{nj} \leq \epsilon_{n+1}. \tag{H.21}$$